

On the catalytic hydrogenation of CO₂ and carboxylic acid esters

Citation for published version (APA):

Filonenko, G. (2015). On the catalytic hydrogenation of CO₂ and carboxylic acid esters Eindhoven: Technische Universiteit Eindhoven

Document status and date:

Published: 01/01/2015

Document Version:

Publisher's PDF, also known as Version of Record (includes final page, issue and volume numbers)

Please check the document version of this publication:

- A submitted manuscript is the version of the article upon submission and before peer-review. There can be important differences between the submitted version and the official published version of record. People interested in the research are advised to contact the author for the final version of the publication, or visit the DOI to the publisher's website.
- The final author version and the galley proof are versions of the publication after peer review.
- The final published version features the final layout of the paper including the volume, issue and page numbers.

[Link to publication](#)

General rights

Copyright and moral rights for the publications made accessible in the public portal are retained by the authors and/or other copyright owners and it is a condition of accessing publications that users recognise and abide by the legal requirements associated with these rights.

- Users may download and print one copy of any publication from the public portal for the purpose of private study or research.
- You may not further distribute the material or use it for any profit-making activity or commercial gain
- You may freely distribute the URL identifying the publication in the public portal.

If the publication is distributed under the terms of Article 25fa of the Dutch Copyright Act, indicated by the "Taverne" license above, please follow below link for the End User Agreement:

www.tue.nl/taverne

Take down policy

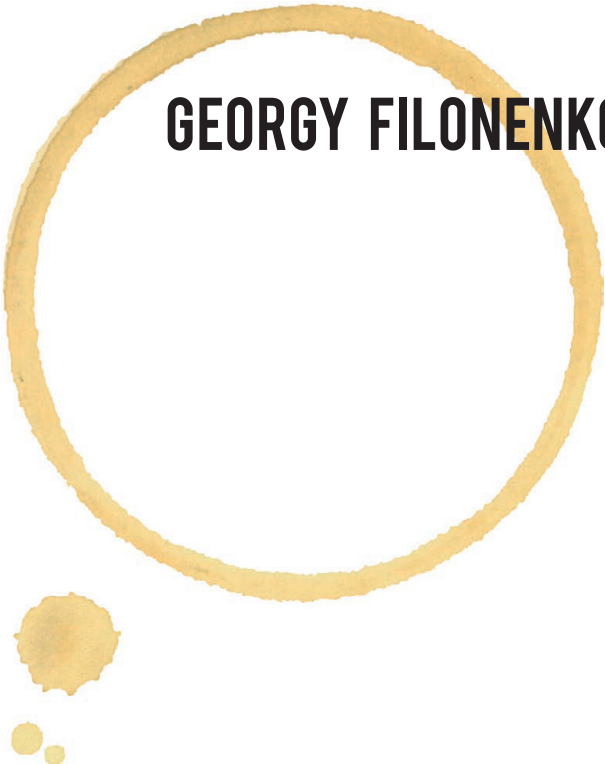
If you believe that this document breaches copyright please contact us at:

openaccess@tue.nl

providing details and we will investigate your claim.

**ON THE CATALYTIC HYDROGENATION
OF CO₂ AND
CARBOXYLIC ACID ESTERS**

GEORGY FILONENKO



On the catalytic hydrogenation of CO₂ and carboxylic acid esters

PROEFSCHRIFT

ter verkrijging van de graad van doctor aan de Technische Universiteit
Eindhoven, op gezag van de rector magnificus prof.dr.ir. C.J. van Duijn,
voor een commissie aangewezen door het College voor Promoties, in het
openbaar te verdedigen op dinsdag 28 april 2015 om 16:00 uur

door

Georgy Filonenko

geboren te Elizovo, Rusland

Dit proefschrift is goedgekeurd door de promotoren en de samenstelling van de promotiecommissie is als volgt:

voorzitter:	prof.dr.ir. J.C. Schouten
1 ^e promotor:	prof.dr.ir. E.J.M. Hensen
copromotor:	dr. E.A. Pidko
leden:	prof.dr. R.P. Sijbesma prof.dr. B. de Bruin (UvA) prof.dr. C. Coperét (ETH Zürich) prof.dr. C. Müller (Freie Universität Berlin)
adviseur:	dr. L. Lefort (DSM ChemTech R&D)

To you, Vera.

How wonderful that we have met with a paradox.

Now we have some hope of making progress.

-Niels Bohr

Georgy Filonenko

On the catalytic hydrogenation of CO₂ and carboxylic acid esters

A catalogue record is available from the Eindhoven University of Technology Library

ISBN: 978-90-386-3815-7

Copyright © 2015 by Georgy Filonenko

The work described in this thesis has been carried out within the Inorganic Materials Chemistry group and Institute for Complex Molecular Systems, Eindhoven University of Technology, The Netherlands. The research was supported by Technology Foundation STW and the Netherlands Organization for Scientific Research (NWO). The computational facilities were provided by SurfSARA with financial support from the NWO.



Subject headings: carbon dioxide, hydrogenation, reaction mechanism, metal-ligand cooperation, ruthenium, carboxylic acid esters, reaction kinetics.

Printed by: Gildeprint – The Netherlands

Cover design: Georgy Filonenko and Ivo Filot



Contents:

Chapter 1	<i>Introduction</i>	1
Chapter 2	<i>The impact of metal-ligand cooperation in hydrogenation of CO₂ with Ru-PNP pincer catalyst</i>	23
Chapter 3	<i>Highly efficient reversible hydrogenation of CO₂ with Ru-PNP catalyst. Fine control on both sides of the chemical equilibrium.</i>	47
Chapter 4	<i>Supported gold catalysts for hydrogenation of carbon dioxide to formates</i>	73
Chapter 5	<i>Synthesis and reactivity of lutidine-based bis-NHC ruthenium pincer complexes</i>	95
Chapter 6	<i>Lutidine-derived Ru-CNC pincer complexes for catalytic hydrogenation of CO₂ and carboxylic acid esters</i>	129
Chapter 7	<i>Amino bis-N-heterocyclic carbene pincer ligands for the efficient hydrogenation of esters</i>	149
Summary		171
Acknowledgement		176
List of publications		178
About the author		179

Introduction

Nihil sub sole novum

1.1 Catalytic hydrogenation

Concealed behind a simple definition of a chemical reaction upon which an H₂ equivalent is added to a substrate in the presence of a catalyst, catalytic hydrogenation reactions have the greatest impact on the human society. Discovered by Paul Sabatier in 1897,¹ catalytic hydrogenation sparked the rapid development of the chemical industry. Probably the most remarkable example in this class of reactions is the Haber-Bosch process used for the fixation of atmospheric nitrogen. This major energy consumer in chemical industry (ca. 1.5% of global energy)² provides over 80% of nitrogen found in human body tissues.³ Hydrogenation reactions are encountered in the vast majority of industrial processes ranging from oil refining and fuel production to fine chemical synthesis of pharmaceuticals. After a century of research and development, hydrogenation catalysts evolved from bulk metal powders and clays into sophisticated, rationally designed multicomponent heterogeneous and homogeneous systems. The scope of substrates of catalytic hydrogenation expanded substantially and, nowadays, we can efficiently perform reactions that seemed unfeasible 50 years ago. The majority of substrates are organic compounds that contain a reducible functionality. Depending on their nature, hydrogenation of these functional groups may require different conditions and different types of catalysts.

One class of compounds that has so far largely lacked attention from the catalysis community in the context of hydrogenation are derivatives of carboxylic and carbonic acids. Importance of these compounds can hardly be overestimated. The carboxylic acid ester functionality is common in natural compounds. Biomass feedstock, fats and oils contain a significant fraction of oxygen in the form of ester groups. Therefore, the efficient conversion of esters is expected to become more important for the chemical industry in the near future, considering the depletion of fossil feedstock and growing societal pressure for making chemical industry sustainable. Surprisingly, even such simple molecules as carbon dioxide (CO₂) present a challenge for catalytic hydrogenation. Being essentially a carbonic

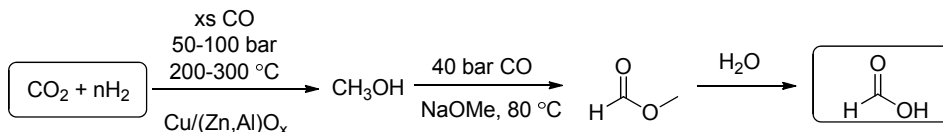
acid anhydride, CO₂ is the main product of fossil fuel combustion and one of the major greenhouse gases. Finally, it is an abundant carbon feedstock with yet unrealized potential. Consequently, selective catalytic hydrogenation of CO₂ is highly desirable for the development of more sustainable processes in chemical industry. In view of the above considerations, the emphasis of the introduction chapter as well as this thesis in general will be put on catalytic hydrogenation of CO₂ and esters.

1.2 Hydrogenation of carbon dioxide: past experience and modern trends

The major motivation for the chemical utilization of CO₂ has a substantial “environmental” component. There is a general consensus that a rapid increase of atmospheric CO₂ concentration (400 ppm in 2014, Mauna Loa Observatory, Hawaii) witnessed in the last century is mainly associated with the human industrial activities.⁴ As a countermeasure, the search for efficient technologies for CO₂ capture, sequestration and utilization has been initiated. Despite the recent recognition of the problems associated with CO₂-induced climate change, catalytic reduction of CO₂ has at least a century-long history. In early 1910s, Sabatier discovered that in the presence of a nickel catalyst CO₂ can be hydrogenated to methane at 300-400°C. In principle, this reaction can be the basis of the carbon neutral H₂ storage process, in which the synthetic methane is directly utilized as a fuel, while the CO₂ produced upon its combustion is recycled to generate CH₄.⁵ However, due to the harsh conditions employed in CO₂ methanation process and, more importantly, the very low cost of the CO₂ hydrogenation product, this approach was only realized on the demonstration scale. An alternative path involves the hydrogenation of CO₂ to methanol in the presence of a heterogeneous catalyst.⁶ Comprised mainly of Al₂O₃-ZnO-supported copper, these catalysts operate efficiently at elevated temperatures and pressures typically in the range of 200-300 °C and 50-100 bar. In the traditional methanol synthesis process that uses syngas, the conversion of CO₂ to CH₃OH is complementary to the main reaction of CO hydrogenation. Potentially, a more sustainable process utilizing CO₂ as the only carbon source for the methanol synthesis can be established.⁶ If such a process employs H₂ produced from renewable resources, the resulting methanol can be considered a sustainable fuel.

Another product of CO₂ reduction is formic acid (FA), which represents the major focus of the current work. Industrially, FA is produced by carbonylation of CH₃OH with subsequent hydrolysis of methyl formate (Scheme 1.1).⁷ In addition to being a commodity chemical, FA has recently been proposed as one of the potential green fuels of the future,⁸

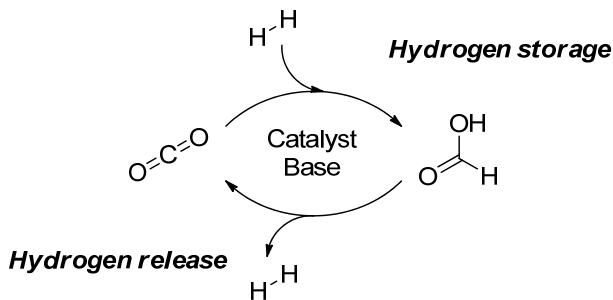
because it is easy to obtain hydrogen from FA in a very efficient manner by its selective dehydrogenation towards H₂ and CO₂. The chemical loop, formed in this way, allows to utilize CO₂ as the intermediate hydrogen carrier. The overall process is atom efficient and carbon neutral, that complies with principles of sustainable chemistry with the condition that renewable hydrogen is used for the CO₂ reduction step.



Scheme 1.1. Industrial production of formic acid via carbonylation of methanol and methyl formate hydrolysis.

However, the practical implementation of FA-based hydrogen storage is impeded by the unfavorable thermodynamics of the FA formation from H₂ and CO₂ ($\Delta G = 34 \text{ kJ mol}^{-1}$). This can be overcome by using stoichiometric amounts of base reagents during the reduction. The reaction product in this case is a formate salt, rather than a free formic acid. In this thesis, for the sake of conciseness, the term “CO₂ hydrogenation” is exclusively used to refer to the reaction yielding formates unless specified otherwise.

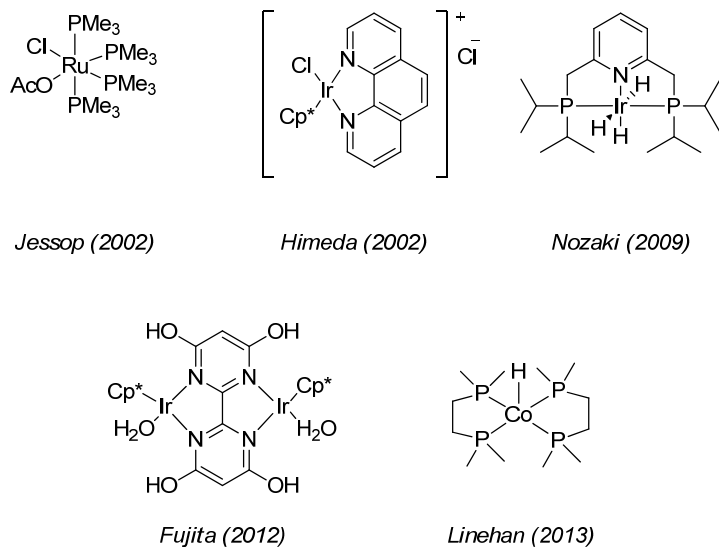
The product yields in hydrogenation of CO₂ to formates are often expressed in terms of acid-to-amine ratio (AAR). The maximal value for the AAR is determined by the acid-base equilibrium between HCOOH and the base promoter employed. For this reason, the maximal AAR can vary for different bases and different reaction conditions.



Scheme 1.2. A chemical loop for HCOOH-based hydrogen storage.

Catalysis in both reactions of the chemical loop based on FA as the intermediate hydrogen storage carrier (Scheme 1.2.) has a long history. Already at the start of the 20th century, the use of noble metal sponges for the hydrogenation of CO₂ and dehydrogenation of FA has been demonstrated. In 1914, Bredig and Carter⁹ successfully performed synthesis

of potassium formate from bicarbonate salt at remarkably low temperature of 70 °C under 60 bar H₂. The same catalyst promoted the base-free reduction of gaseous CO₂ to produce very dilute solutions of free formic acid in water. Dehydrogenation of FA was catalyzed by a variety of metal sponges more than a century ago. Metallic palladium, platinum, copper and stannous oxide powders were shown to generate H₂ and CO₂ from HCOOH at temperatures of 110-280°C.¹⁰ Nearly all early examples utilized bulk metal powders as catalysts and, accordingly, their direct utilization in the chemical industry would be associated with prohibitive catalyst prices. After over a hundred years of research, a supported catalyst for hydrogenation of CO₂ was disclosed by Petri et al,¹¹ who employed Au/TiO₂ catalyst for hydrogenation supercritical CO₂ in the presence of a triethylamine base (NEt₃) at 40 °C. The reaction product was recovered as a formic acid adduct with NEt₃ with AAR up to 1.715. This reaction has created a basis for a process involving a thermal cleavage of the acid-amine adduct to yield pure anhydrous FA, which has been patented in 2012 by BASF.¹²



Scheme 1.3. State-of-the-art homogeneous catalysts for CO₂ hydrogenation

Few alternatives to conventional supported heterogeneous catalysts have also been developed in recent years. They rely on immobilization or grafting of well-defined transition metal complexes onto a solid support. Zhang and co-workers¹³ described a silica-based catalyst employing a Ru(PPh₃)₃Cl₂ complex coordinated to the surface-grafted ammine linkers. This system showed a good CO₂ hydrogenation activity in repetitive

operation. Baffert et al.¹⁴ described an Ru complex bound to a mesoporous silica support via an N-heterocyclic carbene ligand incorporated into the silica framework.

With abovementioned exceptions, hydrogenation of CO₂ to formates remains homogeneously catalyzed. Numerous attempts were made to employ different noble metal complexes for CO₂ hydrogenation.¹⁵ Early reports by Graf and Leitner^{16,17} set a TON benchmark at 3400 using mono- and diphosphine rhodium complexes derived from [Rh(COD)Cl]₂. Subsequently, Noyori and co-workers reported an Ru-based homogeneous catalytic systems for the production of FA in supercritical CO₂.^{18,19} Authors were able to double the TON values previously attained with Rh and reached the TON of 7200. Further development of the Rh-catalyzed CO₂ hydrogenation by the group of Leitner resulted in 1997 in a new TOF (turnover frequency) benchmark value at 1335 h⁻¹ although the stability of the catalyst was not demonstrated and TON values remained rather low.²⁰

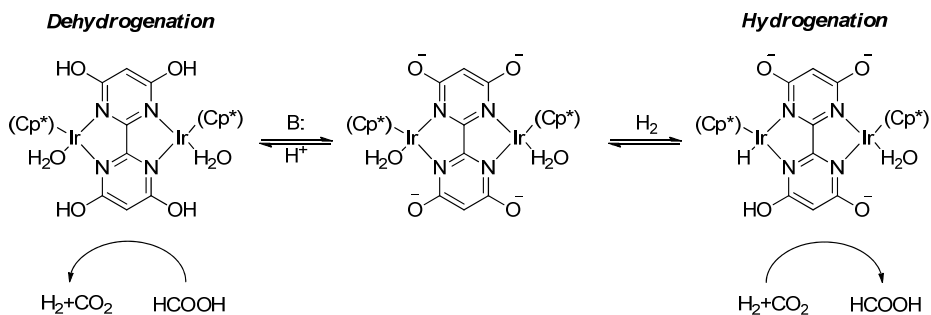
A particularly active Ru-based system has been discovered by Jessop and co-workers five years later. An outstanding reaction rate of about 95 000 h⁻¹ has been observed upon the hydrogenation of supercritical CO₂ with [RuCl(OAc)(PMe₃)₄] complex (Scheme 1.3) at the temperature as low as 50 °C.²¹ Next significant improvement in catalyst productivity has been reported by Himeda and co-workers in 2007. Authors developed an IrCp* catalysts with phenantroline-derived ligands (Scheme 1.4)²² that allowed reaching TON values of 222 000 at 200 °C and 60 bar pressure of equimolar H₂/CO₂. Although the activity of Himeda's catalyst (TOF = 33 000 h⁻¹) was somewhat lower than that of Jessop's catalyst, the possibility of operating in aqueous solutions at high temperature had no former precedents. Finally, in 2009, the group of Nozaki disclosed an iridium catalyst bearing a lutidine-based PNP pincer ligand (Scheme 1.3)²³ that showed activities corresponding to TOF values of up to 150 000 h⁻¹ attainable at 200 °C and 60 bar pressure. These reaction rates remained the record in the field until 2014.

In recent years, significant effort has been devoted to the search of catalysts based on non-noble metals. The group of Linehan has pioneered in this area²⁴ by presenting a catalytic system comprised of a cobalt hydride bis-diphosphine catalyst and a Verkade-type base²⁵ promoter (Scheme 1.3). This base promoter complementary to the Co complex under study was selected on the basis of an elegant thermodynamic analysis. The resulting catalyst/promoter combination was highly active at ambient temperature and pressures. Maximal activity of 74 000 h⁻¹ was reached already at 21 °C under 20 bar pressure of equimolar H₂/CO₂ gas mixture. Another important class of non-noble metal catalysts for hydrogenation of CO₂ is based on well-defined iron pincer catalysts. Beller²⁶ and Milstein²⁷

reported phosphine-based Fe complexes that performed with moderate efficiency in hydrogenation of CO₂ and carbonates to formate salts. Although activity of iron catalysts in CO₂ hydrogenation is rather low, the decomposition of FA with Fe catalysts can be very facile. Initially reported by Beller²⁸ and Milstein,²⁹ iron catalysts are now capable of very efficient acceleration of FA dehydrogenation. Bielinski et al.³⁰ reported the staggering TOF of 120 000 h⁻¹ developed by an Fe pincer catalyst operating at 80 °C in the presence of 10 %_{mol} LiBF₄ promoter.

Despite very good activities could be developed by non-noble metal catalysts in both hydrogenation of CO₂ and dehydrogenation of FA, these systems have three major drawbacks. Firstly, these catalysts contain polydentate phosphine ligands, that can greatly contribute to the catalyst price. Taken together with a non-trivial handling of phosphine complexes, this diminishes the benefits of having a non-noble metal catalyst because they are, in fact, neither cheaper, nor easier to synthesize. Secondly, in some instances, the use of non-noble metal catalyst for hydrogenation of CO₂ requires exotic promoters (e.g. Linehan's catalyst). The commercial price of the Verkade superbase necessary to achieve a high catalytic activity of the cobalt complex is ca. 407-fold higher than that of NEt₃ often used in combination with Ru and Ir-based catalyst. Moreover, the use of extremely strong bases for hydrogenation of CO₂ makes the recovery of pure FA from the acid-base adduct unfeasible due to high stability of the latter. For the same reason, the use of superbases will inevitably hamper the dehydrogenation of HCOOH. Finally, very few of the non-noble metal catalysts are capable of accelerating both hydrogenation of CO₂ and dehydrogenation of FA under comparable conditions, that is necessary for an FA-based H₂ storage process.

Almost universally, noble metal catalysts are superior in reversible hydrogenation of CO₂. Nozaki's Ir-PNP was among the first catalysts that showed an outstanding performance in both generation and decomposition of formate salts. Apart from high hydrogenation activity, it was capable of liberating H₂ from formic acid salts with a TOF of 120 000 h⁻¹ at 80 °C. More recently, Fujita and co-workers reported reversible CO₂ hydrogenation in aqueous medium catalyzed by the tetrahydroxy-2,2'-bipyrimidine ligated Ir complex (Scheme 1.3). A remarkable feature of this catalyst was the possibility to steer the activity in both reactions by modulating the acidity of the medium (Scheme 1.4). At elevated pH the hydroxypyrimidine ligand was deprotonated resulting in the activation of the catalyst towards hydrogenation of CO₂. The reverse reaction could be triggered by protonating the Ir complex at low pH.



Scheme 1.4. A pH responsive behavior of Fujita's catalyst for reversible CO₂ hydrogenation

With the development of active catalysts for the reversible CO₂/formate transformation, a new concept of formate-based hydrogen battery was put forward and realized practically on a lab-scale. Beller and co-workers reported on the possibility of a cyclic storage of H₂ by CO₂ hydrogenation and subsequent H₂ release by HCOOH decomposition in a catalytic system comprised of Ru(dppe)₂ complex in combination with amine bases.³¹ Apart from providing very high activity for decomposition of formates, the system allowed for stable continuous operation in a cyclic mode for at least 15 charge/discharge repetitions. Hsu et al³² reported another system based on an Ru complex bearing a tetradentate PNNP ligand. Unfortunately, no kinetic data was presented for this system, despite the possibility of H₂ storage and release was clearly demonstrated.

So far, the reversible hydrogenation was demonstrated only for the CO₂/HCOOH pair. Despite recent reports outline the possibility to use methanol as a liquid hydrogen carrier,^{33,34} the reversibility in hydrogenation of CO₂ to methanol is not yet achieved. With respect to FA-based hydrogen storage, the practical implementation of this concept would require a significant progress towards better catalytic performance under milder reaction conditions. In our view, the thorough analysis of this reaction is crucial for unraveling the nature of more complex transformations.

1.3 Catalytic hydrogenation of esters

Similar to carbon dioxide, carboxylic acid esters are very weak electrophiles. Therefore, their reducibility is significantly lower than that of other carbonyl compounds (e.g. ketones). Conventionally, the reduction of esters to corresponding alcohols is performed in stoichiometric reactions using metal hydride reagents (most typically NaBH₄ or LiAlH₄).^{35,36} These compounds are highly reactive and sensitive to ambient atmosphere making their utilization inconvenient due to the necessity of exclusion of air and intensive

cooling during the reaction. Finally, a stoichiometric amount of inorganic waste is generated upon the workup of such a reduction. A recent paper by Nolan and co-workers³⁷ presented an alternative KOH-catalyzed reduction of esters, employing PhSiH₃ as a reducing agent. The biggest disadvantage of this procedure is the high price of silane that has to be used in stoichiometric amounts.

Molecular hydrogen is an attractive alternative to metal hydrides and silanes. It is the most atom efficient reducing agent and produces no waste when involved into reaction. Finally, H₂ is manifold cheaper than any other reductant. Apart from the necessity for elevated operating pressures, the use of hydrogen for reduction of esters is associated with one more obstacle. Namely, the number of catalysts for this process is scarce. This exemplifies the biggest difference with the reduction of CO₂. The latter can be promoted by a great number of transition metal complexes, although the activity is generally mediocre. Reduction of esters, on the other hand, was only limited to hydrogenation of fats until 1980 when Grey et al. disclosed a ruthenium catalyst capable of reducing activated esters. Activated methyl and trifluoroethyl trifluoroacetate esters were hydrogenated to corresponding alcohols with good yields (>88%), whereas the conversions of unactivated esters were significantly lower.³⁸⁻⁴⁰ Some years later, Matteoli and co-workers reported that an Ru(CO)₂(CH₃COO)₂(PBu₃)₂ complex could also bring the hydrogenation of dimethyl oxalate to methyl glycolate to full conversion.⁴¹ At longer reaction times, small fraction of methyl glycolate was further hydrogenated to ethylene glycol.

In 1991, Hara and Wada reported a catalytic system that could hydrogenate anhydrides and lactones.^{42,43} The catalyst was formed *in situ* from Ru(acac)₃ and trioctylphosphine (**A** on Scheme 1.5) and showed the best performance in the presence *p*-toluenesulfonic acid or phosphoric acid additives. Teunissen and Elsevier later altered the Hara and Wada system to make it suitable for the hydrogenation of non-cyclic esters.⁴⁴ They found that the combination of TriPhos^{Ph} ligand with Ru(acac)₃ (**B** on Scheme 1.5) in methanol resulted in the highest conversion of dimethyl oxalate towards mainly ethylene glycol (95 %). The catalyst performance was further enhanced by the introduction of metallic zinc additive to accelerate the reduction of the initial Ru³⁺ species and therefore achieve a fast precatalyst formation. The same group of researchers further studied hydrogenation of aromatic and aliphatic esters⁴⁵ with a particular focus on the hydrogenation of dimethyl phthalate that had at that time only a single precedent of catalytic hydrogenation.⁴⁶ The performance of the Elsevier's catalytic system in dimethyl phthalate hydrogenation strongly depended on additives. While the addition of zinc deteriorated the catalytic activity, such promoters as

NEt₃ and HBF₄ allowed to increase significantly the yields. Ultimately, a 78% yield of 1,2-bis-(hydroxymethyl)-benzene was achieved using 1.5 %_{mol} catalyst in ⁱPrOH solvent in combination with HBF₄ at 85 bar H₂ pressure and 100 °C. Subsequent works on the optimization of the TriPhos system originally developed by Teunissen and Elsevier focused on hydrogenation of non-activated esters, although no significant improvement of the catalytic activity was achieved.⁴⁷⁻⁴⁹

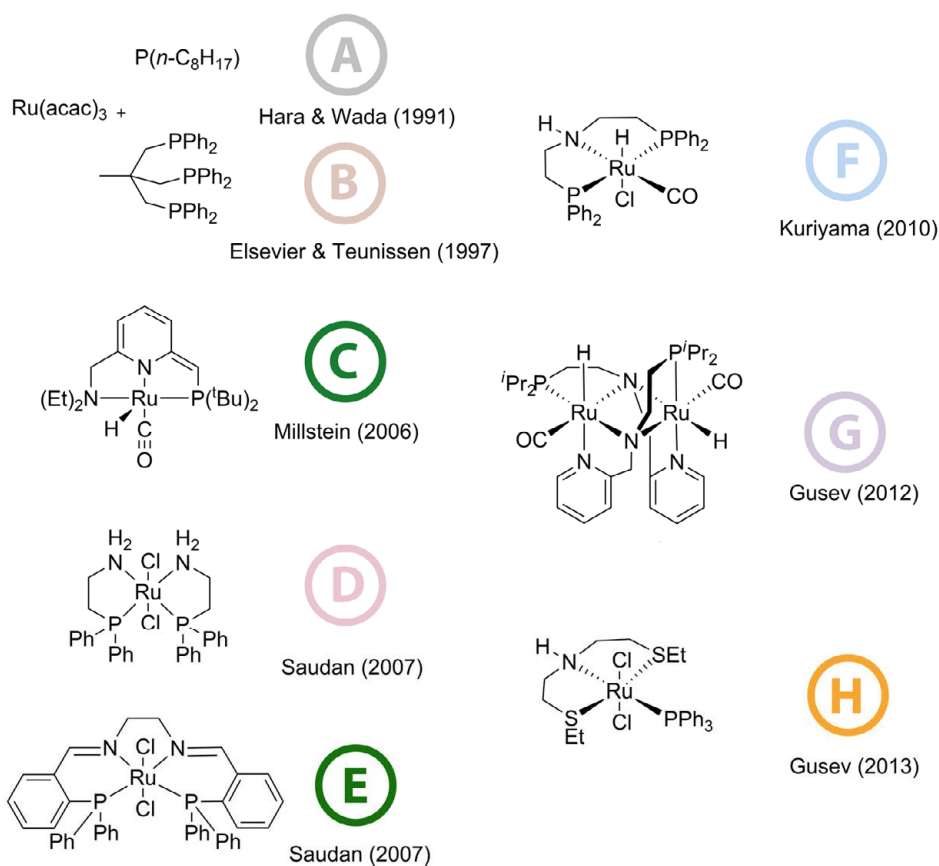
A major improvement was delivered in 2006 by the group of Milstein that disclosed a ruthenium lutidine-based pincer-type catalysts **C** (Scheme 1.5) for ester hydrogenation.⁵⁰ Milstein catalyst **C** was able to hydrogenate a broad range of substrates (Scheme 1.5) at a relatively mild temperature (typically 115 °C) and a very low hydrogen pressure of only 5.4 bar. Remarkably, catalyst **C** requires no additives, whereas normally, the presence of strong alkoxide base promoters was needed. The major drawback of the Milstein catalyst was that it showed a high efficiency only at high catalyst loadings (typically around 1%_{mol}).

A year later Saudan et al. described a set of ruthenium complexes with chelating N,P ligands for the reduction of esters with H₂.⁵¹ These compounds can be classified as Noyori-type catalysts⁵²⁻⁵⁵ that were previously shown to be highly active in asymmetric hydrogenation of ketones to alcohols. Surprisingly they had never been applied for the hydrogenation of esters. Preliminary tests involving methyl benzoate as a model substrate pointed to catalysts **D** and **E** (Scheme 1.5) as the most active candidates. Catalyst **D** was further explored for the hydrogenation of a wide range of benzoic acid esters. Typical loadings for **D** were in the range of 0.01-0.05 %_{mol} with operating temperatures of 60-100 °C at 10-50 bar H₂ pressure. Under these conditions a maximum of 4 h was necessary to bring the hydrogenation to 99% completion.

The catalytic activities reported by Saudan et al were one order of magnitude higher than those of the catalyst reported by Teunissen and Elsevier, and even two orders of magnitude higher than the Milstein catalyst **C**. This emphasizes the very high efficiency at which catalyst **D** operates, but probably the most striking improvement made by Saudan et al was the discovery of the possibility to carry out a chemoselective hydrogenation of esters using catalyst **E**. Authors overcame a typical problem of ester hydrogenation catalysts, that is the intolerance to other reducible functionalities such as carbon-carbon double bonds. The data summarized in Table 1.1 shows that the degree of substitution at the double bond and its location directly influences the chemoselectivity of the reduction. Whereas internal alkene functionality could be preserved, terminal alkenes and α,β -unsaturated substrates lost the alkene function upon the hydrogenation. After additional analysis authors found

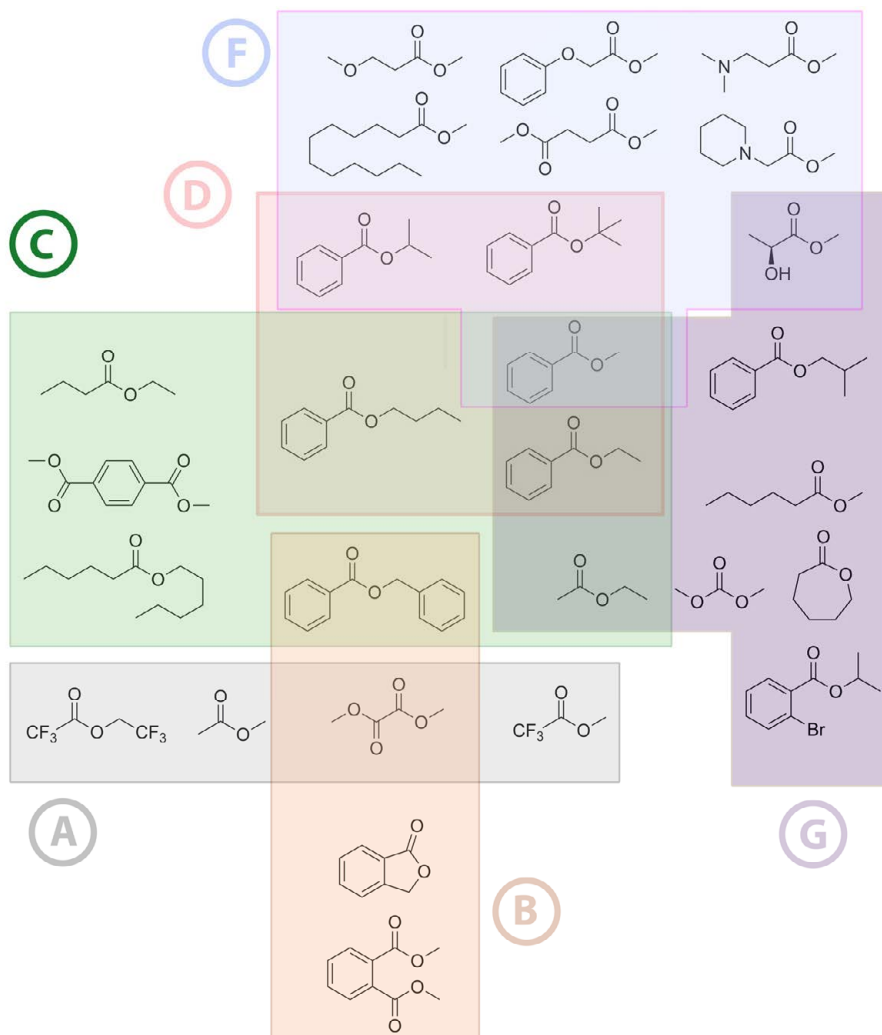
that the ester reduction path is kinetically preferred over the olefin reduction. This points to a principle possibility to improve the yields of unsaturated alcohols by the optimization of the process conditions. After this breakthrough report, some progress was made by Clarke and co-workers on the improvement of the performance of the Noyori-type catalysts.⁵⁶

Parallel to the research on the Noyori-type catalysts, the use of new ligand types in ester hydrogenation catalysts was attempted. For example, N-heterocyclic carbenes (NHC) were incorporated into lutidine-derived pincer catalysts by the groups of Milstein⁵⁷ and Song.⁵⁸ Although the activity of the resulting Ru-NHC catalysts was improved compared to their phosphine-based analogues, it was still substantially lower than that of the Noyori type catalysts.



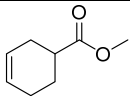
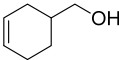
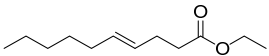
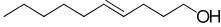
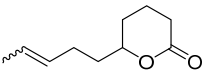
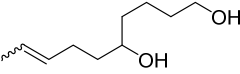
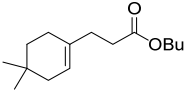
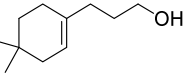
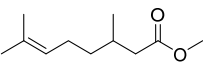
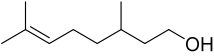
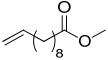
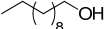
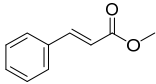
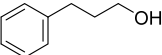
Scheme 1.5. Examples of the milestone ester hydrogenation catalysts in chronological prospective.

The next major step in improving the efficiency of ester hydrogenation catalysts was delivered in 2011 by researchers from Tagasako corp. They disclosed a catalytic system specifically designed for industrial applications.⁵⁹ Inspired by the findings by Saudan et al.⁵¹ indicating that the deactivation of catalyst **D** was probably due to catalyst carbonylation with methanol, the main emphasis was devoted to the development of a methanol tolerant catalytic system. The proposed way to suppress the deactivation involved the use of a PNP pincer ligand that would prevent excessive carbonylation by protecting at least three sites at the metal center.



Scheme 1.6. Euler diagram representation of the overlapping substrate scopes of selected ester hydrogenation catalysts

Table 1.1. Hydrogenation of esters containing a C=C bond with catalyst **E**.⁵¹

Entry	Substrate	Major product	Product ratio ^a	Y, %	TON ^c
1			98/2	90	1800
2			99/1	93	1860
3 ^b			98.5/1.5	85	1700
4			>98/2	95	1900
5			99/1	94	1880
6			35/65	94	1880
7			12/88	87	1740

S/C = 2000, 5 %_{mol} NaOMe, 50 bar H₂, 100 °C, 2.5 h, in THF solvent; ^a unsaturated alcohol/saturated alcohol; ^b Solvent = toluene, base = KOMe, 3h reaction. ^c TON calculated for total yield

These studies led to the development of a ruthenium complex **F** that has been patented and named Ru-MACHO[®] because, according to the authors, it “resembles a brawny athlete holding the ruthenium”.⁵⁹ Catalyst **F** showed good activity even when methanol was used as a solvent, thus simplifying the workup of the products of methyl ester hydrogenation. Catalyst **F** operated efficiently under conditions, similar to that of Firmenich catalysts **D** and **E**. Typically, the reactions were carried out at 100 °C and 50 bar H₂ pressure. Catalyst loadings varied in the range of 500-1000 ppm relative to the substrate. Hydrogenation of esters using catalyst **F** was shown to preserve chirality at the positions adjacent to the ester group. For example, at a substrate-to-catalyst ratio of 2000 and the abovementioned

conditions, 2-((*L*)-menthoxy)ethanol was obtained in 87 % yield from the corresponding methyl ester (see Scheme 1.6 for other examples).

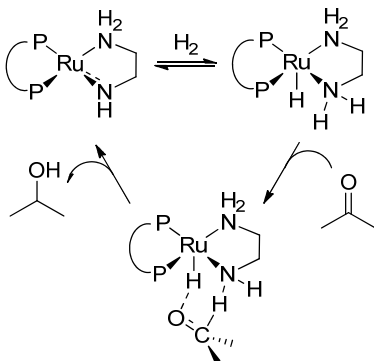
Finally, Gusev and co-workers developed a group of ester hydrogenation catalysts that are the most active to date. In 2012 they introduced an Ru-PNN pincer catalyst based on picolylamine-derived backbone (**G**, Scheme 1.5).⁶⁰ The catalyst was active at high substrate to catalyst ratios of 2000-20 000 and provided very high yields of alcohols when hydrogenation was conducted at 100 °C and 50 bar H₂ pressure. Further research by the same group led to the disclosure of an Ru-SNS pincer catalyst **H** (Scheme 1.5) that currently holds the activity record in the field of ester hydrogenation. Unprecedented turnover numbers of 58 400 were obtained in hydrogenation of neat ethyl acetate at only 40 °C. An outstanding hydrogenation TOF of 4 900 h⁻¹ was obtained in 2 hours at 100°C and 50 bar H₂ with methyl hexanoate as a model substrate. Importantly, a high catalytic activity of **H** has been demonstrated at temperatures as low as 40 °C and substrate-to-catalyst ratios as high as 80 000 (ca. 13 ppm).

1.4 Bifunctional molecular catalysis

Although different metals and ligands can comprise a catalyst for hydrogenation of CO₂ and esters, all the highly active catalysts described so far share a common feature. They cannot be viewed as conventional single-site catalysts, where the reactivity is defined by the metal center, while the role of the ligand is limited to altering the electronic and steric properties of the metal center. Instead, in these systems, the ligand can participate in catalytic reaction and work in concert with the metal center to transform the substrates along the predefined reaction path. Such a bifunctional behavior has led to a concept generally referred to as the metal-ligand cooperation (MLC), and the respective ligands are usually referred to as cooperative or non-innocent ligands.

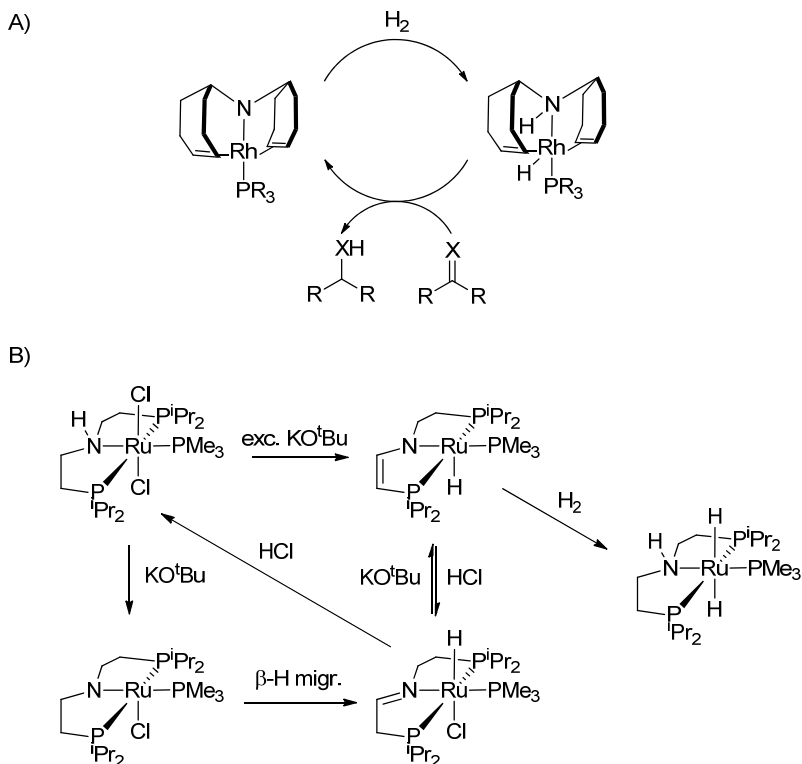
Noyori-type catalysts show a pronounced bifunctional behavior.^{52,53} Typical catalysts of this type contain a ruthenium amide function that assists in H₂ cleavage over Ru-NR bond (Scheme 1.7). An Ru amino hydride complex, produced in this reaction, contains RuH^{δ-} and NRH^{δ+} functions that can interact with hydrogenation substrate in the second coordination sphere. Subsequent concerted transfer of the hydride and proton to carbonyl group of the substrate regenerates the initial amido complex and yields the hydrogenated product. Ketones are typical substrates for such hydrogenation reaction that can proceed at near-ambient temperatures with extremely low catalyst loadings. Common TON values attainable in hydrogenation of ketones using Noyori type catalysts can reach several

hundred thousand. Finally, introduction of a chiral center in the diamine or hybrid aminophosphine bidentate ligands leads to catalysts with superb hydrogenation enantioselectivity.



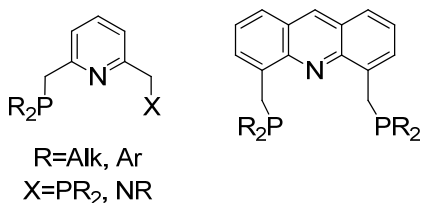
Scheme 1.7. Selected steps of cooperative hydrogenation according to Noyori-Morris mechanism

A similar behavior can be encountered in complexes with amino-pincer ligands. The major difference with Noyori type catalysts is the presence of three donor groups on the ligand that binds in *meridional* manner. Typical example is the rhodium complex disclosed by Grutzmacher et al.⁶¹ A Rh(I) amidopincer with a sawhorse-type structure can react with H₂ in a concerted manner and transfer the resulting hydride from the metal centre and the proton from amino group to the substrate (Scheme 1.8 a). Substrate molecule in this case can contain a C=O or C=N double bond that upon the transfer of an H₂ equivalent from an Rh hydrido complex is transformed to an alcohol or amine, respectively. Amino phosphine pincer ligands similar to those employed in Ru-MACHO catalyst can also exhibit metal ligand cooperative behavior. Schneider and co-workers⁶² described the reactivity of a related ruthenium complex (Scheme 1.8 b) towards deprotonation and addition of dihydrogen. Surprisingly, multiple deprotonation steps can take place for this complex. Reaction with first equivalent of KO^tBu base yields a five-coordinated amino complex. Subsequent β -hydride migration results in imidino bound Ru hydride complex that is six-coordinated. This complex can undergo a second deprotonation to yield a five-coordinate complex with a double bond formed within the ethylene linker. As a result, such a complex can cooperatively add up to two H₂ molecules.

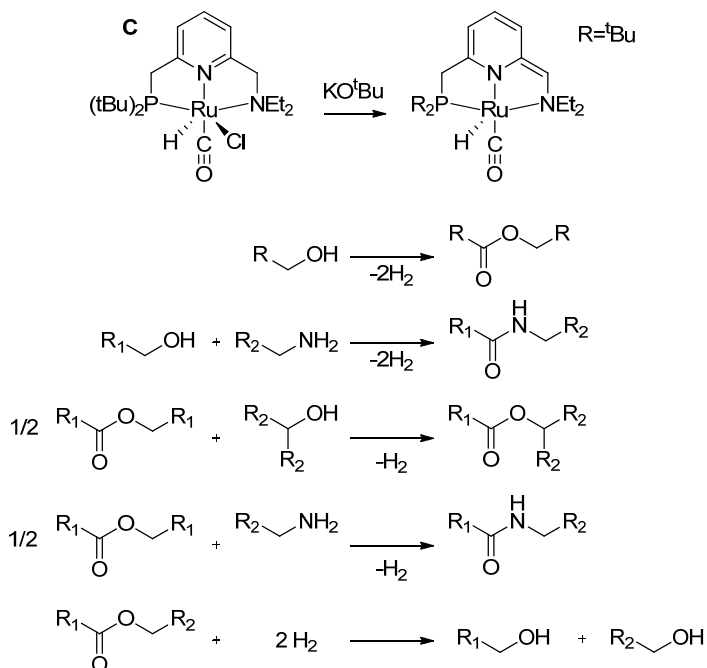


Scheme 1.8. Cooperative action of amino pincer ligands in Rh (A)⁶¹ and Ru (B)⁶² complexes

The cooperative function in these complexes is associated with the amino group located in an immediate vicinity to the metal center, more specifically, within a distance of one chemical bond from the metal. The second large class of cooperative ligands has its cooperative site located two or even four bonds away from the metal. These ligands are based on nitrogen containing heterocycles such as lutidine and acridine⁶³ representing the backbone for the respective pincers (Scheme 1.9).



Scheme 1.9. Long-range cooperative ligands developed by Milstein



Scheme 1.10. Activation with base and catalytic reactivity of the Milstein's catalyst

The bifunctional behavior on aromatic pincers was mainly developed by the group of Milstein.⁶⁴ Pincer ligands showing a long range cooperation contain phosphine or mixed phosphine/amine donor groups bound to the aromatic backbone through methylene linkers. One of the best known examples of this class of compounds is the Ru-PNN complex **C**, often referred to as Milstein catalyst, that was described earlier in this Chapter (Scheme 1.5). The pincer ligand in **C** can undergo deprotonation at the pyridylmethylenic carbon atom resulting in the dearomatization of the pyridine ring. An "activated" complex has a vacant site due to the removal of the halide ligand upon the reaction with a strong base (e.g. KO^tBu). Similarly to Noyori-type catalysts, dearomatized Ru-PNN can heterolytically cleave H₂ and transfer it onto carbonyl substrates in a catalytic manner. More remarkable is the ability of the Milstein catalyst to 'borrow' hydrogen from saturated substrates and release it as H₂ gas. Unsaturated substrates can either be released or engage in further chemical transformations. This property was used to develop a set of new catalytic dehydrogenative coupling reactions (Scheme 1.10). Complex **C** promotes acceptorless dehydrogenative coupling of alcohols to form esters, coupling of alcohols and amines towards amides, acylation of esters with secondary alcohols and production of

amides from amines and esters. Finally, Milstein catalyst is active in hydrogenation of esters similar to other bifunctional catalysts described above.

It is important to note that such an acid-base bifunctional behavior is not restricted to homogeneous catalysts only. Heterogeneous catalysts can also exhibit a cooperation between the metal component and the catalyst support, which usually takes place at the interface between the catalyst components. The formal resemblance between homogeneous and heterogeneous MLC is striking. For example, Ag clusters were proposed to act in concert with Al-O sites of alumina supports upon heterolytic activation of H₂.⁶⁵ Similar to homogeneous systems, metal provides a Lewis acid site, while the support provides the base site. This acid-base pair facilitates the heterolytic cleavage of dihydrogen to form metal hydride species and hydroxide group on the metal/oxide perimeter.

Supported gold catalysts were also shown to benefit from the metal-support cooperation. The group of Yates showed that partial oxidation of acetic acid on Au/TiO₂ involves a support-assisted dehydration/deoxygenation of the acid, while the metal was responsible for binding of the resulting ketylidene intermediate.⁶⁶ The same group of researchers has also demonstrated the crucial role of the support in gold-catalyzed oxidation of CO. Authors found that the cooperation between the metal and the support is essential for high activity, while exclusion of one of the components leads to a near 10-fold drop in activity.⁶⁷ These data were in fact the extrapolation of the results of the earlier study showing the importance of the metal-support synergy in Au/Ti-O_x ensembles for the activation of H₂.⁶⁸

With respect to catalytic hydrogenation, gold is usually significantly less active than other noble metals. Dissociation of hydrogen, a crucial step in hydrogenation reactions, can occur on the edges of small Au particles, but is very difficult on closed metal surfaces. For that reason Au is often referred to as “the noblest of all” metals.⁶⁹ In particular, Au(311) and Au(111) surfaces are not active in dissociation of hydrogen even at 500 K. Nevertheless, when stabilized on a support gold nanoparticles are capable of activating H₂ at relatively low temperatures. An elegant work by Haruta and co-workers⁷⁰ described the importance of the Au/TiO₂ interface for H₂ dissociation. In particular, the authors managed to correlate the interface area with hydrogen oxidation activity. An important conclusion of this work was that “*by tuning the size of gold particles and by choosing proper metal oxide supports, a novel type of heterogeneous catalyst will emerge showing unique product selectivity completely different from that obtained by palladium and platinum catalysts*”.⁷⁰ Two years later, a stunning new catalytic activity of gold in CO₂ hydrogenation was

discovered¹¹ for the Au/TiO₂ system. Four years after Haruta's claim, gold nanoparticles supported on MgCuCr₂O₄-spinel were found to be highly selective in oxidation of ethanol to acetaldehyde.⁷¹

In summary, state-of-the-art catalysts for hydrogenation of CO₂ and carboxylic acid esters show an acid/base bifunctional behavior. Concerted action, whether one considers amine/amide transformation or ligand aromatization/dearomatization mechanism, is believed to be crucial for the high performance of the respective catalysts. Although, the beneficial role of MLC is commonly accepted, it is not always clear how ligand participation impacts the catalytic reaction. Therefore, we will devote a significant part of this Thesis to unraveling the reactivity of cooperative catalysts and explaining the influence of cooperative transformations on catalysis.

1.5 Scope of the thesis

Hydrogenation of carbon dioxide and carboxylic acid esters typically requires a bifunctional catalyst to proceed with high efficiency. Nevertheless, the exact role of ligand-assisted transformations in catalytic reactions remains under debate. Several metal-ligand cooperative paths have been proposed to contribute to the catalytic cycles in CO₂ hydrogenation with Ir-PNP and Ru-PNN catalysts.⁷²⁻⁷⁴ Chapter 2 deals with elucidating the mechanistic role of metal-ligand cooperation in catalytic CO₂ hydrogenation promoted by an Ru-PNP complex, which is structurally analogous to the most active Ir-based catalyst reported to date.²³ The ability of this complex to activate H₂ and CO₂ via bifunctional mechanism sparked a particular interest of analyzing metal-ligand cooperative transformations of Ru-PNP. We analyze the reactivity and kinetic behavior of the stable intermediates derived from the reactions of Ru-PNP with the substrates of the catalytic reaction to establish their role in catalysis and to figure out whether the bifunctional activation of CO₂ by Ru-PNP is beneficial for catalytic activity.

Chapter 3 focuses on the exploration of the activity of Ru-PNP in reversible CO₂ hydrogenation, mechanistic analysis of this reaction and the utilization of this fundamental knowledge for the optimization of the activity of Ru-PNP in both reactions of reversible CO₂ hydrogenation. The first part of Chapter 3 deals with the catalytic dehydrogenation of formic acid. In particular, we address the role of the base promoter, typically used in this reaction. The second part of the chapter is devoted to the optimization of the catalytic hydrogenation of CO₂ with Ru-PNP using combined experimental and theoretical approach.

Chapter 4 deals with the development of a heterogeneous catalytic system for CO₂ hydrogenation to formates based on supported Au catalysts. Here, we aim at optimizing the catalyst performance and investigating the nature of the active site in the promising catalysts.

In Chapter 5, we report on the development of a new class of cooperative pincer catalysts for hydrogenation reactions. We synthesize ruthenium bis-N-heterocyclic carbene pincer complexes and study their reactivity in cooperative activation of H₂ and CO₂ as well as aliphatic and aromatic nitriles. The catalytic activity of these newly developed lutidine-based Ru-CNC pincer catalysts is investigated in Chapter 6. The main focus was laid on the analysis of the differences between the cooperative PNP and CNC ligand platforms in hydrogenation of CO₂ and carboxylic acid esters.

Finally, in Chapter 7 we will show how the modification of the cooperative function of a ruthenium CNC pincer complex impacts its catalytic activity in ester hydrogenation. We will report on a dramatic increase of the catalytic activity of a ruthenium bis-NHC pincers when a lutidine-based backbone is replaced with the amine linker functionality. We show how a careful selection of the cooperative ligand allows enabling the ester hydrogenation activity in otherwise inactive metal species. The new catalysts reported in this chapter exhibit unprecedented performance in homogeneous ester hydrogenation.

1.6 Referenced and notes

- (1) Sabatier, P.; Senderens, J. B. *Compt. Rend.*, **1899**, 128, 1173
- (2) Smith, B. E. *Science* **2002**, 297, 1654.
- (3) Howarth, R. W. *Harmful Algae* **2008**, 8, 14.
- (4) Stocker, T. F. et al. in *Climate Change 2013: The Physical Science Basis. Working Group I: Contribution to the Intergovernmental Panel on Climate Change; 5th Assessment Report*, Cambridge University Press, **2013**
- (5) M. Sterner, "Bioenergy and renewable power methane in integrated 100% renewable energy systems", Kassel University Press, **2009**
- (6) Olah, G. A. *Angew. Chem. Int. Ed.* **2005**, 44, 2636.
- (7) Reutemann, W.; Kieczka, H. In *Ullmann's Encyclopedia of Industrial Chemistry*; Wiley-VCH Verlag GmbH & Co. KGaA: **2000**
- (8) Joó, F. *ChemSusChem* **2008**, 1, 805.
- (9) Bredig, G.; Carter, S. R. *Berichte*, **1914**, 47, 541.
- (10) Sabatier, P. E., Reid E. *Catalysis in organic chemistry*; D. van Nostrand company: New York, **1923**
- (11) Preti, D.; Resta, C.; Squarzialupi, S.; Fachinetti, G. *Angew. Chem. Int. Ed.* **2011**, 50, 12551
- (12) Fachinetti, G.; Preti, D., Process for preparing formic acid. International patent, WO2012168905 A1, **2012**
- (13) Zhang, Y.; Fei, J.; Yu, Y.; Zheng, X. *Catal. Commun.* **2004**, 5, 643.
- (14) Baffert, M.; Maishal, T. K.; Mathey, L.; Copéret, C.; Thieuleux, C. *ChemSusChem* **2011**, 4, 1762.
- (15) Federsel, C.; Jackstell, R.; Beller, M. *Angew. Chem. Int. Ed.* **2010**, 49, 6254.

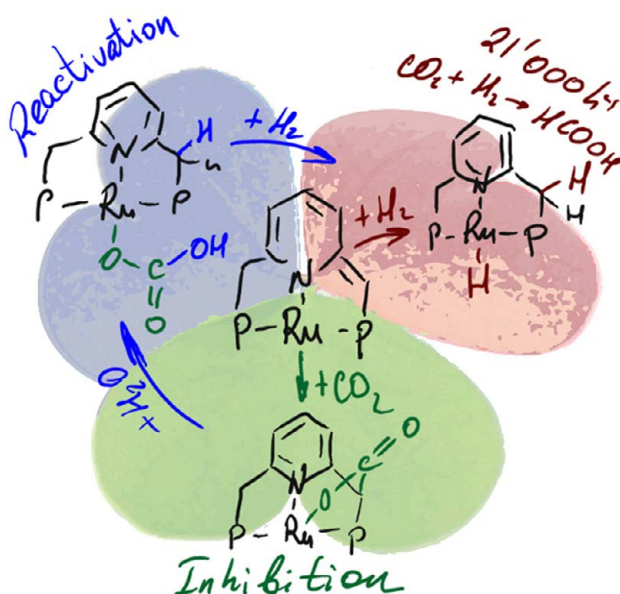
- (16) Graf, E.; Leitner, W. *Chem. Commun.* **1992**, 623.
- (17) Gassner, F.; Leitner, W. *Chem. Commun.* **1993**, 1465.
- (18) Jessop, P. G.; Ikariya, T.; Noyori, R. *Nature* **1994**, 368, 231.
- (19) Jessop, P. G.; Hsiao, Y.; Ikariya, T.; Noyori, R. *J. Am. Chem. Soc.* **1996**, 118, 344.
- (20) Angermund, K.; Baumann, W.; Dinjus, E.; Fornika, R.; Görls, H.; Kessler, M.; Krüger, C.; Leitner, W.; Lutz, F. *Chem. Eur. J.* **1997**, 3, 755.
- (21) Munshi, P.; Main, A. D.; Linehan, J. C.; Tai, C.-C.; Jessop, P. G. *J. Am. Chem. Soc.* **2002**, 124, 7963.
- (22) Himeda, Y.; Onozawa-Komatsuzaki, N.; Sugihara, H.; Kasuga, K. *Organometallics* **2007**, 26, 702.
- (23) Tanaka, R.; Yamashita, M.; Nozaki, K. *J. Am. Chem. Soc.* **2009**, 131, 14168.
- (24) Jeletic, M. S.; Mock, M. T.; Appel, A. M.; Linehan, J. C. *J. Am. Chem. Soc.* **2013**, 135, 11533.
- (25) D'Sa, B. A.; McLeod, D.; Verkade, J. G. *J. Org. Chem.* **1997**, 62, 5057.
- (26) Ziebart, C.; Federsel, C.; Anbarasan, P.; Jackstell, R.; Baumann, W.; Spannenberg, A.; Beller, M. *J. Am. Chem. Soc.* **2012**, 134, 20701.
- (27) Langer, R.; Diskin-Posner, Y.; Leitner, G.; Shimon, L. J. W.; Ben-David, Y.; Milstein, D. *Angew. Chem. Int. Ed.* **2011**, 50, 9948.
- (28) Boddien, A.; Mellmann, D.; Gärtner, F.; Jackstell, R.; Junge, H.; Dyson, P. J.; Laurency, G.; Ludwig, R.; Beller, M. *Science* **2011**, 333, 1733.
- (29) Zell, T.; Butschke, B.; Ben-David, Y.; Milstein, D. *Chem. Eur. J.* **2013**, 19, 8068.
- (30) Bielinski, E. A.; Lagaditis, P. O.; Zhang, Y.; Mercado, B. Q.; Würtele, C.; Bernskoetter, W. H.; Hazari, N.; Schneider, S. *J. Am. Chem. Soc.* **2014**, 136, 10234.
- (31) Boddien, A.; Federsel, C.; Sponholz, P.; Mellmann, D.; Jackstell, R.; Junge, H.; Laurency, G.; Beller, M. *Energy Environ. Sci.* **2012**, 5, 8907.
- (32) Hsu, S.-F.; Rommel, S.; Eversfield, P.; Müller, K.; Klemm, E.; Thiel, W. R.; Plietker, B. *Angew. Chem. Int. Ed.* **2014**, 53, 7074.
- (33) Rodríguez-Lugo, R. E.; Trincado, M.; Vogt, M.; Tewes, F.; Santiso-Quinones, G.; Grützmacher, H. *Nat. Chem.* **2013**, 5, 342.
- (34) Nielsen, M.; Alberico, E.; Baumann, W.; Drexler, H.-J.; Junge, H.; Gladiali, S.; Beller, M. *Nature* **2013**, 495, 85.
- (35) Comprehensive Organic Synthesis, Vol. 8 (Eds.: B. M. Trost, I. Fleming), Pergamon, New York, **1991**
- (36) J. Seyden-Penne, Reductions by the Alumino- and Borohydride in Organic Synthesis, 2nd ed., Wiley-VCH, New York, **1997**
- (37) Fernandez-Salas, J. A.; Manzini, S.; Nolan, S. P. *Chem. Commun.* **2013**, 49, 9758.
- (38) Grey, R. A.; Pez, G. P.; Wallo, A.; Corsi, J. *Chem. Commun.* **1980**, 783.
- (39) Pez, G. P.; Grey, R. A.; Corsi, J. *J. Am. Chem. Soc.* **1981**, 103, 7528.
- (40) Grey, R. A.; Pez, G. P.; Wallo, A. *J. Am. Chem. Soc.* **1981**, 103, 7536.
- (41) Matteoli, U.; Menchi, G.; Bianchi, M.; Piacenti, F. *J. Organomet. Chem.* **1986**, 299, 233.
- (42) Kara, Y.; Wada, K. *Chem. Lett.* **1991**, 20, 553.
- (43) Hara, Y.; Inagaki, H.; Nishimura, S.; Wada, K. *Chem. Lett.* **1992**, 21, 1983.
- (44) T. Teunissen, H.; J. Elsevier, C. *Chem. Commun.* **1997**, 667.
- (45) T. Teunissen, H. *Chem. Commun.* **1998**, 1367.
- (46) Matteoli, U.; Bianchi, M.; Menchi, G.; Prediani, P.; Piacenti, F. *J. Mol. Catal.* **1984**, 22, 353.
- (47) Rosi, L.; Frediani, M.; Frediani, P. *J. Organomet. Chem.* **2010**, 695, 1314.
- (48) Hanton, M. J.; Tin, S.; Boardman, B. J.; Miller, P. *J. Mol. Catal. A: Chem.* **2011**, 346, 70.
- (49) van Engelen, M. C.; Teunissen, H. T.; de Vries, J. G.; Elsevier, C. *J. Mol. Catal. A: Chem.* **2003**, 206, 185.
- (50) Zhang, J.; Leitner, G.; Ben-David, Y.; Milstein, D. *Angew. Chem. Int. Ed.* **2006**, 45, 1113.
- (51) Saudan, L. A.; Saudan, C. M.; Debieux, C.; Wyss, P. *Angew. Chem. Int. Ed.* **2007**, 46, 7473.
- (52) Noyori, R. *Angew. Chem. Int. Ed.* **2002**, 41, 2008.
- (53) Ikariya, T.; Murata, K.; Noyori, R. *Org. Biomol. Chem.* **2006**, 4, 393.
- (54) Samec, J. S. M.; Backvall, J.-E.; Andersson, P. G.; Brandt, P. *Chem. Soc. Rev.* **2006**, 35, 237.

- (55) Gladiali, S.; Alberico, E. *Chem. Soc. Rev.* **2006**, *35*, 226.
- (56) Carpenter, I.; Eckelmann, S. C.; Kuntz, M. T.; Fuentes, J. A.; France, M. B.; Clarke, M. L. *Dalton Trans.* **2012**, *41*, 10136.
- (57) Fogler, E.; Balaraman, E.; Ben-David, Y.; Leitun, G.; Shimon, L. J. W.; Milstein, D. *Organometallics* **2011**, *30*, 3826.
- (58) Sun, Y.; Koehler, C.; Tan, R.; Annibale, V. T.; Song, D. *Chem. Commun.* **2011**, *47*, 8349.
- (59) Kuriyama, W.; Matsumoto, T.; Ogata, O.; Ino, Y.; Aoki, K.; Tanaka, S.; Ishida, K.; Kobayashi, T.; Sayo, N.; Saito, T. *Org. Process Res. Dev.* **2011**, *16*, 166.
- (60) Spasyuk, D.; Smith, S.; Gusev, D. G. *Angew. Chem. Int. Ed.* **2012**, *51*, 2772.
- (61) Maire, P.; Büttner, T.; Breher, F.; Le Floch, P.; Grützmacher, H. *Angew. Chem. Int. Ed.* **2005**, *44*, 6318.
- (62) Friedrich, A.; Drees, M.; Käss, M.; Herdtweck, E.; Schneider, S. *Inorg. Chem.* **2010**, *49*, 5482.
- (63) Gunanathan, C.; Milstein, D. *Acc. Chem. Res.* **2011**, *44*, 588.
- (64) Gunanathan, C.; Milstein, D. *Science* **2013**, *341*
- (65) Hirunsit, P.; Shimizu, K.-i.; Fukuda, R.; Namuangruk, S.; Morikawa, Y.; Ehara, M. *J. Phys. Chem. C* **2014**, *118*, 7996.
- (66) Green, I. X.; Tang, W.; Neurock, M.; Yates, J. T. *J. Am. Chem. Soc.* **2012**, *134*, 13569.
- (67) Green, I. X.; Tang, W.; McEntee, M.; Neurock, M.; Yates, J. T. *J. Am. Chem. Soc.* **2012**, *134*, 12717.
- (68) Green, I. X.; Tang, W.; Neurock, M.; Yates, J. T. *Angew. Chem. Int. Ed.* **2011**, *50*, 10186.
- (69) Hammer, B.; Norskov, J. K. *Nature* **1995**, *376*, 238.
- (70) Fujitani, T.; Nakamura, I.; Akita, T.; Okumura, M.; Haruta, M. *Angew. Chem. Int. Ed.* **2009**, *48*, 9515.
- (71) Liu, P.; Hensen, E. J. M. *J. Am. Chem. Soc.* **2013**, *135*, 14032.
- (72) Yang, X. *ACS Catal.* **2011**, *1*, 849.
- (73) Tanaka, R.; Yamashita, M.; Chung, L. W.; Morokuma, K.; Nozaki, K. *Organometallics* **2011**, *30*, 6742.
- (74) Huff, C. A.; Sanford, M. S. *ACS Catal.* **2013**, *3*, 2412.

The impact of metal-ligand cooperation in hydrogenation of CO₂ with Ru-PNP pincer catalyst

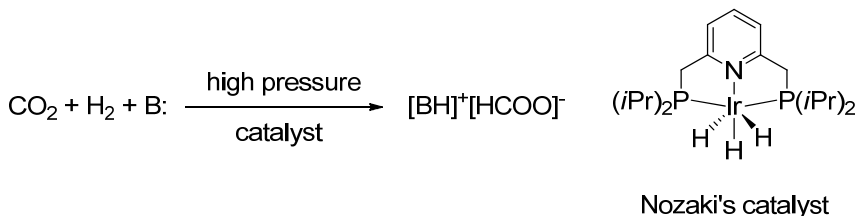
All that glitters is not gold

ABSTRACT: The lutidine-derived ruthenium PNP pincer complex is a highly active catalyst for CO₂ hydrogenation to formates. Ligand-assisted transformations of the catalyst under CO₂ hydrogenation conditions were shown to strongly affect the catalyst performance. While the product of cooperative H₂ activation yields a catalytically active bis-hydrido species, the competing metal-ligand cooperative addition of CO₂ leads to pronounced inhibition of the activity. The addition of water during the reaction restores the catalytic performance of the inhibited catalyst by activating alternative reaction pathways. The mechanism of the underlying chemical transformations is proposed on the basis of kinetic experiments, NMR reactivity studies and DFT calculations.



2.1 Introduction

The utilization of carbon dioxide as a C1 building block in chemical synthesis is gaining increasing attention and is driven by the necessity for sustainable chemical technologies.¹⁻⁴ One of the pathways for CO₂ conversion utilizes its rich catalytic coupling chemistry. Coupling of CO₂ with alkenes,⁵⁻⁷ alkynes,⁸ or epoxides⁹⁻¹¹ to form functionalized products have been discussed as promising CO₂ valorization routes. Since carbon atom in CO₂ is fully oxidized, the sole alternative to coupling reactions is reduction. Molecular hydrogen, the most atom efficient reducing agent, can react with CO₂ to form methanol¹²⁻¹⁵ or formic acid (FA). The latter attracted significant attention as a potential hydrogen carrier. For example, a liter of liquid formic acid contains 53 g of H₂. That is 360 % of what a hydrogen tank can accommodate at a pressure of 350 bar in the same volume. Efficient production of formic acid via catalytic hydrogenation of CO₂ would create a basis for a cheap, sustainable and reversible formate-based H₂ storage process that, in turn, would pave the way towards the development of cleaner energy technologies.¹⁶⁻¹⁹

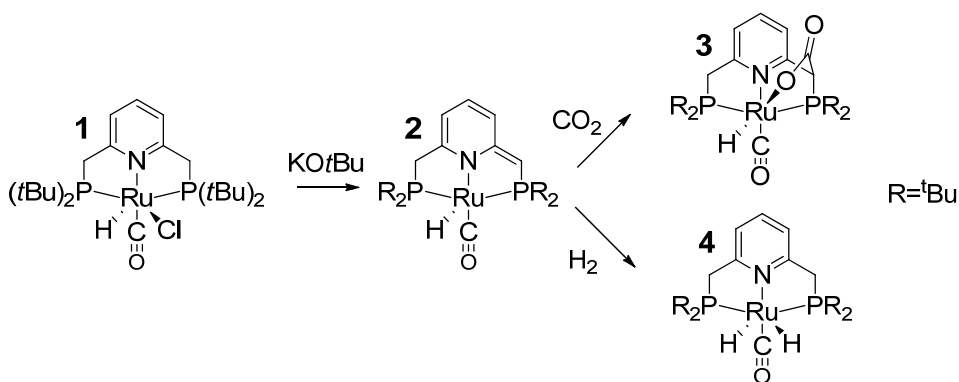


Scheme 2.1. Hydrogenation of CO₂ to formates and the state-of-the-art catalyst for this reaction

Generation of formic acid from carbon dioxide (Scheme 2.1) is a catalyzed reaction. Without any additives the reaction is thermodynamically unfavorable (gas phase $\Delta G = 33 \text{ kJ mol}^{-1}$). Therefore a base promoter is usually added to the reaction mixture to shift the equilibrium towards the reaction products. In this way formate salts, rather than free formic acid, are produced.^{20,21} With few exceptions²²⁻²⁴ most efficient catalytic systems are based on noble metals,²⁵ such as Rh²⁶, Ir²⁷⁻²⁹, Ru³⁰⁻³³. Among them, the highest turnover frequencies (TOF) of $150\,000 \text{ h}^{-1}$ at $200 \text{ }^\circ\text{C}$ were reached using Ir pincer catalyst developed by Nozaki and co-workers (Scheme 2.1).²⁸ An important feature of this catalyst is the lutidine derived PNP pincer ligand that can potentially participate in catalysis. This behavior stems from the “non-innocent” nature of the ligand. Namely, the neutral tridentate PNP ligand can undergo a deprotonation upon a reaction with strong base, followed by dearomatization of the pyridine ring (see Scheme 2.2 for example). This yields five-

coordinate metal species and an adjacent reactive site on the sidearm of the dearomatized PNP* ligand. The combination of the unsaturated metal center and the basic site of the ligand in close proximity results in highly reactive species with a bifunctional character and a broad reactivity range. If both the metal and the ligand sites are participating in further chemical transformations of the complex, the phenomenon is called metal-ligand cooperation. The non-innocent behavior of the nitrogen-centered pincer ligands is often invoked to explain the unique catalytic properties of this class of transition metal complexes.³⁴⁻³⁹ Particularly, Nozaki catalyst was proposed to make use of the PNP ligand non-innocence to promote heterolytic H₂ cleavage as one of the steps in the catalytic cycle for CO₂ hydrogenation.²⁹

Cooperative behavior of the PNP ligand was also shown for ruthenium pincer complexes. For example Ru-PNP pincer **1**⁴⁰ readily yields five coordinate complex **2** with dearomatized ligand upon reaction with KO^tBu (**1**→**2** on Scheme 2.2). Reaction of **2** with H₂ results in a dihydrido complex **4**.⁴¹ Interestingly, **2** can also activate the CO₂ molecule via metal-ligand cooperation. Product of this reaction, complex **3**^{39,40} features a unique mode of CO₂ activation that remains largely unexplored. We propose that Ru-PNP pincer may have potential in catalytic hydrogenation of CO₂, since it is capable of activating both substrates of this reaction. The activity of Ru-PNPs in CO₂ hydrogenation has not been evaluated yet. Consequently, no analysis of relative contribution of complexes **3** and **4** to the catalytic reaction has been made. Highly active Ru-based CO₂ hydrogenation catalysts are rare. Ruthenium homogeneous catalysts either show only a moderate catalytic performance³³ or require operation under harsh reaction conditions.^{30-32,41}



Scheme 2.2. Metal-ligand cooperative transformations of Ru-PNP in the presence of H₂ and CO₂

In this study we combined *in situ* NMR spectroscopy and density functional theory (DFT) calculations to investigate transformations of Ru-PNP catalyst under catalytically relevant conditions. Activity of **3** and **4** in CO₂ hydrogenation was studied to determine the role of different substrate activation modes in reactions catalyzed by cooperative Ru-PNP complexes. Our study points to a high catalytic activity of ruthenium PNP under mild conditions. We show that the cooperated activation of CO₂ in **3** has a negative effect on catalysis, that can be remediated by the introduction of water to convert the less active and stable intermediates into more catalytic competent ones.

2.2 Catalytic activity and reactivity of Ru-PNP pincer complex

Complexes **3** and **4** provide a starting point for the current investigation of the catalytic CO₂ hydrogenation activity of Ru-PNP (Figure 2.1). Reactions were carried out at 70 °C and a constant pressure of 40 bar (initial composition H₂/CO₂ = 1/1) in THF solutions containing DBU (1,8-diazabicyclo[5.4.0]undec-7-ene) as a base necessary to shift the reaction equilibrium towards the production of formate. The pressure decrease during the catalytic reaction was compensated by a continuous addition of H₂. Initial screening experiments demonstrated a superior catalytic performance when the reactions were promoted by the non-nucleophilic base DBU instead of NEt₃ typically used in this reaction.

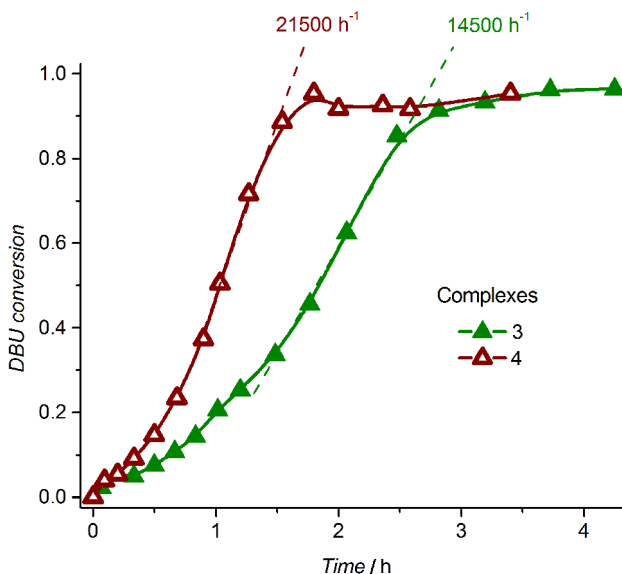


Figure 2.1. Time-evolution of the formation of 2HCOOH-DBU adduct upon CO₂ hydrogenation (30/5 mL THF/DBU, $p(\text{H}_2/\text{CO}_2)=40$ bar, pressure loss compensated with H₂, $T = 70^\circ\text{C}$) by complexes **3** and **4** (2.5 μmol).

By pretreating complex **2** with CO₂ or H₂ prior to the catalytic reaction, we were able to ensure the presence of complexes **3** or **4**, respectively, in the reaction mixture. The results in Figure 2.1 indicate that a high catalytic activity could be achieved with complex **3** under the selected reaction conditions. The maximal reaction rate (TOF) of 14 500 h⁻¹ was reached in this case after a prolonged induction period that probably occurs due to the transformation of **3** to the catalytically active state at the initial stage of the reaction. The activity was significantly improved when the catalytic reaction was carried out with complex **4** instead of **3**. In combination with DBU, catalyst **4** allows reaching maximal TOF of 21 500 h⁻¹ after a significantly shorter induction period.

Complexes **3** and **4** show a significantly different behavior in catalysis (Figure 2.1). To trace the origin of this difference we performed reactivity studies using NMR spectroscopy and supporting DFT calculations. As a starting point of this study, the formation of **3** and **4** from the deprotonated complex **2** in the presence of H₂ and CO₂ was analyzed. Previous works by Milstein and co-workers demonstrated that the ligand-assisted addition of H₂ and CO₂ to the deprotonated **2** yields dihydrido complex **4** and the product of [1,3]-addition of CO₂ – complex **3**.⁴²⁻⁴⁵ We further analyzed the relative stability of these species and the mechanism of their formation by DFT calculations. Figure 2.2 shows the optimized structures of the involved reaction intermediates and transition states together with the computed energetics of the elementary reaction steps.⁴⁶ Both reactions start with the formation of molecular complexes of **2** with the substrate molecules. Despite very similar thermodynamics of complexation with CO₂ and H₂, the nature of the formed species is different. No specific interaction between CO₂ and dearomatized PNP* ligand was observed in **2-CO₂**. On the contrary, **2-H₂** represents a classical example of a σ-H₂ complex⁴⁷⁻⁵¹ featuring a highly symmetric η²-coordination of dihydrogen with short Ru-H distances and a considerably elongated H-H bond (*r*(H-H) = 0.821 Å vs. 0.747 Å for the free molecule).

The cooperative [1,3]-addition of CO₂ (**2-CO₂**→**TS_{2,3}**→**3**) is exothermic by -51 kJ mol⁻¹ and proceeds with a low activation barrier of 34 kJ mol⁻¹. When corrected for entropic effects, the reaction and activation Gibbs free energies are, respectively, equal to -31 and 50 kJ mol⁻¹. This evidences a pronounced entropy loss due to the decrease in the degrees of freedom upon the chemical binding of the non-specifically coordinated CO₂. The **TS_{2,3}** is an early transition state that features a distorted CO₂ molecule that forms an elongated bonds with the basic C1 site of the ligand (*r*(C1-C2) = 2.543 Å) and the Ru center (*r*(Ru-O1) = 2.537 Å). The structure of **TS_{2,3}** suggests that the bending of the linear

CO₂ molecule that is necessary for the attack by the basic C1 center at the deprotonated PNP* pincer arm is the major contributor to the activation energy. The optimized structure of **3** agrees well with the single-crystal X-ray diffraction data reported by Milstein and co-workers.⁴² The accuracy of our calculations is supported by a very good match between the calculated E^\ddagger and G^\ddagger (85 and 81 kJ mol⁻¹, respectively) and the experimental values (94 and 83 kJ mol⁻¹)⁴² determined for the reverse **3** → **2** + CO₂ transformation.

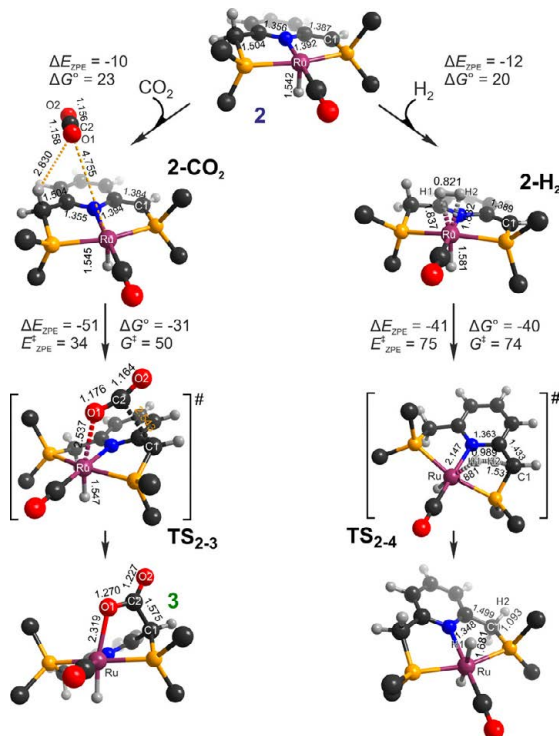


Figure 2.2. Optimized structures of reaction intermediates and transition states involved in the metal-ligand cooperative activation of H₂ and CO₂ by **2** (representation of ^tBu substituents at phosphines simplified for clarity). ZPE-corrected reaction (ΔE_{ZPE}) and activation energies (E_{ZPE}^\ddagger), reaction and activation Gibbs free energies (ΔG° and G^\ddagger) are in kJ mol⁻¹ for individual elementary steps.⁴⁶

Dissociation of H₂ over **2** gives a dihydrido Ru-PNP complex **4** (**2-H₂** → **TS₂₋₄** → **4**, Figure 2.2) and proceeds with an activation barrier ($E_{ZPE}^\ddagger = 75$ kJ mol⁻¹) substantially higher than that computed for the reaction with CO₂. Since H₂ is effectively immobilized within the σ -complex **2-H₂**, the entropic contribution to the reaction and activation energy in this case is negligible. As a result the overall reaction **2** + H₂ → **4** ($\Delta G^\circ = -40$ kJ mol⁻¹) is more thermodynamically favorable than the reaction with CO₂ (**2** + CO₂ → **3**, $\Delta G^\circ = -8$

kJ mol^{-1}). The polarized H_2 molecule in the $\text{TS}_{2,4}$ undergoes a heterolytic cleavage over a $\text{Ru}\cdots\text{C1}$ acid-base pair resulting in **4**.

These results suggest that both complexes **3** and **4** can potentially be present in the reaction mixture during the catalytic hydrogenation of CO_2 . Indeed, whereas the reaction of **2** with H_2 to the dihydrido complex **4** is more thermodynamically favorable, the alternative path towards the CO_2 adduct **3** proceeds with a much lower activation barrier. This implies that despite the formation of **4** is preferred under hydrogen atmosphere, the formation of **3** as a kinetic product could not be ruled out. Particularly, in the presence of excess base necessary to promote CO_2 hydrogenation, one cannot exclude the transient formation of **2**, which can form **3** in presence of CO_2 . The analysis of the reactivity of **3** is crucial to establish its role in catalysis. To assess the involvement of **3** in CO_2 hydrogenation we explored its reactivity towards the components of the reaction mixture, namely H_2 , CO_2 and the DBU base, by NMR spectroscopy. Chemical transformations evidenced by NMR spectroscopy along with the respective DFT-computed reaction energetics are summarized in Scheme 2.3.

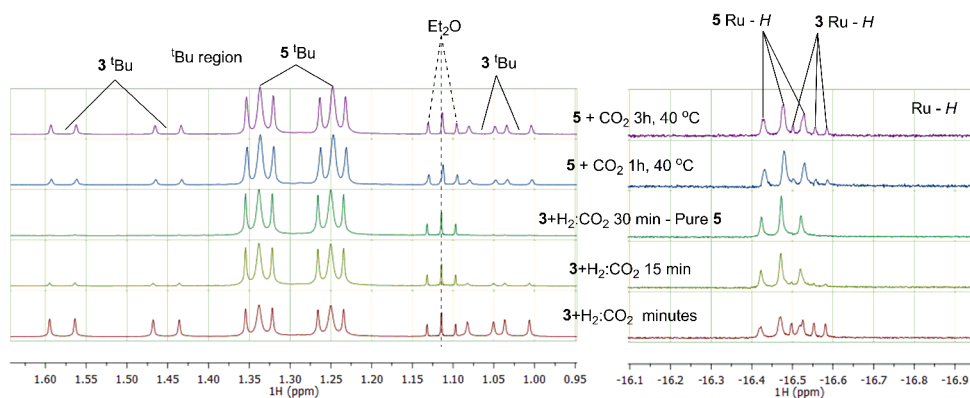
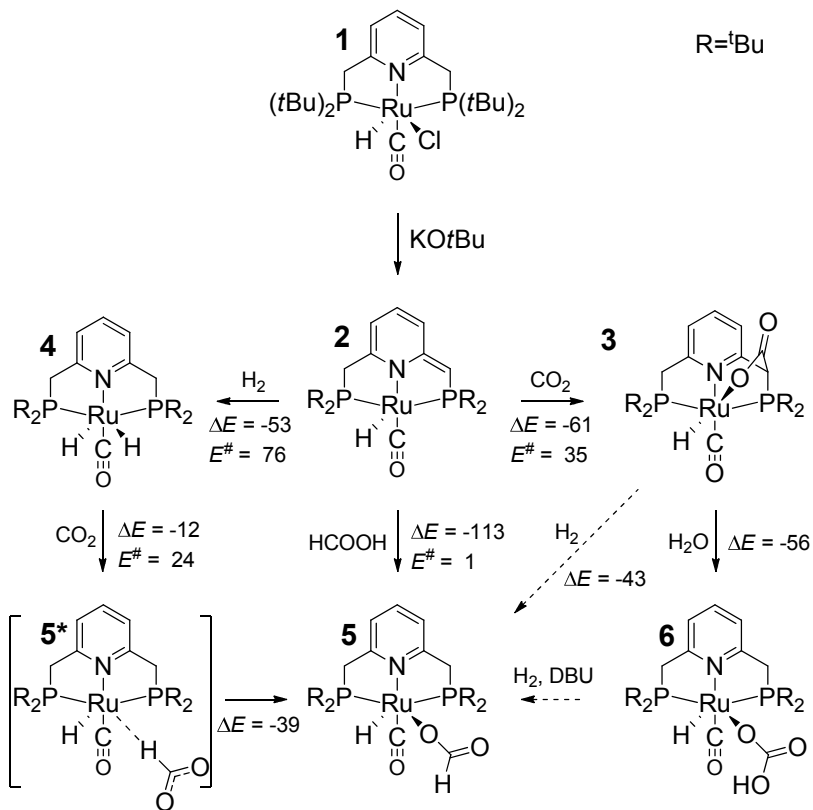


Figure 2.3. ^1H NMR follow up of the transformation of **3** to **5** upon exposure to 3 bar of equimolar H_2/CO_2 or pure CO_2 . For details see Experimental section.

In THF-d_8 the ^1H NMR spectrum of **3** contains a high field ruthenium hydride resonance at $\delta = -16.5$ ppm as a doublet of doublets from coupling to two non-equivalent phosphorus nuclei ($^2J_{\text{PH}} = 22$ and 11 Hz). The ^{31}P NMR spectrum contains two signals at $\delta = 115$ and 109 ppm ($^2J_{\text{PP}} = 251$ Hz). When exposed to 3 bar of equimolar H_2/CO_2 mixture resonances of complex **3** disappear within minutes to give new species **5** (Scheme 2.3). The ^1H NMR spectrum of the Ru-formate complex **5** contains a new Ru-H signal at $\delta = -16.5$ ppm as a triplet ($^2J_{\text{PH}} = 20$ Hz), and the ^{31}P NMR spectrum contains a broad singlet at 88 ,

indicating that the phosphorus nuclei are equivalent. A new singlet at $\delta = 8.3$ ppm, observed upon formation of **5** is assigned to the proton of the HCOO^- anion. (Figure 2.3)



Scheme 2.3. The experimentally observed transformations of Ru-PNP complexes in the presence of H_2 and CO_2 (**5*** is suggested by DFT). The DFT-computed ZPE-corrected reaction (ΔE) and activation (E^\ddagger) energies are given in kJ mol^{-1} .

Nearly identical behavior of **3** was observed under 8 bar total pressure of pure H_2 (Figure 2.4). In the presence of H_2 , **5** cannot be transformed back to **3** and only partial reversibility can be achieved when the atmosphere is changed to pure CO_2 . Exposure of **5** to 3 bar pure CO_2 yielded ca. 16 % of **3** upon heating at 40°C within 3 hours. Under 8 bar CO_2 the amount of **3** in solution increases to ca. 33 % based on integral intensity of **3**+**5**. This result suggests that the generation of **3** under the catalytic reaction conditions is unlikely due to the inevitable presence of hydrogen in the reaction media. DFT calculations show that the reaction **3**→**5** is strongly exothermic ($\Delta E_{\text{ZPE}} = -43 \text{ kJ mol}^{-1}$). We suppose that this transformation proceeds via intermediate formation of **2** and **4** and subsequent reaction with CO_2 . Although these transformations are associated with substantial activation

barriers, related rearrangements of CO₂-added PNN-type ruthenium pincer complexes are known and were proposed to proceed via a similar deprotonated state by Sanford and co-workers.⁴³

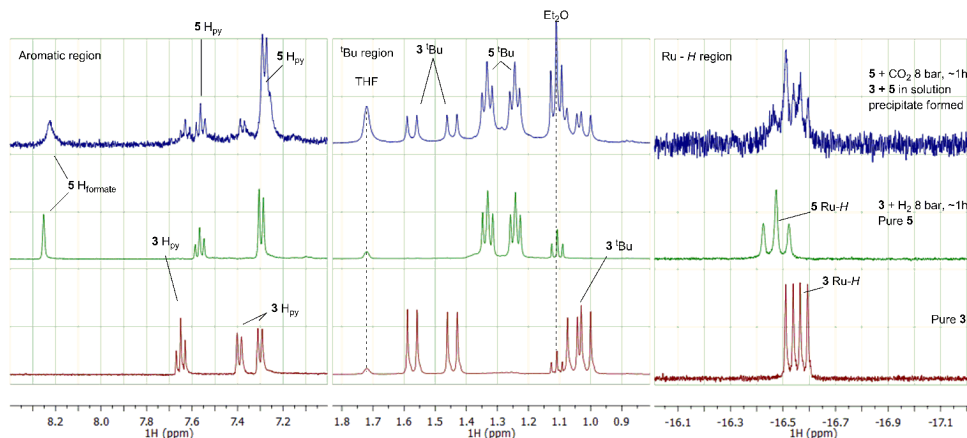


Figure 2.4. ¹H NMR data for transformation of **3** to **5**. Total 8 bar pressure of pure CO₂ or H₂. For details see Experimental section.

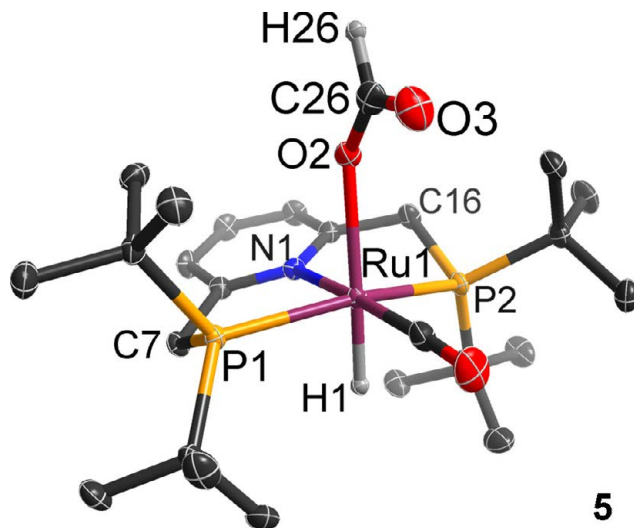


Figure 2.5. X-ray crystal structure of **5** (ellipsoids at 50% probability level). Hydrogen atoms of the PNP ligand and solvent molecules are omitted for clarity. Selected distances and angles are discussed in the text. For analysis details refer to the Experimental section.

Complex **5** can be synthesized independently from benzene solutions of **2** contacted with FA vapors. According to DFT calculations this reaction proceeds via a barrierless protonation of the dearomatized PNP* ligand in **2** (Scheme 2.3). The ¹³C NMR of **5**

contains a signal at $\delta = 170.9$ ppm, which is consistent with the formation of a metal formate complex. FTIR spectrum of **5** features two typical absorption bands at $\nu = 1909$ cm^{-1} and 1599 cm^{-1} assigned to CO and HCOO^- ligands, respectively. Complex **5** can be readily crystallized allowing thus to determine the solid-state structure of **5** that is shown in Figure 2.5. The Ru complex **5** has an octahedral coordination environment and contains an η^1 -coordinated formate moiety with a Ru1-O2 distance ($2.2457(13)$ Å), similar to that reported for other η^1 -ruthenium formate complexes.^{52,53} The ruthenium-ligand distances are nearly identical to a structurally related PNS-Ru formate complex, although the Ru-O bond is significantly longer in **5** than in the PNS-Ru formate (1.983 Å).⁵⁴ The latter was prepared via reaction between CO_2 and related dihydrido complex bearing a PNS ligand.

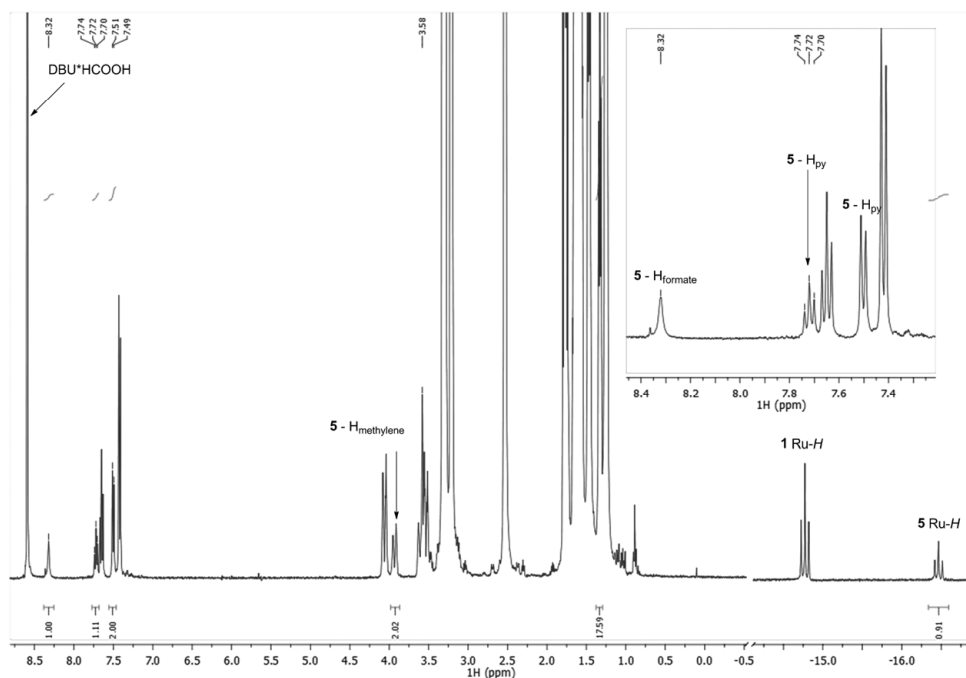


Figure 2.6. ^1H NMR spectral data for the catalytic tube reaction using **1** as a precatalyst ($T = 70^\circ\text{C}$, $p(\text{H}_2/\text{CO}_2=1/1) = 8$ bar). Resonances corresponding to **5** are labeled and integrated where possible. Insert shows the aromatic region in ^1H NMR.

The rapid formation of **5** can also be observed upon the exposure of **4** to CO_2 . DFT calculations (Scheme 2.3) suggest that the direct addition of CO_2 to the Ru-H moiety results in the computed metastable intermediate **5*** containing a non-coordinated HCOO^- anion ($\Delta E = -12$ kJ mol^{-1} , $E^\ddagger = 24$ kJ mol^{-1}), which rearranges to a more stable octahedral

complex **5** ($\Delta E = -39 \text{ kJ mol}^{-1}$). Complex **5** is the only identified compound formed during the catalytic CO_2 hydrogenation with **1** carried out on the NMR scale under 8 bar equimolar CO_2/H_2 mixture at 70°C in the presence of DBU (Figure 2.6). Together with the formation of DBU·HCOOH adduct, we observed a partial transformation of the precatalyst **1** to the formate complex **5** as the only NMR-detectable product within 45 minutes reaction time.

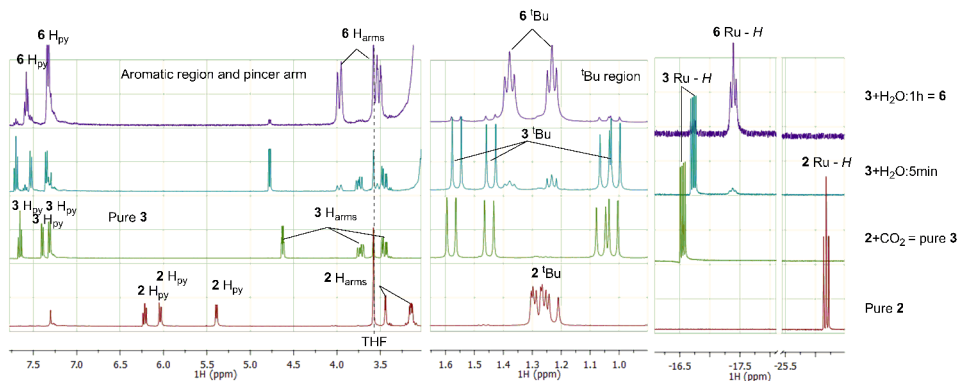


Figure 2.7. ^1H NMR data for formation of **6** by hydrolysis of **3**. For details see Experimental section.

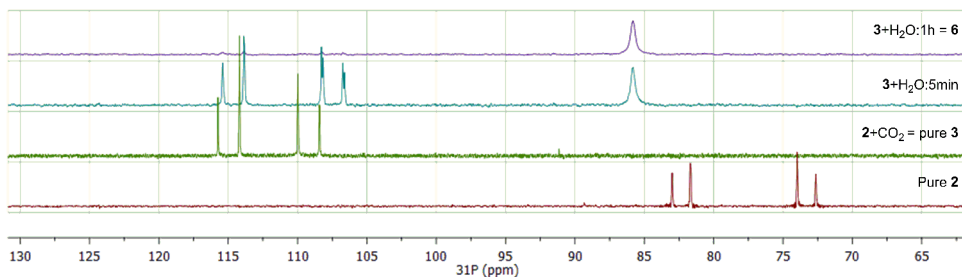


Figure 2.8. ^{31}P NMR data for formation of **6** by hydrolysis of **3**. For details see Experimental section.

The transformation to complex **5** can be viewed as a potential route for reverting the inhibiting effect of the formation of complex **3**. Taking into account the inferior performance of complex **3**, one should seek the opportunities to avoid its presence during catalysis. In fact, transformations of **3** are almost exclusively associated with the cleavage of C–C bond between the added CO_2 moiety and the ligand sidearm. Related transformations of carbonic acid derivatives are common in bioorganic chemistry. Particularly, mandelylthiamine derivatives were shown to undergo hydrogenolysis with subsequent C–C cleavage, yielding bicarbonate as one of the products.⁵⁵ A similar pathway for transformation of **3** was identified by DFT calculations. According to DFT, **3** can undergo a strongly exothermic hydrolysis ($\Delta E = -56 \text{ kJ mol}^{-1}$) to yield a bicarbonate

complex **6** (Scheme 2.3) The reaction of **3** with water can be observed experimentally. The NMR spectroscopic data (Figures 2.7 and 2.8) are consistent with predictions, made by DFT calculations. The ^1H NMR spectra of **3** in the presence of excess water (25-30 equiv. $\text{H}_2\text{O}/\text{Ru}$) showed a gradual decrease of the Ru-H resonance of **3** at $\delta = -16.5$ ppm, and the appearance of a new Ru-H resonance associated with **6** (Figure 2.7). The ^1H NMR spectrum of **6** contains a characteristic Ru-H signal as a triplet at -17.5 ($^2J_{\text{PH}} = 19$ Hz) suggesting the equivalency of P^tBu_2 groups. Methylene arm of **3** is protonated upon release of added CO_2 , and four corresponding protons appear at $\delta = 3.79$ and 3.38 ppm in ^1H NMR spectrum of **6**. Upon hydrolysis a broad singlet at $\delta = 84.4$ ppm appears in the ^{31}P NMR spectrum (Figure 2.8). These resonances appear within minutes after addition of water to solutions of **3** in THF-d_8 . The infrared spectrum of **6** contains features a band due to a carbonate vibration at $\nu = 1626$ cm^{-1} . This value is close to the one obtained for another η^1 -Ru bicarbonate complex.⁵⁶ Hydrolysis of **3** leads to nearly quantitative formation of **6** within an hour. It is important to note that the reaction occurs in an atmosphere of CO_2 (3 bar) when the reversible transformation of **3** to **2** is suppressed. Consequently, this transformation can be applied during catalyst pretreatment if presence of **3** is not desired.

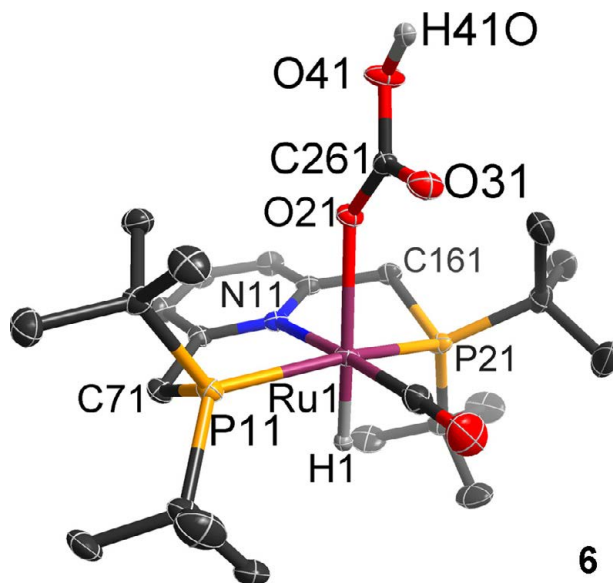


Figure 2.9. X-ray crystal structure of **6** (ellipsoids at 50% probability level). Hydrogen atoms of the PNP ligand and solvent molecules are omitted for clarity. Selected distances and angles: are discussed in the text. For analysis details refer to the Experimental section.

Compound **6** crystallizes as two polymorphs, triclinic and monoclinic, present in the same crystal (see Experimental section). The structure of the major triclinic polymorph is presented in Figure 2.9. Complex **6** is a distorted octahedron with P11-Ru1-P21 angle of $158.70(2)^\circ$. The ruthenium coordination sphere of **6** is nearly identical to that of **5**, and the ruthenium-oxygen bond distance is within 0.01 \AA of the Ru-O bond in **5**. Complex **6** is a relatively rare example of a η^1 -Ru-bicarbonate complex: most ruthenium bicarbonate complexes are η^2 -coordinated.^{57,58}

The base promoter, typically used in CO_2 hydrogenation to shift the unfavorable reaction equilibrium,²⁰ is the final component of the reaction mixture applied in our reactivity study. As follows from the NMR-scale catalytic experiment, complex **5** is not reactive in presence of strong non-nucleophilic DBU base. Similarly, precatalyst **1** cannot be deprotonated by DBU even at elevated temperatures. Surprisingly under hydrogen atmosphere in the presence of DBU complex **6** undergoes a rapid transformation to formate complex **5**. As follows from ^1H NMR data summarized in Figure 2.10, in the presence of H_2 **6** undergoes a facile transformation to **5** within 1 hour when heated at 70°C in THF. Similarly to the NMR scale catalytic hydrogenation experiment, formate complex **5** was the sole product of this transformation. Observed reactivity of **6** further justifies the utility of selective hydrolysis as a tool to control the catalyst pretreatment.

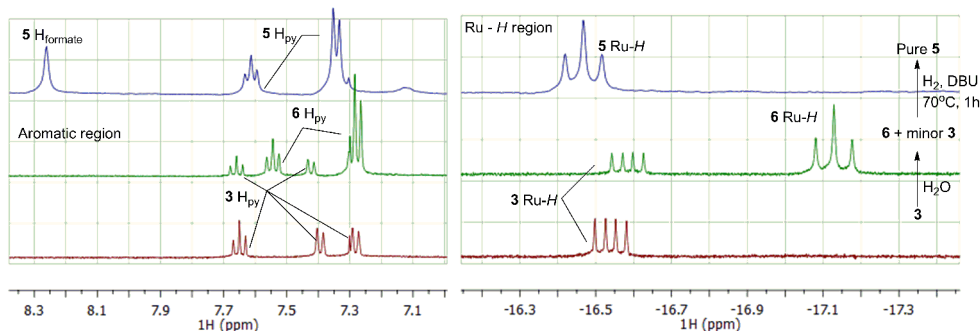
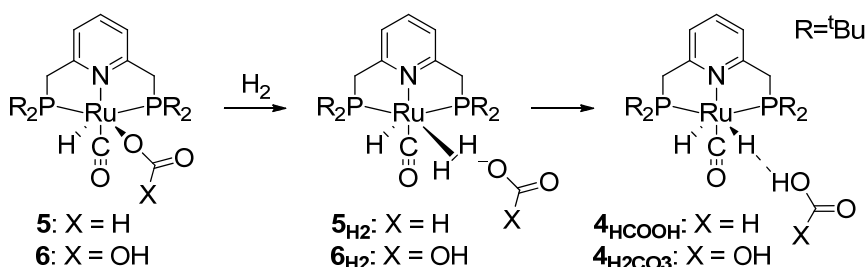


Figure 2.10. ^1H NMR spectra for hydrogenolysis of **6**.

Finally, we used DFT calculations to propose a plausible reaction path for the transformation of **5** and **6** in the presence of H_2 (Scheme 2.4). In case of **6**, the HCO_3^- anion can be substituted by H_2 to form $\mathbf{6}_{\text{H}_2}$ ($E^\ddagger = 65 \text{ kJ mol}^{-1}$, $\Delta E = 31 \text{ kJ mol}^{-1}$). This step is followed by a facile heterolytic dissociation of H_2 ($E^\ddagger = 6 \text{ kJ mol}^{-1}$, $\Delta E = -7 \text{ kJ mol}^{-1}$) to $\mathbf{4}_{\text{H}_2\text{CO}_3}$ (Scheme 3.3). Subsequent reaction with DBU is necessary to eliminate a $\text{DBU}\cdot\text{H}_2\text{CO}_3$ adduct and to ensure the favorable thermodynamics of the overall process (**6** +

$\text{H}_2 + \text{DBU} \rightarrow \mathbf{4} + \text{DBU} \cdot \text{H}_2\text{CO}_3$, $\Delta E = -18 \text{ kJ mol}^{-1}$). Similar transformations involving **5** proceed with nearly identical energetics. Although not observed experimentally, these transformations can contribute to the catalytic cycle of CO_2 hydrogenation.



Scheme 2.4 Proposed mechanism of hydrogenolysis of formate and bicarbonate complexes **5** and **6**, respectively.

In summary, Ru-PNP pincer can undergo chemical transformations involving every component of the reaction mixture either separately or combined. Complexes **3** and **4** are catalytically active, but their performance differs strongly. While catalyst **4** provides a high activity, complex **3** shows significantly lower performance. Complexes **5** and **6** can easily be generated during the catalyst activation procedure. Therefore, their contribution to catalysis should also be accurately assessed.

2.3 Catalytic activity of Ru-PNP pincer catalyst: contribution of stable intermediates.

The insights obtained from the reactivity studies described above were further applied to catalysis by Ru-PNP in an attempt to remediate the inhibiting effect of the formation of **3**. As suggested by the reactivity studies, **3** can be selectively converted to the bicarbonate complex **6** in the presence of water. Such a transformation has a pronounced beneficial effect for the catalytic activity of **3** in the hydrogenation of CO_2 . Generation of complex **6** by treatment of **3** with of ca. 2000 equiv. $\text{H}_2\text{O}/\mathbf{3}$ prior to the catalytic test results in the activity similar to that observed for dihydrido complex **4** ($\text{TOF} = 21\,000 \text{ h}^{-1}$), although the induction period is not avoided.

The beneficial role of hydrolysis of **3** was also demonstrated in a separate experiment, in which water was introduced in situ during the catalytic reaction with **3**. The total conversion in this experiment was kept below 10% to ensure the reliability of the test. The injection of water led to a 50% increase of the hydrogenation rate (Figure 2.12). These

results evidence the promoting effect of the conversion of **3** to **6** for the hydrogenation activity. They also suggest that the formation of **3** during the catalysis should be avoided.

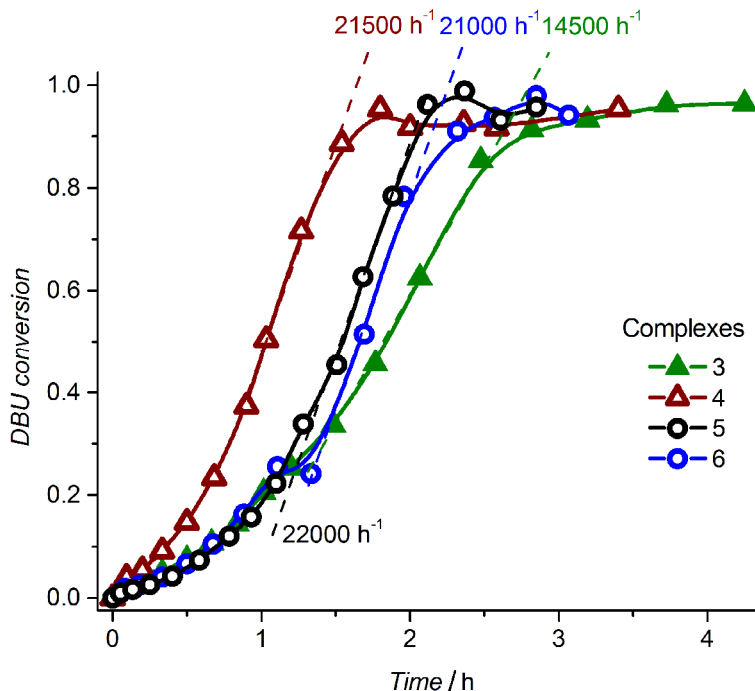


Figure 2.11. Summary of CO_2 hydrogenation activity of complexes **3** - **6** (30/5 mL THF/DBU, $p(\text{H}_2/\text{CO}_2)=40$ bar, pressure loss compensated with H_2 , $T = 70^\circ\text{C}$, $2.5 \mu\text{mol}$ catalyst)

Our reactivity studies show, that in the presence of H_2 and DBU **6** can be further transformed to **5**. We propose that this transformation involves hydrogenolysis of **6** to **4** and subsequent reaction with $\text{DBU}\cdot\text{H}_2\text{CO}_3$ that is the only carbon source present in the reaction medium. Consequently, the catalytic behavior of complex **6** should be similar to that of **5**. Indeed, the kinetic trace obtained for the **3**/ H_2O system representing complex **6** is nearly identical to that obtained using pure **5** as the catalyst (Figure 2.11). DFT results point to **5** as the most thermodynamically stable compound among the Ru-PNP derivatives considered in this chapter. This implies that **5** is a potential resting state in the catalytic reaction. This proposition is supported by the fact that NMR experiments that evidenced the sole formation of **5** during the catalytic reaction (Figure 2.6).

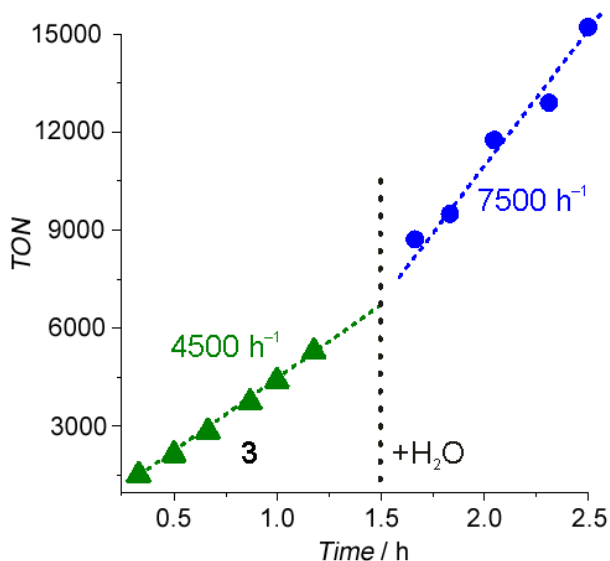


Figure 2.12 The effect of H_2O injection to the catalytic reaction with **3** (30/5 mL THF/DBU, 0.53 μmol catalyst, $p(H_2/CO_2 = 37/3) = 40$ bar)

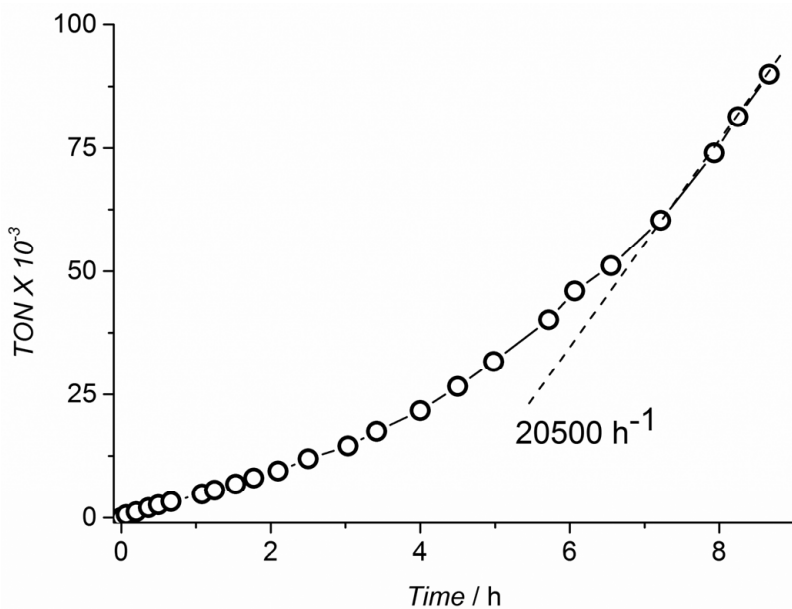


Figure 2.13. Catalytic hydrogenation of CO_2 using 0.42 μmol of **1**

Upon the completion of all reactions, the conversion of DBU to corresponding formate adduct was nearly quantitative, corresponding to an acid-to-amine ratio of 1.8 ± 0.1 . The

maximal TON attainable in these experiments was limited by the available DBU base. A separate experiment was conducted to evaluate the stability of the Ru-PNP catalyst under the CO₂ hydrogenation conditions. With a lower catalyst concentration, a TON of more than 90 000 was achieved without any sign of catalyst deactivation observed. The maximal TOF detected in this experiment was 20 500 h⁻¹ (Figure 2.13). The observed acceleration of the reaction overtime may point to two possibilities. Firstly, it can be the consequence of the setup design, where the pressure loss is compensated with H₂ that leads to a gradual elevation of H₂/CO₂ ratio from 1/1 to ca. 3/1 in the course of the reaction. In this case the reaction acceleration would suggest the preference for elevated H₂ partial pressures that is consistent with literature reports.³³ Alternatively, it may indicate the formation of transient species, responsible for the catalytic activity, that we could not observe with NMR spectroscopy. The search for this transient species will be continued in the next Chapter of this thesis.

2.4 Conclusions and outlook

The role of ligand-assisted transformations of lutidine-based Ru-PNP complexes in catalytic hydrogenation of CO₂ was investigated. Although majority of reports highlight the beneficial role of ligand non-innocence, we found that transformations, involving ligand participation are not beneficial for the catalytic CO₂ hydrogenation. Complex **3** that is the product of ligand-assisted CO₂ activation was identified as the state responsible for the inhibited catalytic performance. We have identified an “emergency rescue” pathway to avoid the formation of **3** via its selective hydrolysis. Reaction with water converts **3** to the bicarbonate complex **6** and restores the activity of the system by providing a pathway towards formation of the active species. The Ru-formato complex **5** was identified as the most thermodynamically stable complex by DFT calculations. This is supported by the results of NMR reactivity studies, in which **5** was the sole species observed under the catalytic conditions. Taken together, these data allows proposing **5** as the resting state in the catalytic cycle of CO₂ hydrogenation.

It is demonstrated that Ru-PNP catalyst in combination with DBU is exceptionally active under mild conditions. The results presented here provide new insight into the complex reactivity pathways that can be encountered in CO₂ hydrogenation when cooperative ligands are involved. Finally, this Chapter builds the foundation for further research on the catalytic properties of Ru-PNP in reversible hydrogenation of carbon dioxide. In the next Chapter we will focus on the optimization of the activity of Ru-PNP

and explore its potential in the reverse reaction – dehydrogenation of FA. Secondly, an effort will be made to analyze the mechanism of CO₂ hydrogenation in detail using DFT calculations.

2.5 Experimental section

General: all manipulations unless otherwise stated were performed using Schlenk or high vacuum line (10^{-4} – $5 \cdot 10^{-5}$ mbar) techniques. Argon was dried with a Sicapent column. Air sensitive compounds were stored in a MBraun glovebox under an atmosphere of dry nitrogen or argon. Solvents were dispensed from alumina drying column apparatus (Janssen-Engineering: Nuenen, The Netherlands) and degassed prior to use. 1,8-diazabicyclo[5.4.0]undec-7-ene (DBU) was purchased from Fluorochem and vacuum distilled from calcium hydride. Deuterated solvents were purchased from Eurisotop and dried over Na/benzophenone (C₆D₆, THF-d₈) or phosphorus pentoxide (CD₂Cl₂), degassed using three freeze-pump-thaw cycles prior to use. Compounds **1**⁵⁹, **2**⁶⁰ were prepared according to literature procedures. Compound **3**⁴² was prepared by published procedure with diethyl ether instead of pentane. Complex **4**⁶⁰ was generated in situ by treatment of **2** with hydrogen at 3 bar. Spectral data for **4** is consistent with literature data.⁶⁰ Other chemicals were purchased from Sigma and used without purification.

NMR spectra were recorded on Varian Mercury 400 MHz spectrometer; chemical shifts were referenced to residual solvent peaks. ESI-MS measurements were performed on Thermo Scientific LCQ Fleet apparatus, concentrations of formic acid were analyzed using Shimadzu HPLC setup with 25mM phosphate buffer of pH = 2 as mobile phase. Toluene concentrations were determined using Shimadzu GC-17A instrument.

Catalytic hydrogenation procedures

Small scale hydrogenation experiments were performed in a 10 mL stainless steel autoclave at 40 bar H₂/CO₂=1/1 pressure at 70°C (3mL THF, 0.5 mL base, 2,5±0.2 μmol of **1** as a catalyst). The presence of a weak base NEt₃ proved to be insufficient to provide high turnover numbers (TON) in ethanol or THF (750 and 160 correspondingly). A stronger non-coordinating base DBU (1,8-diazabicyclo[5.4.0]undec-7-ene) in combination with THF provides full conversion of the base throughout 1 hour reaction with TON of 1960, thus making precise activity estimation impossible. A scaled-up experiments were performed for activity estimation.

Large scale catalytic hydrogenation tests were performed in Top Industrie 100 mL stainless steel autoclave. The vessel was evacuated overnight at 150°C, purged several times with nitrogen, and the reaction medium containing the catalyst (2,5±0.2 μmol) was introduced by cannula transfer. The autoclave was flushed with a first reactive gas (either CO₂ or H₂), preheated to reaction temperature of 70 °C under CO₂ or H₂ and filled with H₂/CO₂ equimolar mixture up to 40 bar total pressure. Samples were withdrawn via dip-tube installation (dead volume 4μl, sampling volume 110 μl), diluted to 1mL and immediately analyzed by HPLC and GC-FID. To insure presence of only **3** or **4** in the loaded mixture, THF solutions of **1** were treated with 1 eq. of KO^tBu and purged with hydrogen of carbon dioxide (that resulted in immediate color change from green-blue to yellow) before loading

in the autoclave. Compound **5** was prepared according to the procedure described in this work and loaded as solid. The reaction medium contained 30 mL THF, 5 mL DBU, 100 μ l toluene an internal standard. Water addition (100 μ l) was done prior to loading via syringe.

Synthetic procedures and spectral data for new compounds **5** and **6**

Synthesis of formate complex 5: **2** (49 mg, 0.0915 mmol) was dissolved in 1 mL of dry benzene and treated with formic acid vapors in Ar at room temperature. A white precipitate immediately forms. Treatment was continued for 3 minutes and 5 mL diethyl ether was added to precipitate the compound from the solution. Solvent was removed by filtration and the solid was dried in vacuo. **5** is sparingly soluble in THF, though soluble in dichloromethane. Crystals for X-ray diffraction were grown from dilute dichloromethane solution by slow pentane or ether vapor diffusion at room temperature. Y: 42 mg (80%). Dichloromethane solutions of **5** are stable for at least 48 hours at room temperature under argon. ^1H NMR(400 MHz, CD_2Cl_2): δ 8.40 (s, 1H, O-C(O)H), 7.60 (t, $J_{\text{H-H}}=7.8\text{Hz}$, 1H, py- H_{para}), 7.28(d, $J_{\text{H-H}}=7.8\text{Hz}$, 2H, py- H_{meta}), 3.74(d, $J_{\text{H-H}}=16.4\text{Hz}$, 2H, -CHHP), 3.40(dt, $J_{\text{H-H}}=16.4\text{Hz}$, 2H, -CHHP), 1.31(t, 18H, P-(C-(CH_3) $_3$) $_2$), 1.22(t, 18H, P-(C-(CH_3) $_3$) $_2$), -16.49(t, $J_{\text{P-H}}=19.4\text{Hz}$, 1H, Ru-H). $^{31}\text{P}\{^1\text{H}\}$ NMR(161 MHz, CD_2Cl_2): δ 88.0(s). $^{13}\text{C}\{^1\text{H}\}$ NMR (101 MHz, CD_2Cl_2) δ 209.32 (s, Ru-CO), 170.94 (s, C1), 163.76 (t, $J = 5.1$ Hz, C2), 138.09 (s, C4), 120.54 (t, $J = 4.4$ Hz, C3), 37.47 (t, $J = 6.4$ Hz, C5), 36.86 (t, $J = 6.0$ Hz, C8 or 9), 35.52 (t, $J = 10.3$ Hz, C8 or 9), 30.06 (t, $J = 2.7$ Hz, C6 or 7), 29.78 (t, $J = 2.2$ Hz, C6 or 7). IR(film): 1909 cm^{-1} (ν_{CO}), 1599 cm^{-1} (ν_{COO} , formate). EA: Calcd. $\text{C}_{25}\text{H}_{45}\text{NO}_3\text{P}_2\text{Ru}\cdot 0.5\text{Et}_2\text{O}$: C 53.03, H 8.14, N 2.33. Found: C 53.11, H 8.07, N 2.39.

Generation and Characterization of bicarbonate complex **6:** **2** (21,6 mg, 0.041 mmol) was loaded in Wilmad quick pressure NMR tube (thin wall, 7 in.) in THF- d_8 and pressurized with 3 bar CO_2 to generate **3** quantitatively. After measurement, the tube was capped with a septum and 20 μ l of degassed water was added to the tube. Following addition the tube was re-pressurized with 3 bar of CO_2 and shaken to mix the media. The spectra were recorded for 1,5 h until the signal to noise ratio started to degrade due to precipitation of crystalline **6**. The solvent was decanted, and the solid was washed with a little THF. The solid was dried under vacuum and suspended in dichloromethane. Though **6** is not well soluble in CD_2Cl_2 , the solubility was sufficient for NMR characterization. Crystals for X-ray diffraction were grown from dilute dichloromethane solution by slow pentane vapor diffusion at room temperature. This yields 16.8mg (69%) of **6**. ^1H NMR(400 MHz, CD_2Cl_2): δ 7.57(t, $J_{\text{H-H}}=8\text{Hz}$, 1H, py- H_{para}), 7.25(d, $J_{\text{H-H}}=7.6\text{Hz}$, 2H, py- H_{meta}), 3.79(d, $J_{\text{H-H}}=16.4\text{Hz}$, 2H, -CHHP), 3.38(dt, $J_{\text{H-H}}=15.2\text{Hz}$, $J_{\text{P-H}}=3.7\text{Hz}$, 2H, -CHHP), 1.36(t, $J_{\text{P-H}}=6.4\text{Hz}$, 18H, P-(C-(CH_3) $_3$) $_2$), 1.22(t, $J_{\text{P-H}}=6.9\text{Hz}$, 18H, P-(C-(CH_3) $_3$) $_2$), -17.21(t, $J_{\text{P-H}}=19.2\text{Hz}$, 1H, Ru-H). $^{31}\text{P}\{^1\text{H}\}$ NMR(CD_2Cl_2): δ 86.1(s). $^{31}\text{P}\{^1\text{H}\}$ NMR(THF- d_8): δ 85.8(s). ESI-MS(m/z): 526.24 (PNP-RuHCO $^+$), 558,16 (PNP-Ru(HCO $_3$) $^+$) ratio 3/1. IR(film): 1910 cm^{-1} (ν_{CO}), 1626 cm^{-1} (ν_{COO} , bicarbonate)

Due to low solubility of **6** in CD_2Cl_2 (ca. 18 $\mu\text{mol/mL}$) carbon spectrum of appropriate quality was not obtained

NMR follow-up procedures and related data

Conversion of 3 to bicarbonate complex 6

Generation of **6** upon treatment of **3** with water was followed by ^1H and ^{31}P measurements. We observed clean formation of **3** upon reaction of **2** with CO_2 . Upon addition of water, signals of **3** gradually disappeared, giving rise to a new resonance pattern, identical of those of **1**. The latter indicated the restoration of phosphorus nuclei equivalency as well as equivalency of pincer arm protons.

NMR Scale Catalytic Reactions

1 (20 mg, 0.0356 mmol) was placed in thick wall Wilmad Quick pressure NMR tube. THF- d_8 (0,2 mL) was added in a glovebox, Excess DBU was added and the tube was pressurized with equimolar H_2/CO_2 mixture up to 8 bar and incubated at $70\text{ }^\circ\text{C}$ for 45 minutes. ^1H measurements were performed before and after heating to reveal that **1** was partially converted to formate complex **5**.

Reversible transformation 3 to 5

Two NMR experiments were performed to probe the reversibility of transformation of **3** to formate complex **5**.

Procedure 1: **3** (7.8 mg, 0.0136 mmol) in THF- d_8 (0.2 mL) was loaded in a heavy wall NMR tube and put under 8 bar of hydrogen. Within 1 hour **3** was completely transformed in **5**. A little crystalline solid was formed during this process. Removal of the H_2 atmosphere and replacement with CO_2 (8 bar) resulted in formation of **3**. Transformation of **5** to **3** started immediately but further measurements were interrupted by precipitation of either **3** or **5** and almost complete loss of signal.

Procedure 2: Approx. 10-fold lower concentration of **3** was maintained during this test to prevent precipitation of any intermediates and provide adequate NMR data. **3** (1.9 mg, 0.0033 mmol) THF- d_8 (0.5 mL) was loaded in a thin wall NMR tube and put under 3 bar of $\text{H}_2/\text{CO}_2/\text{Ar}$ (1/1/1) mixture. Transformation to **5** was monitored at room temperature by ^1H NMR. Within 1 hour **3** was completely transformed in **5**. No precipitation was observed during this process. To trigger the reverse reaction, the tube was purged five times with carbon dioxide and brought to 3 bar of static CO_2 pressure. **3** was not formed at room temperature, but traces of **3** did appear when the tube was heated to $40\text{ }^\circ\text{C}$. Therefore the transformation of **5** to **3** is significantly slower, and only ca 25% conversion of **5** is observed after 3 h at $40\text{ }^\circ\text{C}$.

NMR follow up of transformation 6 to 5 in presence of DBU and H₂.

3 (3,5 mg, 0.006 mmol) was placed in thin wall NMR tube THF- d_8 (0.5 mL) and treated with $2.5\ \mu\text{l}$ of water under CO_2 (3 bar) to form **6** as indicated by ^1H NMR. Excess DBU was added, which resulted in precipitation of **6**. The tube was purged with hydrogen, pressurized with 3 bar H_2 and dwelled at $70\text{ }^\circ\text{C}$. Upon heating we observed transformation of **6** to **5**. Under these conditions some amount of **3** (<25 %) persists in the reaction medium. This amount of **3** as well converts to **5** upon exposure to H_2 .

Crystal structure analysis of new compounds 5 and 6

Crystal structure analysis of 6

X-ray reflections were measured on a Bruker Kappa ApexII diffractometer with sealed tube and Triumph monochromator ($\lambda = 0.71073\text{ \AA}$). Indexing of the reflections with Dirax⁶¹ showed the

presence of two crystal domains in the triclinic and a monoclinic crystal system, respectively. The intensities were integrated using Eval15.⁶² Based on the non-overlapping reflections both crystal structures were solved with automated Patterson methods in the DIRDIF-08 software.⁶³ The crystal structure of the triclinic domain (**6a**) could successfully be solved and refined in space group $P\bar{1}$ (no. 2), the monoclinic domain (**6b**) in space group P21/c (no. 14). Least-squares refinement was performed with SHELXL-97⁶⁴ against F2 of all reflections. Based on the non-overlapping reflections, the completeness was 48.5% in **6a**, and 79.9% in **6b**. With these initial structural models it was possible to split the intensities of the overlapping reflections based on the calculated structure factors. The scale factor of 5.64 was used between **6a** and **6b**. Datasets of 99.7% completeness (**6a**) and 97.7% completeness (**6b**) were obtained and used to finalize the structure refinement. Non-hydrogen atoms were refined freely with anisotropic displacement parameters. Hydrogen atoms were located in difference Fourier maps. O-H and Ru-H hydrogen atoms in **6a** were refined freely with isotropic displacement parameters, in **6b** they were kept fixed on their located position. C-H hydrogen atoms in both structures were refined with a riding model. In both structures the CH₂Cl₂ solvent molecules were refined with a disorder model. Restraints were used for distances, angles and isotropic behavior in these disordered moieties. Geometry calculations and checking for higher symmetry was performed with the PLATON program.⁶⁵ CCDC 948170 and 948171 contain the supplementary crystallographic data for **6a** and **6b**. These data can be obtained free of charge from The Cambridge Crystallographic Data Centre via www.ccdc.cam.ac.uk/data_request/cif

Crystal structure analysis of 5

The X-ray diffraction experiment was performed on a Bruker Kappa ApexII diffractometer with sealed tube and Triumph monochromator ($\lambda = 0.71073 \text{ \AA}$). Intensity data were integrated with the Eval15 software.⁶² The structure was solved with Direct Methods using the program SIR-2011.⁶⁶ Least-squares refinement was performed with SHELXL-97⁶⁴ against F2 of all reflections. Non-hydrogen atoms were refined freely with anisotropic displacement parameters. All hydrogen atoms were located in difference Fourier maps. Hydrogen atoms H1 and H26 were refined freely with isotropic displacement parameters, all other hydrogen atoms were refined with a riding model. Geometry calculations and checking for higher symmetry was performed with the PLATON program.⁶⁵ CCDC 948172 contains the supplementary crystallographic data for compound **5**. These data can be obtained free of charge from The Cambridge Crystallographic Data Centre via www.ccdc.cam.ac.uk/data_request/cif

Computational details

Calculations were performed by Dr. E. A. Pidko. Density functional theory (DFT) with the PBE0 (also denoted as PBE1PBE and PBEh)⁶⁷ hybrid exchange-correlation functional was used for the quantum-chemical calculations. Prior benchmark studies have shown the high accuracy of this method among a set of hybrid exchange-correlation functionals for the description of a wide range of systems⁶⁸ such as transition metal catalyzed reactions⁶⁹ and magnetic systems.⁷⁰ Furthermore, we have performed extensive tests of the accuracy of different DFT methods for modeling CO₂ hydrogenation to carbon dioxide. Such popular exchange-correlation functionals as M06, M06-L and B3LYP were included in the comparison. The experimentally determined exothermicity (-31 kJ mol^{-1}

¹) of the CO₂ conversion to formic acid was reproduced well only by the PBE0 functional (−23 kJ mol^{−1}).

Full geometry optimizations and saddle-point searches were performed within Gaussian 09.⁷¹ The full electron 6-311G(d,p) basis set was used for all atoms except ruthenium for which the LanL2DZ basis set was employed. To test the accuracy of the selected methodology, selected elementary reaction step (H₂ dissociation over **2**) was also modeled using a larger triple-zeta+polarization quality basis set (Def2-TZVPP)⁷² for Ru center and 6-311+G(d,p) for light atoms. The thus computed energetics agreed within 5 kJ mol^{−1} with that predicted by the standard calculations. The polarisable continuum model (PCM) with standard parameters for THF solvent, as implemented in the Gaussian 09 program package, was used during the geometry optimization and frequency analysis to account for bulk solvent effects.

We have observed that the expansion of the basis set with diffuse functions has a negligible effect on the computed energetics, while it resulted in a much slower SCF convergence (when PCM model was used for solvent effects). We therefore decided to limit ourselves to ZPE-corrected energies as well as free energies uniformly computed at the same level of theory. The choice of the computational methodology was justified by a set of single-point energy calculations for the transformations **4**+CO₂→**5***→**5**→**2**_{HCOOH}. Reaction energies for the respective transformations with the current PBE0/(LanL2DZ,6-311G(d,p)) method are: -23, -44, +93 kJ mol^{−1}. Single point energy correction at the PBE0/(TZVPP,6-311+G(d,p)) gives the following reaction energies: -21, -45, +94, evidencing a perfect agreement between the two methodologies.

The nature of the stationary points was evaluated from the analytically computed harmonic modes. No imaginary frequencies were found for the optimized structures, confirming that these correspond to local minima on the potential energy surface. All transition states exhibited a single imaginary frequency, corresponding to the eigenvector along the reaction path. The assignment of the transition state structure to a particular reaction path was tested by perturbing the structure along the reaction path eigenvector in the directions of the product and the reagent followed by geometry optimization. The reaction and activation energies reported in the manuscript were corrected for zero point (E_{ZPE}) energy contribution computed using the results of the normal-mode analysis.

2.6 Notes and References

- (1) Cokoja, M.; Bruckmeier, C.; Rieger, B.; Herrmann, W. A.; Kühn, F. E. *Angew. Chem. Int. Ed.* **2011**, *50*, 8510.
- (2) Sakakura, T.; Choi, J.-C.; Yasuda, H. *Chem. Rev.* **2007**, *107*, 2365.
- (3) Huang, K.; Sun, C.-L.; Shi, Z.-J. *Chem. Soc. Rev.* **2011**, *40*, 2435.
- (4) *Carbon Dioxide as Chemical Feedstock*; Wiley-VCH Verlag GmbH & Co. KGaA, **2010**.
- (5) Greenhalgh, M. D.; Thomas, S. P. *J. Am. Chem. Soc.* **2012**, *134*, 11900.
- (6) Ohishi, T.; Zhang, L.; Nishiura, M.; Hou, Z. *Angew. Chem. Int. Ed.* **2011**, *50*, 8114.
- (7) Lejkowski, M. L.; Lindner, R.; Kageyama, T.; Bódizs, G. É.; Plessow, P. N.; Müller, I. B.; Schäfer, A.; Rominger, F.; Hofmann, P.; Futter, C.; Schunk, S. A.; Limbach, M. *Chem. Eur. J.* **2012**, *18*, 14017.
- (8) Zhang, L.; Cheng, J.; Carry, B.; Hou, Z. *J. Am. Chem. Soc.* **2012**, *134*, 14314.
- (9) Whiteoak, C. J.; Kielland, N.; Laserna, V.; Escudero-Adán, E. C.; Martin, E.; Kleij, A. W. *J. Am. Chem. Soc.* **2013**, *135*, 1228.

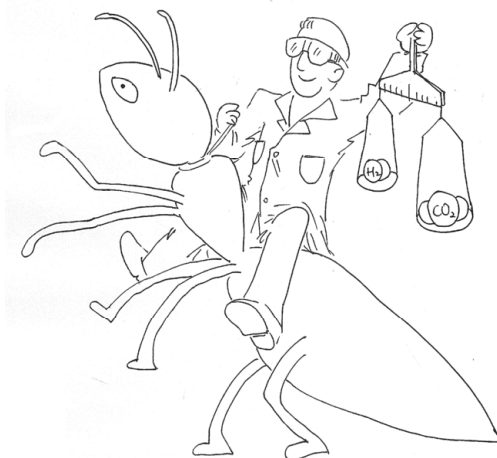
- (10) Chatelet, B.; Joucla, L.; Dutasta, J.-P.; Martinez, A.; Szeto, K. C.; Dufaud, V. *J. Am. Chem. Soc.* **2013**, *135*, 5348.
- (11) Sakai, T.; Tsutsumi, Y.; Ema, T. *Green Chem.* **2008**, *10*, 337.
- (12) Olah, G. A. *Angew. Chem. Int. Ed.* **2005**, *44*, 2636.
- (13) Olah, G. A.; Prakash, G. K. S.; Goepfert, A. *J. Am. Chem. Soc.* **2011**, *133*, 12881.
- (14) Wesselbaum, S.; vom Stein, T.; Klankermayer, J.; Leitner, W. *Angew. Chem. Int. Ed.* **2012**, *51*, 7499.
- (15) Wesselbaum, S.; Moha, V.; Meuresch, M.; Brosinski, S.; Thenert, K. M.; Kothe, J.; vom Stein, T.; Englert, U.; Hoelscher, M.; Klankermayer, J.; Leitner, W. *Chem. Sci.* **2015**, *6*, 693
- (16) Boddien, A.; Mellmann, D.; Gärtner, F.; Jackstell, R.; Junge, H.; Dyson, P. J.; Laurenczy, G.; Ludwig, R.; Beller, M. *Science* **2011**, *333*, 1733.
- (17) Fellay, C.; Dyson, P. J.; Laurenczy, G. *Angew. Chem. Int. Ed.* **2008**, *47*, 3966.
- (18) Boddien, A.; Federsel, C.; Sponholz, P.; Mellmann, D.; Jackstell, R.; Junge, H.; Laurenczy, G.; Beller, M. *Energy. Environ. Sci.* **2012**, *5*, 8907.
- (19) Joó, F. *ChemSusChem* **2008**, *1*, 805.
- (20) Schaub, T.; Paciello, R. A. *Angew. Chem. Int. Ed.* **2011**, *50*, 7278.
- (21) Zhang, Z.; Hu, S.; Song, J.; Li, W.; Yang, G.; Han, B. *ChemSusChem* **2009**, *2*, 234.
- (22) Ziebart, C.; Federsel, C.; Anbarasan, P.; Jackstell, R.; Baumann, W.; Spannenberg, A.; Beller, M. *J. Am. Chem. Soc.* **2012**, *134*, 20701.
- (23) Langer, R.; Diskin-Posner, Y.; Leitus, G.; Shimon, L. J. W.; Ben-David, Y.; Milstein, D. *Angew. Chem. Int. Ed.* **2011**, *50*, 9948.
- (24) Federsel, C.; Boddien, A.; Jackstell, R.; Jennerjahn, R.; Dyson, P. J.; Scopelliti, R.; Laurenczy, G.; Beller, M. *Angew. Chem. Int. Ed.* **2010**, *49*, 9777.
- (25) Federsel, C.; Jackstell, R.; Beller, M. *Angew. Chem. Int. Ed.* **2010**, *49*, 6254.
- (26) Angermund, K.; Baumann, W.; Dinjus, E.; Fornika, R.; Görls, H.; Kessler, M.; Krüger, C.; Leitner, W.; Lutz, F. *Chem. Eur. J.* **1997**, *3*, 755.
- (27) Himeda, Y.; Onozawa-Komatsuzaki, N.; Sugihara, H.; Kasuga, K. *Organometallics* **2007**, *26*, 702.
- (28) Tanaka, R.; Yamashita, M.; Nozaki, K. *J. Am. Chem. Soc.* **2009**, *131*, 14168.
- (29) Tanaka, R.; Yamashita, M.; Chung, L. W.; Morokuma, K.; Nozaki, K. *Organometallics* **2011**, *30*, 6742.
- (30) Jessop, P. G.; Hsiao, Y.; Ikariya, T.; Noyori, R. *J. Am. Chem. Soc.* **1996**, *118*, 344.
- (31) Munshi, P.; Main, A. D.; Linehan, J. C.; Tai, C.-C.; Jessop, P. G. *J. Am. Chem. Soc.* **2002**, *124*, 7963.
- (32) Urakawa, A.; Jutz, F.; Laurenczy, G.; Baiker, A. *Chem. Eur. J.* **2007**, *13*, 3886.
- (33) Huff, C. A.; Sanford, M. S. *ACS Catal.* **2013**, *3*, 2412.
- (34) Gunanathan, C.; Milstein, D. *Acc. Chem. Res.* **2011**, *44*, 588.
- (35) Benito-Garagorri, D.; Kirchner, K. *Acc. Chem. Res.* **2008**, *41*, 201.
- (36) van der Vlugt, J. I.; Reek, J. N. H. *Angew. Chem. Int. Ed.* **2009**, *48*, 8832.
- (37) Friedrich, A.; Drees, M.; Käss, M.; Herdtweck, E.; Schneider, S. *Inorg. Chem.* **2010**, *49*, 5482.
- (38) Yang, X. *ACS Catal.* **2011**, *1*, 849.
- (39) Balaraman, E.; Gunanathan, C.; Zhang, J.; Shimon, L. J. W.; Milstein, D. *Nat. Chem.* **2011**, *3*, 609.
- (40) Zhang, J.; Leitus, G.; Ben-David, Y.; Milstein, D. *Angew. Chem. Int. Ed.* **2006**, *45*, 1113.
- (41) Huff, C. A.; Sanford, M. S. *J. Am. Chem. Soc.* **2011**, *133*, 18122.
- (42) Vogt, M.; Gargir, M.; Iron, M. A.; Diskin-Posner, Y.; Ben-David, Y.; Milstein, D. *Chem. Eur. J.* **2012**, *18*, 9194.
- (43) Huff, C. A.; Kampf, J. W.; Sanford, M. S. *Organometallics* **2012**, *31*, 4643.
- (44) Khaskin, E.; Iron, M. A.; Shimon, L. J. W.; Zhang, J.; Milstein, D. *J. Am. Chem. Soc.* **2010**, *132*, 8542.
- (45) Zhang, J.; Leitus, G.; Ben-David, Y.; Milstein, D. *J. Am. Chem. Soc.* **2005**, *127*, 10840.
- (46) Filonenko, G. A.; Conley, M. P.; Copéret, C.; Lutz, M.; Hensen, E. J. M.; Pidko, E. A. *ACS Catal.* **2013**, *3*, 2522.

- (47) Kubas Gregory, J. *Acc. Chem. Res.* **1988**, *21*, 120.
- (48) Kazansky, V. B.; Pidko, E. A. *Catal. Today* **2005**, *110*, 281.
- (49) Crabtree, R. H.; Lavin, M. *Chem. Commun.* **1985**, 1661.
- (50) Crabtree, R. H. *Acc. Chem. Res.* **1990**, *23*, 95.
- (51) Alcaraz, G.; Grellier, M.; Sabo-Etienne, S. *Acc. Chem. Res.* **2009**, *42*, 1640.
- (52) Baratta, W.; Ballico, M.; Del Zotto, A.; Herdtweck, E.; Magnolia, S.; Peloso, R.; Siega, K.; Toniutti, M.; Zangrando, E.; Rigo, P. *Organometallics* **2009**, *28*, 4421.
- (53) Bontemps, S.; Vendier, L.; Sabo-Etienne, S. *Angew. Chem. Int. Ed.* **2012**, *51*, 1671.
- (54) Gargir, M.; Ben-David, Y.; Leitius, G.; Diskin-Posner, Y.; Shimon, L. J. W.; Milstein, D. *Organometallics* **2012**, *31*, 6207.
- (55) Howe, G. W.; Bielecki, M.; Kluger, R. *J. Am. Chem. Soc.* **2012**, *134*, 20621.
- (56) Jazsar, R. F. R.; Bhatia, P. H.; Mahon, M. F.; Whittlesey, M. K. *Organometallics* **2003**, *22*, 670.
- (57) Ellul, C. E.; Saker, O.; Mahon, M. F.; Apperley, D. C.; Whittlesey, M. K. *Organometallics* **2007**, *27*, 100.
- (58) Allen, O. R.; Dalgarno, S. J.; Field, L. D.; Jensen, P.; Willis, A. C. *Organometallics* **2009**, *28*, 2385.
- (59) Gnanaprakasam, B.; Zhang, J.; Milstein, D. *Angew. Chem. Int. Ed.* **2010**, *49*, 1468.
- (60) Montag, M.; Zhang, J.; Milstein, D. *J. Am. Chem. Soc.* **2012**, *134*, 10325.
- (61) Duisenberg, A. *J. Appl. Cryst.* **1992**, *25*, 92.
- (62) Schreurs, A. M. M.; Xian, X.; Kroon-Batenburg, L. M. J. *J. Appl. Cryst.* **2010**, *43*, 70.
- (63) Beurskens, P. T.; Beurskens, G.; de Gelder, R.; Garcia-Granda, S.; Gould, R. O.; Smits, J. M. M. 2008 The DIRDIF2008 program system, Crystallography Laboratory, University of Nijmegen, The Netherlands.
- (64) Sheldrick, G. *Acta Cryst. A* **2008**, *64*, 112.
- (65) Spek, A. *Acta Cryst. D* **2009**, *65*, 148.
- (66) Burla, M. C.; Caliandro, R.; Camalli, M.; Carrozzini, B.; Cascarano, G. L.; Giacovazzo, C.; Mallamo, M.; Mazzzone, A.; Polidori, G.; Spagna, R. *J. Appl. Cryst.* **2012**, *45*, 357.
- (67) Adamo, C.; Barone, V. *J. Chem. Phys.* **1999**, *110*, 6158.
- (68) Zhao, Y.; Truhlar, D. G. *Acc. Chem. Res.* **2008**, *41*, 157.
- (69) Zhao, Y.; Truhlar, D. G. *J. Chem. Theory Comput.* **2009**, *5*, 324.
- (70) Valero, R.; Costa, R.; de P. R. Moreira, I.; Truhlar, D. G.; Illas, F. *J. Chem. Phys.* **2008**, *128*, 114003.
- (71) *Gaussian 09 Revision D.01*, Frisch, M. J.; Trucks, G. W.; Schlegel, H. B.; Scuseria, G. E.; Robb, M. A.; Cheeseman, J. R.; Scalmani, G.; Barone, V.; Mennucci, B.; Petersson, G. A.; Nakatsuji, H.; Caricato, M.; Li, X.; Hratchian, H. P.; Izmaylov, A. F.; Bloino, J.; Zheng, G.; Sonnenberg, J. L.; Hada, M.; Ehara, M.; Toyota, K.; Fukuda, R.; Hasegawa, J.; Ishida, M.; Nakajima, T.; Honda, Y.; Kitao, O.; Nakai, H.; Vreven, T.; Montgomery, J. A., Jr.; Peralta, J. E.; Ogliaro, F.; Bearpark, M.; Heyd, J. J.; Brothers, E.; Kudin, K. N.; Staroverov, V. N.; Kobayashi, R.; Normand, J.; Raghavachari, K.; Rendell, A.; Burant, J. C.; Iyengar, S. S.; Tomasi, J.; Cossi, M.; Rega, N.; Millam, N. J.; Klene, M.; Knox, J. E.; Cross, J. B.; Bakken, V.; Adamo, C.; Jaramillo, J.; Gomperts, R.; Stratmann, R. E.; Yazyev, O.; Austin, A. J.; Cammi, R.; Pomelli, C.; Ochterski, J. W.; Martin, R. L.; Morokuma, K.; Zakrzewski, V. G.; Voth, G. A.; Salvador, P.; Dannenberg, J. J.; Dapprich, S.; Daniels, A. D.; Farkas, Ö.; Foresman, J. B.; Ortiz, J. V.; Cioslowski, J.; Fox, D. J.; Gaussian, Inc.: Wallingford CT, 2009.
- (72) Andrae, D.; Häußermann, U.; Dolg, M.; Stoll, H.; Preuß, H. *Theoret. Chim. Acta* **1990**, *77*, 123.

Highly efficient reversible hydrogenation of CO₂ with Ru-PNP catalyst. Fine control on both sides of chemical equilibrium

- Ποεχαυυ!

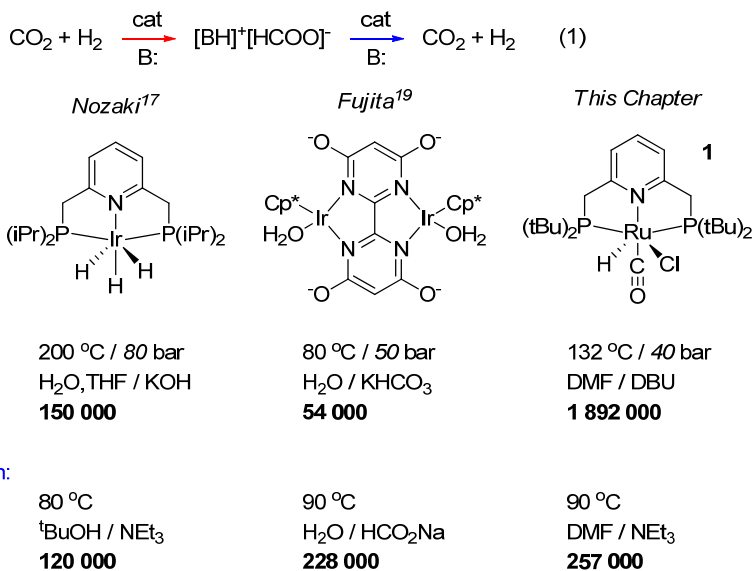
ABSTRACT: The use of hydrogen as a fuel requires both safe and robust technologies for its storage and transportation. Formic acid (FA) produced via the catalytic hydrogenation of CO₂ is recognized as a potential intermediate H₂ carrier. Herein, we present a development of a formate-based H₂ storage system employing an Ru-PNP pincer catalyst. The high stability of this system allows for cyclic operation with an exceptionally fast loading and liberation of H₂. Kinetic studies highlight the crucial role of the base promoter which defines the total H₂ capacity attainable via the hydrogenation of CO₂. The strength of the base is found to control the rate determining step (RDS) in FA dehydrogenation. Mechanistic analysis of CO₂ hydrogenation provided a similar RDS control opportunity for the hydrogenation reaction. It is demonstrated that the RDS of the hydrogenation pathway can be controlled by the partial pressure of H₂. The change in the reaction conditions suggested by the mechanistic analysis allowed a near 2.5-fold decrease in apparent activation energy.



This Chapter is published in: *ChemCatChem* **2014**, 6, 1526 and
Catal. Sci. Technol. **2014**, 4, 3474

3.1 Introduction

In Chapter 2 it was demonstrated that Ru-PNP catalyst **1** exhibits a high activity in hydrogenation of CO₂ to formates. These findings inspired us to continue a search for the application of this catalyst in the reversible storage of H₂ (equation (1), Scheme 3.1). Molecular hydrogen, being one of the most promising candidates for storage of renewable energy, suffers from low volumetric energy density in its gaseous form. Therefore, safe and economical storage and transportation techniques are required to make future hydrogen economy viable.¹⁻⁴ Among the many potential approaches,^{5,6} chemical binding of H₂ to produce liquid fuels is recognized as one of the promising solutions for the efficient and reversible H₂ storage.⁷ For example, formic acid (FA) generated via catalytic reduction of CO₂ is an attractive hydrogen carrier.⁸⁻¹² Its catalytic decomposition produces CO-free H₂ that can be directly used in fuel cell applications.¹³⁻¹⁵ If both reactions in Eq. 1 (Scheme 3.1) could be efficiently performed in a single vessel using the same catalyst, one would obtain a formate-based hydrogen battery as conceptually put forward by the group of Beller.¹⁶ Its practical implementation requires a step change in the catalytic activity of the reversible CO₂ hydrogenation.



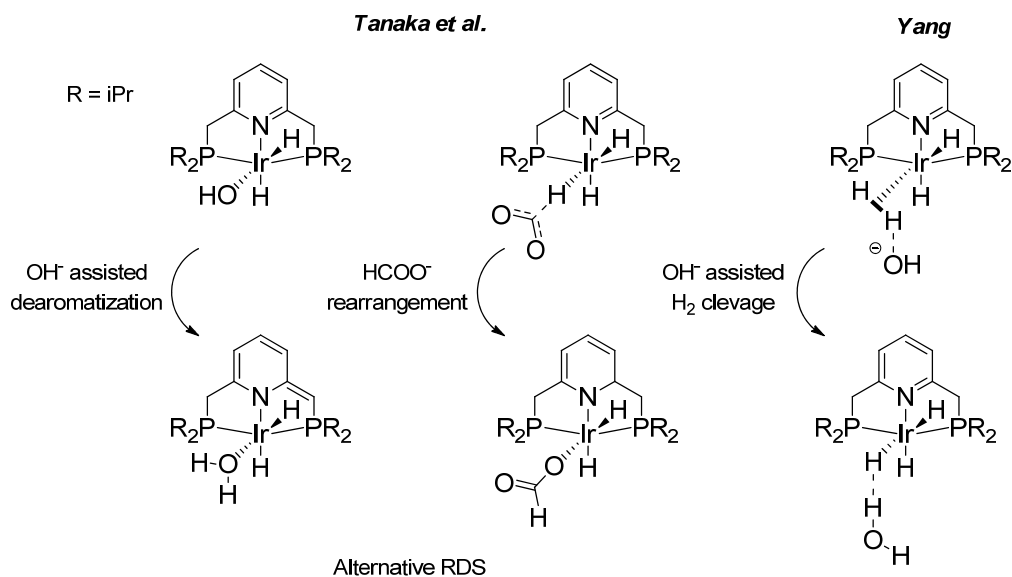
Scheme 3.1. State-of-the-art catalytic systems for reversible CO₂ hydrogenation.

So far, the best performance in reversible hydrogenation of CO₂ was achieved with homogeneous noble metal catalysts, namely iridium and ruthenium complexes. The record in CO₂ hydrogenation activity was set in 2009 by Nozaki and co-workers for an iridium pyridine-based PNP-pincer catalyst (Scheme 3.1). This catalyst allows reaching turnover frequencies (TOF) as high as 150 000 h⁻¹ at 200 °C and 50 bar.^{17,18} Fujita et al. introduced a pH-switchable Ir catalyst that attained very high rates in FA dehydrogenation (TOF = 228 000 h⁻¹ at 90 °C) and, at the same time, showed substantial activity in CO₂ hydrogenation (TOF = 53 800 h⁻¹ at 80 °C and 50 bar).¹⁹ Ruthenium catalysts are generally less active. The highest rate of CO₂ hydrogenation (TOF = 95 000 h⁻¹) reported to date for Ru-based systems was achieved using a ruthenium trimethylphosphine complex in combination with triethylamine (NEt₃) base promoter under supercritical conditions.²⁰ No reversibility was shown for this system. Beller et al. described a very stable homogeneous system consisting of RuH₂(dppm)₂ as catalyst and trialkylamine as base, and demonstrated its applicability in consecutive H₂ storage/release cycles with only minor loss of activity.¹⁶ Recently, non-noble metal homogeneous Fe and Co catalyst have also been shown to be active in FA dehydrogenation²¹ and CO₂ hydrogenation.²² However, these systems typically suffer from low performance or the necessity to use expensive chemicals as promoters. Moreover, expensive polydentate phosphine ligands used in these systems contribute greatly to the catalyst price. This in turn may annihilate the potential commercial benefits of such homogeneous catalysts despite being based on the earth-abundant metals.

In the previous chapter, it was shown that a lutidine-based Ru-PNP pincer catalyst **1**,²³ structurally related to the Nozaki's system, can hydrogenate CO₂ in THF with DBU (1,8-diazabicyclo[5.4.0]undec-7-ene) as a base promoter with a maximal rate of 22 000 h⁻¹.²⁴ A set of stable intermediate states of the catalyst was identified and their interconversion was analyzed. However, the performance of Ru-PNP in hydrogenation of CO₂ has not been yet optimized. To succeed in this undertaking a detailed mechanistic study is necessary. In particular, it is important to establish the role of different intermediates derived from Ru-PNP in the catalytic cycle of FA production. Finally the nature of the rate determining step and corresponding activation barrier is of crucial interest since they determine the intrinsic efficiency of the catalyst.

The hydrogenation of carbon dioxide to formates has been a subject of many experimental and theoretical studies, which mostly focused on homogeneous catalytic systems.²⁵⁻²⁹ Despite the apparent simplicity of the overall reaction, the mechanism of the catalytic hydrogenation of CO₂ to formates is still debated. One of the first examples of an

active catalyst for CO₂ hydrogenation under supercritical conditions, [Ru(H)₂(PMe₃)₃],²⁰ has been studied computationally by Sakaki and co-workers.^{30,31} The authors identified CO₂ insertion into the Ru-H bond as the rate determining step (RDS) under water free conditions, whilst the coordination of H₂ to Ru-formate species was shown to determine the reaction rate in the presence of water. An elegant investigation by Urakawa et al. revealed that CO₂ insertion is a facile process, whereas the H₂ insertion in the Ru-formate complex represents the rate determining step for [Ru(dmpe)₂H₂]-catalyzed CO₂ hydrogenation.³² These findings were used to rationalize the increased activity of most of the catalytic systems at elevated H₂ partial pressure, which represented a major inconsistency with the earlier proposal.



Scheme 3.2. Rate determining steps proposed by Tanaka et al.¹⁸ and Yang³⁶ for hydrogenation of CO₂ with Ir-PNP pincer

The mechanism of CO₂ hydrogenation by Nozaki's Ir-PNP catalyst¹⁷ has also been investigated computationally. The presence of a non-innocent PNP pincer ligand that can be directly involved in catalytic transformations³³⁻³⁵ increases the complexity of the mechanistic analysis. In the presence of a strong base, the PNP ligands can be deprotonated resulting in the formation of a basic cooperative site on the side-arm of the dearomatized PNP ligand that can participate in substrate activation.^{33,34} As a result, two alternative pathways were proposed for the hydrogenation of CO₂ with Ir-PNP,¹⁸ the first of which

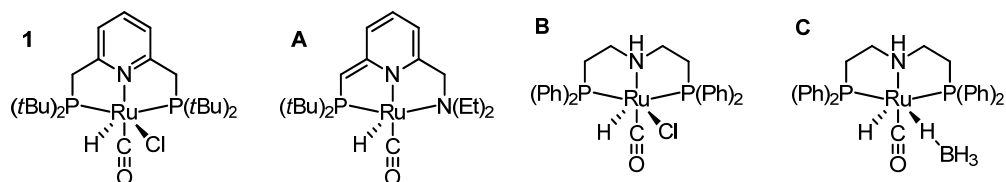
involves the deprotonative ligand dearomatization as the key reaction step. (Scheme 3.2) The alternative mechanism involves the OH⁻-assisted hydrogen cleavage in a σ -H₂ complex necessary for the catalyst regeneration as the RDS. The latter mechanism was supported by theoretical studies by Yang³⁶ and Ahlquist³⁷ who found that the direct base-assisted H₂ dissociation was more favorable than the ligand-assisted pathways. A similar conclusion was drawn for iron- and cobalt-based PNP catalysts.³⁶

The application of related ruthenium pincers in CO₂ hydrogenation has been described by our group and by the group of Sanford.^{24,38} In particular Huff and Sanford³⁸ reported that Ru-PNN pincer³⁹ catalyst can promote CO₂ hydrogenation with a turnover frequency of 2 200 h⁻¹ in the presence of carbonate bases. A mechanism involving the dearomatization of the PNN ligand at the final step of the reaction has been proposed. This proposal was confirmed in reactivity studies, employing KO^tBu to liberate HCOO⁻ at the end of the catalytic cycle. However, the possibility of ligand deprotonation with catalytically superior K₂CO₃ base has not been confirmed yet.

In this study we explored the potential of Ru-PNP catalyst in the reversible hydrogenation of CO₂ to formates. We demonstrate the high activity of Ru-PNP in dehydrogenation of FA and study the influence of the base promoter on the catalyst performance. Furthermore, we optimize the performance of Ru-PNP in hydrogenation of CO₂ using DFT calculations to analyze the reaction mechanism and kinetic experimentation to verify the theoretical predictions.

3.2 Catalytic dehydrogenation of formic acid

As a starting point of this study, we evaluated FA dehydrogenation activity of several Ru pincer catalysts known for their high activity in hydrogenation and dehydrogenation of polar substrates (Scheme 3.3).^{32,36} The catalytic experiments were carried out in a batch reactor under continuous addition of FA. In this way catalyst activity and stability could be investigated simultaneously. The dosage of the formic acid was performed simultaneously with evolved gas analysis. The rates of gas evolution rate and FA dosage can be directly used to estimate the rate of the catalytic reaction. Table 3.1 summarizes the results of the catalytic FA dehydrogenation tests using different Ru pincer catalysts (Scheme 3.3) under different reaction conditions.



Scheme 3.3. Pincer catalysts used in the initial FA dehydrogenation screening experiments

Table 3.1. Summary of dehydrogenation activity tests with Ru pincer catalysts.

Entry	Catalyst	Solvent	Base	T, °C	TOF, h ⁻¹	TON
1	1	THF	DBU	65	50 800	204 700
2	1	THF	NEt ₃	65	43 700	205 400
3	1	PC ^[a]	DBU	90	55 100	131 800
4	1	EtOH	DBU	65-90	Inactive	-
5	1	DMF	DBU	90	93 100	310 000
6	1	DMF	NEt ₃	65	46 495	n.d. ^[b]
7	1	DMF	NEt ₃	90	257 000	326 500
8	1	DMF	N(C ₆ H ₁₃) ₃	90	256 000	706 500
9	A	DMF	NEt ₃	65-90	Inactive	-
10	A	THF	DBU	65	Inactive	-
11	B	THF	DBU	65	Inactive	-
12	B	DMF	NEt ₃	65-90	39 600	105 900
13	C	DMF	NEt ₃	65-90	24 500	23 200

Conditions: 1.42 μmol catalyst, 30 mL solvent, base 33.5 mmol (nitrogen based); [a] propylene carbonate [b] not determined.

Surprisingly, the known pincer catalysts **A** - **C** widely used in hydrogen transfer reactions either did not provide any activity or rapidly deactivated in the course of the reaction. For example, Milstein's catalyst **A**, known to hydrogenate CO₂ to formates³⁸ did not show any activity in formate dehydrogenation. Ruthenium MACHO-type catalysts **B** and **C** showed good performance only when DMF solvent was used. However, their activity degraded overtime. Independent of the reaction medium, initial tests revealed a superior catalytic performance of **1** for FA dehydrogenation. The best performance in terms of catalyst stability and reaction rates was achieved when the reaction was performed using

DMF as a solvent. Unlike in other polar solvents (propylene carbonate, ethanol), no permanent catalyst deactivation was observed in this medium, even under highly acidic conditions. In all experiments, the evolved gas was an equimolar mixture of H₂ and CO₂ with no detectable traces of CO.

The combination of **1** with NEt₃ in DMF results in the exceptionally high rate of FA dehydrogenation of 257 000 h⁻¹ at 90 °C (Table 3.1). In a separate experiment with a low catalyst loading (0.356 μmol), a TON of 1 063 000 was reached within several hours (Figure 3.1) without any catalyst deactivation observed. The loss of triethylamine during operation at 90 °C represents a major drawback of this system. However, it can be remediated by using the less volatile N(C₆H₁₃)₃ base (entry 8, Table 3.1). To the best of our knowledge, these results represent the highest FA dehydrogenation activity reported so far.

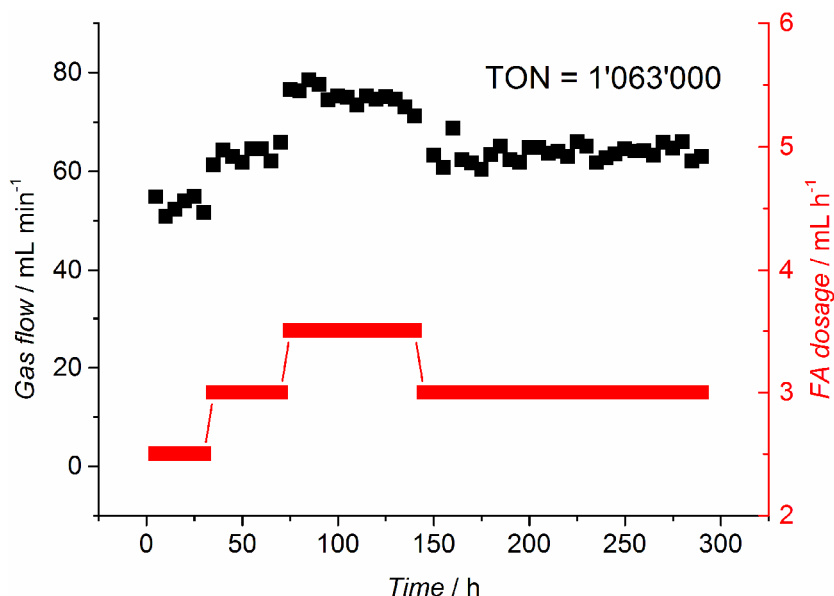


Figure 3.1. Continuous decomposition of FA with catalyst **1** and NEt₃ as a base in DMF (Conditions: 30 mL DMF, 9.43 mL NEt₃, 90 °C, 0.356 μmol **1**).

When the non-nucleophilic DBU base was used in continuous FA dehydrogenation, **1** showed a marginal activity in DMF at 65 °C. The increase of the reaction temperature to 90 °C allowed achieving a high rate of over 90 000 h⁻¹ and TON values of 310 000 (entry 5, Table 3.1). This behavior points to the possibility to control H₂ evolution by varying the reaction temperature in a relatively narrow range. Results of a variable temperature experiment confirm this hypothesis (Figure 3.2). Firstly, the reactor was charged with ca. 0.8 equivalents of FA per DBU. A very low activity (TOF < 6 000 h⁻¹) was observed at 65

°C. After a rapid increase of the reaction temperature to 90 °C, intense gas evolution started and the reaction proceeded steadily overtime until the FA dosage was stopped. The temperature was then lowered to 65 °C or 50 °C and the FA injection was repeated. Prior to the temperature increase the rate of FA decomposition was again marginal. Only after the temperature was increased to 90 °C high gas evolution rates were obtained. This cyclic procedure was repeated four times. In all cycles, a highly reproducible catalytic performance was achieved. These results suggest that this catalytic system offers a possibility to control the gas evolution rate in a narrow temperature interval and also shows high stability in a wide range of reaction conditions.

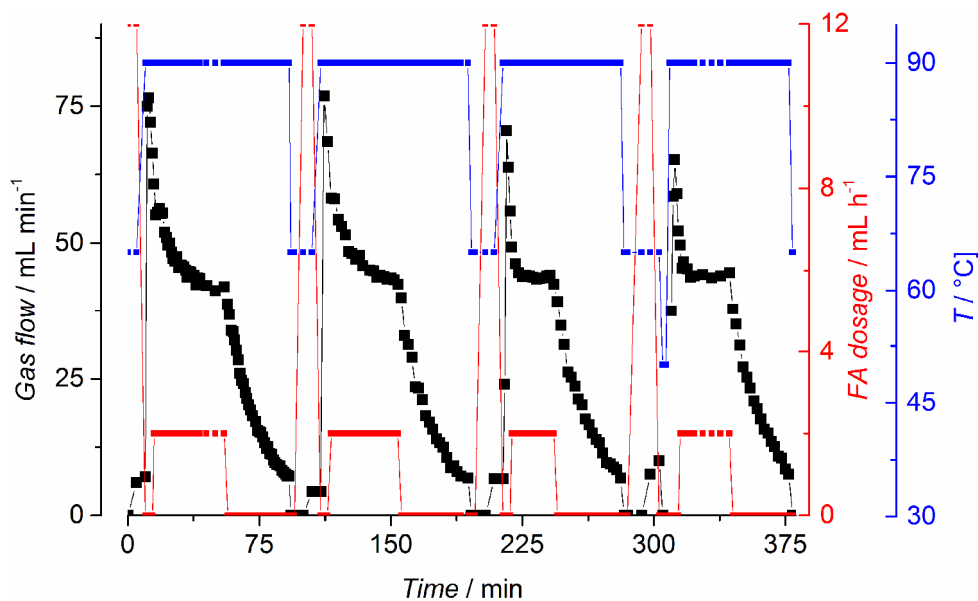


Figure 3.2. Temperature-switchable FA dehydrogenation with **1** in DMF/DBU (Conditions: DMF/DBU = 30/5 mL, 1.42 μ mol **1**).

The nature of the base promoters had a significant influence on the dehydrogenation activity of **1**. To understand their role in FA dehydrogenation we investigated the kinetics of this reaction in a batch mode. The temperature dependence of the gas evolution ($H_2 / CO_2 = 1 / 1$) as a function of substrate concentration (expressed for convenience as the acid-to-amine ratio, AAR) is displayed on Figure 3.3a. In the presence of NEt_3 , the reaction rate increased with the consumption of the substrate (towards lower AAR), evidencing effective inhibition of the catalytic reaction by the substrate. Apparent reaction order in substrate was determined to be approximately -0.4 . The activation energy for FA decomposition in the presence of NEt_3 was 74 kJ mol^{-1} . A strikingly different behavior was

observed in the presence of the DBU base promoter. The reaction followed first order behavior with respect to formate concentration and showed an apparent activation barrier of 108 kJ mol^{-1} .

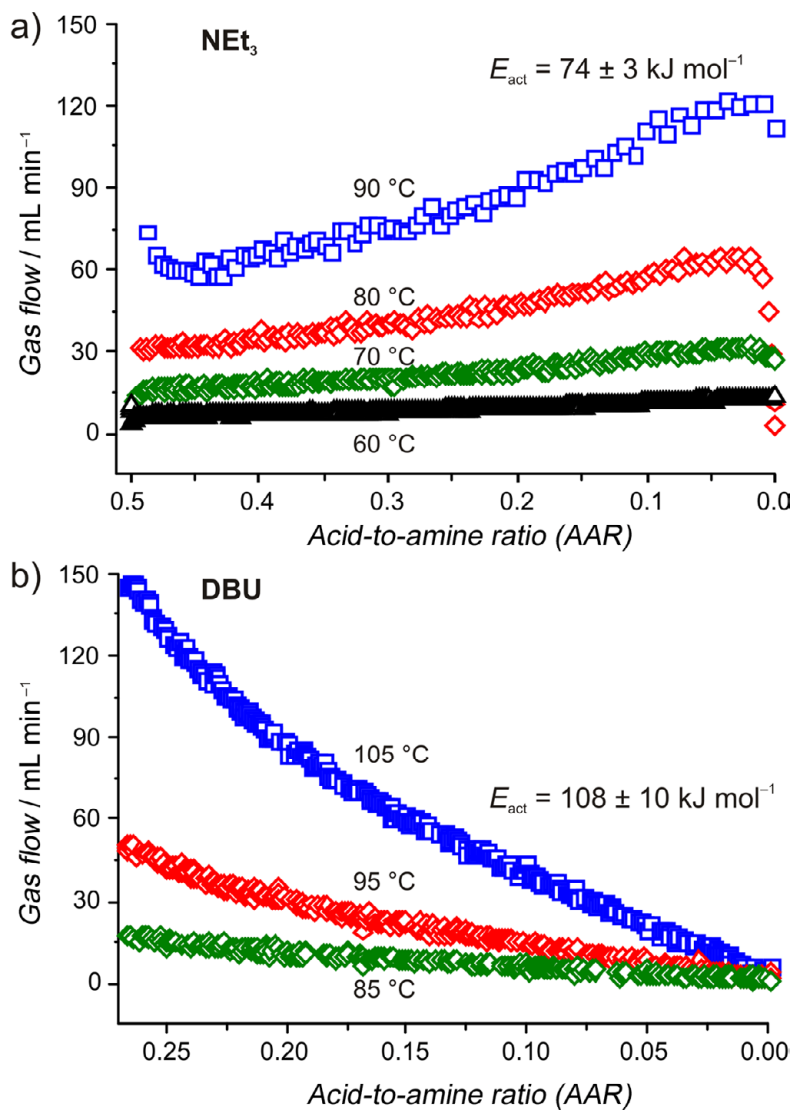


Figure 3.3. Kinetic traces for FA dehydrogenation with **I** in DMF at different temperatures in the presence of (a) NEt₃ and (b) DBU. Conditions: 30 mL DMF, 9.43 mL NEt₃ and 0.356 μmol **I** (a) or 5 mL DBU and 4.63 μmol **I** (b)

The pronounced difference in the kinetics of FA dehydrogenation for DBU and NEt_3 suggests that the base is directly involved in the elementary steps of the catalytic reaction. We propose that the rate determining step (RDS) is different for the NEt_3 and DBU cases. We performed the dehydrogenation reaction using a deuterium labeled substrate to get a further insight. A significant kinetic isotope effect (KIE) of 3.47 was observed with DCOOD when dehydrogenation was performed in the presence of NEt_3 . On the other hand, the KIE observed for dehydrogenation of HCOOD was negligible (KIE = 1.04). That indicates that in the case of a rather weak triethylamine base, the C-H cleavage step (hydride abstraction from HCOO^- anion) is in fact rate limiting. Similar observations have previously been reported by Oldenhof et al for a base-free Ir-catalyzed dehydrogenation of FA.⁴⁰ When the stronger DBU base is employed, the C-H bond cleavage step has only a small, if any, influence on the overall kinetics. This proposal is supported by small kinetic isotope effects for the dehydrogenation of both DCOOD (1.48) and HCOOD (1.42). Consequently, the reaction rate is controlled by the rate of the H_2 formation by recombination of the protonated DBU and Ru-bound hydride species.

Figure 3.4 shows proposed catalytic cycles for the dehydrogenation of FA and hydrogenation of CO_2 . For both reactions the key role of the dihydrido complexes similar to **4** has been postulated earlier.^{32,36} The first step of the dehydrogenation reaction (blue arrows in Figure 3.4) is the base-promoted H_2 formation via the recombination of the hydride ligand and a proton from BH^+ (where B is a base). This step determines the rate of the dehydrogenation reaction in the presence of DBU. H_2 release from the $\mathbf{4}^+-\text{H}_2$ σ -complex yields a cationic complex $\mathbf{4}^+$, which is converted to **5** via coordination of the formate anion. The catalytic cycle is closed via the rearrangement of **5** into a transient species $\mathbf{5}^*$, from which CO_2 evolves resulting in the initial complex **4**. A similar mechanism has been proposed earlier for an iron-based pincer catalyst for FA dehydrogenation developed by Milstein and co-workers.²¹ The low basicity of triethylamine facilitates H_2 recombination making the CO_2 release step rate determining. The reaction rate is controlled in this case by the C-H cleavage step ($\mathbf{5} \rightarrow \mathbf{4}$) that does not directly involve NEt_3 .⁴⁰ The ΔE value for the transformation $\mathbf{5} \rightarrow \mathbf{4}$ reported in the previous chapter (75 kJ mol^{-1}) coheres perfectly with the apparent activation energy of 74 kJ mol^{-1} measured for the FA dehydrogenation in the presence of NEt_3 . In a perfect agreement with the suggested mechanism, NEt_3 -mediated dehydrogenation shows only a low sensitivity to FA concentration, while in the presence of DBU the dehydrogenation reaction shows near first order in formate concentration.

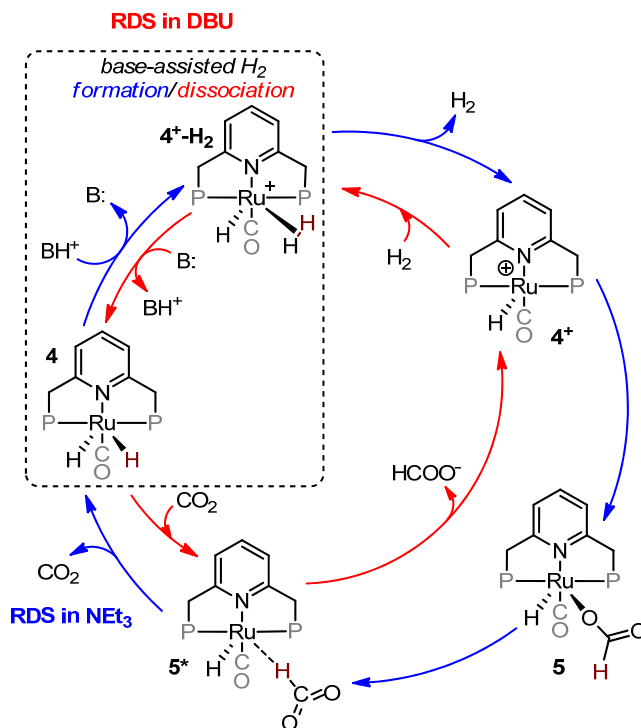


Figure 3.4. Proposed catalytic cycles for hydrogenation of CO₂ (red) and FA dehydrogenation (blue) with Ru PNP catalyst.

3.3 Catalytic hydrogenation of CO₂ – highly active and reversible

Previously, CO₂ insertion (step. 4 → 5*, red arrows, Figure 3.4.) was postulated to be the rate determining step in the conversion of CO₂ to formates.^{30,41} This implies that the base primarily influences the reaction thermodynamics but not the kinetics. In this way, the base determines the product yield and thus the H₂ storage capacity rather than the reaction rate. The latter proposal is in agreement with the results of CO₂ hydrogenation experiments with **1** in DMF (entries 2 and 3, Table 3.2). Having a substantial effect on the final acid-amine ratio (AAR), the strength of the base promoter does not influence the reaction rate (entries 2 and 3, Table 3.2). In the presence of NEt₃, CO₂ hydrogenation at 65 °C yields a relatively low AAR of 0.26. This implies that more than 70 % of the base is not used for the H₂ storage. Consistent with findings of Beller and co-workers,¹⁶ a decrease in the reaction temperature increases AAR up to 1 at room temperature (Figure 3.5a). Despite substantial reactivity in the H₂ evolution reaction of the DMF/NEt₃ combination, the low H₂ capacity

of the amine-based system at the catalytically relevant temperatures represents its major drawback.

Table 3.2. Summary of hydrogenation activity tests using catalyst I.

Entry	Solvent	Base	Catalyst (μmol)	T, $^{\circ}\text{C}$	P H_2/CO_2 (bar/bar)	TOF, h^{-1}
1	THF	DBU	1.42	65	20/20	25 500
2	DMF	NEt_3	1.42	65	20/20	34 000
3	DMF	DBU	1.42	65	20/20	36 000
4	DMF	DBU	0.356	65	30/10	65 000
5	DMF	DBU	1.42	90	30/10	266 000
6	DMF	DBU	0.178	110	30/10	737 000
7	DMF	DBU	0.178	120	30/10	1 100 000
8	DMF	DBU	0.178	132	30/10	1 892 000
9	DMF	DBU	0.178	90	2.5/2.5	60 000
10	DMF	DBU	0.178	65	2.5/2.5	7 900

Conditions: 30 mL solvent, 33.5 mmol (nitrogen based) base, temperatures and pressures are given in Table. For details refer to Experimental section.

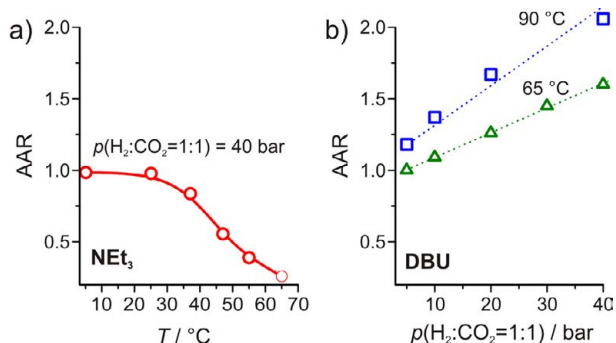


Figure 3.5. Pressure and temperature dependence of AAR for (a) NEt_3 and (b) DBU bases.

The use of a stronger DBU base allows obtaining much higher FA yields compared to a weaker NEt_3 base. Reaction at 65 $^{\circ}\text{C}$ leads to an AAR of 1.6 and the initial TOF of 36 000 h^{-1} similar to one obtained with triethylamine. In agreement with previous reports,^{32,38,42} the activity can further be enhanced by carrying out the reaction at a higher H_2 partial pressure (Table 3.2). At a H_2/CO_2 molar ratio of 3/1 ($P_{\text{total}} = 40$ bar), a TOF of

65 000 h⁻¹ was obtained at 65 °C, which increases to the value of 1 892 000 h⁻¹ when the reaction is carried out at 132 °C. This rate is more than one order of magnitude higher than the current record value reported for Nozaki's Ir-PNP pincer catalyst, which operates at a higher temperature and pressure.¹⁷ In a high-temperature experiment (entries 7 and 8, Table 3.2) the kinetic trace followed the first-order behavior with respect to the product formation.

With the exceptional performance of **1** in DMF/DBU we were able to hydrogenate CO₂ at a low pressure (entries 9 and 10, Table 3.2 and Figure 3.6). A high reaction rate of 60 000 h⁻¹ was obtained at a total pressure of only 5 bar of an equimolar H₂/CO₂ mixture at 90 °C. For comparison, this is superior to the TOF developed by the Fujita's Ir catalyst¹⁹ (Scheme 3.1) at a comparable temperature of 80 °C and a 10-fold higher pressure, indicating thus higher intrinsic reactivity of the Ru-PNP catalyst. The possibility to efficiently carry out the reaction at such a low pressure can be viewed as yet another advantage of the current catalytic system. Indeed, a pressure of 5 bar can be tolerated by a vast majority of common reaction vessels. This expands greatly the applicability of Ru-PNP catalyst for hydrogen storage.

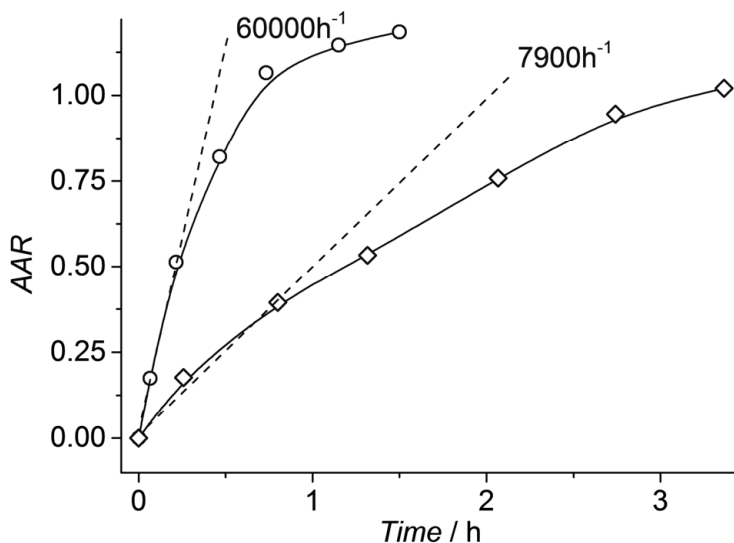


Figure 3.6. Low-pressure hydrogenation of CO₂ with **1** (1.42 μmol). 30 mL DMF, 33.5 mmol DBU, H₂/CO₂ = 2.5/2.5 (bar), circles - 90°C, diamonds - 65°C

Unlike for the DMF/NEt₃ system, the increase of the reaction temperature in the case of DMF/DBU leads to the stabilization of a higher AAR, in other words, to a higher formate yield (Figure 3.5). The H₂ capacity of DMF/DBU system also strongly depends on

the total pressure. Stepwise increase of the pressure from 5 to 40 bar led to higher formate concentrations. A maximum AAR of 2.1 was obtained by carrying out CO₂ hydrogenation at 90 °C and 40 bar. These data exemplify the crucial difference between DBU and NR₃-based systems. The high capacity of the latter can only be achieved at low temperatures at the expense of the reaction rate. Having a molar volume similar to NEt₃, DBU offers a nearly six-fold higher FA loading capacity at 65 °C.

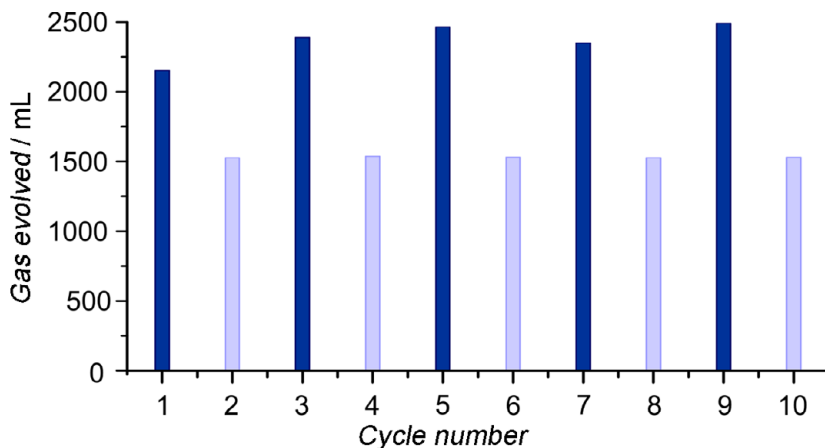
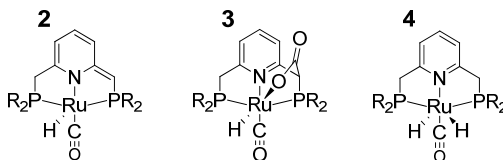


Figure 3.7. Gas evolution in the H₂ storage/release cycles with **1** in DMF/DBU. Storage: 65°C under 40 bar (dark bars) and 5 bar (light bars) H₂/CO₂ = 1/1. Release was performed after decompression of the system at 65°C followed by heating to 90°C (Conditions: DMF/DBU = 30/5 mL, 1.42 μmol **1**).

To further investigate the possibility of cyclic operation with **1** in DMF/DBU, we performed a series of hydrogen storage/release cycles over a time span of a week. Alternating high and low-pressure loading procedures were employed to evaluate the sensitivity of the system to the variation of the operation conditions. The results of these measurements are summarized in Figure 3.7. In all cycles the evolved H₂/CO₂ gas volumes were consistent with AARs measured by the direct sampling of the reaction mixture. Final AAR values of 1.6 and 1.1 were observed for high pressure (40 bar) and low pressure (5 bar) loading procedures, respectively. The complete H₂ liberation time did not exceed 1 h, upon which gas evolution peaked at over 160 mL min⁻¹ corresponding to TOF values higher than 150 000 h⁻¹. H₂/CO₂ charging times were less than 3 h depending on the temperature program. The cyclic operation was carried out without the addition of extra-base between the cycles that was necessary for the stable performance of the previously reported amine-based system.¹⁶ No catalyst deactivation was observed in the course of these experiments.

3.4 The mechanistic analysis of CO₂ hydrogenation: involvement of metal-ligand cooperation and control over rate determining steps

The rate determining step in formic acid dehydrogenation with Ru-PNP can be controlled by the base promoter. However such a possibility is not known for the CO₂ hydrogenation reaction. If existed, it could provide a tool for controlling the catalytic efficiency. However, without an established CO₂ hydrogenation mechanism the search for such a tool is nothing but hopeless. We previously described a set of stable complexes **2** - **4** that can potentially be encountered in the hydrogenation reaction with **1** (Scheme 3.4). Our results suggested an inhibiting effect of metal-ligand cooperation in complex **3** on catalysis. However, previous studies on related catalytic systems outline the possible beneficial role of ligand participation in CO₂ hydrogenation by Ir-PNP^{18,36,37} or Ru-PNN³⁸ pincer catalysts. Therefore, to support our findings we analyzed CO₂ hydrogenation activity of complexes **2** - **4** and the associated reaction mechanisms using DFT calculations.



Scheme 3.4. A set of starting complexes, subjected to mechanistic analysis.

Catalysis with 4: The dihydrido complex **4**, described as the most active catalyst in the previous Chapter, provides the most favorable hydrogenation pathway (Figure 3.8). The starting point of the reaction is an energy-neutral binding of CO₂ to **4** resulting in **4-CO₂**. Weak intermolecular contacts between the O atoms of CO₂ and acidic CH₂ protons of the PNP pincer arms in **4-CO₂** ($r(\text{O}\cdots\text{H}) = 2.584 \text{ \AA}$) direct the CO₂ coordination towards the Ru-H moiety. This allows a facile attack of CO₂ by Ru-bound hydride resulting in a formate anion (**4-CO₂** → **TS_{4,5}** → **5***). The reaction is exothermic by -13 kJ mol^{-1} and shows a very low activation barrier of 23 kJ mol^{-1} . The reaction can further follow two directions denoted as Cycle I and I[†]. Further transformations of **5*** determine the preference for either of the Cycles. In Cycle I, the Ru \cdots H-coordinated formate anion in **5*** is replaced by H₂ yielding a cationic $\sigma\text{-H}_2$ Ru-PNP complex charge-compensated by an HCOO⁻ anion hydrogen bonded with the CH₂ moieties of the ligand (**5*** + H₂ → **5-H₂**). Subsequent heterolytic dissociation of H₂ over an acid-base pair comprised of the Ru center and the adjacent formate anion results in a molecular complex of **4** with formic acid (**4-FA**). The direct availability of a proton-accepting species (formate anion) close to the dissociating H₂

molecule leads to a less strained $\text{TS}_{5,4}$ structure and, accordingly, to an extremely low activation barrier for the dissociation reaction. Reaction of **4-FA** with the DBU base at the next step releases DBU-FA product and regenerates the initial complex **4**. This reaction completes the Cycle I. Alternatively, competing Cycle I^a proceeds via the rearrangement of $\mathbf{5}^*$ to a stable formate complex **5** ($\mathbf{5}^* \rightarrow \mathbf{5}$, $\Delta E = -39 \text{ kJ mol}^{-1}$, Figure 3.7) featuring a direct Ru-O coordination ($r(\text{Ru-O}) = 2.261 \text{ \AA}$). To proceed further along the catalytic Cycle I^a, the ionization of **5** (i.e. the formation of an ion pair $\mathbf{5}^*$) and the replacement of HCOO^- ligand with H_2 has to take place. This reaction also yields $\mathbf{5-H}_2$ but shows a higher activation barrier of 65 kJ mol^{-1} .

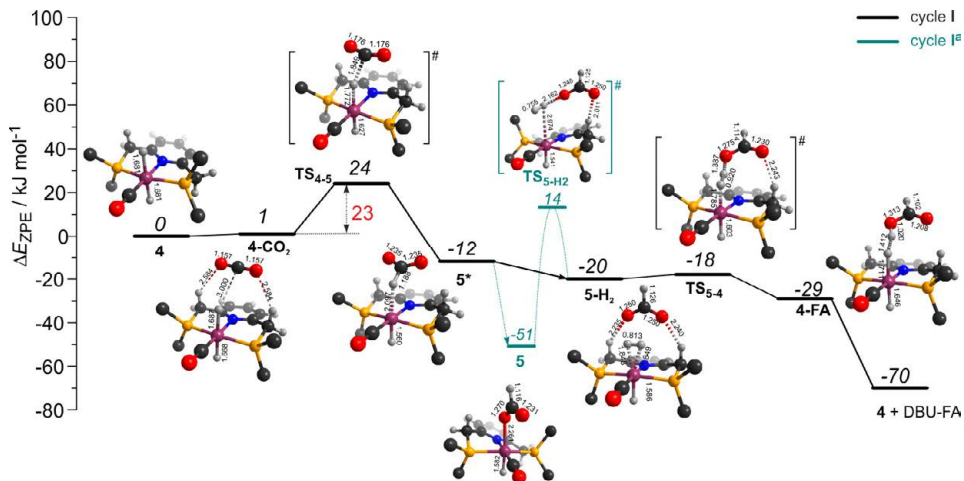


Figure 3.8. DFT computed reaction energy diagram and optimized structures of the intermediate and transition states (CH_3 groups at the ^tBu substituents of the PNP ligand and solvent molecules are omitted for clarity) for the hydrogenation of CO_2 with **4**.

Hydrogenation with **2 – the metal-ligand cooperative path:** The dearomatized pyridine-based Ru pincer complexes have been suggested to play a key role in catalytic CO_2 hydrogenation.³⁸ The catalytic cycle II over **2** largely overlaps with cycle I discussed above. The two cycles differ in the mechanism of the product formation via the transformations of the formate complex $\mathbf{5}^*$, which in cycle II involves a direct deprotonation of the PNP ligand resulting in a one-step FA formation. The DFT computed reaction energy diagram for CO_2 hydrogenation with **2** is shown in Figure 3.9. Heterolytic dissociation of H_2 over **2** yielding **4** is the first and the most energy demanding step of the cycle ($E^\ddagger = 76 \text{ kJ mol}^{-1}$). It is followed by a facile CO_2 activation by the dihydrido species **4** resulting in $\mathbf{5}^*$. The weakly bound HCOO^- in $\mathbf{5}^*$ plays then a role of a base that attacks the acidic CH_2 moiety at the PNP pincer arm resulting in its deprotonation and the formation of FA hydrogen-bonded

with a basic C1 site at Ru-PNP* (**2-FA**). The reaction and activation energies are very similar for this step ($\Delta E = 46 \text{ kJ mol}^{-1}$ and $E^\ddagger = 47 \text{ kJ mol}^{-1}$). Due to the high basicity of the deprotonated pincer arm in **2**, the reverse FA dissociation reaction is effectively barrierless. Therefore, to promote the catalytic cycle FA has to be eliminated from the complex by a strongly exothermic ($\Delta E = -51 \text{ kJ mol}^{-1}$) reaction with DBU. The DBU-FA product is formed at this step and the starting complex **2** is regenerated.

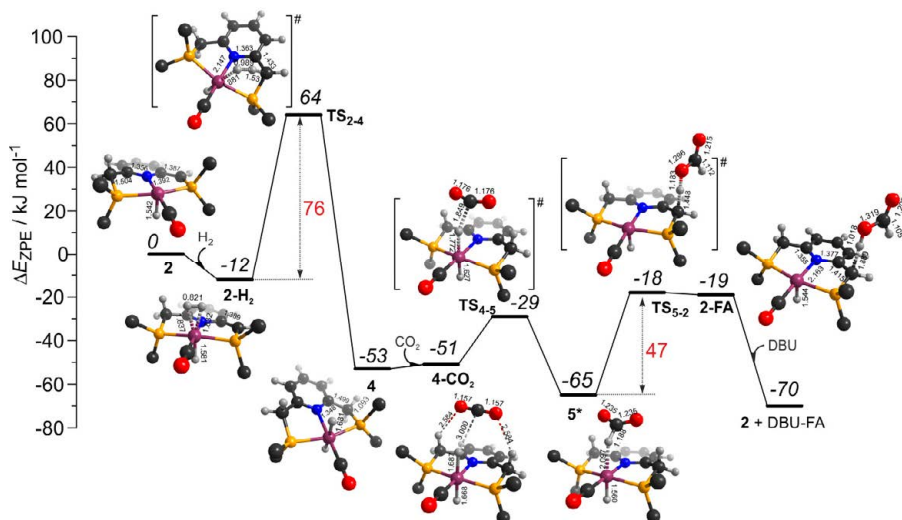


Figure 3.9. DFT computed reaction energy diagram and optimized structures of the intermediate and transition states (CH_3 groups at the ^tBu substituents of the PNP ligand and solvent molecules are omitted for clarity) for the hydrogenation of CO_2 with **2** (Cycle II).

Catalysis with CO_2 adduct **3:** Potentially, the CO_2 adduct **3** can also act as catalytic species for CO_2 hydrogenation. In a recent study by Huff and Sanford on the mechanism of CO_2 hydrogenation using related Ru-PNN catalyst, the role of the CO_2 adduct analogous to **3** has been discussed.³⁸ Although the mechanism for the catalytic reaction involving such species was proposed, the authors concluded that it most likely represents a minor pathway in the overall catalytic process. The DFT-computed reaction energy diagram for the **3**-catalyzed hydrogenation of CO_2 is shown in Figure 3.10. To initiate Cycle III, complex **3** undergoes a rather unfavorable reaction ($\Delta E = 33 \text{ kJ mol}^{-1}$, $E^\ddagger = 69 \text{ kJ mol}^{-1}$) with H_2 that results in the opening of the Ru-O coordination and the formation of **3 $^\circ$ -H $_2$** . The coordinated dihydrogen molecule undergoes then a heterolytic dissociation over a cationic Ru center and the basic carboxylate moiety on the pincer arm in **3 $^\circ$** . The reaction in this

case is less energetically favorable and proceeds with a higher barrier ($3^\circ\text{-H}_2 \rightarrow \text{TS}_{3-7} \rightarrow 7$, $\Delta E = 9 \text{ kJ mol}^{-1}$, $E^\ddagger = 15 \text{ kJ mol}^{-1}$) than the respective step in cycle I ($5\text{-H}_2 \rightarrow \text{TS}_{5-4} \rightarrow 4\text{-FA}$, $\Delta E = -9 \text{ kJ mol}^{-1}$, $E^\ddagger = 2 \text{ kJ mol}^{-1}$). Reaction of **7** with CO_2 yields a formate complex **8** that is similar to **5*** in Cycle I. This step is slightly endothermic ($\Delta E = 4 \text{ kJ mol}^{-1}$) and shows an activation barrier of 45 kJ mol^{-1} . Subsequent barrierless proton transfer from the ligand-bound COOH moiety to the HCOO^- anion in **8** results in formic acid hydrogen-bonded to the activated complex 3° (3°-FA). The removal of FA by the reaction with DBU regenerates the initial CO_2 -adduct **3**.

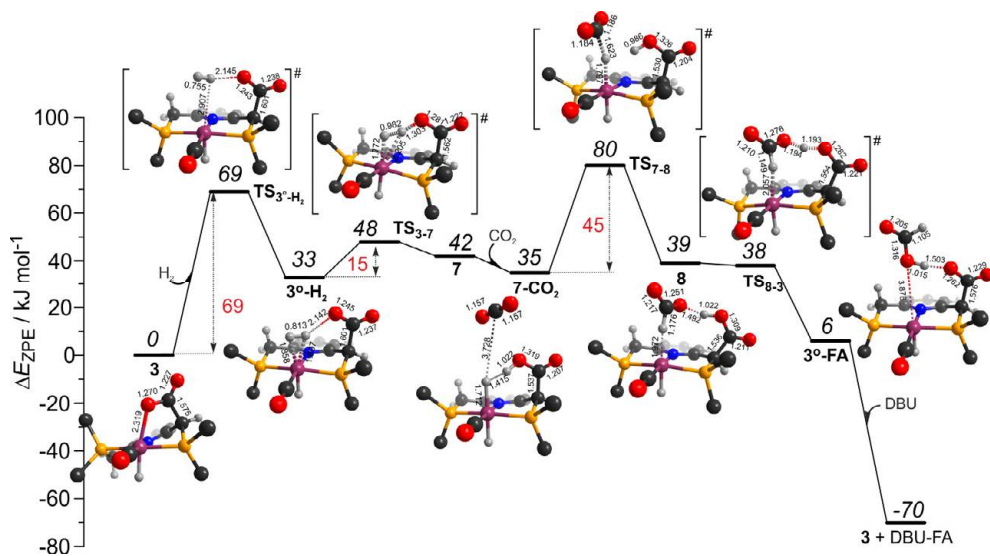


Figure 3.10. DFT computed reaction energy diagram and optimized structures of the intermediate and transition states (CH_3 groups at the ^tBu substituents of the PNP ligand and solvent molecules are omitted for clarity) for the hydrogenation of CO_2 with **3** (Cycle III)

The impact on catalysis: The computational results presented above suggest that all candidate Ru-PNP complexes **2-4** can potentially contribute to the overall catalytic reaction. To directly compare the above three alternative mechanisms for CO_2 hydrogenation by Ru-PNP, we further analyzed reaction Gibbs free energy diagrams for the respective three catalytic cycles (Figure 3.11).

The dihydrido complex **4** provides the lowest free energy reaction path for the conversion of CO_2 to FA-DBU along the Cycle I. The reaction in this case does not involve the metal-ligand cooperation in Ru-PNP and proceeds via the direct hydrogenolysis of transient species **5*** containing a non-coordinated formate anion ($5^* + \text{H}_2 \rightarrow 5\text{-H}_2 \rightarrow 4\text{-FA}$).

FA). DFT calculations predict a very low apparent activation energy of only 24 kJ mol⁻¹ for Cycle I associated with the initial CO₂ activation step (**4** + CO₂ → **5***, Figure 3.8). The free energy barrier ΔG^\ddagger for this transformation is 67 kJ mol⁻¹ (Figure 3.11). The subsequent facile hydrogenolysis of **5*** is competing with its rearrangement to a formate complex **5**, that is the most thermodynamically stable complex among the structures considered here. This finding is in line with the results of reactivity studies evidencing the exclusive formation of **5** under near-catalytic conditions described in the previous chapter.²⁴ When **5** is formed, the reaction follows the Cycle I^a. Here the polarization of **5** followed by H₂ insertion (**5** + H₂ → **5-H₂**, Figure 3.8) determines the overall rate of the catalytic reaction. This route is characterized by $E_{app}^{\ddagger, DFT}$ of 65 kJ mol⁻¹.

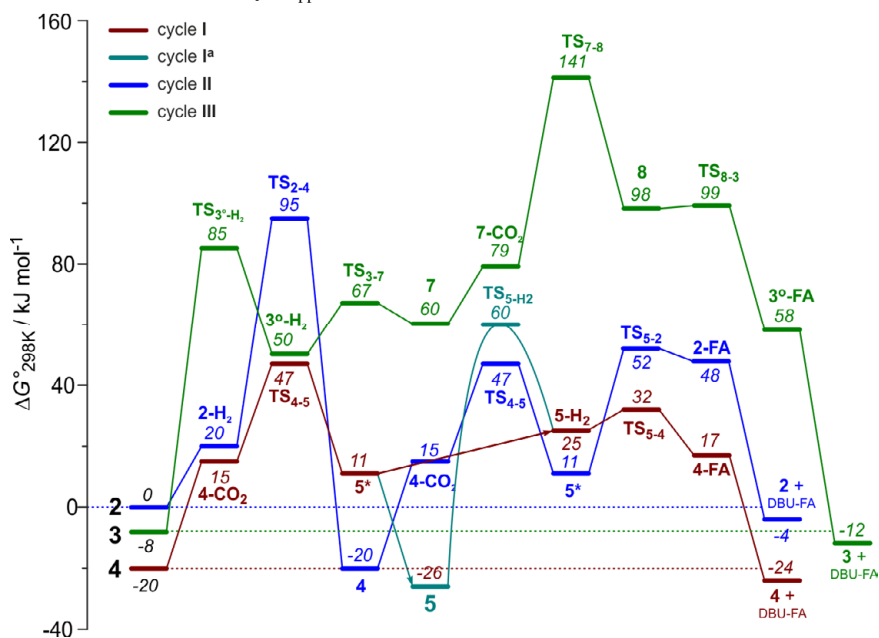


Figure 3.11. A comparison of Gibbs free energy diagrams for catalytic cycles I, II and III plotted relative to the dearomatized Ru-PNP species **2**.

For catalytic reaction involving ligand dearomatization (Cycle II, Figures 3.9 and 3.11) the cooperative H₂ activation by **2** represents the RDS. Because the formation of a **2-H₂** σ -complex is thermodynamically unfavorable, this route proceeds with a moderate $E_{app}^{\ddagger, DFT}$ of 64 kJ mol⁻¹ (**2** + H₂ → **4**, Figure 3.9), that in free energy terms provides a high barrier of 95 kJ mol⁻¹ (**2** + H₂ → **4**, Figure 3.11). Therefore, we expect the catalytic activity of **2** to be significantly lower than that of **4** (i.e. Cycle I/I^a). To validate this proposal we performed a catalytic CO₂ hydrogenation experiments with Ru-PNP catalyst precursor **1** using a strong

KO^tBu base that ensures a high concentration of **2** in solution during catalysis. In agreement with DFT predictions a very low activity was observed in this case. Turnover numbers after 2 hour reaction time were only 728 and 649 in THF and DMF solvents, respectively. On the contrary, when a non-nucleophilic DBU base, which cannot promote the ligand dearomatization,²⁴ was used as a promoter, much higher TON_{2h} values of 12 829 and 38 642 were obtained respectively in THF and DMF.

The catalytic path with **3** (Cycle III) shows a prohibitively high activation free energy barrier (Figure 3.11). Although the initial coordination of H₂ (**3** + H₂ → **3^o-H₂**, Figure 3.10) shows activation energy (E^\ddagger) of only 69 kJ mol⁻¹, the overall barrier in this case is represented by the energy difference between the initial state **3** and the high energy **TS₇₋₈** for the CO₂ activation. ($E_{\text{app}}^{\ddagger,\text{DFT}} = 80$ kJ mol⁻¹ Figure 3.10). In free energy terms this reaction is even more unfavorable ($\Delta G_{\text{app}}^{\ddagger,\text{DFT}} = 149$ kJ mol⁻¹ Figure 3.11). In line with the experimental findings²⁴ discussed in Chapter 1, this points to a lower intrinsic catalytic activity of **3** compared to that of **2** and **4**.

Thus, DFT calculations point to competing Cycles I and I^a as the most favorable catalytic pathway for CO₂ hydrogenation by Ru-PNP. We assume that the relative contribution of I and I^a would be defined by the composition of the reaction media. The reaction through Cycle I can be promoted in the presence of excess H₂ that would ensure the rapid substitution of the non-coordinated HCOO⁻ in **5*** with H₂ towards **5-H₂**. On the other hand, Cycle I^a will be preferred under CO₂-rich atmosphere. Since hydrogenation via Cycles I and I^a should proceed with different apparent activation barriers, corresponding to different rate-determining steps, the experimental validation of our proposal is possible through the kinetic measurements at varying H₂ partial pressures.

To verify theoretical predictions, we investigated the kinetics of CO₂ hydrogenation by complex **1** (Figure 3.12) with H₂/CO₂ molar ratio ($p_{\text{total}} = 40$ bar) fixed at 30/10 and 37/3, that would ensure the preference for either of the Cycles I^a or I. At a H₂/CO₂ ratio of 30/10 (*bar/bar*), the reaction showed apparent activation energy ($E_{\text{app}}^{\ddagger}$) of 57 kJ mol⁻¹ that is in very good agreement with the computed value ($E_{\text{app}}^{\ddagger,\text{DFT}}$) of 65 kJ mol⁻¹ for Cycle I^a. The rate enhancement previously observed upon a slight increase of the partial pressure of H₂⁴³ is in line with the proposition on the rate-determining nature of the **5** + H₂ → **5-H₂** step in this case. As a result of the high activation energy, a strong temperature dependency of the reaction rate is observed. Whereas the initial TOF is only 266 000 h⁻¹ at 90 °C the reaction at 132 °C shows initial turnover frequency (TOF) of 1 892 000 h⁻¹.

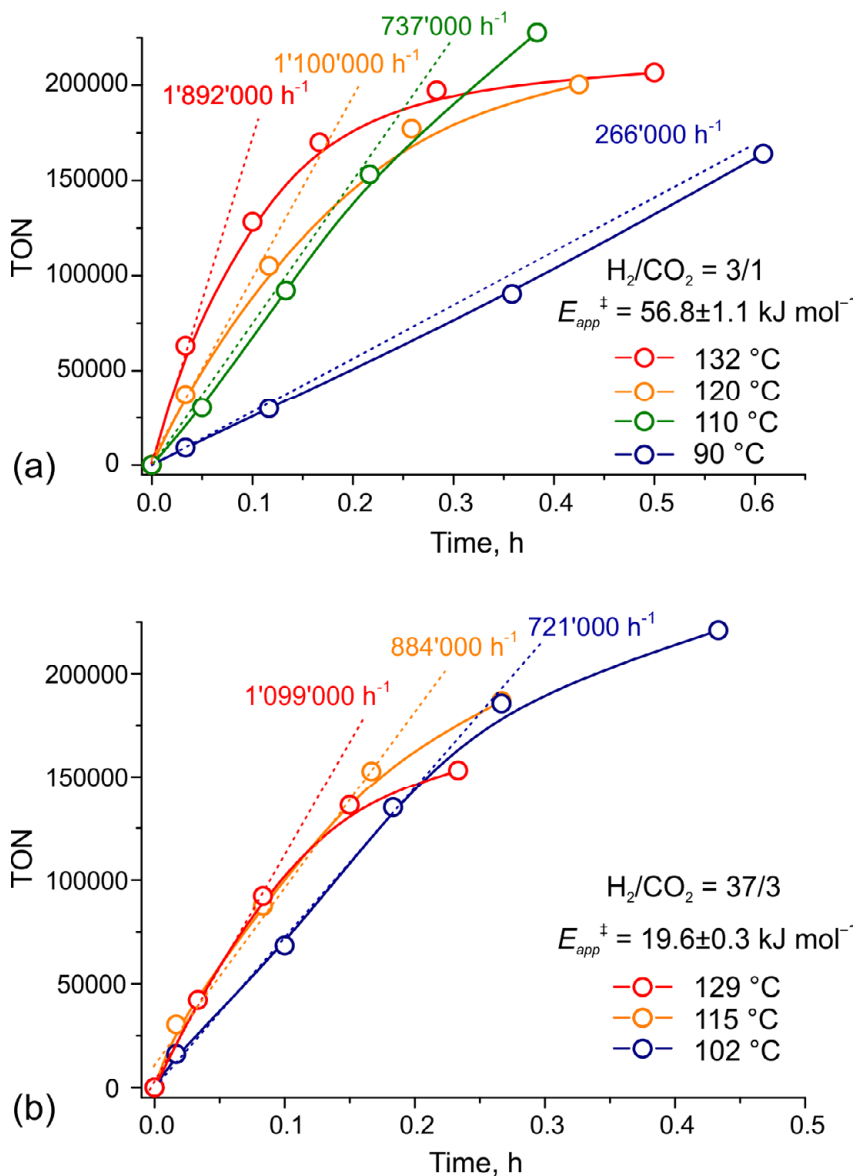


Figure 3.12. Kinetic traces for CO₂ hydrogenation by **1** at different temperatures and H₂/CO₂ ratio of (a) 3/1 and (b) 37/3 ($p_{total} = 40 \text{ bar}$)

When the reaction is carried out in the presence of a large excess of H₂ (H₂/CO₂ = 37/3), the apparent activation energy drops to 20 kJ mol⁻¹, which is in perfect agreement with the value of 24 kJ mol⁻¹ predicted for the direct hydrogenolysis path (Cycle I, Figure 3.8). In line with the proposal on the RDS nature of the CO₂ activation step in

Cycle I, the reaction rate in this case is lower due to the decreased partial pressure of CO₂. Since the activation barrier of a catalytic transformation is the direct measure of catalyst efficiency, we can claim that selection between Cycles I and I^a allows us to control the catalytic efficiency via selection of the RDS. An important consequence of the low activation barrier for CO₂ hydrogenation at a high H₂/CO₂ molar ratio is the possibility to achieve higher rates at lower temperature. For example the reaction proceeds with initial rate of 721 000 h⁻¹ at 102 °C at 37/3 ratio between H₂ and CO₂, whereas a nearly 10°C higher temperature is needed to achieve the same rate under 30/10 H₂/CO₂ ratio. From the Arrhenius plot one can estimate TOF values above 100 000 h⁻¹ to be attainable at ambient temperature if the low energy pathway is selected. These findings render the Ru-PNP complex **1** in combination with the non-nucleophilic DBU base the most active CO₂ hydrogenation catalysts reported to date.

3.5 Conclusions

In this Chapter we described the development of a highly active homogeneous catalytic system based on a lutidine-derived Ru-PNP pincer complex for the reversible hydrogenation of CO₂. To the best of our knowledge, the catalytic activities obtained for both the CO₂ hydrogenation and FA dehydrogenation reactions are the highest reported to date. When used in combination with DBU, catalyst **1** allows controlling hydrogen liberation activity in a narrow temperature interval. Our results point to the key role of the base strength in determining the formate capacity of the system under the catalytically relevant conditions. Strong bases are required to generate high acid/amine ratios at elevated temperature when the reaction times are short. Base strength was found to affect the nature of the rate-controlling step in FA dehydrogenation. While the C-H cleavage step is controlling the rate in the presence of weak bases, the initial H₂ recombination determines the rate when the reaction is carried out in the presence of strong bases.

The mechanistic analysis of CO₂ hydrogenation revealed that the participation of the non-innocent PNP ligand in catalysis is not favored, that is evidenced by prohibitively high activation barriers for hydrogenation using complexes **2** and **3**. Instead, the dihydrido complex **4** provides the most favorable pathway for CO₂ hydrogenation via two competing mechanisms (Cycle I and I^a) neither of which involves metal-ligand cooperation. The selection between corresponding mechanisms can easily be achieved by varying H₂ partial pressure. At H₂/CO₂ ratio of 30/10 the hydrogenation proceeds with apparent activation energy of 57 kJ mol⁻¹ while at H₂/CO₂ = 37/3 this value drops to 20 kJ mol⁻¹ that

corresponds to the switch from Cycle I^a to Cycle I in perfect agreement with DFT predictions. A near 2.5-fold decrease of the apparent activation energy of the hydrogenation under optimized conditions represents a major improvement of the intrinsic catalytic efficiency of Ru-PNP-based system.

3.6 Experimental

General considerations

All manipulations unless otherwise stated were performed using Schlenk techniques. Catalytic hydrogenation tests and cycling experiments were performed in 100 mL stainless steel autoclave equipped with gas compensation device and flowmeter for evolved gas detection. CO₂ hydrogenation was carried out at a constant pressure. Samples were taken via a dip tube installation and immediately analyzed with HPLC and GC-FID. The reaction was triggered by catalyst addition to a pressurized and preheated vessel. TOF values are determined at the initial reaction stage where possible. In a typical experiment 30 mL solvent, 5 mL DBU (33.4 mmol), 1 mL toluene or THF (used as an internal standard) and appropriate amount of catalysts dispensed from the stock solution were used. The kinetic traces represent single run results. Dehydrogenation reactions were performed using double lined glass reactor and syringe pump for FA supply. Gas evolution was analyzed with Bronkhorst flowmeter or foam flowmeters. Gas composition was analyzed by GC-TCD and verified to be H₂:CO₂ = 1:1 with no CO traces detectible. TOF values were estimated from gas evolution rate for both gas detection methods. Small scale CO₂ hydrogenation experiments were performed in A96 parallel reactor at 70 °C under 40 bar of equimolar H₂/CO₂ mixture. In a typical experiment 3 mL THF or DMF, and appropriate amount of base DBU (3.3 mmol) or KOtBu (0.33 mmol) were mixed with 0.1 μmol of catalyst. The reaction was quenched after 2 hours by addition of water/ethanol mixture and immediately analyzed. Concentrations of formic acid were analyzed using Shimadzu HPLC setup with 25 mM phosphate buffer of pH = 2 as mobile phase using Prevail Organic Acid column. GC measurements, where appropriate, were performed using Shimadzu GC-17A instrument.

Density Functional Theory Calculations

DFT calculations were performed by Dr. E.A. Pidko. Similar to our previous work,²⁴ calculations were performed with the PBE0 (also denoted as PBE1PBE and PBEh)⁴⁴ hybrid exchange-correlation functional using Gaussian 09, revision D.01 program.⁴⁵ The high accuracy of this method has been demonstrated by previous benchmark studies on a wide set of different chemical systems^{46,47} and by our own accuracy tests employing different DFT methods for modelling CO₂ hydrogenation to formic acid.²⁴ The full electron 6-311G(d,p) basis set^{48,49} was used for all atoms except ruthenium, for which the LanL2DZ basis set^{50,51} was employed. The polarizable continuum model (PCM) with standard parameters for THF and DMF solvents, as implemented in the Gaussian 09 rev. D.01 program package, was used during the geometry optimization and frequency analysis to account for bulk solvent effects. Because the differences in reaction free energies computed with

PCM model of THF and DMF solvents do not exceed 5 kJ mol⁻¹ (see Supporting Information), only the results obtained for the THF solvent are discussed here. The accuracy of this computational method was tested by calculating energetics of selected elementary reaction steps ($2 + \text{H}_2 \rightarrow 4^{47}$ and $4 + \text{CO}_2 \rightarrow 5^*$, Scheme 1) using a larger triple-zeta+polarization quality basis set combination employing Def2-TZVPP⁵² basis set for the Ru center and 6-311+G(d,p) for the light atoms. The resulting reaction and activation energies agreed within 5 kJ mol⁻¹ with those using the standard methodology. Note that the expansion of the basis set with diffuse functions has a negligible effect on the computed energetics, while it resulted in a much slower SCF convergence (when PCM model was used to account for solvent effects). The nature of the stationary points was evaluated from the analytically computed harmonic modes. No imaginary frequencies were found for the optimized structures, confirming that these correspond to local minima on the potential energy surface. All transition states exhibited a single imaginary frequency, corresponding to the eigenvector along the reaction path. The assignment of the transition state structure to a particular reaction path was tested by perturbing the structure along the reaction path eigenvector in the directions of the product and the reagent followed by geometry optimization. For catalytic cycles I, II and III starting from the activated species 3^0-H_2 IRC calculations were performed to additionally confirm the assignment of the transition states. The reaction (ΔE) and activation energies (E^\ddagger) reported in the manuscript were corrected for zero point (E) energy contribution computed using the results of the normal-mode analysis. Free energy values (ΔG°) were computed using the results of the normal-mode analysis within the ideal gas approximation at a pressure of 1 atm and temperatures of 298 K.

3.7 Notes and References

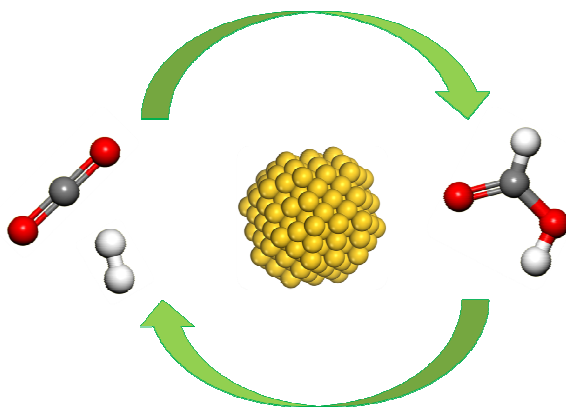
- (1) Cokoja, M.; Bruckmeier, C.; Rieger, B.; Herrmann, W. A.; Kühn, F. E. *Angew. Chem. Int. Ed.* **2011**, *50*, 8510.
- (2) Huang, K.; Sun, C.-L.; Shi, Z.-J. *Chem. Soc. Rev.* **2011**, *40*, 2435.
- (3) Sakakura, T.; Choi, J.-C.; Yasuda, H. *Chem. Rev.* **2007**, *107*, 2365.
- (4) Maeda, C.; Miyazaki, Y.; Ema, T. *Catal. Sci. Technol.* **2014**, *4*, 1482.
- (5) Eberle, U.; Felderhoff, M.; Schüth, F. *Angew. Chem. Int. Ed.* **2009**, *48*, 6608.
- (6) Yang, J.; Sudik, A.; Wolverton, C.; Siegel, D. J. *Chem. Soc. Rev.* **2010**, *39*, 656.
- (7) Yadav, M.; Xu, Q. *Energy Environ. Sci.* **2012**, *5*, 9698.
- (8) Boddien, A.; Gaertner, F.; Federsel, C.; Sponholz, P.; Mellmann, D.; Jackstell, R.; Junge, H.; Beller, M. *Angew. Chem. Int. Ed.* **2011**, *50*, 6411.
- (9) Boddien, A.; Gaertner, F.; Mellmann, D.; Sponholz, P.; Junge, H.; Laurenczy, G.; Beller, M. *Chimia* **2011**, *65*, 214.
- (10) Enthaler, S. *ChemSusChem* **2008**, *1*, 801.
- (11) Joó, F. *ChemSusChem* **2008**, *1*, 805.
- (12) Fellay, C.; Dyson, P. J.; Laurenczy, G. *Angew. Chem. Int. Ed.* **2008**, *47*, 3966.
- (13) Loges, B.; Boddien, A.; Junge, H.; Beller, M. *Angew. Chem. Int. Ed.* **2008**, *47*, 3962.
- (14) Nielsen, M.; Alberico, E.; Baumann, W.; Drexler, H.-J.; Junge, H.; Gladiali, S.; Beller, M. *Nature* **2013**, *495*, 85.
- (15) Rodríguez-Lugo, R. E.; Trincado, M.; Vogt, M.; Tewes, F.; Santiso-Quinones, G.; Grützmacher, H. *Nat. Chem.* **2013**, *5*, 342.

- (16) Boddien, A.; Federsel, C.; Sponholz, P.; Mellmann, D.; Jackstell, R.; Junge, H.; Laurency, G.; Beller, M. *Energy Environ. Sci.* **2012**, *5*, 8907.
- (17) Tanaka, R.; Yamashita, M.; Nozaki, K. *J. Am. Chem. Soc.* **2009**, *131*, 14168.
- (18) Tanaka, R.; Yamashita, M.; Chung, L. W.; Morokuma, K.; Nozaki, K. *Organometallics* **2011**, *30*, 6742.
- (19) Hull, J. F.; Himeda, Y.; Wang, W.-H.; Hashiguchi, B.; Periana, R.; Szalda, D. J.; Muckerman, J. T.; Fujita, E. *Nat. Chem.* **2012**, *4*, 383.
- (20) Munshi, P.; Main, A. D.; Linehan, J. C.; Tai, C.-C.; Jessop, P. G. *J. Am. Chem. Soc.* **2002**, *124*, 7963.
- (21) Zell, T.; Butschke, B.; Ben-David, Y.; Milstein, D. *Chem. Eur. J.* **2013**, *19*, 8068.
- (22) Jeletic, M. S.; Mock, M. T.; Appel, A. M.; Linehan, J. C. *J. Am. Chem. Soc.* **2013**, *135*, 11533.
- (23) Gnanaprakasam, B.; Zhang, J.; Milstein, D. *Angew. Chem. Int. Ed.* **2010**, *49*, 1468.
- (24) Filonenko, G. A.; Conley, M. P.; Copéret, C.; Lutz, M.; Hensen, E. J. M.; Pidko, E. A. *ACS Catal.* **2013**, *3*, 2522.
- (25) Drees, M.; Cokoja, M.; Kühn, F. E. *ChemCatChem* **2012**, *4*, 1703.
- (26) Fan, T.; Chen, X.; Lin, Z. *Chem. Commun.* **2012**, *48*, 10808.
- (27) Creutz, C.; Chou, M. H.; Hou, H.; Muckerman, J. T. *Inorg. Chem.* **2010**, *49*, 9809.
- (28) Huang, K.-W.; Han, J. H.; Musgrave, C. B.; Fujita, E. *Organometallics* **2006**, *26*, 508.
- (29) Schaub, T.; Paciello, R. A. *Angew. Chem. Int. Ed.* **2011**, *50*, 7278.
- (30) Ohnishi, Y.-y.; Matsunaga, T.; Nakao, Y.; Sato, H.; Sakaki, S. *J. Am. Chem. Soc.* **2005**, *127*, 4021.
- (31) Ohnishi, Y.-y.; Nakao, Y.; Sato, H.; Sakaki, S. *Organometallics* **2006**, *25*, 3352.
- (32) Urakawa, A.; Jutz, F.; Laurency, G.; Baiker, A. *Chem. Eur. J.* **2007**, *13*, 3886.
- (33) Gunanathan, C.; Milstein, D. *Acc. Chem. Res.* **2011**, *44*, 588.
- (34) van der Vlugt, J. I.; Reek, J. N. H. *Angew. Chem. Int. Ed.* **2009**, *48*, 8832.
- (35) Balaraman, E.; Milstein, D. *Top. Organomet. Chem.* **2014**, *77*, 1.
- (36) Yang, X. *ACS Catal.* **2011**, *1*, 849.
- (37) Ahlquist, M. S. G. *J. Mol. Catal. A: Chem.* **2010**, *324*, 3.
- (38) Huff, C. A.; Sanford, M. S. *ACS Catal.* **2013**, *3*, 2412.
- (39) Zhang, J.; Leitus, G.; Ben-David, Y.; Milstein, D. *Angew. Chem. Int. Ed.* **2006**, *45*, 1113.
- (40) Oldenhof, S.; de Bruin, B.; Lutz, M.; Siegler, M. A.; Patureau, F. W.; van der Vlugt, J. I.; Reek, J. N. H. *Chem. Eur. J.* **2013**, *19*, 11507.
- (41) Musashi, Y.; Sakaki, S. *J. Am. Chem. Soc.* **2000**, *122*, 3867.
- (42) Drake, J. L.; Manna, C. M.; Byers, J. A. *Organometallics* **2013**, *32*, 6891.
- (43) Filonenko, G. A.; van Putten, R.; Schulpen, E. N.; Hensen, E. J. M.; Pidko, E. A. *ChemCatChem* **2014**, *6*, 1526.
- (44) Adamo, C.; Barone, V. *J. Chem. Phys.* **1999**, *110*, 6158.
- (45) *Gaussian 09 Revision D.01*, Frisch, M. J.; Trucks, G. W.; Schlegel, H. B.; Scuseria, G. E.; Robb, M. A.; Cheeseman, J. R.; Scalmani, G.; Barone, V.; Mennucci, B.; Petersson, G. A.; Nakatsuji, H.; Caricato, M.; Li, X.; Hratchian, H. P.; Izmaylov, A. F.; Bloino, J.; Zheng, G.; Sonnenberg, J. L.; Hada, M.; Ehara, M.; Toyota, K.; Fukuda, R.; Hasegawa, J.; Ishida, M.; Nakajima, T.; Honda, Y.; Kitao, O.; Nakai, H.; Vreven, T.; Montgomery, J. A., Jr.; Peralta, J. E.; Ogliaro, F.; Bearpark, M.; Heyd, J. J.; Brothers, E.; Kudin, K. N.; Staroverov, V. N.; Kobayashi, R.; Normand, J.; Raghavachari, K.; Rendell, A.; Burant, J. C.; Iyengar, S. S.; Tomasi, J.; Cossi, M.; Rega, N.; Millam, N. J.; Klene, M.; Knox, J. E.; Cross, J. B.; Bakken, V.; Adamo, C.; Jaramillo, J.; Gomperts, R.; Stratmann, R. E.; Yazyev, O.; Austin, A. J.; Cammi, R.; Pomelli, C.; Ochterski, J. W.; Martin, R. L.; Morokuma, K.; Zakrzewski, V. G.; Voth, G. A.; Salvador, P.; Dannenberg, J. J.; Dapprich, S.; Daniels, A. D.; Farkas, Ö.; Foresman, J. B.; Ortiz, J. V.; Cioslowski, J.; Fox, D. J.; Gaussian, Inc.: Wallingford CT, 2009.
- (46) Zhao, Y.; Truhlar, D. G. *J. Chem. Theor. Comput.* **2009**, *5*, 324.
- (47) Valero, R.; Costa, R.; de P. R. Moreira, I.; Truhlar, D. G.; Illas, F. *J. Chem. Phys.* **2008**, *128*, 114003.
- (48) Krishnan, R.; Binkley, J. S.; Seeger, R.; Pople, J. A. *J. Chem. Phys.* **1980**, *72*, 650.

- (49) McLean, A. D.; Chandler, G. S. *J. Chem. Phys.* **1980**, *72*, 5639.
- (50) Hay, P. J.; Wadt, W. R. *J. Chem. Phys.* **1985**, *82*, 270.
- (51) Hay, P. J.; Wadt, W. R. *J. Chem. Phys.* **1985**, *82*, 299.
- (52) Andrae, D.; Häußermann, U.; Dolg, M.; Stoll, H.; Preuß, H. *Theoret. Chim. Acta* **1990**, *77*, 123.

Supported gold catalysts for hydrogenation of carbon dioxide to formates

ABSTRACT: The activity of supported gold catalysts in hydrogenation of carbon dioxide was investigated. The initial screening experiments involving 18 different heterogeneous Au catalysts revealed Au/Al₂O₃ Aurolite catalyst as the best performing one. The crucial role of metal-support interactions was demonstrated by comparative experiments with unsupported Au nanoparticles that provided no activity in CO₂ hydrogenation. The results of cyanide leaching tests complemented by XPS, STEM and TPR results indicate the importance of metallic Au⁰ nanoparticles for the catalytic reaction. Kinetic studies point to possible internal mass-transfer limitations for the CO₂ hydrogenation by Au/Al₂O₃. The reaction proceeds with a negligible apparent activation barrier and shows nearly no temperature dependence of the reaction rate. This points to the possibility of the low temperature operation without the loss of catalytic activity. Finally, equilibrium formate yields obtained with Au/Al₂O₃ are consistent with ones, obtained in homogeneous hydrogenation of CO₂.



4.1. Introduction

Hydrogenation of carbon dioxide to formate salts in the presence of homogeneous catalysts has been extensively discussed in the previous Chapters. Despite high catalytic activities, the use of homogeneous catalysis in large-scale industrial applications has its limitations. While applicable for FA-based hydrogen storage, the utilization of homogeneous catalysts for the large-scale production of formic acid via the direct hydrogenation of CO₂ may be unfeasible from the economic viewpoint. Defined by their nature, homogeneous catalysts are soluble in the reaction medium and, accordingly, involve tedious and costly separation steps to be used again.¹ Therefore, an easily separable heterogeneous catalyst for CO₂ hydrogenation is highly desired.

The first example of a heterogeneously catalyzed CO₂ hydrogenation to formates dates back to 1914. In the original paper by Bredig and Carter,² the use of Pd black for the reduction of carbonates and gaseous CO₂ to formates has been described. Nevertheless, the necessity to utilize bulk noble metal as a catalyst strongly reduces the applicability of this system. Until recently, no active heterogeneous catalysts that would operate at low metal loading and show high stability have been reported. Only in 2011, Preti et al. described a catalytic system for the hydrogenation of supercritical CO₂ involving a commercially available Au/TiO₂ catalyst with metal loadings as low as 1 % wt and neat triethylamine base as a promoter.³ Au/TiO₂ demonstrated a stable catalytic activity for 37 days. The catalytic reaction at 40 °C produced in the FA·NEt₃ adduct with the acid-amine ratio of 1.715, from which anhydrous FA could be isolated by distillation. Taking into account recent reports on gold catalysis for the decomposition of FA,⁴ the discovery of Preti et al. allows not only to produce FA from CO₂, but also to perform the reversible H₂ storage using gold catalysts.³ Therefore, this Chapter is focused on improving the performance of the supported gold catalysts and investigating the nature of the active component, responsible for catalysis.

4.2. Results and discussion

4.2.1. Catalyst screening and catalyst activation studies

Inspired by the findings of Preti et al.,³ we focused our initial efforts on the evaluation of catalytic activity of different Au catalysts to identify a superior catalyst formulation to be used in further detailed studies. The reactions were carried out under 40 bar pressure of equimolar H₂/CO₂ mixture at 70 °C for 20 h. Triethylamine was used as a base promoter in combination with ethanol solvent. We first evaluated the activity of small unsupported Au

nanoparticles stabilized by dodecanethiol (DDT) and triphenylphosphine (TPP) ligands. The colloidal catalysts are denoted as Au(3.6)-DDT, Au(2.4)-TPP, Au(1.8)-TPP, respectively, where the number stands for the mean diameter of the nanoparticles determined by TEM. For the TPP-stabilized catalysts, the size of the nanoparticles was varied by the changing the reducing agent upon their preparation (see Experimental section). Independently of the particle size and the type of the stabilizing ligand, none of the unsupported Au samples exhibited activity in CO₂ hydrogenation (entries 1-3, Table 4.1). These results point to the necessity of the support for the high activity of heterogeneous Au catalysts in CO₂ hydrogenation to formates.

Further investigation of supported gold catalysts revealed that catalytic performance depended strongly on the nature of the support. In general, high activities were obtained with the catalysts employing basic supports. In particular, the CO₂ hydrogenation by gold supported on Al₂O₃, MgO and basic hydrotalcites (HT) led to higher formate yields and showed higher turnover numbers (TON) as compared to the reactions with the catalysts based on more acidic supports such as CeO₂, Cu and Mg-Cu chromites (Table 4.1). The activity of Au nanoparticles on an inert Norit active carbon support was negligible. The latter is consistent with the zero activity of unsupported Au nanoparticles and implies the importance of metal-support interactions for the catalytic activity of gold.

The activity screening tests point to the sub-optimal catalytic performance of the benchmark Au/TiO₂ catalyst. By using an Au/Al₂O₃ Aurolite catalyst containing the same amount of Au (1 wt %) a nearly two-fold higher FA yield and, accordingly, TON values were achieved (entries 4 and 6, Table 4.1). In view of the superior catalytic activity, Au/Al₂O₃ Aurolite catalyst was selected for further detailed investigation and performance optimization.

To verify the catalyst composition, the Au/Al₂O₃ samples were characterized with HAADF-STEM and elemental analysis. The electron microscopy data summarized in Figure 4.1 evidence a homogeneous distribution of Au particles with a majority of the particles being below 2 nm in diameter. ICP-OES analysis on two separate batches of the commercial catalysts, confirms the specified Au loading of $1.0 \pm 0.1 \text{ \%}_{\text{wt}}$ (see the Experimental Section for details).

Table 4.1. Final acid-amine ratios (AAR) and turnover numbers in Au catalyst screening study

Entry	Catalyst	AAR	TON
1	Au(3.6)-DDT	0	0
2	Au(2.4)-TPP	0.001	0.6
3	Au(1.8)-TPP	0	0
4	Au/Al ₂ O ₃ (AUROLite)	0.205	215
5	Au/MgO	0.108	113
6	Au/TiO ₂ (AUROLite)	0.096	111
7	Au/MgAl - HT	0.015	91
8	Au/Mg ₃ Cr – HT	0.007	52
9	Au/ZnGa – HT	0.002	17
10	Au/Norit-RX-3	0.004	15
11	Au/CeO ₂	0.002	8
12	Au/MgCuCr ₂ O ₄	0.003	7
13	Au/CuCr ₂ O ₄	0.002	6
14	Au/MgCoCr ₂ O ₄	0.002	6
15	Au/MgCr ₂ O ₄	0.002	6
16	Au/ZnO (AUROLite)	0.002	2
17	Au/Hydroxyapatite	0	0
18	Au/MgNiCr ₂ O ₄	0	0

Conditions: 3 mL EtOH, 0.5 ml (3.5 mmol) NEt₃, 70 °C, 40 bar H₂/CO₂, 20h; TON values are calculated per total gold content. HT = hydrotalcites; typically 0.6 mg Au used for supported catalysts. 824, 1.6, 0.7 mg Au used in Entries 1,2 and 3, respectively.

Table 4.2. Key parameters and the values of Au dispersion and specific surface area.^a

Structure	n _s	a _m (m ²)	M (g/mol)	ρ (g/cm ³)	v _m (m ³)	D	S _{sp} (m ² /g)
fcc	1.15	8.75·10 ⁻²⁰	196.97	19.31	1.69·10 ⁻²⁹	0.43	113.8

^a n_s = number of surface atoms per 10⁻¹⁹ m²; a_m = area occupied by a surface atom; M = atomic mass; ρ = mass density; v_m = volume occupied by an atom in bulk Au; D = Au dispersion; S_{sp} = specific surface area.

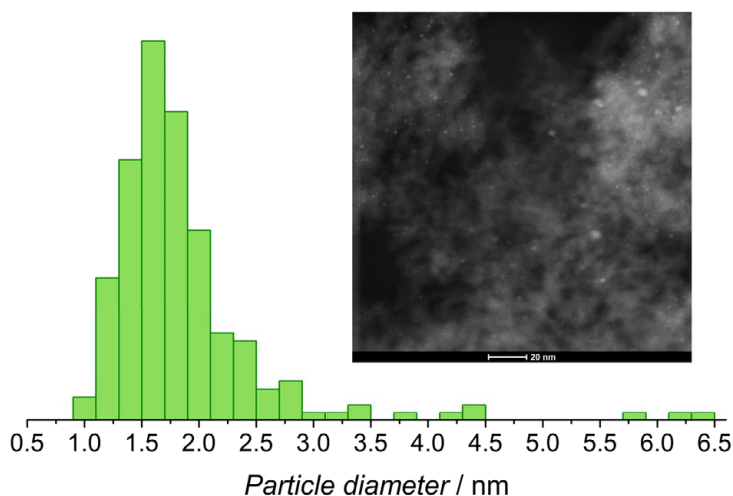


Figure 4.1. HAADF-STEM and particle size distribution data for Au/Al₂O₃.

Table 4.3. CO₂ hydrogenation data using Au/Al₂O₃ catalyst pretreated at different conditions ^a

T (°C)	TON	
	H ₂	O ₂
200	223	139
300	236	238
400	166	198
500	126	183

^a Pretreatment done in 10% gas in helium flow; ramp rate = 5.0 °C/min; dwell time = 3 h; catalysis: 3 mL EtOH, 0.5 mL NEt₃, 40 bar 1:1 H₂:CO₂, 20 h.

Since catalyst preactivation can potentially affect its performance, we investigated the influence of the thermal treatment of Au/Al₂O₃ on its activity in CO₂ hydrogenation. Oxidative and reductive treatments of Au/Al₂O₃ were carried out at different temperatures in the range of 200 - 500 °C and the catalytic performance of the resulting materials was then evaluated (Table 4.3). The activation at 300 °C under oxidizing and reducing conditions resulted in the highest TON values of ca. 237 among the catalysts considered. The increase of the pretreatment temperature to 500 °C led to a significant decrease of activity by 25 and 50 % for the oxidized and reduced materials, respectively.

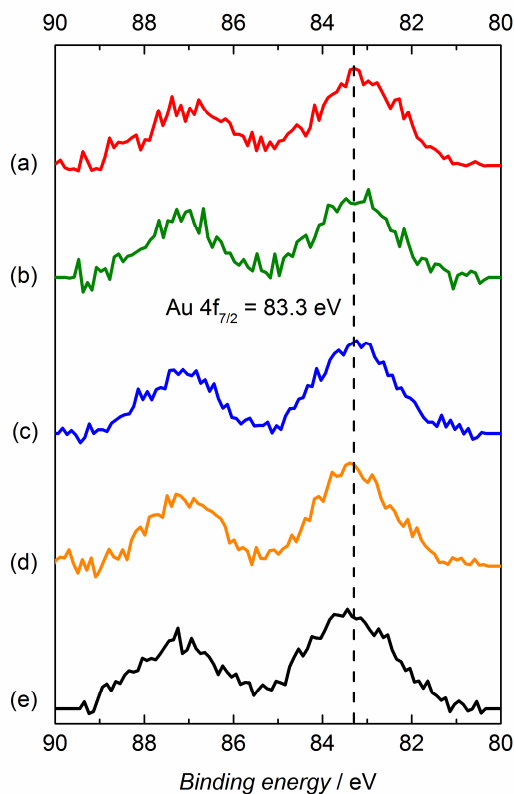


Figure 4.2. Section of the XPS spectra of (a) Au/Al₂O₃ as-received; after reduction at: (b) 300 °C; (c) 500 °C; and oxidation at: (d) 300 °C; (e) 500 °C. Broken line indicates BE = 83.3 eV for Au 4f_{7/2} selected for analysis.

To get an insight into the influence of the catalyst pretreatment procedure on the oxidation state of Au in the catalyst, the catalysts activated at different temperatures in oxidative and reductive conditions were studied by X-ray photoelectron spectroscopy (XPS). The XPS spectra are shown in Figure 4.2. Due to the low Au loading in Au/Al₂O₃ only the most intensive Au 4f_{7/2} line was analyzed. Independently of the pretreatment history, all catalysts were characterized by very similar XPS spectra. We observed Au 4f_{7/2} peak at binding energies (BE) of 83.3 eV, that was slightly lower than the BE for bulk metallic Au⁰ (84.0 eV). This is consistent with the literature values for supported spherical Au nanoparticles, where the charge transfer from the support induces a partial negative charge on Au resulting in a marginal shift of BE to 83.3-83.4 eV.^{25,28-30} We did not observe cationic gold species that would be evidenced by a positive shift of the BE to values over 85.6 eV in neither of the samples.⁵ An apparent similarity between oxidized and reduced

samples was further supported by the results of H₂-TPR that showed the absence of reducible species up to 800 °C. Taken together, these data imply that the variation of the catalytic performance upon thermochemical activation is not associated with the change in Au oxidation state but rather has a thermal origin. The decrease in activity for the catalysts treated at higher-temperatures may be associated with the sintering of Au particles. Alternatively, the observed activity variations could originate from the change in the level of hydration and, therefore, reactivity of the alumina surface.^{6,7}

Our previous study⁸ suggests a strong influence of solvent and base on the catalytic CO₂ hydrogenation. In an attempt to further optimize the catalytic performance of the Au/Al₂O₃ catalyst in CO₂ hydrogenation, its activity was evaluated in ethanol, DMF and THF solvents in combination with NEt₃ and DBU base promoters (Table 4.4.). In agreement with the results obtained using homogeneous catalyst and discussed in the previous chapters,⁹ turnover numbers were found to strongly correlate with the polarity of the solvent (DMF > EtOH >> THF). The highest activity of Au/Al₂O₃ was observed when a strongly polar aprotic DMF solvent was used in combination with the NEt₃ base.¹⁰ This combination allowed achieving a nearly 20 % higher FA yield and TON values compared to hydrogenation in ethanol and nearly six-fold higher than that in THF. In contrast to the homogeneously catalyzed reactions discussed in the previous chapter, in the presence of a stronger DBU base a lower FA yield was obtained and the reaction was accompanied with a severe leaching of Au from the catalyst. The latter was evidenced by the formation of a gold mirror on the reaction vessel wall. The exclusion of air and moisture in the reaction medium had a negative impact on the performance of Au/Al₂O₃ (Entries 2 vs. 3, Table 4.4). This may indicate that, in agreement with previous literature reports,¹¹ small quantities of water promote the formation of FA. The use of neat triethylamine without solvent similar to the procedure originally described by Preti et al.³ resulted in a very low activity that is less than 15.6 % of that in DMF/NEt₃ medium.

Finally, our screening data suggests that the metal-support interaction is crucial for the catalytic activity of Au/Al₂O₃. Although only Au⁰ species were observed by XPS, the presence of support may also induce the stabilization of sub-nanometer metal clusters. Since they are typically in a very intimate contact with the support due to high coordinative unsaturation, sub-nanometer clusters can show some catalytic performance or even be responsible for catalyst activity in the first place. To investigate this possibility we applied a cyanide leaching procedure to remove Au⁰ nanoparticles from the catalyst, while leaving small metal clusters intact. Upon treatment of Au/Al₂O₃ with sodium cyanide over 99 % of

Au was removed from the catalyst as evidenced by elemental analysis. The remaining Au content was ca. 0.01 %_{wt}. The leached catalyst exhibited no catalytic activity in a subsequent hydrogenation test after calcination at 300 °C. These results support the proposition of Au⁰ as the active site for CO₂ hydrogenation to FA. The designation of metallic Au⁰ as the part of the active site in Au catalyzed hydrogenation reactions has been found in literature, with their activity towards H₂ dissociation attributed either to low coordinated corner and edge Au atoms^{12,13} or Au-support interphase.¹⁴ Small particles with a diameter of only a few nanometers are therefore required as they possess a larger fraction of low coordinate metal and high support contact perimeter. The exact role of the support itself still remains heavily debated within the field. Bus and Panayotov both assign low-coordinated Au⁰ sites away from the Au-support perimeter as the active sites for H₂ dissociation, with the latter study also suggesting some atomic H spills over to the support.¹³⁻¹⁷ On the contrary, Fujitami *et al.* proposed the Au-support interface to be the active site for heterolytic H₂ dissociation. Authors demonstrated the synergy between Au particles and the titania support for H₂ activation.^{12-14,18}

Table 4.4. Solvent and base screening in hydrogenation of CO₂ using Au/Al₂O₃

Entry	Solvent	Base	TON ^a	AAR ^a	Remarks
1	none	NEt ₃	90	0.034	Neat base, 0.5mL
2	EtOH	NEt ₃	114	0.042	Air/moisture free
3	EtOH	NEt ₃	500	0.205	
4	DMF	NEt ₃	580	0.207	
5	THF	NEt ₃	100	0.037	
6	DMF	DBU	120	0.045	

Conditions: 3 mL solvent, 0.5 mL base, 40 bar 1:1 H₂:CO₂ 70° C, 20 h reaction time, TON calculated per surface Au, ^a average of two runs

4.2.2. Kinetics of CO₂ hydrogenation using Au/Al₂O₃ catalyst

Using the optimized solvent/base composition we further performed a kinetic investigation of the gold catalyst performance. We analyzed the influence of the catalyst loading, gas compositions and temperature on the activity (expressed as the initial rate, TOF^o) and the final yield of formate, expressed as the Acid-to-Amine Ratio (AAR). An overview of the catalytic results is given in Table 4.5.

We first verified that under the conditions employed the CO₂ hydrogenation has the first order in catalyst concentration. Indeed, with a two-fold increase of the catalyst loading the absolute rate of FA formation doubled, indicating the first order in the catalyst concentration (Entries 1 and 2, Table 4.5, and Figure 4.8 in the Experimental section). When normalized per amount of catalyst the initial TOF equals to ca. 120 h⁻¹ in both cases.

Table 4.5. Summary of the kinetic study for catalytic CO₂ hydrogenation to FA over Au/Al₂O₃

Entry	Catalyst, mg	H ₂ /CO ₂ (bar/bar)	T, °C	Time, h	TOF ^o (h ⁻¹) ^a	TON ^a	Final AAR
1	304	20:20	70	24	118	1088	0.199
2	603	20:20	70	23	123	676	0.246
3	602	22.5:17.5	70	21	120	674	0.245
4	603	30:10	70	23	112	577	0.210
5	601	20:20	85	23	114	299	0.109
6	602	20:20	100	4	80	112	0.041
7	602	20:20	100	5	108	123	0.045

Conditions: 30 mL DMF, 5 mL NEt₃, 1 mL THF internal standard; ^a initial TOF and TON values per surface Au (D=0.43);

Much to our surprise, the partial pressure variation had a nearly negligible impact on the initial TOF of the hydrogenation reaction (Entries 2-4 in Table 4.5 and Figure 4.9 in the Experimental section). The kinetic measurements performed under 40 bar H₂/CO₂ pressure with the relative H₂/CO₂ composition varying in the range from 1/1 to 3/1 showed TOF^o values identical within a 6 % margin. On the other hand, the partial pressure variation affected the reaction equilibrium and led to a lower formate yield at elevated H₂ pressures consistently with our data reported in Chapter 3 for the homogeneously catalyzed hydrogenation.⁸ These results point to the zero apparent reaction order in H₂ and CO₂ concentrations. This suggests the independence of the rate determining step on either of H₂ and CO₂ or possible operation of the catalyst in internal mass transfer limited regime.

We further carried out the kinetic measurements at different reaction temperatures. In agreement with the results in Chapter 3^{8,19} and the reports by Beller and co-workers,²⁰, the increase of the reaction temperature led to a strong decrease in the final formate concentration (Entries 2 and 5-8, Table 4.5). The temperature dependence of the final AAR complements perfectly the results of the our studies on the homogeneously catalyzed CO₂ hydrogenation in DMF/NEt₃ (Figure 4.3). This implies that the catalytic reactions in every

instance were brought to a completion (determined by the reaction equilibrium under particular conditions) with no signs of catalyst deactivation.

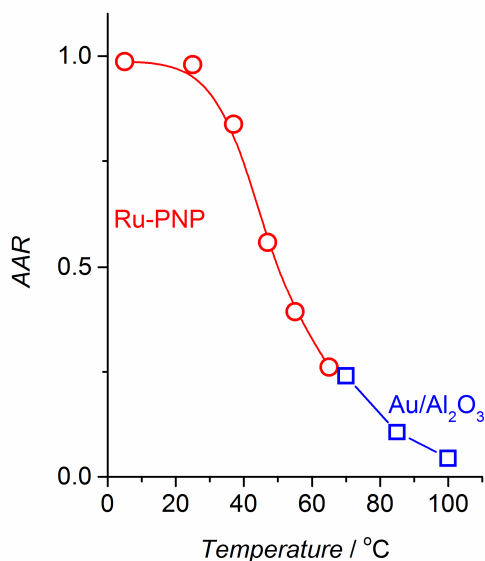


Figure 4.3. Temperature dependence of the final AAR obtained in CO_2 hydrogenation with $\text{Au}/\text{Al}_2\text{O}_3$ and Ru-PNP catalyst in DMF/NEt_3 .⁸

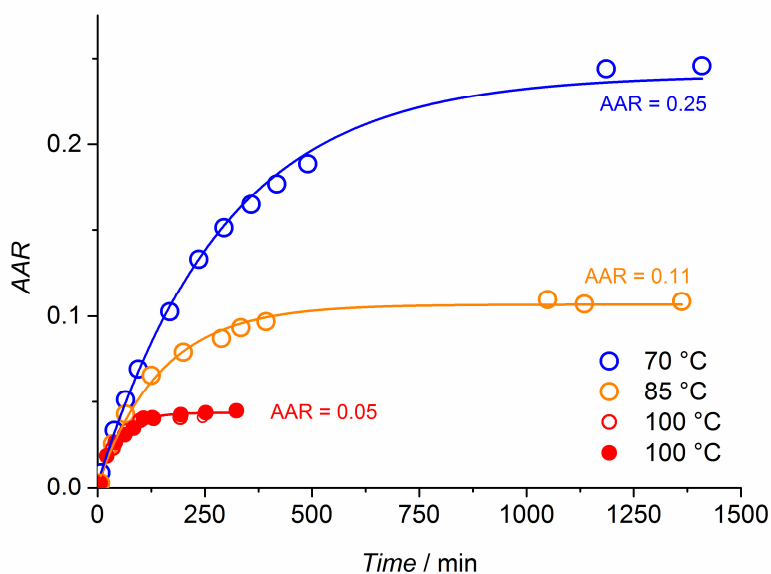
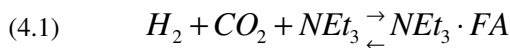


Figure 4.4. Temperature dependence of CO_2 hydrogenation kinetics. Solid lines represent an exponential function fit (see Experimental section for details). Reaction conditions are indicated in Table 4.4.

Surprisingly, the measured initial rates of reaction did not change significantly upon the variation of the reaction temperature (Figure 4.4). The estimation of the apparent activation energy from the Arrhenius plot constructed initial TOF values for the catalytic reactions carried out at 70 °C, 85 °C and 100 °C yields $E_{app} = -4 \text{ kJ mol}^{-1}$. Alternatively, the activation parameters could be obtained from the kinetic data modeling. The kinetic traces on the Figure 4.4 can be accurately fitted ($R^2 > 0.98$) with an exponential rate law in the following manner. The catalytic reaction was described by the Equation 4.1 that corresponds to a dynamic equilibrium between gaseous reactants, base and the reaction product:



Assuming k^+ and k^- to be the rate constants of the forward and reverse reactions, respectively, equilibrium constant defined as $K = k^+/k^-$ and the initial NEt_3 concentration defined as A_0 , the following analytical expression for the change in product concentration with time $NEt_3 \cdot FA(t)$ can be obtained:

$$(4.2) \quad NEt_3 \cdot FA(t) = A_0 \frac{k^+}{k^+ + k^-} - A_0 \frac{k^+}{k^+ + k^-} e^{-(k^+ + k^-)t}$$

Fitting of AAR vs time plots allows for a function of the following type:

$$(4.3) \quad \frac{NEt_3 \cdot FA(t)}{A_0} = AAR(t) = X - Ye^{Zt}, \text{ where}$$

$$X = \frac{k^+}{k^+ + k^-} \text{ and } Z = -(k^+ + k^-)$$

This in turn allows for the estimation of forward reaction rate constant as:

$$(4.4) \quad k^+ = -X \times Z,$$

Resulting k^+ values plotted in the Arrhenius coordinates allow for estimation of activation barrier of the forward reaction at $E_{app}^+ = 5 \text{ kJ mol}^{-1}$ (Figure 4.5 b) that is very close to the value estimated from the initial TOF^o values. The low apparent activation energies determined using both methods are in agreement with the observed independence of the reaction rate on the temperature. The reverse reaction rate constant derived as

$$(4.5) \quad k^- = -Z - k^+,$$

allows for estimating the barrier for the reverse FA dehydrogenation reaction as $E_{app}^- = 74 \text{ kJ mol}^{-1}$ (see Experimental part). This value is very close to the barrier

determined for the same reaction with Ru-PNP in DMF/NEt₃, where the C-H cleavage in the metal bound formate anion was proposed as the rate-determining step. Importantly, theoretical calculations by Mavrikakis and co-workers predicted this step to proceed over the Au(111) surface with a barrier of 77 kJ mol⁻¹ ²¹ in a quantitative agreement with the value determined from the kinetic measurements.

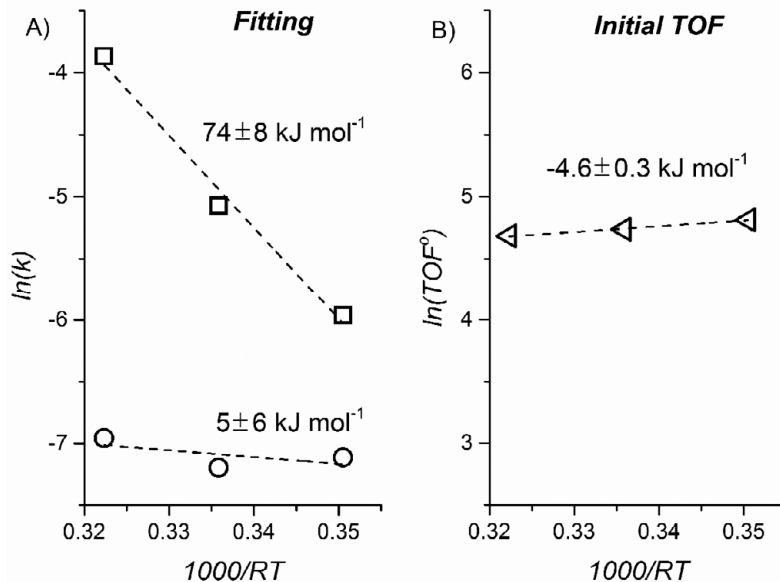


Figure 4.5. Arrhenius plots for A) forward (circles) and reverse (squares) reaction rate constants determined from model fitting and B) experimentally measured initial TOF values

To summarize, the analysis of the kinetics of CO₂ hydrogenation in the presence of Au/Al₂O₃ points to the stable catalytic performance of this heterogeneous catalysts that allows reaching the equilibrium formate yields in a wide range of conditions. The catalytic reaction proceeds with a negligible apparent activation energy and shows a zero reaction order in partial pressures of H₂ and CO₂. The latter may indicate the saturation of the active sites under the reaction conditions. Indeed, if one considers the activity of the gold-support interface,¹⁴ a very low number of the reactive site at the perimeter of Au nanoparticles is expected for the catalyst with only 1%_{wt} loading of the active component. Based on these data and our previous results¹⁹ we can propose the mechanism for CO₂ hydrogenation over Au/Al₂O₃ (Figure 4.6). Somewhat similar to the case of homogeneous catalysis, hydrogenation starts with dissociation of H₂ on Au/support interphase, producing surface hydroxyl and metal hydride species, this step is initiated with desorption of the solvent

molecule to liberate the vacant site for H₂ activation. Subsequent hydride attack on CO₂ molecule results eventually into the metal bound formate group. We propose that the transformations of these species determine the rates of both forward and reverse reaction. The energetics of the reverse reaction ($E_{app}=74 \text{ kJ mol}^{-1}$) is also in agreement with the mechanistic proposal and literature data.^{8,21}

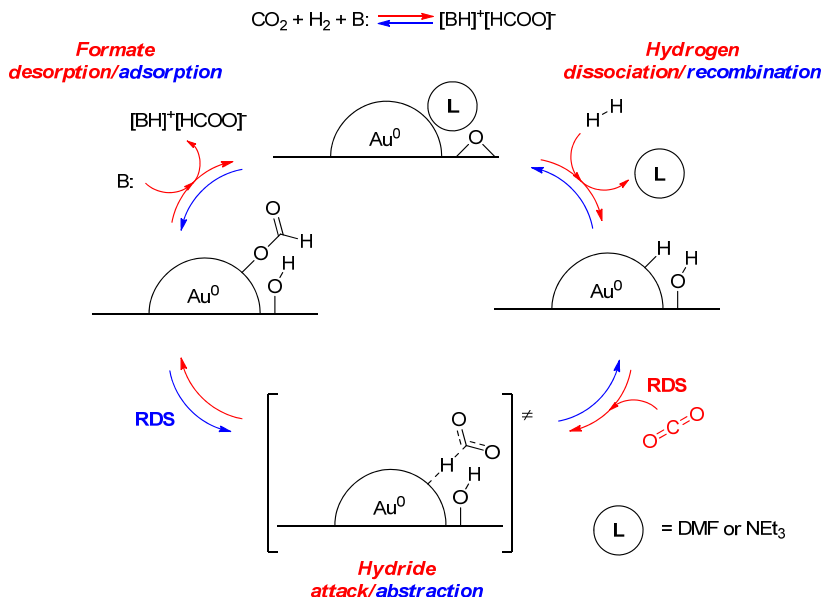
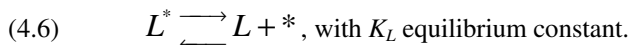
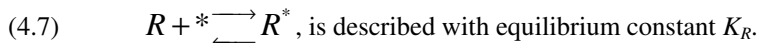


Figure 4.6. Proposed reversible CO₂ hydrogenation mechanism over Au/Al₂O₃ catalyst

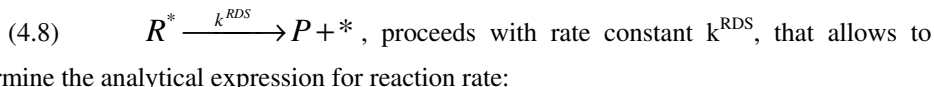
An apparent activation energy of the forward reaction if the reactive sites are saturated with solvent or base molecules, can be derived analytically. Liberation of reactive sites from the adsorbate can be describes as:



Subsequent reagent adsorption, simplified as:



Finally, the product formation step:



$$(4.9) \quad r = k^{RDS} \frac{K_R a_R}{1 + K_R a_R + K_L a_L}, \text{ that at high adsorbate coverage gives:}$$

$$(4.10) \quad r = k^{RDS} \frac{K_R a_R}{K_L a_L}, \text{ which can be used for apparent activation energy}$$

determination as:

$$(4.11) \quad E_{act}^{app} = E_{act}^{RDS} + \Delta H_R - \Delta H_L$$

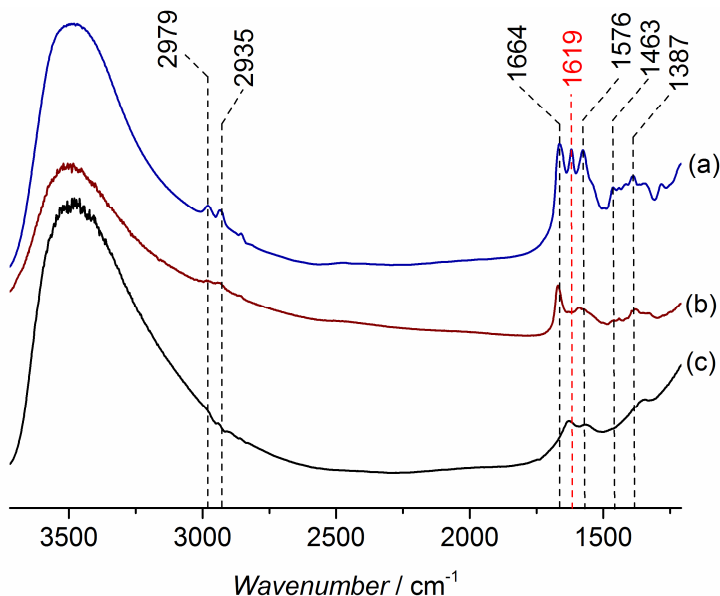


Figure 4.7. FTIR spectra of (a) DMF/NEt₃ spent, (b) DMF/NEt₃ blank and (c) fresh Au/Al₂O₃ after evacuation at 100 °C. New band at $\nu = 1619 \text{ cm}^{-1}$ observed after catalysis. See text for assignments.

This dependence suggests a strong media component binding and even stronger adsorption of reactants which is expected for adsorption of CO₂ on basic alumina support. Due to the assumption that $K_L a_L \gg (1 + K_R a_R)$, we also expect the presence of reaction media components, DMF and NEt₃, on the catalyst surface. To probe the species adsorbed on the catalyst surface were further employed FTIR technique (Figure 4.7). We observed the strong adsorption of reaction components on the catalyst surface that was indicated by a significant difference between spectra of fresh catalyst and the one after contacting the DMF/NEt₃. The majority of observed bands were assigned to DMF, NEt₃, and the γ -Al₂O₃ support: peaks at 2979, 2935 were assigned to C-H vibrations of NEt₃, $\nu = 1664 \text{ cm}^{-1}$ was assigned to DMF C=O, the peaks at $\nu = 1576, 1463$ and 1387 cm^{-1} were generally assigned

to carbonate structures, and the broad peak beyond $\nu = 3000 \text{ cm}^{-1}$ was assigned to surface OH species including adsorbed H_2O .²²⁻²⁴

The unique feature of the spent sample is the presence of absorption band at $\nu = 1619 \text{ cm}^{-1}$ that was assigned to C=O vibration of a formate anion species. This peak definitely originated from the catalytic reaction since solvent, base and carbon dioxide alone or combined cannot lead to the appearance of observed band. These data indicates a build-up of formate species on the catalyst surface, that is in agreement with our earlier proposal on the rate limiting nature of the formate transformation step. The location of adsorbed formate groups cannot be determined unambiguously, thus, we cannot rule out neither Au metal or alumina support. The former is consistent with our proposed mechanism, although the possibility of formate migration to the oxide support have also been observed in the dehydrogenation of FA previously.^{15,22-28}

4.3. Conclusions

Out of eighteen supported and colloid nanoparticle catalyst including the benchmark Au/TiO₂, the best performance in hydrogenation of CO₂ was achieved with Au/Al₂O₃. The support was shown to have a crucial impact on the catalytic performance since unsupported Au nanoparticles exhibited no CO₂ hydrogenation activity. The potential involvement of sub-nanometer cationic Au clusters in catalysis was ruled out by cyanide leaching experiments, where removal of Au⁰ nanoparticles, comprising 99% of gold content, led to the elimination of catalytic activity. This observation, complemented by the XPS data, renders the Au⁰ sites in contact with alumina support the active site for CO₂ hydrogenation.

Au/Al₂O₃ showed stable performance with no signs of catalyst deactivation. In the temperature range of 70 - 100 °C hydrogenation was brought to completion with equilibrium formate concentrations consistent with ones, produced by a homogeneous catalyst from our previous study in a wide temperature range.⁸ A kinetic investigation revealed the independence of reaction rate on the temperature variation that was assigned to internal limitations, namely the product desorption from the catalyst surface. Very low activation energy of 5 kJ mol^{-1} was estimated from kinetic analysis for hydrogenation reaction. Further reaction analysis allowed for estimating the reverse reaction activation barrier. The obtained value of 74 kJ mol^{-1} was in perfect agreement with our experimental data for homogeneous dehydrogenation of FA using Ru-PNP pincer catalyst⁸ and literature data on gold catalyzed dehydrogenation of FA.²¹

4.4. Experimental section and supplementary results

Preparation of dodecanethiol stabilised AuNPs

Performed according to literature procedure.^{29,30} Aqueous $\text{HAuCl}_4 \cdot 3\text{H}_2\text{O}$ (3.0 mL, 0.03 M) was added to an Erlenmeyer flask containing 30 mL toluene and TOAB (1.0 g). The Erlenmeyer flask was filled with an additional toluene (20 mL) and the mixture was stirred vigorously for 30 min. Aqueous NaBH_4 (2.5 mL, 0.4 M) was added dropwise to the Erlenmeyer flask until the mixture turned clear. The addition of an extra drop turned the mixture deep purple/black, at which point the remainder of the NaBH_4 solution was added. Dodecanethiol (200 μL , DDT) was added after 30 min of stirring. After 75 min, and the aqueous phase was removed using a separatory funnel. The mixture was washed twice with water in the separatory funnel and toluene phase was evaporated. Ethanol (100 mL) was added followed by sonication for 10 min. The purple residue was then collected by centrifugation. The dried nanoparticles were again re-dispersed in toluene (25 mL) to give a solution that was 3.6 mM with respect to gold. The nanoparticles were characterised using TEM.

Preparation of triphenylphosphine stabilised AuNPs

Performed according to literature procedure.^{50, 51} Aqueous $\text{HAuCl}_4 \cdot 3\text{H}_2\text{O}$ (50 mL, 0.05 M) was prepared in a round-bottomed flask, to which toluene (40 mL) containing TOAB (1.6 g) was added. A double layer formed with the top (organic) layer turning a deep orange while the aqueous layer became a slightly deeper yellow. Additional toluene (25 mL) was added and the mixture was stirred vigorously for 10 min and allowed to settle to separate the aqueous and organic layers. Triphenylphosphine (2.3 g) was added and the mixture was stirred for an additional 10 min, during which the organic layer turned white. Aqueous NaBH_4 (10 mL, 0.4 M) was added to a stirred emulsion. The mixture was stirred for 3 h, and transferred to a separatory funnel. The aqueous layer was discarded, and a total of 200 mL H_2O was used to wash the organic layer. The organic phase was then freeze dried. Solid was then suspended in hexane (100 mL) and filtered. The solid was further washed with hexane, a methanol/water (2:3) mixture, and the concentrated NaNO_2 solution (400 mL, 6.25 M). The solid nanoparticles were dissolved in 10 mL CHCl_3 and vacuum filtered. The solution was transferred to a beaker and pentane (50 mL) was added slowly. Two layers formed: a clear upper layer containing the CHCl_3 , and a dark purple bottom layer containing the AuNPs suspended in the pentane. The mixture was filtered using a Buchner filter and dried in air. The collected AuNPs were characterised using TEM.

Preparation of triphenylphosphine stabilised AuNPs with the moderate strength reducing agent 9-borabicyclo[3.3.1]nonane (9-BBN)

Performed according to literature procedure.³¹ The gold precursor $(\text{PEt}_3)\text{AuCl}$ (0.0359 g) was added to 20 mL acetonitrile in a round-bottom flask. Toluene (80 mL) was then added under stirring. Triphenylphosphine (0.1707 g) was added and the mixture was stirred for 1.5 h. The 9-BBN (0.8 mL) was added to the reaction mixture and stirring continued for 45 min during which the clear mixture

turned a pale yellow and then pale purple. The mixture was centrifuged (4200 rpm) for 15 min. The supernatant was discarded and replaced with hexane to wash the nanoparticles (repeated three times). The brittle nanoparticles were dried in the centrifuge tubes using a light argon flow and stored in a clear vial under ambient conditions. The nanoparticles were characterised using TEM.

CO₂ hydrogenation procedures

Commercial AUROLite Au/Al₂O₃ (1 wt.% Au) was used unless stated otherwise. The Au/Al₂O₃ was stored in an argon glovebox upon delivery. Remaining catalysts were prepared according to published procedures.³²⁻³⁶ In a typical hydrogenation experiment, Au/Al₂O₃ (60 mg) was weighed out in a glovebox and transferred to a 10 mL stainless steel autoclave in air. The autoclave was loaded with 0.5 mL base (e.g. NEt₃ or DBU), 3.0 mL solvent (e.g. EtOH, DMF, or THF). The autoclave was closed and flushed three times with 20 bar H₂ and filled with 40.0 bar H₂/CO₂ mixture. Reactions were performed at 70 °C for 20 h. Formic acid concentrations were determined by HPLC.

Kinetic studies were performed in 100 mL Top Industrie autoclave. Typical loadings: 30 mL DMF, 5 mL NEt₃, 1mL THF and ca. 600 mg Au/Al₂O₃. The autoclave was flushed three times with 20 bar H₂ at room temperature, then loaded with approx. 7-8 bar H₂ and heated to 70 °C. The vessel was then depressurised and immediately filled with 40 bar of a 1:1 H₂/CO₂ gas mixture using a digital flow controller. The introduction of the mixed gas marked the start of the experiment. Aliquots of the reaction mixture were obtained using a manual sampler and the concentration was determined using a combination of HPLC and GC. Multiple samples were collected within the first hour of reaction, followed by less frequent sampling at later stages.

Supplementary kinetic data

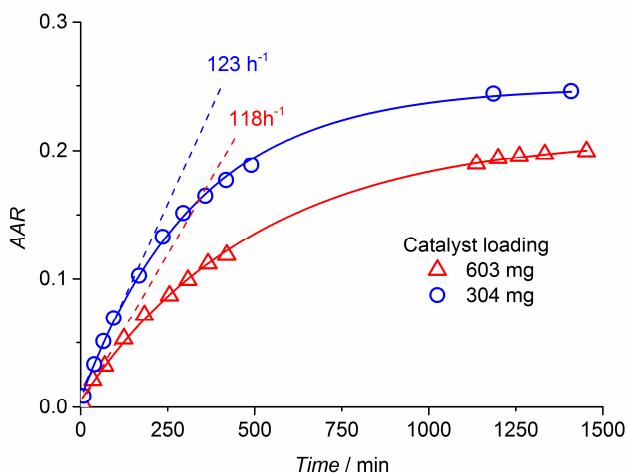


Figure 4.8. Catalyst-loading variation data using Au/Al₂O₃. Conditions are given in Table 4.4.

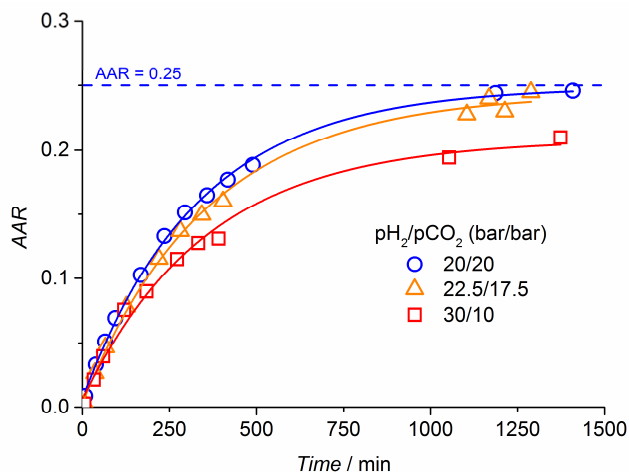


Figure 4.9. Partial pressure variation data for Au/Al₂O₃ catalysed CO₂ hydrogenation; Conditions are given in Table 4.4.

Analysis of the temperature dependent kinetics: model fitting parameters

$$AAR(t) = X - Ye^{Zt}$$

An exponential function was used to fit the kinetic data. Model parameters are listed below:

Table 4.5. Exponential fit parameters for temperature dependent kinetic experiments

T, °C	X	RSD X, %	Y	RSD Y, %	Z	RSD Z, %
70	0.24047	2.2	0.23794	2.2	-0.00338	3.8
85	0.10676	1.7	0.1058	3.0	-0.00702	7.5
100	0.04361	2.3	0.4448	4.7	-0.02184	10.6

Catalyst pretreatment³⁷

Au/Al₂O₃ (300 mg) was pretreated by either reduction or oxidation in 10% H₂ (5 mL/min H₂ in 45 mL/min He) or 10% O₂ (10 mL/min O₂ in 90 mL/min He) respectively. Pretreatments were carried out at 200 °C, 300 °C, 400 °C, and 500 °C ($T_{ramp} = 5$ °C/min, $t_{dwell} = 3$ h) to give a total of 8 pretreated samples. Reduced samples were collected and stored in a glovebox, whereas oxidised samples were stored under ambient conditions. Catalysts were characterised using TEM and XPS.

Cyanide leaching of Au/Al₂O₃ (AUROLite)

The procedure for Au extraction through cyanidation was adapted from literature.³⁸ In a fume hood, crushed Au/Al₂O₃ (0.4470 g) and aqueous NaOH (10 mL, pH 12) was added to a two-neck round-bottom flask with stirrer. 10 mg NaCN was introduced. The catalyst colour changed from purple to white, and the mixture was stirred for two hours. The cyanide treated catalyst, Au/Al₂O₃-

CN, was suction filtered and washed with 400 mL distilled water, dried overnight at 110 °C, and oxidised at 300 °C. The catalyst was characterized using XPS and ICP-OES.

Characterization methods

TEM images were taken of the unsupported gold catalysts. If necessary, the AuNPs were crushed into a fine powder and suspended in a small quantity of ethanol by sonication. TEM images were acquired using a FEI Tecnai 20 (type Sphera) TEM operating with a 200 kV. HAADF-STEM images were acquired on a CryoTitan (300 kV) at room temperature. The Au/Al₂O₃ samples were crushed and suspended in ethanol, sonicated and dispersed over a Cu grid with a holey carbon film. Images were acquired with a Fishione HAADF detector using a probe convergence angle of 10 mrad, a dwell time of 32 μs and a camera length of 89 mm. For particle size measurements images at a nominal magnification of 320 kx, corresponding to a pixel size of 0.17 nm, were used, which allows reliable detection of particles as small as ~ 0.8 nm. The mean diameters, standard deviations, and particle size distributions were determined using digital images analysed within the software package ImageJ.

For *XPS analysis* spent samples were oven dried at 60 °C under vacuum. Samples were crushed into a fine powder and analyzed using a K-Alpha XPS apparatus (Thermo Scientific). Spectra were obtained using the aluminium anode (Al-K_α = 1486.68 eV), with 50 scans in the Au 4f region. All spectra were calibrated using adventitious carbon at C 1s = 284.8 eV and fitted using a Shirley background, with the Au 4f peaks having a fixed deconvolution of 3.7 eV.

Temperature Programmed Reduction

Prior to TPR, Au/Al₂O₃ was either dried (95.2 mg Au/Al₂O₃, 110 °C in He, 4 h) or oxidised (84 mg Au/Al₂O₃, 300 °C in 10% O₂, 1 h). TPR was subsequently performed on the catalyst against a Cu reference (2.4 mg, 26.2 wt.% Cu) by linearly heating the catalyst to 800 °C in 10% H₂. Gas consumption was monitored using a TCD detector.

Thermogravimetric Analysis

Measurements were performed on a Mettler TGA/DSC-1 apparatus using alumina crucibles, dry air as purge gas (20 mL/min) and N₂ as protective gas (40 mL/min). Each run used approx. 20 mg Au/Al₂O₃, with $T_{ramp} = 10$ °C/min and $T_{max} = 750$ °C.

Fourier Transformed Infrared Spectroscopy

Infrared spectra were recorded using a Bruker Vertex V70v FTIR spectrometer. A mixture of Au/Al₂O₃: KBr (1:3) by mass was crushed into a fine powder using 13 mg Au/Al₂O₃ and 39 mg KBr. The resulting powder was homogenized and pressed into a pellet using 3,000 kg force. The pellet was transferred to the FTIR and an initial measurement was taken. The FTIR chamber was slowly evacuated to 10⁻⁶ mbar, and subsequently heated to 70 °C and 100 °C ($T_{ramp} = 5$ °C/min, $t_{dwell} = 15$ min). Spectra were recorded after each dwell period and upon return to room temperature. We only report the spectra obtained at 100 °C. Analysis using FTIR was applied to fresh and spent (EtOH/NET₃, and DMF/NET₃ solvent-base systems respectively) Au/Al₂O₃.

Inductively Coupled Plasma Optical Emission Spectroscopy

Each catalyst was crushed into a fine powder and two weighed (15-25 mg). Each sample was transferred to a 50 mL beaker. Aqua regia (5.00 mL) was added to the beaker, and the mixture was vigorously stirred under a medium heat (~60 °C) with a watch glass cover. The Au/Al₂O₃ turned white and brown fumes were produced. Once the aqua regia became a pale yellow and the brown fumes disappeared (30-60 min), the beaker was taken off the heat and cooled to room temperature. The watch glass and beaker walls were rinsed with DI-H₂O, and 0.5 mL concentrated H₂SO₄ solution (98 wt.% H₂SO₄) was added to the beaker and the mixture was heated (70-80 °C) under stirring until all the crushed powder was dissolved. The mixture was cooled to room temperature, and diluted to 50 mL in a volumetric flask using DI-H₂O. Measurements were performed at $\lambda_{max} = 242.795$ nm and $\lambda_{max} = 267.595$ nm using a SPECTRO BLUE ICP-OES apparatus.

TEM characterization data for Au-NPs

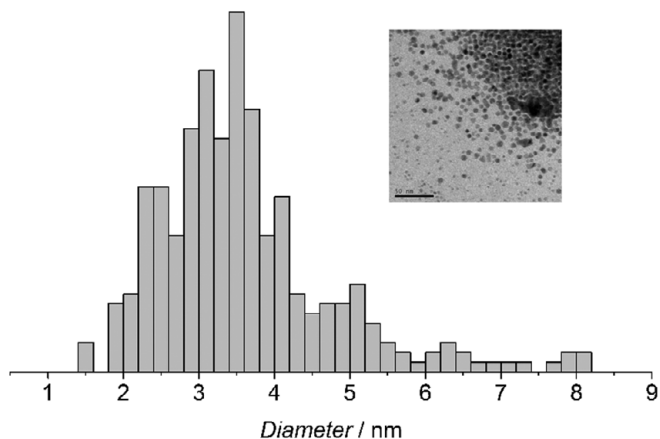


Figure 4.10. TEM and particle size distribution data for NaBH₄ reduced AuNP-DDT

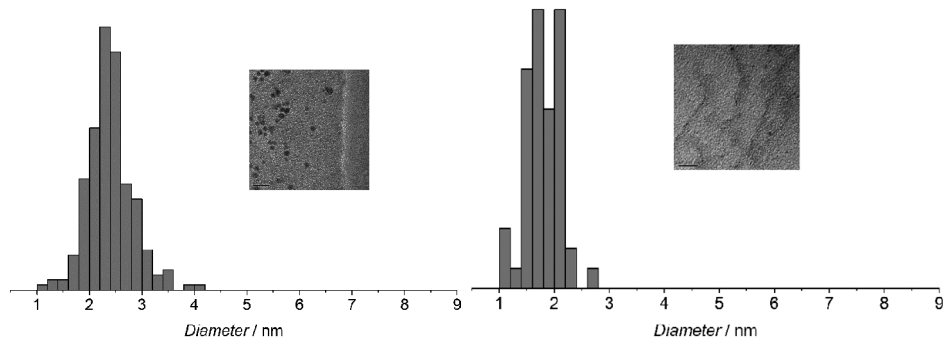


Figure 4.11. TEM and particle size distribution data for NaBH₄(left) and 9-BBN (right) reduced AuNP-TPP

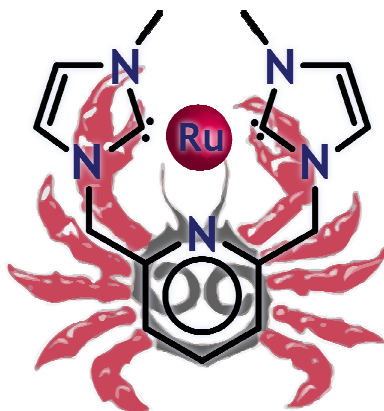
4.5. References

- (1) Behr, A.; Neubert, P. In *Applied Homogeneous Catalysis* **2012**, 189
- (2) Bredig, G.; Carter, S. R. *Berichte*, **1914**, *47*, 541.
- (3) Preti, D.; Resta, C.; Squarzialupi, S.; Fachinetti, G. *Angew. Chem. Int. Ed.* **2011**, *50*, 12551.
- (4) Ojeda, M.; Iglesia, E. *Angew. Chem. Int. Ed.* **2009**, *48*, 4800.
- (5) Brown, M. A.; Ringleb, F.; Fujimori, Y.; Sterrer, M.; Freund, H.-J.; Preda, G.; Pacchioni, G. *J. Phys. Chem. C* **2011**, *115*, 10114.
- (6) Wischert, R.; Copéret, C.; Delbecq, F.; Sautet, P. *Angew. Chem. Int. Ed.* **2011**, *50*, 3202.
- (7) Wischert, R.; Laurent, P.; Copéret, C.; Delbecq, F.; Sautet, P. *J. Am. Chem. Soc.* **2012**, *134*, 14430.
- (8) Filonenko, G. A.; van Putten, R.; Schulpen, E. N.; Hensen, E. J. M.; Pidko, E. A. *ChemCatChem* **2014**, *6*, 1526.
- (9) Filonenko, G. A.; Conley, M. P.; Copéret, C.; Lutz, M.; Hensen, E. J. M.; Pidko, E. A. *ACS Catal.* **2013**, *3*, 2522.
- (10) Jessop, P. G.; Ikariya, T.; Noyori, R. *Chem. Rev.* **1995**, *95*, 259.
- (11) Jessop, P. G.; Hsiao, Y.; Ikariya, T.; Noyori, R. *J. Am. Chem. Soc.* **1996**, *118*, 344.
- (12) Panayotov, D. A.; Burrows, S. P.; Yates, J. T.; Morris, J. R. *J. Phys. Chem. C* **2011**, *115*, 22400.
- (13) Bus, E.; Miller, J. T.; van Bokhoven, J. A. *J. Phys. Chem. B* **2005**, *109*, 14581.
- (14) Fujitani, T.; Nakamura, I.; Akita, T.; Okumura, M.; Haruta, M. *Angew. Chem. Int. Ed.* **2009**, *48*, 9515.
- (15) Gazsi, A.; Ugrai, I.; Solymosi, F. *Appl. Catal. A: Gen.* **2011**, *391*, 360.
- (16) Bi, Q.-Y.; Du, X.-L.; Liu, Y.-M.; Cao, Y.; He, H.-Y.; Fan, K.-N. *J. Am. Chem. Soc.* **2012**, *134*, 8926.
- (17) Ojeda, M.; Iglesia, E. *Angew. Chem. Int. Ed.* **2009**, *48*, 4800.
- (18) Schimpf, S.; Lucas, M.; Mohr, C.; Rodemerck, U.; Brückner, A.; Radnik, J.; Hofmeister, H.; Claus, P. *Catal. Today* **2002**, *72*, 63.
- (19) Filonenko, G. A.; Hensen, E. J. M.; Pidko, E. A. *Catal. Sci. Technol.* **2014**, *4*, 3474.
- (20) Boddien, A.; Federsel, C.; Sponholz, P.; Mellmann, D.; Jackstell, R.; Junge, H.; Laurenczy, G.; Beller, M. *Energy Environ. Sci.* **2012**, *5*, 8907.
- (21) Singh, S.; Li, S.; Carrasquillo-Flores, R.; Alba-Rubio, A. C.; Dumesic, J. A.; Mavrikakis, M. *AIChE* **2014**, *60*, 1303.
- (22) Venkov, T.; Klimev, H.; Centeno, M. A.; Odriozola, J. A.; Hadjiivanov, K. *Chem. Commun.* **2006**, *7*, 308.
- (23) Busca, G.; Lorenzelli, V. *Mater. Chem.* **1982**, *7*, 89.
- (24) Huang, A.; Cao, L.; Chen, J.; Spiess, F.-J.; Suib, S. L.; Obee, T. N.; Hay, S. O.; Freihaut, J. D. *J. Catal.* **1999**, *188*, 40.
- (25) Rege, S. U.; Yang, R. T. *Chem. Eng. Sci.* **2001**, *56*, 3781.
- (26) Raphulu, M. C.; McPherson, J.; Lingen, E.; Anderson, J. A.; Scurrrell, M. S. *Gold Bull.* **2010**, *43*, 21.
- (27) Denkwitz, Y.; Karpenko, A.; Plzak, V.; Leppelt, R.; Schumacher, B.; Behm, R. J. *J. Catal.* **2007**, *246*, 74.
- (28) Rethwisch, D. G.; Dumesic, J. A. *Appl. Catal.* **1986**, *21*, 97.
- (29) Ha, J.-M.; Solovyov, A.; Katz, A. *Langmuir* **2009**, *25*, 10548.
- (30) Saunders, A. E.; Sigman, M. B.; Korgel, B. A. *J. Phys. Chem. B* **2004**, *108*, 193.
- (31) Shem, P. M.; Sardar, R.; Shumaker-Parry, J. S. *Langmuir* **2009**, *25*, 13279.
- (32) Liu, P.; Degirmenci, V.; Hensen, E. J. M. *J. Catal.* **2014**, *313*, 80.
- (33) Ciftci, A.; Ligthart, D. A. J. M.; Pastorino, P.; Hensen, E. J. M. *Appl. Catal. B: Environmental* **2013**, *130–131*, 325.
- (34) Liu, P.; Hensen, E. J. M. *J. Am. Chem. Soc.* **2013**, *135*, 14032.
- (35) Liu, P.; Li, C.; Hensen, E. J. M. *Chem. Eur. J.* **2012**, *18*, 12122.
- (36) Liu, P.; Guan, Y.; Santen, R. A. v.; Li, C.; Hensen, E. J. M. *Chem. Commun.* **2011**, *47*, 11540.

- (37) Chen, J.; Halin, S. J. A.; Pidko, E. A.; Verhoeven, M. W. G. M.; Ferrandez, D. M. P.; Hensen, E. J. M.; Schouten, J. C.; Nijhuis, T. A. *ChemCatChem* **2013**, *5*, 467.
- (38) Guan, Y.; Hensen, E. J. M. *Phys. Chem. Chem. Phys.* **2009**, *11*, 9578.

Synthesis and reactivity of lutidine-based bis-NHC ruthenium pincer complexes.

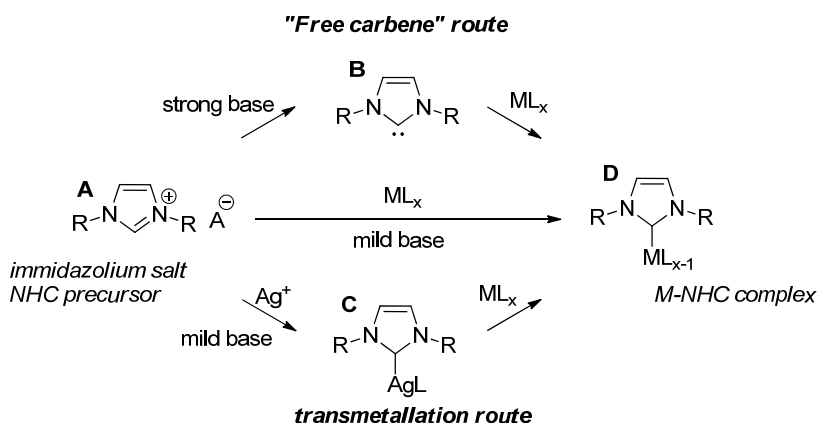
ABSTRACT: A remarkable versatility of the ligand coordination mode was discovered for a new family of ruthenium lutidine-based bis-N-heterocyclic carbene (NHC) pincer complexes. The metallation of the bis-imidazolium salts ligand precursors with $\text{RuHCl}(\text{CO})(\text{PPh}_3)_3$ can be achieved in the presence of a sterically hindered phosphazene base. A “normal” bis-NHC complex **1** is formed by the metallation of ligand **L**₁ (3,3'-[pyridine-2,6-diyl]bis(methylene)]bis(1-mesityl-1H-imidazol-3-ium) bromide) in THF. Increasing the steric demand of the substituents at the NHC groups leads to complex **3**, where both normal and abnormal NHC binding modes are realized. Aromatic and aliphatic nitriles can be cooperatively activated by Ru-CNC in situ during the complexation or post-synthetically. The resulting complexes **4-6** contain ketimino group bound to both metal and ligand via Ru-N and C-C bonds respectively. The pincer ligand in Ru-CNCs shows pronounced non-innocence in reactions with strong bases (**7**) and heterolytic cleavage of H_2 resulting in a bis-hydrido complex (**8**), which transforms to a formate complex (**9**) by a reaction with CO_2 . The dearomatized Ru-CNC complex (**7**) reacts with CO_2 to yield very stable [4+2]- CO_2 addition products (**10**) and (**10a**). In contrast to the analogous reaction with Ru-PNP, the CO_2 addition to Ru-CNC is irreversible.



Parts of this Chapter are published in: *ACS Catal.* **2014**, *4*, 2667 and
ACS Catal., **2015**, *5*, 1145

5.1 Introduction

The pincer ligand platform has proven its versatility in a wide range of catalytic transformations.¹ Particularly challenging polar bond hydrogenation reactions can be efficiently carried out using transition metal pincer complexes. Ruthenium lutidine-based PNX-type (X=P, N, S) pincers stand out among other representatives of this class due to their high catalytic activity in acceptorless dehydrogenation², hydrogenation of esters, amination of alcohols, hydrogen exchange reactions³⁻⁶ and CO₂ hydrogenation.⁷⁻⁹ Despite their broad utility, phosphine ligands have several disadvantages. Their preparation often requires highly sensitive organometallic reagents, and accordingly, the use of inert atmosphere is imperative. In addition, the availability of phosphorus is limited due to the intensive depletion of natural resources of phosphorus. Another class of strong donor ligands - N-heterocyclic carbenes (NHCs) – relies on abundant C, H, N elements and requires minor synthetic effort to generate. Therefore, it has attracted considerable attention of catalysis researchers.

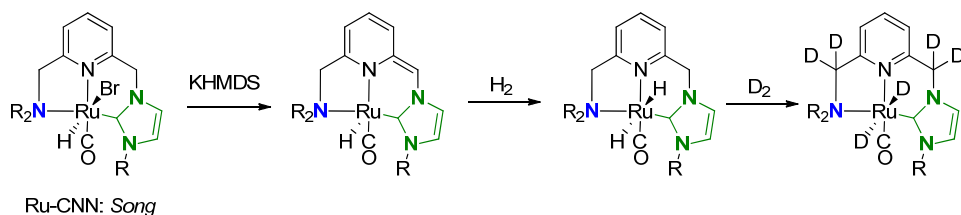


Scheme 5.1. Synthetic routes towards M-NHC complexes

NHCs are neutral ligands that contain a divalent carbon atom with a six electron valence shell.¹⁰ By definition, NHCs contain one carbene atom and at least one nitrogen atom in the cyclic molecule. In this work, the main focus will be on the utilization of imidazolylidenes (**B**, Scheme 5.1), that are the most common NHCs based on the imidazole cycle. Imidazolylidenes are usually prepared by deprotonation of the corresponding imidazolium salts (**A**, Scheme 5.1) with a strong base (e.g. BuLi, KO^tBu or KHMDS). The resulting free NHC can further react with a metal precursor to form a desired NHC complex **D** (Scheme 5.1). In some cases free carbenes can be extremely reactive and therefore, one

can employ different techniques to carry out the complexation without isolating the free NHC itself. One of the most widely used techniques involves the generation of an intermediate silver NHC complex, **C** (Scheme 5.1) that can transfer the carbene moiety to the target metal. An alternative strategy is to carry out the direct NHC complexation via the reaction of azolium salt **A** with a mild base in the presence of a metal precursor. This technique will be successfully applied throughout this Chapter.

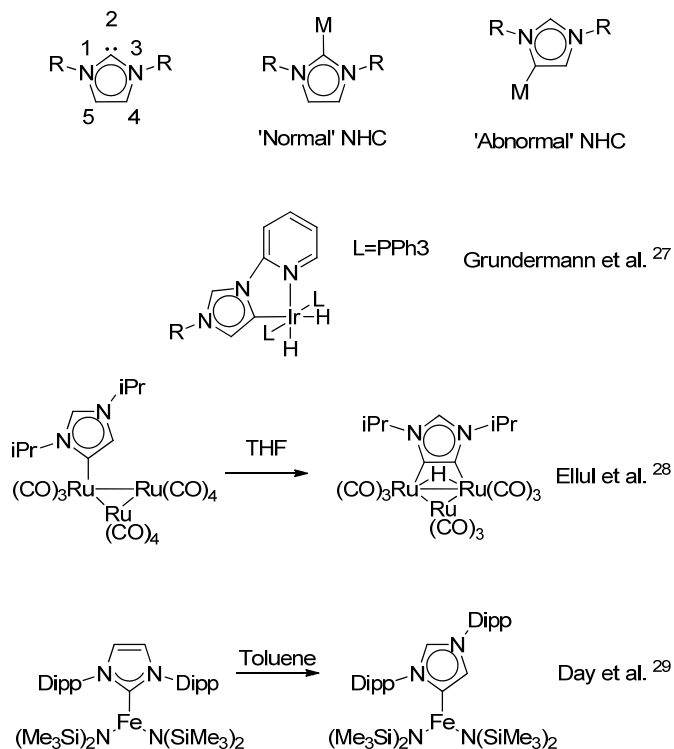
The azolium salts (**A**) are easy to handle and prepare. These compounds are air stable and their synthesis is simple and straightforward. Catalysts based on NHC ligands often outperform their phosphine based counterparts.¹¹⁻¹⁶ The precedents of the higher performance of the NHCs as compared to phosphines can be found in metathesis reaction,¹³ selective asymmetric hydrogenation,¹⁷ transfer hydrogenation¹⁵ and alkylation.¹⁶ Because of the high stability of the metal-carbon bond, NHC complexes can be successfully utilized for catalysis in aqueous medium.¹² In the context of pincer chemistry discussed in the previous chapters, the replacement of phosphine donors in Ru-PNN with NHC ligands yields Ru-CNN catalysts (Scheme 5.2) that match or outperform their phosphine-based counterparts in ester hydrogenation.¹⁸⁻²¹ Interestingly, incorporation of the NHC donor in the pincer framework preserves the cooperative properties of the ligand. For example Ru-CNN pincers reported by Song and co-workers¹⁸ show chemical reactivity towards ligand dearomatization and heterolytic H₂ activation (Scheme 5.2) that is also common for phosphine-based pincers.²² Although many ruthenium bis-NHC pincers have been reported,²³⁻²⁶ only two examples contain cooperative CNC ligands.^{21,27} Therefore, no comparison to existing PNP analogues was offered so far.



Scheme 5.2. Non-innocence of the CNN pincer ligand in Ru-CNN catalyst

The use of NHC donor groups in pincer ligands introduces an additional level of complexity in the system under study. Despite a great number of synthetic methodologies has been developed to date, the coordination of the NHC group requires a specific approach that depends on the structure and properties of a particular ligand.²⁸ Furthermore, the coordination mode of NHC is not uniquely defined. Different coordination modes of such

moieties to a transition metal can potentially occur. For example, besides the conventional NHC coordination via the C2 carbon, these moieties can bind to the transition metal via the C5 carbon of the imidazolium ring yielding the so-called “abnormal” (AN) NHCs (Scheme 5.3). Such AN-NHCs attracted significant attention since the first isolation of an Ir-AN-NHC complex by Grundermann et al. (Scheme 5.3).²⁹ In recent years, a number of studies on the unusual binding behavior of NHC ligands were reported. Ellul et al.³⁰ demonstrated the possibility of activation of both C4 and C5 positions in a binuclear AN ruthenium carbene complex. A very recent study by Day et al.³¹ reported the possibility of “normal”-to-“abnormal” rearrangements in three-coordinated Fe complexes (Scheme 5.3).



Scheme 5.3. Types of NHC binding modes and examples of related complexes

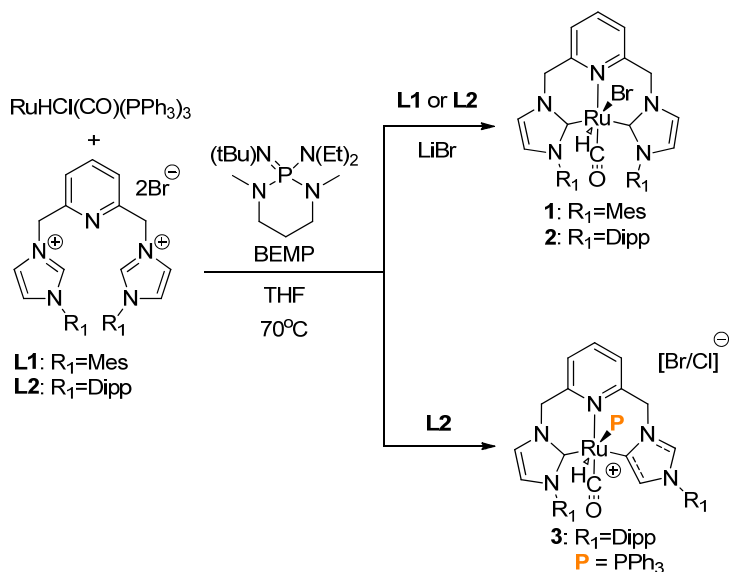
Inspired by the excellent catalytic performance of Ru-PNP pincers, we targeted our synthetic effort at the preparation of related ruthenium CNC pincers. This Chapter deals particularly with synthesis and reactivity of Ru-CNC complexes and investigation of metal-ligand cooperative behavior of these systems

5.2 Synthesis of CNC pincers: normal vs. abnormal NHC binding

The preparation of pincer complex **1** was the first challenge in our synthetic investigation (Scheme 5.4). The coordination of bis-imidazolium salts **L1** and **L2** to ruthenium precursor RuHCl(CO)(PPh₃)₃ could not be achieved when common synthetic strategies were applied. Transmetallation from silver-NHC complex (route A → C → D, Scheme 5.1) was inefficient, despite this approach was earlier employed for the synthesis of related Ru bis-NHC pincers.²¹ While the formation of silver NHCs from **L1** and **L2** was observed, the transfer of the NHC moiety to Ru did not take place. Instead, we observed the scavenging of the triphenylphosphine ligands from the metal precursor by Ag, resulting in a mixture of decomposition products. The use of strong bases such as KHMDS or KO^tBu during the complexation was also investigated. Deprotonation of **L1** with KO^tBu and the subsequent reaction with RuHCl(CO)(PPh₃)₃ resulted in a mixture of products containing only trace amounts of **1** detectible by mass spectrometry but not observed by NMR spectroscopy. Compounds **L1-2** proved to be not suitable for the isolation of the respective free carbenes, despite several reports demonstrate the utility of this approach for clean coordination of related bis-NHC ligands that do not contain flexible methylene pincer arms.³² The attempted synthesis of free carbenes from **L1** and **L2** was not successful and resulted in a mixture of insoluble products.

A successful synthetic procedure towards Ru-CNC pincer complex **1** involved the reaction of bis-imidazolium ligand **L1** containing mesityl (*Mes*) substituents, the base 2-tert-butylimino-2-diethylamino-1,3-dimethylperhydro-1,3,2-diazaphosphorine (BEMP) and RuHCl(CO)(PPh₃)₃ in THF (Scheme 5.4). Initially **1** was obtained as a bromide/chloride mixture as indicated by ¹H NMR and X-ray diffraction (Figure 5.1.). Following the procedure developed by Sun et al.,¹⁸ the pure bromide **1** was isolated when the reaction was conducted in the presence of LiBr. Complex **1** is stable to ambient atmosphere in the solid state and tolerates exposure to liquid water. In CD₂Cl₂ the NHC backbone protons of **1** appear in ¹H NMR spectrum as two doublets at δ = 7.17 and 6.66 ppm (³J_{HH} = 2 Hz) and the pyridine protons appear as a triplet and doublet (δ = 7.82 ppm and 7.46 ppm, ³J_{HH} = 8 Hz). Upon ligand coordination the *ortho*-CH₃ groups and aromatic protons of the mesityl substituents are no longer equivalent and appear as separate singlets. The Ru-H signal is shifted significantly upfield to δ = -15.6 ppm that is typical for hydride ligands in *trans* position to a weak-field halide ligand.¹⁸ Methylene protons in **1** appear as a broad signal at δ = 5.1 ppm.³³ The carbonyl ligand is characterized with a strong IR absorption band at

1946 cm^{-1} . The typical Ru-NHC carbon resonance is observed as a broad singlet at $\delta = 194$ ppm in the ^{13}C NMR spectrum.



Scheme 5.4. Complexation of Ru with bis-NHC ligands in THF.

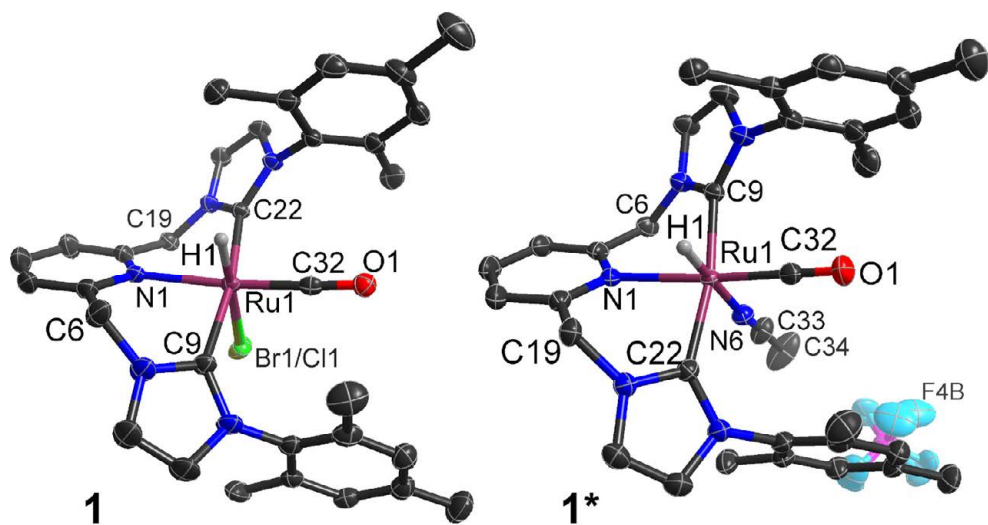
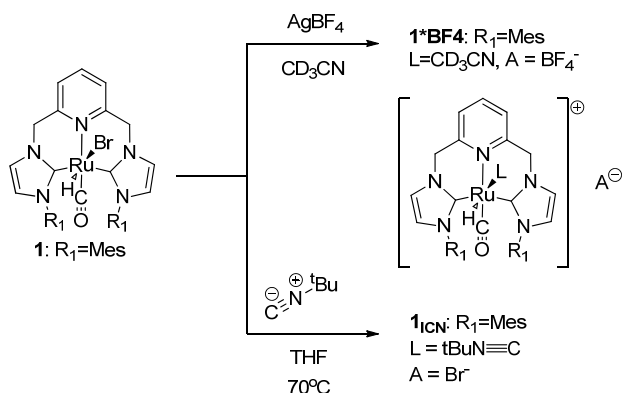


Figure 5.1. X-ray crystal structure of **1**(left) and **1*BF₄**(right) (ellipsoids at the 50% probability level, all hydrogens, except hydride and methylene protons are omitted for clarity). Selected bond lengths [Å]: (**1**) Ru1-C9 2.089, Ru1-C22 2.075, Ru1-Br1 2.689, Ru1-C32 1.808; (**1*BF₄**) Ru1-C9 2.069, Ru1-C22 2.082, Ru1-C32 1.821.

The X-ray crystal structure analysis (Figure 5.1, left) shows the normal coordination of both NHC fragments in **1** with the respective Ru-C distances similar to those in related CNC pincer complexes.¹⁸⁻²⁰ The molecular structure shows the asymmetric ligand coordination, in which the pyridine ring is twisted ca. 59° out of the equatorial plane of the octahedron. NHC groups are located in trans position with respect to the pyridine ring plane. Complex **1** is dynamic in solution resulting in the apparent equivalency of the two NHC sidearms of the ligand observed in ¹H NMR. Similar to the observation made by Heinekey and co-workers for related Ir pincers,³³ complex **1** exists as two atropisomers. Their interconversion via the frustrated rotation around the Ru-NHC bonds is responsible for the dynamics observed on the NMR timescale.



Scheme 5.5. Reactivity of pincer complex **1**.

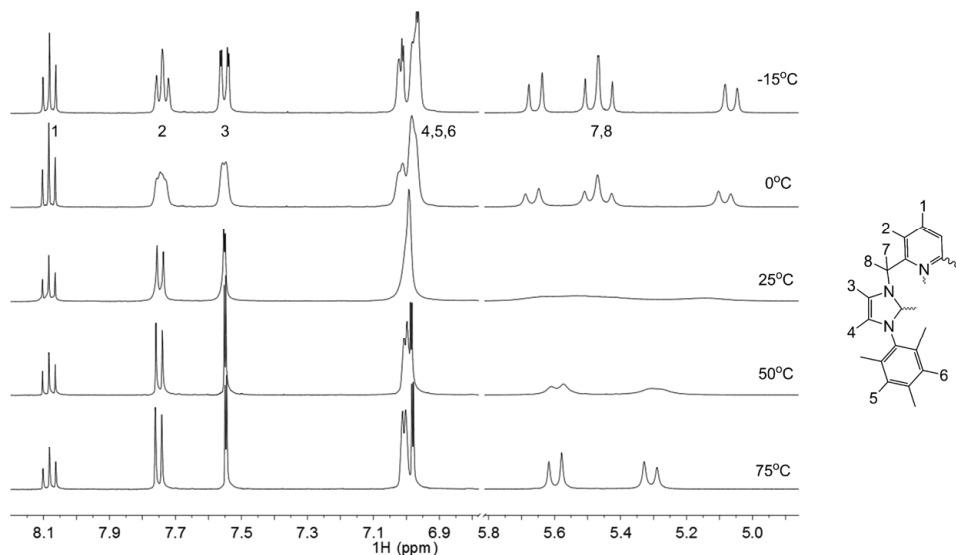


Figure 5.2. Section of VT-NMR of **1*BF₄** in CD_3CN . An insert shows the signal assignments.

Halide ligand in **1** is labile and can be replaced by stronger ligands, e.g. acetonitrile. The ^1H NMR spectrum of **1** in CD_3CN shows a significant downfield shift of the hydride ligand to $\delta = -14.4$ ppm, indicating the replacement of the bromide anion with CD_3CN . The halide abstraction with AgBF_4 results in complex **1*** BF_4 (Scheme 5.5). Single crystal X-ray diffraction data evidence nearly identical geometries of **1** and **1*** BF_4 (Figure 5.1). This complex is a good example for studying the dynamics of *mer*-coordinated **L1**. Variable temperature (VT) NMR (Figure 5.2) reveals that chemical exchange in **1*** BF_4 is more facile than for **1** as is evidenced by the higher coalescence temperature. At temperatures above 25 °C an averaged ^1H NMR spectrum for the two atropisomers of **1*** BF_4 with apparent symmetry of the CNC ligand is observed. The resonance of imidazolium backbone protons that appeared as doublet at room temperature split in two doublets at -15°C . Methylene protons appear as two sets of doublets. The pattern, observed at low temperatures is in agreement with the molecular structure data evidencing non-equivalency of the ligand sidearms.

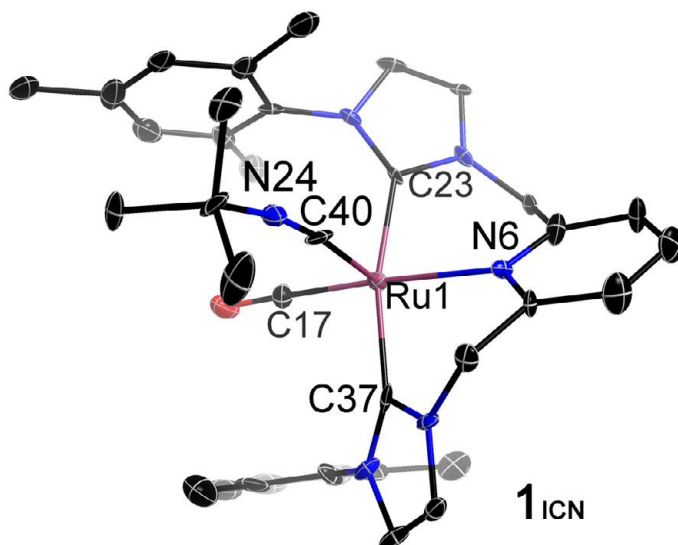


Figure 5.3. X-ray crystal structure of **1**_{ICN} (ellipsoids at the 50% probability level, all hydrogens, except hydride and methylene protons are omitted for clarity). Selected bond lengths [\AA]: Ru1-C23 2.078, Ru1-C37 2.067, Ru1-C40 2.073, Ru1-C17 1.830, Ru1-N6 2.210; C40-N24 1.182

The high lability of the halide ligand in **1** also allows this complex to readily react with isocyanides. The reaction with ^tBu -isocyanide in THF leads to a quantitative formation of **1**_{ICN} (Scheme 5.5) that exhibits a dynamic behavior in solution similar to other complexes

with **L1**. Because **1**_{ICN} shows a more pronounced dynamic behavior, its ¹H NMR characterization was performed at -60°C. The hydride ligand in **1**_{ICN} is characterized by a signal at δ = -7.5 ppm in agreement with the presence of a strong isocyanide ligand *trans* to hydride. Pyridine protons appear as two doublets at δ = 8.1 and 7.89 ppm (*J*_{HH}=7.5Hz) and a triplet at δ = 7.89 ppm. Methylene protons lose apparent equivalency at a low temperature and appear now as four doublets. Molecular structure of **1**_{ICN} shows the pincer ligand arrangement at ruthenium octahedron similar to that in **1** and **1***BF₄ (Figure 5.3).

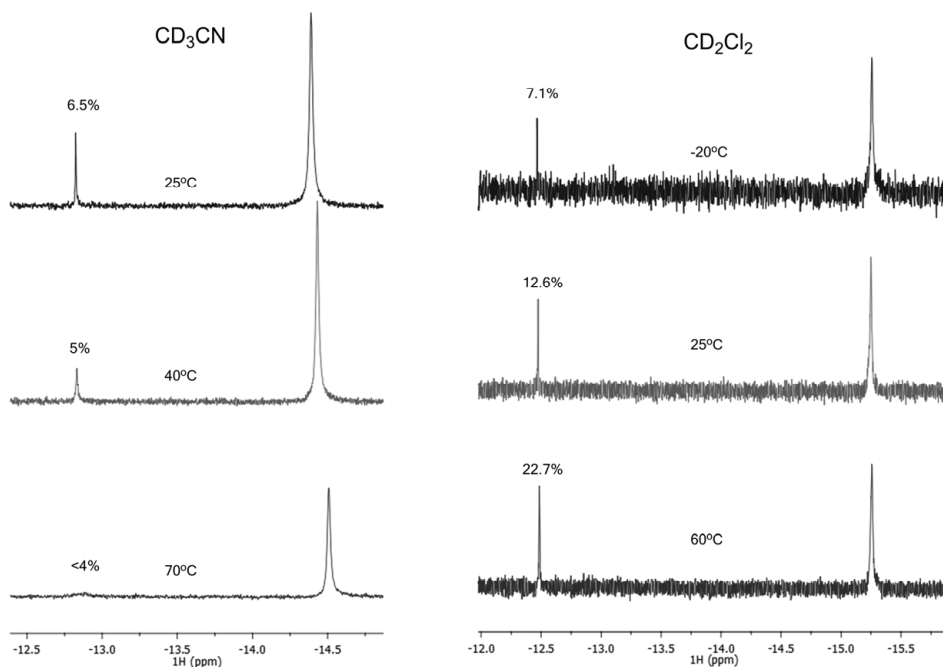


Figure 5.4. Hydride region in ¹H VT-NMR spectra of **2** in CD₂Cl₂ and CD₃CN

The outcome of complexation of the CNC ligand with Ru depends strongly on the bulkiness of the substituents at the NHC donors. The reaction of **L2** containing 2,6-diisopropylphenyl (*dipp*) substituents with RuHClCO(PPh₃)₃ in the presence of LiBr resulted in complex **2** containing NHC groups bound via C2 carbon (Scheme 5.4). This mode is commonly referred to as a “normal” NHC binding. Exchange of the bromide for a trifluoromethylsulfonate anion by treatment of **2** with AgOTf resulted in a more soluble **2***OTf, in which the detection of the Ru-C resonances at δ = 191.3 ppm in ¹³C NMR spectrum was possible. Both **2** and **2***OTf are dynamic on the NMR timescale in solution. In addition to the interconversion of the two atropisomers, the hydride and CO ligands can

exchange their positions in **2** and **2*OTf** in solutions. Two hydride resonances are observed in CD₂Cl₂ ($\delta = -12.5$ and -15.3 ppm) and CD₃CN ($\delta = -12.8$ and -14.5 ppm) in ¹H NMR spectrum of **2**. Relative intensities of these signals depend on the temperature and solvent type indicating the interconversion of the related Ru-CNC species (Figure 5.4). We propose that the high-field resonance corresponds to the hydride is *trans* to halide or acetonitrile ligand, while the lower field resonance can be attributed to a hydride ligand oriented *trans* to pyridine. The observed NMR pattern rules out the presence of the hydride ligands *trans* to the carbonyl group because such a ligand environment would shift the hydride resonance to a significantly lower field (around -5 ppm).³⁴

In the absence of LiBr, the complexation of **L2** with RuHCl(CO)(PPh₃)₃ led to **3** (Scheme 5.4), in which one of the NHC arms coordinates abnormally to Ru through the C5 carbon.^{35,36} The hydride ligand in **3** is *trans* to the PPh₃ as is evident from the large J_{PH} (100 Hz). The signature C2 imidazolium proton of the abnormally bound NHC appears at $\delta = 9.66$ ppm, while the remaining C4 imidazolium proton is significantly shifted upfield to $\delta = 4.46$ ppm. Methylene protons appear as four doublets, two of which are additionally coupled to the imidazolium proton on the C2 position of the abnormally bound NHC group (*dd*, $\delta = 5.1$ ppm, 4.7 ppm $^2J_{HH}=16$ Hz, $^4J_{HH}=1.8$ and 2.7 Hz). Coordinated triphenylphosphine was dynamic on the NMR timescale, but this behavior was not associated with atropisomerisation of the CNC chelate. Namely, the characteristic resonances of the triphenylphosphine ligand were severely broadened both in ¹³C and ¹H NMR while the CNC ligand showed no significant perturbations. This dynamics was exploited to mask the signals of PPh₃ and assign those corresponding to the CNC ligand accurately by performing the NMR measurements at elevated temperature.

The molecular structure provides the final evidence for the abnormal NHC coordination in **3**. The CNC ligand occupies a meridional position in the octahedral complex (Figure 5.5). The Ru-C distance in the abnormally bound NHC is significantly longer than that in normally bound NHC ($\Delta r(\text{Ru-C})=0.045$ Å). One of the isopropyl groups on the substituent of the abnormal NHC was refined with a disorder model. Indeed, in the abnormally bound NHC the substituent points away from the complex resulting in an enhanced dynamics and disorder. Complex **3** crystallizes with a mixed Br/Cl counterion. The halide ratio was refined as Br/Cl = 65/35 and confirmed with microanalyses. Complex **3** is a rare example of bis-NHC pincer with mixed normal/abnormal composition. Such complexation behavior was previously observed only for iron³⁷ and iridium³⁸ pincers. Our findings are consistent with previous reports on Os and Ir NHCs, where counterion and

steric effects were shown to control the NHC coordination mode.³⁹⁻⁴² In particular, it has been demonstrated that in the presence of Br⁻ anions the C-H heterolysis at C2 position is accelerated that results in the preferential normal NHC coordination.⁴² The possibility of selecting the NHC binding mode of the CNC pincer ligand reported here provides yet another useful tool for tuning properties of Ru-CNCs.

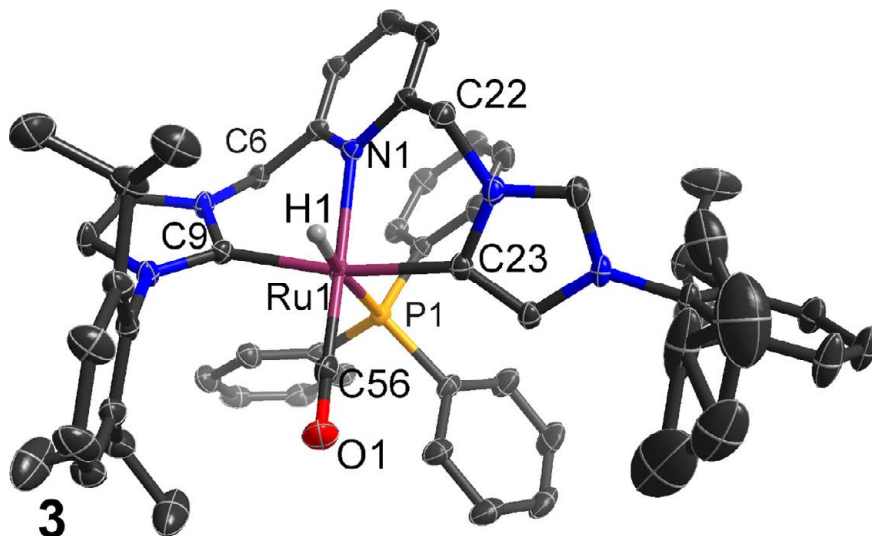
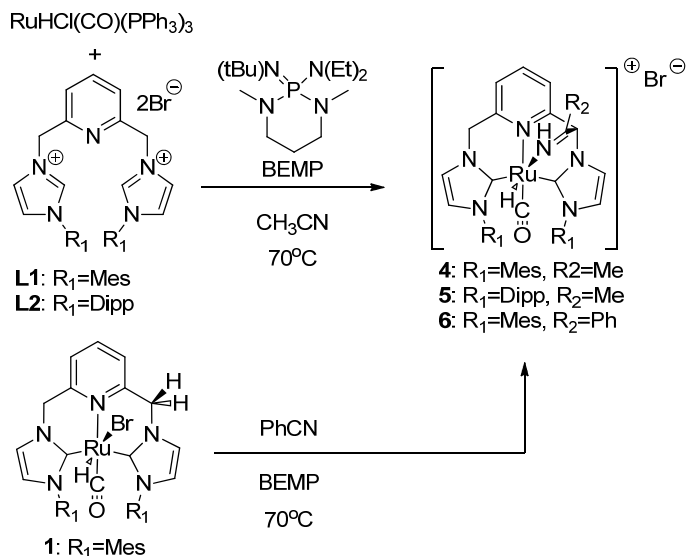


Figure 5.5. X-ray crystal structure of **3** (50% probability ellipsoids, solvent molecules, hydrogens, and the halide anion are omitted for clarity). Selected bond lengths[Å]: Ru1-P1 2.4353(5), Ru1-C9 2.0672(16), Ru1-C23 2.1124(17), Ru1-C56 1.8283(18), Ru1-N1 2.2034(14).

5.3 Cooperative activation of nitriles over Ru-CNCs

The synthesis of **1** was hampered by an extremely low solubility of the reactants. To remediate this problem and optimize the synthesis of Ru-CNC, the reaction in a more polar acetonitrile solvent was attempted. However, in this case the complexation of the Ru precursor with **L1** led to the formation of a CH₃CN adduct **4** (Scheme 5.6). Complex **4** was identified as the product of cooperative nitrile addition across ligand sidearm and Ru centre. Nitrile group is transformed into metal-ligand bound ketimino moiety. The ¹H NMR of **4** contains a high frequency imine proton signal at δ = 9.89 ppm. Three methylene bridge protons appear as two sharp doublets at δ = 5.40 and 5.30 ppm (²J_{HH} = 14 and 8 Hz) and a sharp singlet at δ = 8.53 ppm indicating nitrile insertion into C-H bond of the methylene group. The Ru-NHC resonances of **4** appear at δ = 191.9 and 191.2 ppm in the ¹³C NMR spectrum. Hydride ligand resonance of **4** is significantly shifted downfield to δ = -12.1 ppm that is ca. 3.5 ppm higher than the respective resonance in **1**. Similarly, complex **5** with

diisopropylphenyl (*dipp*) substituents on the NHC groups can be prepared by reacting **L2** with $\text{RuHCl}(\text{CO})(\text{PPh}_3)_3$ in CH_3CN in the presence of BEMP. The NMR spectrum of **5** is similar to that of **4**. Both adducts can be crystallized by vapor diffusion. Crystal structure analysis of **4** and **5** (Figure 5.6) confirms the nitrile addition across the metal center and the methylene bridge of the ligand. The coordination of the CNC ligand in **4** and **5** is similar to that in **1**.



Scheme 5.6. Complexation of Ru with bis-NHC ligands in the presence of nitriles.

Complex **1** can also undergo a direct transformation to nitrile adducts in the presence of BEMP. In CH_3CN ca. 47% of **1** was transformed to **4** overnight. Nearly quantitative conversion was observed for reaction of **1** with benzonitrile. Corresponding adduct **6** was isolated in 91 % yield. Note, that the related phosphine-based pincers did not react with nitriles under these conditions. Cooperatively added nitrile moieties in Ru-CNC are stable upon heating (80 °C), exposure to high vacuum ($3 \cdot 10^{-6}$ mbar) or treatment with formic acid or KOH solutions. Their solutions in methylene chloride tolerate the exposure to air for at least 24 hours.

Organonitrile activation resulting in the formation of a new C-C bond was reported for Rh^{34} and Ir^{35} complexes. The nitrile binding mode in **4** and **5** resembles that in Re-PNP ketimido and enamido adducts with the difference that the addition to Re-PNP occurs only after the deprotonation of the ligand with a strong base.⁴³ Similar nitrile addition with subsequent coordination of imine group to the metal center was previously described for

macrocyclic complexes of Fe, Co, W and Mo.⁴⁴⁻⁴⁶ In addition, iron complexes with tetradentate nitrogen ligands were shown to attack nitriles and form similar adducts in the presence of base (NEt₃)⁴⁷ that draws a parallel with the reactivity of Ru-CNCs.

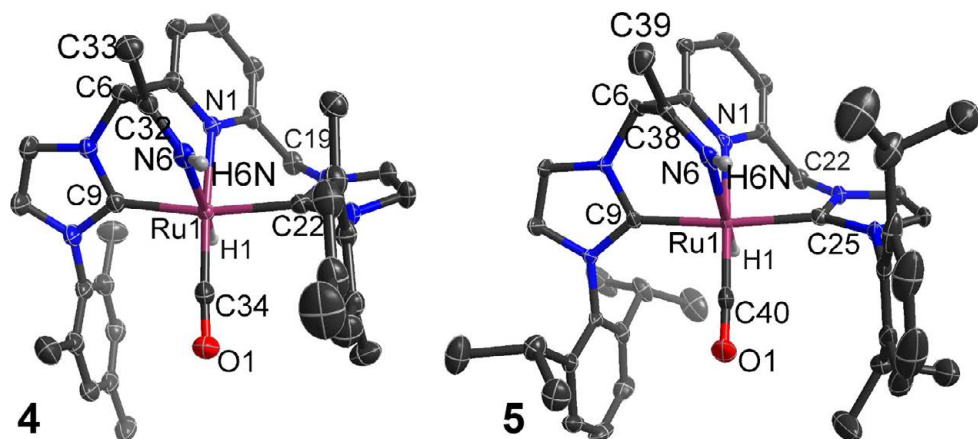


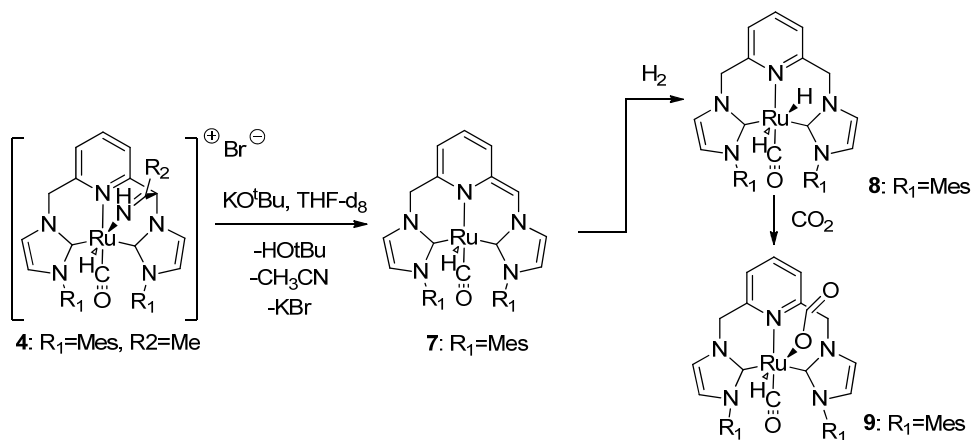
Figure 5.6. X-ray crystal structure of adducts **4**(left) and **5**(right) (ellipsoids at the 50% probability level, all hydrogens, except hydride, counteranion and co-crystallized solvent molecule are omitted for clarity). Selected bond lengths [Å]:**4**: Ru1-N6 2.161, Ru1-C9 2.047, Ru1-C22 2.074, Ru1-C34 1.833, Ru1-N1 2.167 **5**: Ru1-N6 2.162, Ru1-C9 2.061, Ru1-C25 2.082, Ru1-C40 1.827, Ru1-N1 2.195

5.4 Reactivity of Ru-CNCs towards ligand dearomatization – a parallel with PNP pincers

Catalysis with lutidine-derived pincer complexes is often triggered by the activation with a base.^{3,48} The strong base deprotonates the ligand sidearm and generates highly reactive five-coordinate species. The reactivity of Ru-CNCs with strong bases was probed with NMR spectroscopy. The reaction of **1** with KHMDS or KO^tBu at room temperature led to incomplete conversion providing impure mixtures containing dearomatized complex that was further identified as complex **7** (Scheme 5.7). Nitrile adduct **4** can also undergo deprotonation in the presence of base. The reaction of **4** with KO^tBu results in a quantitative formation of the dearomatized complex **7**. The elimination of the imine groups as a free acetonitrile is evidenced by NMR spectroscopy. Relatively unstable **7** was characterized *in situ* by NMR spectroscopy (Figure 5.6). Dearomatization of the pyridine ring is evidenced by significant upfield shift of the corresponding ¹H NMR signals to ca. 6.20 and 4.81 ppm. Two methylene group resonances appear at $\delta = 4.90$ and 4.74 ppm as doublets. The resonance of a single proton from the deprotonated bridge appears at $\delta = 5.83$ ppm and shares a cross peak with carbon resonance at $\delta = 63.5$ ppm in gHMQC

spectroscopy. These results point to a more facile transformation of the nitrile adducts **4-6** to the highly reactive dearomatized Ru-pincer complexes in the presence of a strong base compared to the parent Ru-CNCs **1** and **2**. Consequently similar trends are expected for nitrile adducts and parent Ru-CNCs.

Similar to other lutidine-based Ru pincers analogues,³ **7** reacts with H₂ to form the dihydrido complex **8** (Scheme 5.7). This transformation was observed in an NMR tube experiment in THD-d₈ under 3 bar H₂ pressure. The ¹H resonance of the Ru-H in **8** is shifted downfield to $\delta = -5.94$ ppm that is typical for ruthenium *trans* dihydrido complexes.⁴⁹ Upon addition of H₂, the pyridine ring is rearomatized and all four methylene protons are observed as doublets at $\delta = 5.59$ and 5.33 ppm. The reactivity of the dihydrido complex **8** towards CO₂ is very similar to that of its phosphine-based counterparts (Chapter 2). It readily reacts with carbon dioxide to produce a formato complex. The exposure of solutions of **8** to 3 bar CO₂ in THF-d₈ leads to the formation of an insoluble precipitate of complex **9** (Scheme 5.7). **9** is soluble in dichloromethane, but can only be characterized spectroscopically at a low temperature due to the fast exchange resulting in coalescence and peak broadening at room temperature.



Scheme 5.7. Generation of dearomatized complex **7** and its reactivity with H₂ and CO₂

In the ¹H NMR spectrum of **9** protons of the methylene linker appear as separate doublets. Methyl groups of *mes* substituent of the NHC group are non-equivalent and appear as six separate singlets. The aromaticity of the pyridine ring in **9** is evidenced by the presence of a triplet resonance at $\delta = 7.8$ ppm. The proton of the Ru-bound formato group appears as a singlet at $\delta = 7.7$ ppm.

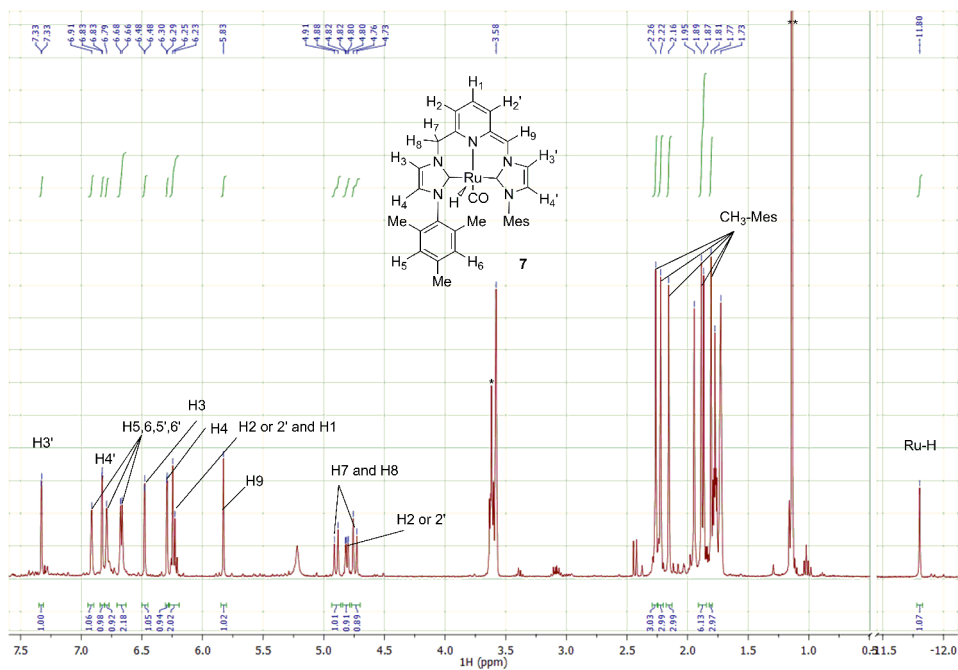


Figure 5.7. ^1H NMR spectrum of the *in situ* generated dearomatized complex **7** in THD-d_8 at 25°C

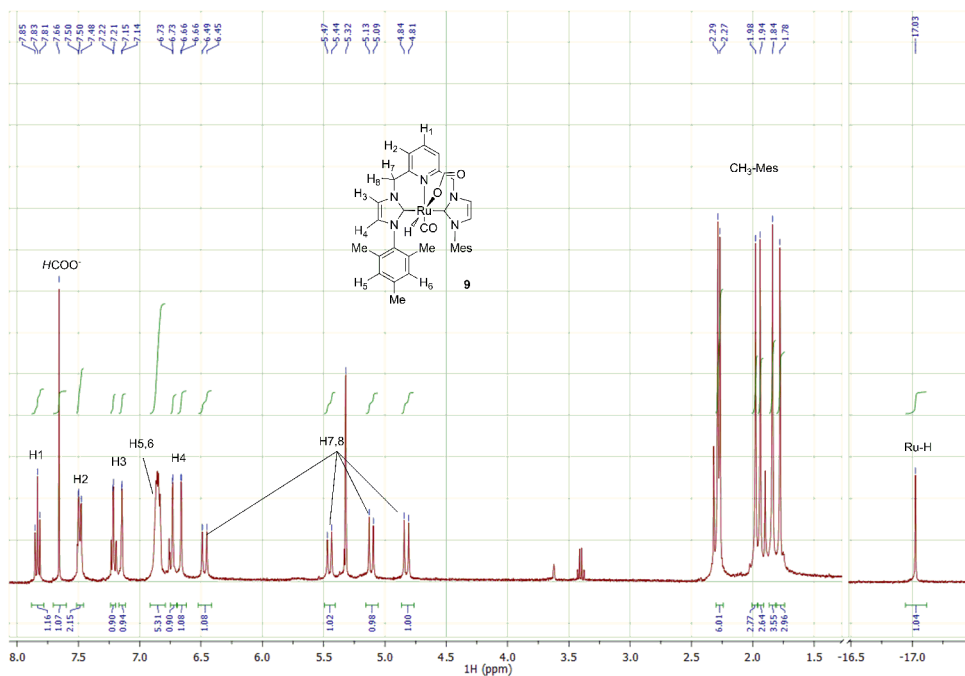


Figure 5.8. ^1H NMR spectrum of the formate complex **9** in CD_2Cl_2 at -15°C

We have also probed the reactivity of **7** towards CO₂ to evaluate the possibility of cooperative CO₂ addition to bis-NHC Ru-CNC pincers. Exposure of **7** to 3 bar CO₂ in THF-d₈ results in an insoluble precipitate, which even upon partial resolution in CD₂Cl₂ cannot provide a definitive NMR spectrum. When the reaction of **7** with CO₂ is carried out in polar DMF-d₇ solvent, the formation of two new hydride resonances at $\delta = -11.66$ and -16.76 ppm in approx. 15/85 ratio was observed. The major complex was identified as the product of the cooperative CO₂ addition **10** (Scheme 5.8). The high-field hydride signal at $\delta = -16.76$ ppm is consistent with its *trans* position to the CO₂ moiety. In agreement with the formation of a chelating fragment upon the addition of CO₂, only three methylene protons were identified in the ¹H NMR spectrum of **10**. Two doublets corresponding to the -CH₂- linker appear at $\delta = 5.29$ and 5.82 ppm with $J^2_{HH} = 13.6$ Hz. The single proton of the pincer arm that has reacted with CO₂ is observed as a singlet at $\delta = 6.14$ ppm. The reaction with CO₂ leads to the rearomatization of the pyridine ring as is evidenced by the presence of a triplet signal at $\delta = 8.1$ ppm ($J^3_{HH} = 7.7$ Hz).

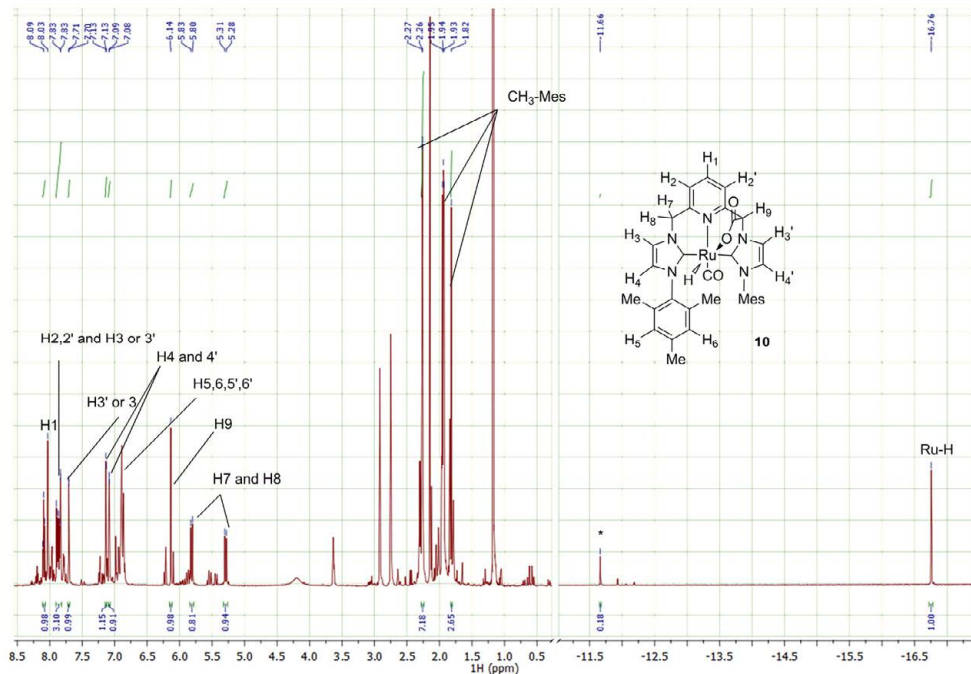
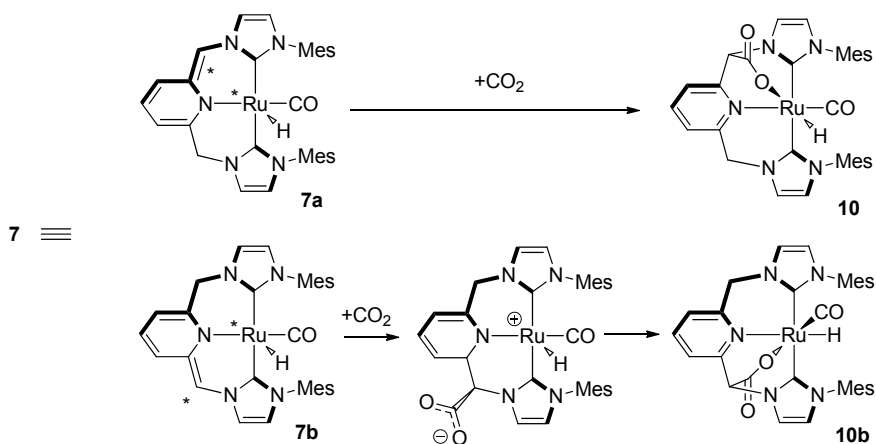


Figure 5.9. ¹H NMR spectrum of reaction mixture containing complex **7** under 2 bar CO₂ pressure in DMF-d₇. Signals of **10** integrated where possible. Hydride resonance of **10b** labeled with *

Because of the very high reactivity of **7**, its reaction with CO₂ did not result in the clean formation of the CO₂ adduct (Figure 5.9). Therefore we attempted the preparation of

10 from complex **1** in a one-pot reaction employing the deprotonation of the complex with a mild DBU base in the presence of 2 bar CO₂. This approach allowed to quantitatively convert complex **1** to the corresponding CO₂ adduct. This clean transformation allowed the identification of the minor compound **10b** as an isomer of CO₂ adduct **10** (Figure 5.10). The major part of the ¹H NMR signals of **10b** overlap with those of the major compound **10**. Nevertheless, we were able to identify three methylene linker protons corresponding to **10b** that appear as singlet at δ = 6.1 ppm and two doublets at δ = 5.4 and 5.8 ppm. Significant downfield shift of the hydride signal to δ = -11.6 ppm in ¹H NMR suggests that the hydride in **10b** is located *trans* to pyridine. The formation of this complex can be explained by the isomerization of **7** in solution. The high flexibility of the chelate in Ru-CNCs discussed above allows the formation of two structurally very similar isomers of **7** that differ in the relative orientation of the deprotonated sidearm of the CNC ligand with respect to the hydride (complexes **7a** and **7b** in Scheme 5.8). In **7a** the basic site is close to the vacant site of Ru complex allowing thus for the one-step cooperative addition of CO₂ across the metal and the ligand towards product **10**. However, the basic site on the side-arm of **7b** is close to the hydride ligand. As a consequence, when CO₂ reacts with the basic site in **7b**, the hydride has to be relocated *trans* to pyridine to allow the chelation with newly formed carboxylate moiety resulting in product **10b**. The nature of this transformation will be analyzed in more detail in the next Chapter.



Scheme 5.8. Reactivity of dearomatized complex **7** with carbon dioxide

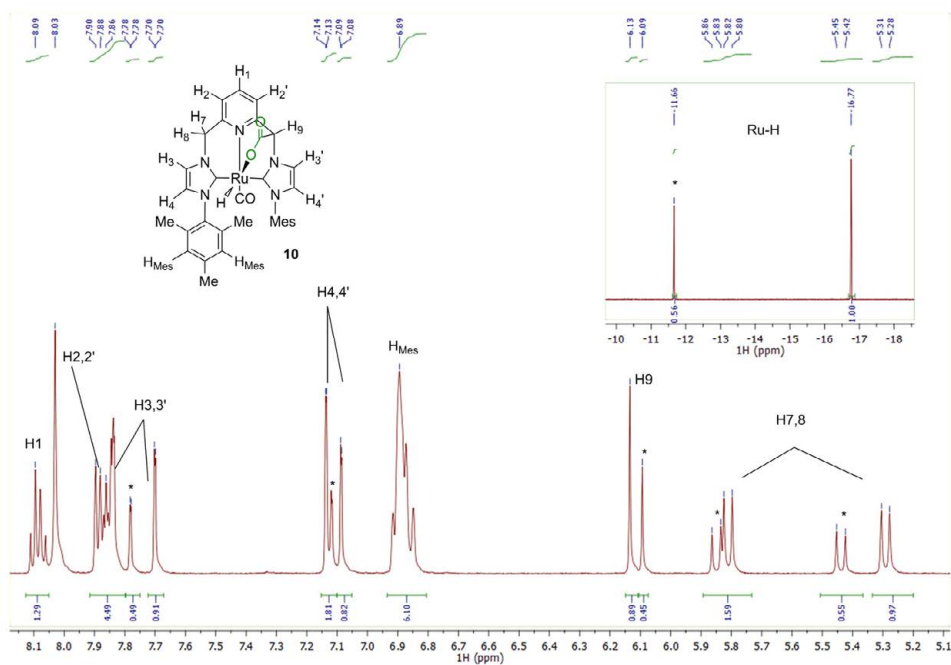


Figure 5.10. Section of ^1H NMR spectrum for reaction of **1** with 2 bar CO_2 in the presence of DBU in DMF-d_7 . Signals of **10** integrated where possible. Resonances of **10b** labeled with *.

We further confirm the presence of cooperatively added CO_2 moiety in **10/10b** using isotopic labeling. When labeled $^{13}\text{CO}_2$ is used to generate **10/10b**, the resonance of the single methylene proton shows $J_{\text{CH}} = 5.3$ Hz typical for a two-bond C-H coupling (Figure 5.11). The same $J_{\text{CH}} = 5.3$ Hz is observed in ^{13}C NMR for doublets at $\delta = 167.26$ and 168.19 ppm corresponding to the metal-ligand bridging CO_2 moiety in **10** and **10b**, respectively. Finally, we noticed that proposed geometry of **10** and **10b** features the hydride ligand in different orientation with respect to the CNC ligand framework. Indeed, selective excitation measurements show that the hydride signal at $\delta = -16.77$ ppm attributed to **10** shares a cross peak with a methylene bridge proton that appears as doublet at $\delta = 5.29$ ppm and a singlet resonance of the $\text{CH}_3\text{-mes}$ group at $\delta = 2.12$ ppm (Figure 5.11a). On the other hand, the hydride resonance at -11.66 corresponding to **10b** correlates only with that of the $\text{CH}_3\text{-mes}$ groups (singlets at $\delta = 1.97$ and 1.95 ppm). DFT optimized geometries for complexes **10** and **10b** are in a perfect agreement with the geometrical features deduced from *DPFGSE 1D NOESY* measurements (Figure 5.12).

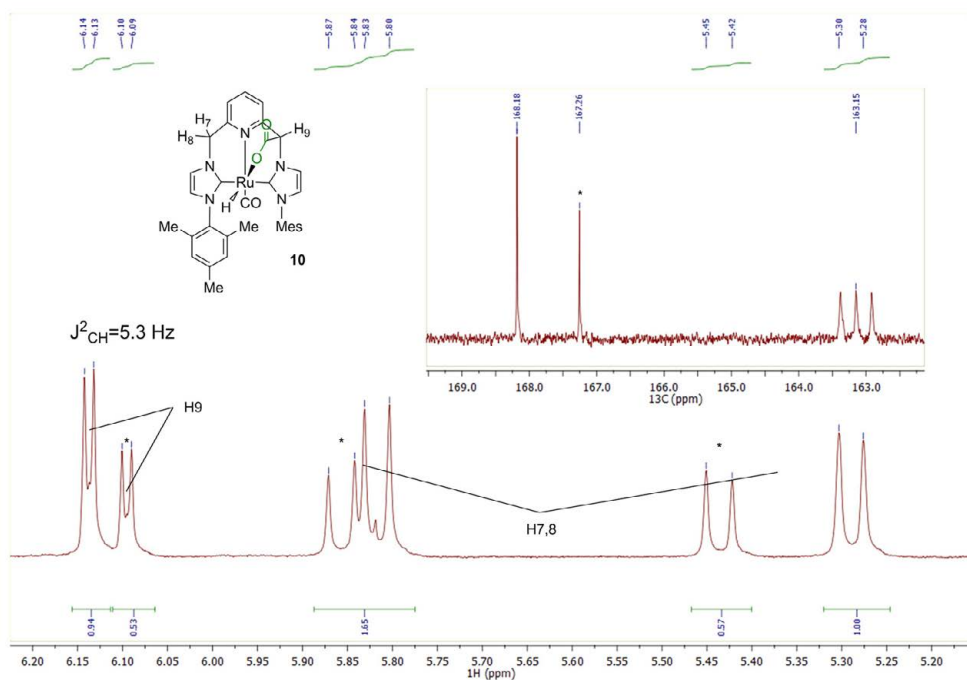


Figure 5.11. Methylenepyridilic region of ^1H NMR spectrum for reaction of **1** with 2 bar ^{13}C in the presence of DBU in $\text{DMF-}d_7$. Singals of **10** integrated where possible. Resonances of **10b** labeled with *. Insert shows ^{13}C spectrum

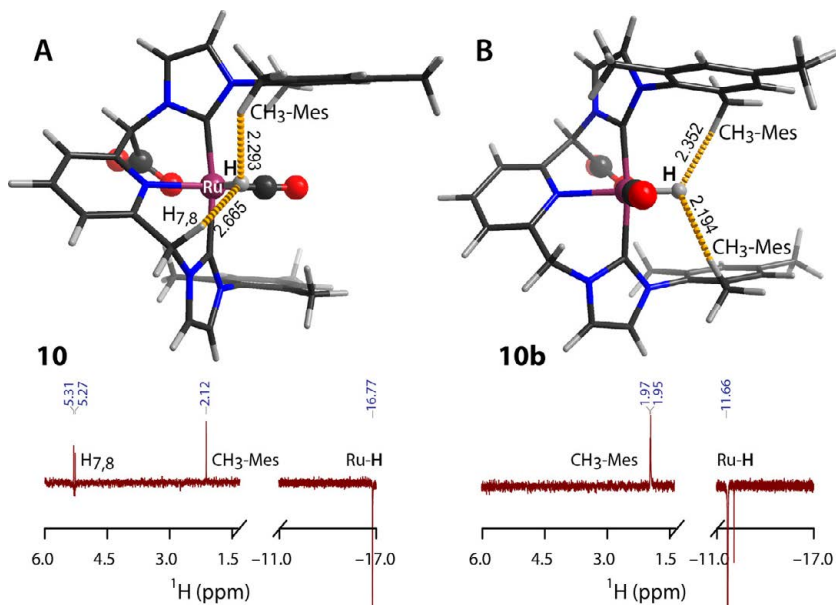


Figure 5.12. DPFGE 1D NOESY data and computed structures for **10(A)** and **10b(B)**

Complexes **10/10b** are stable at 70°C in DMF/DBU mixtures for days. The CO₂ addition is irreversible under practical conditions. Vacuum treatment of the solutions of **10/10b** has no impact on the NMR spectrum. No detectable changes in NMR spectrum are observed upon exposure of the solutions of **10/10b** to 3 bar of H₂, even when heated for several hours at 70°C. These data points to the high stability of **10/10b**. It is particularly important to mention that related Ru-PNP pincers do not react with CO₂ directly in the presence of a mild base. Neither do they bind CO₂ irreversibly. This exemplifies the crucial difference in the reactivity of Ru-PNP and Ru-CNC pincers towards carbon dioxide, that may have significant influence on the catalytic properties of Ru-CNC.

5.5 Conclusions

A new family of lutidine-derived Ru-CNC complexes with highly versatile coordination properties and unique reactivity was described in this Chapter. Firstly, we could alter the NHC coordination mode by a minor variation of the reaction conditions during the complexation. In the presence of LiBr additives, the metallation of **L2** leads to the formation of **2** where both NHC arms are normally bound. In contrast, when no additives were used during the reaction, a mixed normal/abnormal complex **3**. Secondly, Ru-CNC pincers can cooperatively activate nitriles in the presence of phosphazene bases to form ketimino complexes (**4 – 6**). Aromatic and aliphatic nitriles can be activated using this procedure during complexation or post-synthetically.

Similar to the related Ru-PNPs, Ru-CNC reacts with strong bases to give dearomatized species **7** that can cooperatively activate hydrogen and CO₂ to form corresponding complexes **8** and **10**. The dihydrido complex **8** can react with CO₂ to yield formate complex **9**. In sharp contrast with Ru-PNP, the bis-NHC complex **1** reacts with CO₂ in presence of DBU. Furthermore, respective CO₂ adduct **10** is formed irreversibly and shows no further reactivity towards hydrogen, while the reaction of related CO₂ adduct of Ru-PNP results in formate complexes. The implications of these reactivity patterns on catalytic performance of Ru-CNC will be the subject of our investigation in the next Chapter.

5.6 Experimental

General considerations

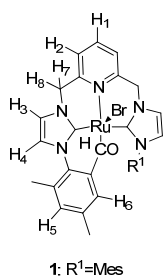
All manipulations unless stated otherwise were performed using Schlenk or high vacuum line ($\sim 5 \cdot 10^{-6}$ mbar) techniques. Argon was dried with a Sicapent column. Air sensitive compounds were stored in an MBraun glovebox under the atmosphere of dry argon. Anhydrous solvents were dispensed from MBraun purification system and degassed prior to use. Acetonitrile (DNA synthesis grade, Biosolve) was distilled over CaH_2 and stored over molecular sieves. BEMP solution was purchased from Sigma and degassed by three freeze-pump-thaw cycles. Deuterated solvents were purchased from Eurisotop and dried over Na/benzophenone (C_6D_6 , THF- d_8), calcium hydride (CD_3CN) or phosphorus pentoxide (CD_2Cl_2), degassed using three freeze-pump-thaw cycles, high-vacuum transferred in storage vessels and used in the glovebox.

1-mesylyl and 1-diisopropylphenyl imidazoles were prepared according to literature procedures and sublimed under vacuum ($8 \cdot 10^{-2}$ mbar) before use at 70 and 80 °C, respectively.

Ligands **L1** and **L2** were prepared according to modified literature procedures using acetonitrile as a solvent. $\text{RuHClCO}(\text{PPh}_3)_3$ was prepared according to literature procedure and recrystallized from dichloromethane before use. Reference complex **9** was prepared according to published procedure.

NMR spectra were recorded on Varian Mercury 400 MHz spectrometer. Chemical shifts were referenced to residual solvent resonances. External traces were used in graphic representations of gCOSY and gHSQC experiments. ESI-MS measurements were performed on Thermo Scientific LCQ Fleet apparatus, isotope distribution patterns were used as a composition proof in addition M/Z signal. Elemental analyses were performed using Perkin-Elmer apparatus (for compound **5**), remaining analyses were performed in Kolbe laboratory.

Synthesis and characterization of complexes:



Complex I

4.5 mL of 1M solution of BEMP in hexane were added to a stirred suspension of $[\text{RuHClCO}(\text{PPh}_3)_3]$ (1.9048g, 2 mmol), ligand **L1** (1.4067g, 2.2 mmol) and LiBr (1.7 g, 19.57 mmol) in ca. 70 mL THF at room temperature in a flask, equipped with a reflux condenser. The mixture was then heated to 70 °C and dwelled for 16 hours. During this time suspended solid turned bright yellow and the solution from colorless turned golden brown. After cooling down, the solution was filtered off using the cannula tipped with 1.7 micron glass microfiber filter (VWR) and washed twice with 5 mL THF to remove air sensitive impurities, originating from the ruthenium precursor. Yellow solid contaminated with unreacted imidazolium salt **L1** was then taken out in air and stirred with 50 mL of deionized water. This suspension was filtered on a nylon membrane filter

(0.45 micron, VWR) and washed copiously with water, a little THF and finally diethyl ether. Resulting solid was dried overnight under high vacuum to yield 930 mg of **1** (65.7% on [Ru] basis).

NOTE: Failure to ensure excess of bromine during synthesis leads to a mixture of chloride and bromide complexes with Br/Cl ratio of 55/45. This sample was used for single crystal X-ray analysis. Crystals of **1** were grown from dilute dichloromethane solution with Et₂O vapor diffusion. Proton NMR spectrum of a mixed halide **1** is nearly identical to one of a pure bromide form

¹H NMR (400 MHz, CD₂Cl₂): δ 7.82 (t, *J* = 7.7 Hz, 1H, py-H1), 7.47 (d, *J* = 7.7 Hz, 2H, py-H2), 7.18 (d, *J* = 1.9 Hz, 2H, imi-H3), 6.89 (s, 2H, mes-H5 or H6), 6.85 (s, 2H, mes-H5 or H6), 6.67 (d, *J* = 1.9 Hz, 2H, imi-H4), 5.10 (d, *J* = 14.7 Hz, 3H, methylene H7-8), 2.31 (s, 6H, mes-CH₃), 2.12 (s, 6H, mes-CH₃), 1.88 (s, 6H, mes-CH₃), -15.57 (s, 1H, Ru-H).

Additional characterization in acetonitrile was performed to achieve proper integration on methylene protons H7-8

¹H NMR (400 MHz, CD₃CN, 25°C): δ 8.00 (t, *J* = 7.7 Hz, 1H, py-H1), 7.68 (d, *J* = 7.7 Hz, 2H, py-H2), 7.48 (d, *J* = 1.9 Hz, 2H, imi-H3), 6.94 (s, 4H, mes-H5, H6), 6.89 (s, 2H, imi-H4), 5.53 (br-s, 2H, methylene H7-8), 5.28 (br-s, 2H, methylene H7-8), 2.30 (s, 6H, mes-CH₃), 1.98 (br-s, overlap with CD₃CN, mes-CH₃), 1.88 (s, 6H, mes-CH₃), -14.34 (s, 1H, Ru-H).

¹³C NMR (101 MHz, CD₂Cl₂, 25°C) δ 207.96 (s, CO), 194.30 (s, Ru-C), 158.75 (s, py- Cq), 138.34 (s, mes- Cq), 138.20 (s, py C1), 137.77 (s, mes- Cq), 137.43 (s, mes- Cq), 136.54 (s, mes- Cq), 128.87 (s, , mes-C5 or C6), 128.38 (s, mes-C5 or C6), 123.64 (s, py C2), 122.18 (s, imi-C4), 121.15 (s, imi-C3), 57.36 (s, methylene sidearm), 21.25 (s, mes-CH₃), 19.34 (s, mes-CH₃), 18.60 (s, mes-CH₃).

IR(film): ν = 1927, 1878 cm⁻¹

ESI/MS (CH₃CN): Calcd. C₃₂H₃₄N₅ORu⁺ ([Ru(L1)HCO]⁺) 606.18. Found: 606.42

EA: Calcd. C₃₂H₃₄N₅OBrRu*0.5THF: C 56.59, H 5.31, N 9.70. Found: C 56.56, H 5.76, N 9.88.

*Generation of complex **1***BF₄*

Complex was prepared as a reference to verify the position and integration of methylene signals and probe the dynamics in **1**: 20 mg of **1** (29 μmol) were dissolved in ca. 0.6 mL CD₃CN and 6.8 mg of silver tetrafluoroborate (35 μmol, 1.2 eq) was added. The formed suspension was agitated for 30 seconds and filtered into a Young tube through 5mm Celite plug. VT-NMR measurements were performed and the liquid was taken out. A droplet of benzene was added and the solution was set aside for crystallization by slow diethyl ether vapor diffusion. Yellow plates were obtained and used for XRD analysis.

The isolation of **1***BF₄ is not claimed since the loss of acetonitrile upon vacuum treatment leads to decomposition of the compound.

ESI/MS: Calcd. C₃₂H₃₅N₅ORu⁺ ([Ru(L1)HCO]⁺) 606.18. Found: 606.38

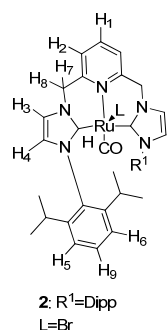
*Generation of complex **1**_{ICN}*

100 mg of **1** (145 μmol) were combined with ca 33 μL of ^tBu isocyanide (291 μmol) in 5mL THF in the glovebox. The flask with suspension was then taken out and stirred at 70°C for 2 hours. The

color of precipitate changed from bright yellow to grey. 20 mL ether was then added to the cooled suspension and the solvent was filtered off. Solids were washed with ether and dried under vacuum to give **1_{INC}** in 91% yield (101 mg).

¹H NMR (500 MHz, CD₂Cl₂) δ 8.08 (d, *J* = 7.5 Hz, 1H, H_{py}), 7.94 (d, *J* = 1.6 Hz, 1H, H_{imi}), 7.89 (t, *J* = 7.7 Hz, 1H, H_{py}), 7.71 (d, *J* = 7.5 Hz, 1H, H_{py}), 7.51 (d, *J* = 1.6 Hz, 1H, H_{imi}), 6.89 (s, 3H, CH_{mes}), 6.84 (s, 1H, CH_{mes}), 6.77 (d, *J* = 1.7 Hz, 1H, H_{imi}), 6.74 (d, *J* = 1.7 Hz, 1H, H_{imi}), 6.24 (d, *J* = 15.1 Hz, 1H, -CH₂-), 5.53 (d, *J* = 14.2 Hz, 1H, -CH₂-), 5.27 (d, *J* = 14.9 Hz, 1H, -CH₂-), 5.14 (d, *J* = 13.4 Hz, 1H, -CH₂-), 2.27 (s, 3H, CH_{3mes}), 2.25 (s, 3H, CH_{3mes}), 1.89 (s, 3H, CH_{3mes}), 1.87 (s, 3H, CH_{3mes}), 1.86 (s, 3H, CH_{3mes}), 1.78 (s, 3H, CH_{3mes}), 1.19 (s, 9H, ^tBu), -7.46 (s, 1H, Ru-H).

¹³C NMR (126 MHz, CD₂Cl₂) δ 203.73 (s), 186.80 (s), 157.26 (s), 148.87 (s), 138.72 (d, *J* = 6.3 Hz), 136.05 (d, *J* = 53.5 Hz), 128.79 (s), 128.53 (s), 124.62 (s), 122.20 (s), 121.82 (s), 56.97 (s), 30.04 (s), 20.76 (s), 18.02 (s).



Complex 2 – bromide form

2.25 mL of 1M solution of BEMP in hexane were added to a stirred suspension of [RuHClCO(PPh₃)₃] (904.8 mg, 0.95 mmol), ligand **L2** (719.2 mg, 1 mmol) and LiBr (1.7 g, 19.57 mmol) in ca. 40 mL THF at room temperature in a flask, equipped with a reflux condenser. The mixture was then heated to 70°C and dwelled for 16 hours. During this time suspended solid dissolved, yielding golden brown solution. After cooling down, the solution was filtered and concentrated, to give viscous oil. 70 mL acetone were added to the resulting oil and clear solution was stirred vigorously for 15 minutes. Finally bright yellow solid precipitated.

Solid was separated by filtration, washed with 5 mL acetone. 70 mL diethyl ether were added to the solid and stirred for additional 10 minutes. The suspension was then filtered, and bright yellow solid was dried under high vacuum overnight at 50°C. Yield: 565 mg (77.4% on [Ru] basis).

Proper and unambiguous characterization is done by converting **2** to **2*OTf** since the solubility of **2** in CD₂Cl₂ and CD₃CN was too low to allow proper detection of Ru-C resonance in ¹³C NMR.

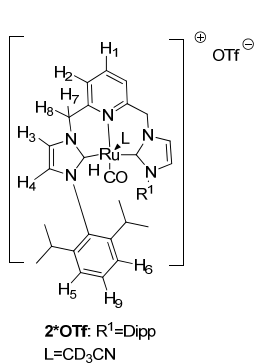
IR(film): ν = 1917 cm⁻¹

ESI/MS: Calcd. C₃₈H₄₆N₅ORu⁺ ([Ru(L2)HCO]⁺) 690.27. Found: 690.44

EA: Calcd. C₃₈H₄₆N₅OBrRu: C 59.29, H 6.02, N 9.10. Found: C 59.35, H 5.97, N 9.04.

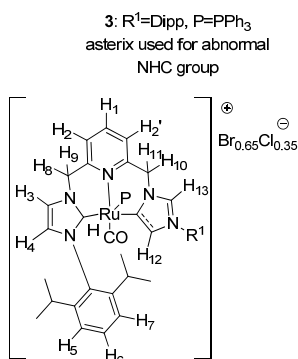
Generation of complex **2*OTf**

Complex was generated to confirm the identity of **2**. 10 mg of **2** (13 μmol) and 4 mg of silver triflate (15.56 μmol) were taken up in 0.6 mL CD₃CN. The suspension, that forms immediately, was agitated and filtered in Young tube through a short Celite plug. NMR evidenced complete conversion of **2**. Since **2*OTf** was prepared exclusively to confirm the identity of **2** and obtain a reliable carbon spectrum, the isolation of **2*OTf** is not claimed. The quantitative conversion of **2** in **2*OTf** supports the validity of this approach. **2*OTf** is stable in solution for weeks, but the attempted crystallizations leads to decomposition.



¹H NMR (400 MHz, CD₃CN) δ 8.04 (t, *J* = 7.7 Hz, 1H, H₁), 7.70 (d, *J* = 7.7 Hz, 2H, H₂), 7.45 (d, *J* = 1.9 Hz, 2H, H₃), 7.37 (t, *J* = 7.8 Hz, 2H, H₉), 7.20 (s, 2H, H₅ or H₆), 7.19 (s, 2H, H₅ or H₆), 7.07 (d, *J* = 1.9 Hz, 2H, H₄), 2.54 – 2.41 (m, 2H, dipp-CH(CH₃)₂), 2.25 (m, 2H, dipp-CH(CH₃)₂), 1.12 (d, *J* = 6.8 Hz, 6H, dipp-CH(CH₃)₂), 1.05 (d, *J* = 6.9 Hz, 6H, dipp-CH(CH₃)₂), 1.00 (d, *J* = 6.8 Hz, 6H, dipp-CH(CH₃)₂), 0.93 (d, *J* = 6.9 Hz, 6H, dipp-CH(CH₃)₂), -14.42 (s, 1H, Ru-H).

¹³C NMR (101 MHz, CD₃CN) δ 205.51 (s, CO), 191.33 (s, br, Ru-C), 158.39 (s, py-C_q), 147.59 (s, dipp-C_q), 147.48 (s, dipp-C_q), 140.56 (s, py-C₁), 137.33 (s, dipp-C_q), 130.67 (s, dipp-C₉), 125.54 (s, imi-C₄), 124.55 (s, py-C₂), 124.29 (s, dipp C₅ and C₆), 122.48 (s, imi-C₃), 56.62 (s, methylene -CH₂-), 29.32 (s, dipp-CH(CH₃)₂), 29.15 (s, dipp-CH(CH₃)₂), 26.17 (s, dipp-CH(CH₃)₂), 26.04 (s, dipp-CH(CH₃)₂), 22.43 (s, dipp-CH(CH₃)₂), 22.13 (s, dipp-CH(CH₃)₂).



Complex 3

1 mL of 1M solution of BEMP in hexane were added to a stirred suspension of [RuHClCO(PPh₃)₃] (476.22 mg, 0.5 mmol) and ligand **L2** (359.6 mg, 0.5 mmol) in ca. 35 mL THF at room temperature in a flask, equipped with a reflux condenser. The mixture was then heated to 70°C and dwelled for 16 hours. During this time solution from colorless turned light brown. After cooling down, the solution was filtered off and pale whitish solid was washed with 5 mL THF to remove air sensitive impurities, originating from ruthenium precursor. The solid, that is contaminated with unreacted imidazolium salt **L2** was then taken out in air and stirred with 50 mL of deionized water. This suspension was filtered on a nylon membrane filter (0.45 micron, VWR) and washed copiously with water, a little THF and finally diethyl ether. Resulting solid was dried overnight under high vacuum to yield 200 mg of **3** with a mixed counteranion (Br/Cl = 65/35, Y:39.4% on [Ru] basis).

NOTE: Unreacted ruthenium precursor can easily be confused with triphenylphosphine ligand, subjected to dynamic behavior in solution. To exclude this, crude **3** should be recrystallized.

Recrystallization: In the glovebox 100 mg of **3** were dissolved in 4 mL CH₃CN in a vial, few droplets of benzene were added (this step is crucial to obtain a sample with good crystallinity), the solution was filtered through a short Celite pad into a vial and placed in a tube with Et₂O to crystallize by slow vapor diffusion at room temperature. After 72 h a crop of pale green square plates was collected and dried under high vacuum overnight. This yields 92mg of pure **3**

The anionic composition of **3** was initially refined with XRD to be Br/Cl = 65/35. Microanalysis (C, H, N, Br, Cl) is in agreement with XRD data.

Resonances of PPh₃ ligand in **3** are significantly broadened both in ¹H and ¹³C measurements. Measurements at elevated temperature were required to assign proton resonances.

¹H NMR (400 MHz, CD₂Cl₂, 40°C) δ 9.66 (d, *J* = 1.6 Hz, 1H, H13), 8.17 (d, *J* = 6.6 Hz, 1H, py-H2 or H2'), 7.56 (t, *J* = 7.6 Hz, 1H, py-H1), 7.50 (d, *J* = 1.9 Hz, 1H, H3), 7.47 (t, *J* = 7.8 Hz, 1H, H6'), 7.40 (t, *J* = 7.8 Hz, 1H, H6), 7.33 (dd, *J* = 7.8, 1.4 Hz, 1H, H5' or 7'), 7.30 (dd, *J* = 7.8, 1.4 Hz, 1H, H5' or 7'), 7.19 (dd, *J* = 4.4, 1.4 Hz, 1H, H5 or 7), 7.17 (dd, *J* = 4.2, 1.4 Hz, 1H, H5 or 7), 7.09 (d, *J* = 1.9 Hz, 1H, H4), 6.93 (d, *J* = 13.3 Hz, 1H, H8 or H9), 6.88 (d, *J* = 6.7 Hz, 1H, py-H2 or H2'), 5.08 (dd, *J*_{HH} = 15.8, *J*_{PH} = 1.8 Hz, 1H, H10 or H11), 5.02 (d, *J* = 13.2 Hz, 1H, H8 or H9), 4.73 (dd, *J*_{HH} = 15.6, *J*_{PH} = 2.7 Hz, 1H, H10 or H11), 4.67 (s, 1H, H12), 3.19 (sept, *J* = 8 Hz, 1H, dipp-CH(CH₃)₂), 2.40 (sept, *J* = 8 Hz, 1H, dipp-CH(CH₃)₂), 2.32 (sept, *J* = 8 Hz, 1H, dipp-CH(CH₃)₂), 2.13 (sept, *J* = 8 Hz, 1H, dipp-CH(CH₃)₂), 1.38 (d, *J* = 6.8 Hz, 3H, dipp-CH(CH₃)₂), 1.27 (d, *J* = 4.7 Hz, 3H, dipp-CH(CH₃)₂), 1.25 (d, *J* = 4.7 Hz, 3H, dipp-CH(CH₃)₂), 1.14 (d, *J* = 6.9, 3H, dipp-CH(CH₃)₂), 1.10 (d, *J* = 6.8 Hz, 3H, dipp-CH(CH₃)₂), 1.01 (d, *J* = 6.8 Hz, 3H, dipp-CH(CH₃)₂), 0.96 (t, *J* = 6.7 Hz, 6H, dipp-CH(CH₃)₂), -7.20 (d, *J* = 101.0 Hz, 1H, Ru-H).

¹³C NMR (101 MHz, CD₂Cl₂, 25°C) *J* constants values are given for CP couplings: δ 207.61 (d, *J* = 6.6 Hz, Ru-CO), 195.38 (d, *J* = 6.3 Hz, Ru-C_nNHC), 158.30 (d, *J* = 8.1 Hz, Ru-C_{abn}NHC), 156.62 (d, *J* = 3.4 Hz, py-Cq), 156.03 (s, py-Cq), 147.09 (s, dipp-Cq), 146.54 (s, dipp-Cq), 145.50 (s, dipp-Cq), 144.92 (s, dipp-Cq), 138.09 (s, py-C1), 136.92 (s, dipp-Cq), 135.36 (s, C13), 131.68 (s, dipp-Cq), 130.14 (s, C6'), 129.65 (s, C6), 127.33 (s, C12), 125.45 (s, py-C3), 124.16 (s, C3), 123.98 (s, C5 or C7), 123.93 (s, C5 or C7), 123.68 (s, py-C2), 123.63 (s, C5' or C7'), 123.61 (s, C5' or C7'), 120.73 (s, C3), 56.52 (d, *J* = 5.2 Hz, abnormal methylene CH₂), 55.62 (s, normal methylene CH₂), 28.62 (s, dipp-CH(CH₃)₂), 28.60 (s, dipp-CH(CH₃)₂), 28.28 (s, dipp-CH(CH₃)₂), 28.06 (s, dipp-CH(CH₃)₂), 25.71 (s, dipp-CH(CH₃)₂), 25.58 (s, dipp-CH(CH₃)₂), 24.38 (s, dipp-CH(CH₃)₂), 23.66 (s, dipp-CH(CH₃)₂), 23.25 (s, dipp-CH(CH₃)₂), 22.07 (s, dipp-CH(CH₃)₂), 21.91 (s, dipp-CH(CH₃)₂).

³¹P{¹H} NMR (162 MHz, CD₂Cl₂, 25°C) δ 33.42 (s).

IR(film): ν = 1927 cm⁻¹

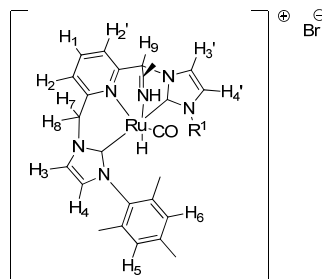
ESI/MS: Calcd. C₅₆H₆₁N₅OPRu⁺ ([Ru(L2)(PPh₃)HCO]⁺) 952.37. Found: 100/30 ratio 951.84/690.28 (3-PPh₃)

EA: Calcd. C₅₆H₆₁N₅OPBr_{0.65}Cl_{0.35}Ru: C 66.17, H 6.05, N 6.89, Br 5.11, Cl 1.22. Found: C 65.95, H 6.11, N 6.83, Br 5.27, Cl

Complex 4

3 mL of 1M solution of BEMP in hexane were added to a stirred suspension of [RuHCICO(PPh₃)₃] (952.4 mg, 1 mmol), ligand **L1** (639.4 mg, 1 mmol) in ca. 40 mL CH₃CN at room temperature in a flask, equipped with a reflux condenser. The mixture was then heated to 70°C and dwelled for 16 hours. During this time suspended solid dissolves resulting in a golden brown solution. After cooling down, the solution was filtered using the cannula tipped with 1.7 micron glass microfiber filter (VWR). The resulting filtrate was evaporated to give brown oil. 35 mL THF were

4: R¹=Mes
asterisk used for a nitrile modified sidearm



then added to the oil to give clear solution. Within 5 – 10 minutes upon stirring a bright yellow solid precipitates. Filtration, washing with a little THF and diethyl ether and finally drying in high vacuum yields 470 mg of **4** (64.6% on [Ru] basis). Assignments are made on the basis of 2D experiments: gCOSY, gHMQC.

¹H NMR (400 MHz, CD₂Cl₂, 25°C) δ 9.89 (s, 1H, NH-imine), 8.68 (d, *J* = 7.6 Hz, 1H, H2'), 8.53 (s, 1H, H9), 8.40 (d, *J* = 1.8 Hz, 1H, H3'), 7.96 (t, *J* = 7.7 Hz, 1H, H1), 7.60 (d, *J* = 7.7 Hz, 1H, H2), 7.29 (d, *J* = 1.8 Hz, 1H, H3), 7.02 (s, 1H, mes', H5' or H6'), 6.99 (s, 1H, mes', H5' or H6'), 6.88 (s, 1H, mes, H5 or H6), 6.86 (s, 1H, mes, H5 or H6), 6.77 (d, *J* = 1.8 Hz, 1H, H4), 6.70 (d, *J* = 1.8 Hz, 1H, H4'), 5.40 (d, *J* = 13.7 Hz, 1H, H7 or H8), 5.30 (d, *J* = 8.0 Hz, 1H, H7 or H8), 2.58 (s, 3H, imine CH₃), 2.35 (s, 3H, mes' *p*-CH₃), 2.28 (s, 3H, mes *p*-CH₃), 2.08 (s, 3H, mes' *o*-CH₃), 1.83 (s, 3H, mes *o*-CH₃), 1.76 (s, 3H, mes *o*-CH₃), 1.50 (s, 3H, mes' *o*-CH₃), -12.06 (s, 1H).

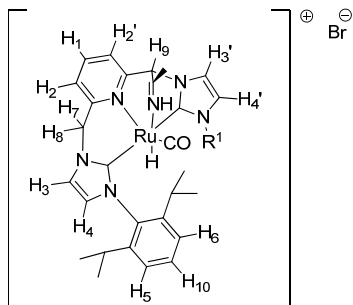
¹³C NMR (100 MHz, CD₂Cl₂, 25°C) all resonances appear as singlets: δ 206.11 (Ru-CO), 191.87 (Ru-C), 191.17 (Ru-C), 176.64 (py- Cq'), 156.91 (py- Cq), 154.50 (imine-Cq), 139.17 (mes- Cq), 138.86 (py-C1), 138.51 (mes- Cq), 137.06 (mes- Cq), 136.34 (mes- Cq), 136.09 (mes- Cq), 135.86 (mes- Cq), 135.58 (mes- Cq), 134.44 (mes- Cq), 129.54 (mes', C5' or C6'), 128.52 (mes', C5' or C6'), 128.46 (mes, C5 or C6), 128.34 (mes, C5 or C6), 125.97 (C2'), 123.51 (C2), 122.43 (C3'), 121.68 (C4'), 121.32 (C3), 121.27 (C4), 64.04 (methylene-CH(CR=CNH)-), 56.84 (methylene CH₂), 28.63 (imine CH₃), 20.85 (mes' *p*-CH₃), 20.77 (mes *p*-CH₃), 17.98 (mes' *o*-CH₃), 17.86 (mes *o*-CH₃), 17.36 (mes *o*-CH₃), 16.94 (mes' *o*-CH₃).

IR(film): ν = 1967, 1923 cm⁻¹

ESI/MS: Calcd. C₃₄H₃₇N₆ORu⁺ ([Ru(L1)HCO(CH₃CN)]⁺) 647.21.. Found: 647.28

EA: Calcd. C₃₄H₃₇N₆OBrRu: C 56.20, H 5.13, N 11.57. Found: C 56.47, H 5.31, N 11.46.

5: R¹=Dipp
asterisk used for a nitrile modified sidearm



Complex 5

3 mL of 1M solution of BEMP in hexane were added to a stirred suspension of [RuHClCO(PPh₃)₃] (952.4 mg, 1 mmol), ligand **L2** (719.2, 1 mmol) in ca. 45 mL acetonitrile at room temperature in a flask, equipped with a reflux condenser. The mixture was then heated to 70°C and dwelled overnight. During first 30 minutes upon heating the suspended solid dissolves giving bright orange-brown solution. Overnight a crop of bright yellow solid precipitates. The solid was isolated by filtration using the cannula tipped with 1.7 micron glass microfiber filter and washed twice with 5 mL THF and then

with 20 mL diethyl ether and dried overnight under high vacuum. Yield 460 mg of **5** (56.8% on [Ru] basis).

Single crystals were grown from dichloromethane solution by slow diffusion of diethyl ether vapor.

Assignments are made on the basis of 2D experiments: gCOSY, gHMQC

¹H NMR: (400 MHz, CD₂Cl₂, 25°C) δ 10.13 (s, 1H, NH-imine), 8.71 (d, *J* = 7.7 Hz, 1H, H2'), 8.59 (d, *J* = 1.5 Hz, 1H, H9), 8.47 (d, *J* = 1.9 Hz, 1H, H3'), 8.00 (t, *J* = 7.7 Hz, 1H, H1), 7.66 (d, *J* = 7.7 Hz, 1H, H2), 7.45 (t, *J* = 7.8 Hz, 1H, H10'), 7.34 (t, *J* = 7.8 Hz, 1H, H10), 7.30 (d, *J* = 1.9 Hz, 1H, H3), 7.29 – 7.23 (m, 2H, H5', 6'), 7.16 (d, *J* = 6.6 Hz, 1H, H5 or 6), 7.12 (d, *J* = 7.8 Hz, 1H, H5 or 6), 6.86 (d, *J* = 1.9 Hz, 1H, H4), 6.81 (d, *J* = 1.8 Hz, 1H, H4'), 5.35 (d, *J* = 13.5 Hz, 1H, H7 or 8), 5.25 (d, *J* = 13.5 Hz, 1H, H7 or 8), δ 2.61 (d, *J* = 1.3 Hz, 1H, imine CH₃), 2.47 (m, 1H, dipp-CH(CH₃)₂), 2.29 (m, 2H, dipp-CH(CH₃)₂), 2.16 (m, 1H, dipp-CH(CH₃)₂), 1.26 (d, *J* = 6.9 Hz, 3H, dipp-CH(CH₃)₂), 1.20 (d, *J* = 6.8 Hz, 3H, dipp-CH(CH₃)₂), 1.10 (d, *J* = 6.8 Hz, 3H, dipp-CH(CH₃)₂), 1.02 (d, *J* = 6.9 Hz, 6H, dipp-CH(CH₃)₂), 1.00 (d, *J* = 6.9 Hz, 3H, dipp-CH(CH₃)₂), 0.88 (d, *J* = 6.7 Hz, 3H, dipp-CH(CH₃)₂), 0.80 (d, *J* = 6.9 Hz, 3H, dipp-CH(CH₃)₂), -12.03 (s, 1H, Ru-H).

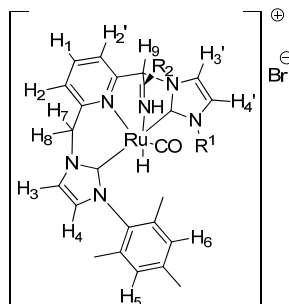
¹³C NMR: (101 MHz, CD₂Cl₂, 25°C) all resonances appear as singlets: δ 205.99 (Ru-CO), 194.19 (Ru-C), 192.72 (Ru-C), 177.18 (py-Cq'), 157.01 (py-Cq), 154.99 (imine Cq), 148.12 (dipp-Cq), 146.82 (dipp-Cq), 146.42 (dipp-Cq), 145.47 (dipp-Cq), 139.30 (py-C1), 136.95 (dipp-Cq), 136.48 (dipp-Cq), 130.20 (C10'), 129.72 (C10), 126.46 (py-C2'), 124.88 (C4), 124.83 (C5' or C6'), 123.99 (C4'), 123.81 (py-C2), 123.75 (C5 or C6), 123.51 (C5 or C6), 123.35 (C5' or C6'), 122.25 (C3'), 120.77 (C3), 64.48 (methylene' -CH(CR=CNH)-), 57.28 (methylene CH₂), 28.96 (imine-CH₃), 28.78 (dipp-CH(CH₃)₂), 28.68 (dipp-CH(CH₃)₂), 28.66 (dipp-CH(CH₃)₂), 28.26 (dipp-CH(CH₃)₂), 26.57 (dipp-CH(CH₃)₂), 26.36 (dipp-CH(CH₃)₂), 25.85 (dipp-CH(CH₃)₂), 22.57 (dipp-CH(CH₃)₂), 22.06 (dipp-CH(CH₃)₂), 21.89 (dipp-CH(CH₃)₂), 21.63 (dipp-CH(CH₃)₂).

IR(film): ν = 1916 cm⁻¹

ESI/MS: Calcd. C₄₂H₅₂N₇ORu⁺ ([Ru(L2)CH₃CNHCO]⁺) 731.30. Found: 731.36

EA: Calcd. C₄₂H₅₂N₇OBrRu: C 59.22, H 6.15, N 11.51. Found: C 59.42, H 5.86, N 11.22.

6: R¹=Mes, R²=Ph
asterisk used for a nitrile modified sidearm



Complex 6

200 mg of **1** (0.291 mmol) was suspended in 3 mL of benzonitrile and 0.3 mL of 1M solution of BEMP in hexane were added. The mixture was then heated to 70°C and dwelled for 16 hours. During this time solution turned red and solid dissolved. After few hours at 70°C yellow precipitate appeared. After overnight reaction the suspension was allowed to cool and 25 mL diethyl ether were added to precipitate more yellow solid. The solution was filtered and washed twice with 10 mL ether. Resulting rich yellow solid was dried overnight under high vacuum to yield 210 mg of **6** (91.6%).

^1H NMR (400 MHz, CD_2Cl_2 , 25°C) δ 10.66 (s, 1H, NH-imine), 9.13 (d, $J = 1.8$ Hz, 1H, H9), 8.89 (d, $J = 7.6$ Hz, 1H, H2'), 8.86 (d, $J = 1.8$ Hz, 1H, H3'), 8.18 (d, $J = 6.8$ Hz, 2H, R^2 *o*-CH), 7.90 (t, $J = 7.7$ Hz, 1H, H1), 7.73 (d, $J = 7.6$ Hz, 1H, H2), 7.60 (m, Hz, 4H, R^2 *o,m,p*-CH), 7.47 (d, $J = 1.8$ Hz, 1H, H3), 7.07 (s, 1H, mes', H5' or H6'), 7.05 (s, 1H, mes', H5' or H6'), 6.91 (s, 1H, mes, H5 or H6), 6.87 (s, 1H, mes, H5 or H6), 6.80 (d, $J = 1.8$ Hz, 1H, H4), 6.71 (d, $J = 1.8$ Hz, 1H, H4'), 5.58 (d, $J = 13.9$ Hz, 1H, H7 or H8), 5.39 (d, $J = 13.4$ Hz, 1H, H7 or H8), 2.40 (s, 3H, mes *p*- CH_3), 2.30 (s, 3H, mes' *p*- CH_3), 2.14 (s, 3H, mes *o*- CH_3), 1.81 (s, 6H, mes' *o*- CH_3), 1.47 (s, 3H, mes *o*- CH_3), -11.44 (s, 1H, Ru-H).

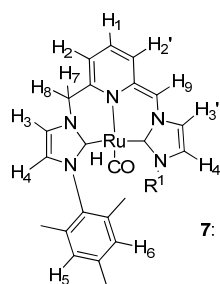
^{13}C NMR (100 MHz, CD_2Cl_2 , 25°C) all resonances appear as singlets: δ 206.24 (Ru-CO), 191.80 (Ru-C), 191.55 (Ru-C), 172.56 (py- Cq'), 157.36 (py- Cq), 155.13 (imine-Cq), 139.74 (arom Cq), 139.27 (py-C1), 138.94 (arom Cq), 137.55 (arom Cq), 136.86 (arom Cq), 136.46 (arom Cq), 136.25 (arom Cq), 136.01 (arom Cq), 134.97 (arom Cq), 133.49 (arom Cq), 132.73 (R^2 CH_{arom}), 130.08 (mes, C5' or C6'), 129.97 (R^2 CH_{arom}), 128.98 (mes, C5 or C6), 128.74 (mes, C5 or C6), 128.66 (mes, C5' or C6'), 126.97 (R^2 CH_{arom}), 126.55 (C2'), 124.13 (C2), 123.23 (C3'), 121.99 (br, C3 and C4), 121.69 (C4'), 62.04 (methylene' $-\text{CH}(\text{CR}=\text{CNH})-$), 57.10 (methylene CH_2), 21.35 (mes *p*- CH_3), 21.19 (mes' *p*- CH_3), 18.48 (mes *o*- CH_3), 18.31 (2C, mes' *o*- CH_3), 17.78 (mes *o*- CH_3), 17.55 (mes *o*- CH_3).

For carbons, denoted as "arom Cq" distinction between quaternary carbons of mesityl wingtip and benzonitrile quaternary carbon cannot be made unambiguously

IR(film): $\nu = 1970, 1922 \text{ cm}^{-1}$

ESI/MS: Calcd. $\text{C}_{39}\text{H}_{39}\text{N}_6\text{ORu}^+$ ($[\text{Ru}(\text{L1})(\text{PhCN})\text{HCO}]^+$) 709.22. Found: 709.33

EA: Calcd. $\text{C}_{39}\text{H}_{39}\text{N}_6\text{OBrRu}$: C 59.39, H 4.98, N 10.65. Found: C 59.67, H 5.13, N 10.71.



7: $\text{R}^1 = \text{Mes}$

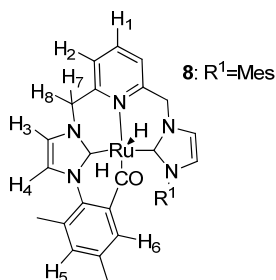
Generation of complex 7

10 mg of **2** (13.7 μmol) was reacted with 1.1 eq of KO^tBu (1.7 mg, 15.1 μmol) in 0.65 mL THF-d_8 at room temperature. The brown solution was filtered in Young tube through a short Celite plug. The procedure was repeated several times for NMR measurements. Complex **7** was not isolated due to its poor stability. Due to in situ preparation procedure we observed KO^tBu , $^t\text{BuOH}$ and THF as major impurities

^1H NMR (400 MHz, THF) δ 7.33 (d, $J = 1.9$ Hz, 1H, H3'), 6.91 (s, 1H, either of H5,5',6,6'), 6.83 (d, $J = 1.9$ Hz, 1H, H4'), 6.79 (s, 1H, either of H5,5',6,6'), 6.68 (s, 1H, either of H5,5',6,6'), 6.66 (s, 1H, either of H5,5',6,6'), 6.48 (d, $J = 1.7$ Hz, 1H, H3), 6.29 (d, $J = 1.7$ Hz, 1H, H4), 6.27 – 6.18 (m, 2H, H1 and H2 or H2'), 5.83 (s, 1H, H9), 4.90 (d, $J = 12.0$ Hz, 1H, H7 or 8), 4.81 (dd, $J = 7.5, 2.3$ Hz, 1H, H2 or H2'), 4.74 (d, $J = 12.4$ Hz, 1H, H7 or 8), 2.26 (s, 3H, CH_3 -Mes), 2.22 (s, 3H, CH_3 -Mes), 2.16 (s, 3H, CH_3 -Mes), 1.95 (s, 3H, free acetonitrile), 1.89 (s, 3H, CH_3 -Mes), 1.87 (s, 3H, CH_3 -Mes), -11.80 (s, 1H, Ru-H).

^{13}C NMR (101 MHz, THF) δ 210.81 (s, Ru-CO), 204.64 (s, Ru-C_{NHC}), 184.27 (s, Ru-C_{NHC}), 175.51 (s, py-Cq), 151.71 (s, py-Cq), 140.67 (s, Mes-Cq), 139.66 (s, Mes-Cq), 138.11 (s, Mes-Cq), 137.75 (s, Mes-Cq), 137.70 (s, Mes-Cq), 136.38 (s, Mes-Cq), 134.75 (s, Mes-Cq), 130.20 (s, C_{py}), 130.17 (s, mes-CH), 128.75 (s, mes-CH), 128.17 (s, mes-CH), 128.13 (s, mes-CH), 122.37 (s, C_{imi}), 120.80 (s, C_{imi}), 119.85 (s, C_{imi}), 119.27 (s, C_{py}), 118.96 (s, C_{imi}), 112.69 (s, C_{py}), 63.52 (s, sidearm C), 58.63 (s, sidearm C), 20.99 (s, CH₃-Mes), 20.97 (s, CH₃-Mes), 19.96 (s, CH₃-Mes), 19.86 (s, CH₃-Mes), 18.98 (s, CH₃-Mes), 18.97 (s, CH₃-Mes).

ESI/MS: Calcd. C₃₂H₃₂N₅ORu⁺ ([Ru(L2)CO]⁺) 604.17. Found: 604.32



Generation of complex 8

The sample of **7**, generated in the previous run in a Wilmad Quick Pressure tube was exposed to 3 bar of H₂ and heated at 40°C for 5 minutes. ¹H spectrum was recorded. Complex **8** was not isolated due to its poor stability. Traces of unreacted **7** were observed in ¹H NMR spectrum

¹H NMR (400 MHz, THF) δ 7.63 (t, $J = 7.6$ Hz, 1H, H1), 7.39 (d, $J = 7.6$ Hz, 2H, H2), 7.25 (d, $J = 1.9$ Hz, 2H, H3), 6.73 (s, 2H, H5 or 6), 6.72 (s, 2H, CH-Mes), 6.61 (d, $J = 1.9$ Hz, 2H, H4), 5.59 (d, $J = 12.4$ Hz, 2H, H7 or 8), 5.33 (d, $J = 12.6$ Hz, 2H, H7 or 8), 2.20 (s, 6H, CH₃-Mes), 1.96 (s, 6H, CH₃-Mes), 1.92 (s, 6H, CH₃-Mes), -5.94 (s, 2H, Ru-H).

Generation of complex 9

The sample of **8**, generated in the previous run in a Wilmad Quick Pressure tube was exposed to 3 bar of CO₂. An insoluble pale yellow precipitate formed immediately. The solid was allowed to settle and the solvent was filtered off using filter tipped cannula attached to the syringe. Remaining solid was redissolved in CD₂Cl₂ and analyzed by ¹H NMR at -15°C. Complex **9** was prepared as a part of reactivity studies, thus, the isolation is not claimed. The ¹H NMR data is presented in the Chapter.

Reaction of complex 7 with CO₂

The sample of **7**, generated in the previous run in a Wilmad Quick Pressure tube in DMF-d₇ was exposed to 3 bar of CO₂ and heated at 70°C overnight. ¹H spectrum was recorded. Resulting mixture of products contained complex **10** as the major species. Traces of complex **10b** could also be detected together with minor unidentified impurities. The ¹H NMR data are discussed and presented in the Chapter body.

Direct generation of 10/10b in reaction with CO₂ in the presence of DBU

5 mg of **1** (7.28 μmol) was added to 0.65 mL DMF-d₇ containing 10 eq. DBU per Ru. The solution was transferred into a light wall Wilmad NMR pressure tube, filled with 2 bar CO₂ and heated overnight at 70°C. We observed clean formation of **3** and **3b** in 64/36 ratio. Similar experiment was

conducted with ^{13}C to probe the C-H coupling between added CO_2 and methylene protons and to detect ^{13}C resonances of added CO_2 in **10** and **10b**. The data summary is presented in the chapter.

Selected NMR data for **10**: ^1H NMR (500 MHz, DMF-d_7) δ 8.11 (t, $J = 7.7$ Hz, 1H, H1), δ 7.89 (d, $J = 7.7$ Hz, 1H, H2 or H2'), 7.86 (d, $J = 7.6$ Hz, 1H, H2 or H2'), 7.83 (d, $J = 1.9$ Hz, 1H, H3 or H3'), 7.70 (d, $J = 1.9$ Hz, 1H, H3 or H3'), 7.13 (d, $J = 1.8$ Hz, 1H, H4 or H4'), 7.09 (d, $J = 1.9$ Hz, 1H, H4 or H4'), 6.92 – 6.85 (m, 4H, H_{Mes}), 6.12 (s, 1H, H9), 5.81 (d, $J = 13.8$ Hz, 1H, H7 or H8), 5.29 (d, $J = 13.4$ Hz, 1H, H7 or H8), -16.76 (s, 1H, Ru-H).

Crystal structure analysis details

X-ray intensities were measured on a Bruker Kappa ApexII diffractometer with sealed tube and Triumph monochromator ($\lambda = 0.71073$ Å) at a temperature of 150(2) K. The intensities were integrated using Eval15. Absorption correction and scaling was performed with SADABS. The structures were solved using the programs SHELXS-97 (compounds **1**, **1-BF4**, **4**, **6**), SHELXT(compound **5**) or DIRDIF-08 (compound **3**). Least-squares refinement was performed with SHELXL-97 (**1**) or SHELXL-2013 (**1-BF4**, **3**, **4**, **5**, **6**) against F^2 of all reflections. Non-hydrogen atoms were refined with anisotropic displacement parameters. Hydrogen atoms in **1** were included in calculated positions. All hydrogen atoms in **1-BF4** were located in difference Fourier maps. In **4**, **5**, **6** and **3** the hydride H-atom was located in difference Fourier maps and all other H-atoms included in calculated positions. The hydride H-atom in **1**, **3**, **4** and the N-H hydrogen in **4** were allowed to refine isotropically. All other hydrogen atoms were refined with a riding model. Geometry calculations and checking for higher symmetry was performed with the PLATON program

CCDC 972638 (compound **1**), 972639 (**1-BF4**), 972640 (**4**), 972641 (**5**), 972642 (**6**) and 972643 (**3**) contain the supplementary crystallographic data for this paper. These data can be obtained free of charge from The Cambridge Crystallographic Data Centre via www.ccdc.cam.ac.uk/data_request/cif.

Compound **1**

$\text{C}_{32}\text{H}_{34}\text{Br}_{0.56}\text{Cl}_{0.44}\text{N}_5\text{ORu}$ + disordered solvent, Fw = 666.06, yellow needle, $0.58 \times 0.22 \times 0.21$ mm³, monoclinic, Cc (no. 9), $a = 14.6916(3)$, $b = 19.3357(3)$, $c = 12.8728(3)$ Å, $\alpha = 111.282(1)^\circ$, $V = 3407.42(11)$ Å³, $Z = 4$, $D_x = 1.298$ g/cm³, $\mu = 1.18$ mm⁻¹. 43803 Reflections were measured up to a resolution of $(\sin \theta/\lambda)_{\text{max}} = 0.77$ Å⁻¹. 13049 Reflections were unique ($R_{\text{int}} = 0.019$), of which 12371 were observed [$I > 2\sigma(I)$]. The crystal structure contains large voids (677 Å³ / unit cell) filled with disordered solvent molecules. Their contribution to the structure factors was secured by back-Fourier transformation using the SQUEEZE routine of the PLATON software, resulting in 203 electrons / unit cell. The halogen position was refined with a model for substitutional disorder (56% bromine, 44% chlorine). 381 Parameters were refined with 4 restraints (floating origin restraints, Ru-H and Ru-Cl distance restraints). $R1/wR2$ [$I > 2\sigma(I)$]: 0.0183 / 0.0445. $R1/wR2$ [all refl.]: 0.0201 / 0.0449. $S = 1.046$. Flack parameter $x = 0.018(4)$. Residual electron density between -0.25 and 0.26 e/Å³.

Compound 1·BF₄

[C₃₄H₃₇N₆ORu](BF₄) + disordered solvent, Fw = 733.57, pale yellow block, 0.31 × 0.24 × 0.16 mm³, triclinic, P $\bar{1}$ (no. 2), a = 10.2126(3), b = 12.2383(3), c = 16.6522(4) Å, α = 96.359(1), β = 100.516(2), γ = 101.949(1) °, V = 1977.96(9) Å³, Z = 2, D_x = 1.232 g/cm³, μ = 0.45 mm⁻¹. 29025 Reflections were measured up to a resolution of (sin θ/λ)_{max} = 0.65 Å⁻¹. 9089 Reflections were unique (R_{int} = 0.017), of which 8311 were observed [I > 2 σ (I)]. The crystal structure contains large voids (401 Å³ / unit cell) filled with disordered solvent molecules. Their contribution to the structure factors was secured by back-Fourier transformation using the SQUEEZE routine of the PLATON software, resulting in 122 electrons / unit cell. The BF₄ anion was refined with a model for orientational disorder. 468 Parameters were refined with 142 restraints (distances, angles and displacement parameters of disordered BF₄). R1/wR2 [I > 2 σ (I)]: 0.0229 / 0.0583. R1/wR2 [all refl.]: 0.0262 / 0.0597. S = 1.039. Residual electron density between -0.49 and 0.37 e/Å³.

Compound 4

[C₃₄H₃₇N₆ORu]Br · CH₃OH + disordered solvent, Fw = 758.72, yellow plate, 0.39 × 0.29 × 0.08 mm³, monoclinic, C2/c (no. 15), a = 21.7318(6), b = 11.4791(3), c = 30.4353(7) Å, α = 107.522(1) °, V = 7240.2(3) Å³, Z = 8, D_x = 1.392 g/cm³, μ = 1.58 mm⁻¹. 39640 Reflections were measured up to a resolution of (sin θ/λ)_{max} = 0.65 Å⁻¹. 8298 Reflections were unique (R_{int} = 0.016), of which 7514 were observed [I > 2 σ (I)]. The crystal structure contains large voids (608 Å³ / unit cell) filled with disordered THF solvent molecules. Their contribution to the structure factors was secured by back-Fourier transformation using the SQUEEZE routine of the PLATON software, resulting in 130 electrons / unit cell. 426 Parameters were refined with no restraints. R1/wR2 [I > 2 σ (I)]: 0.0253 / 0.0593. R1/wR2 [all refl.]: 0.0291 / 0.0607. S = 1.103. Residual electron density between -0.43 and 0.45 e/Å³.

Compound 5

[C₄₀H₄₉N₆ORu]Br + disordered solvent, Fw = 810.83, yellow needle, 0.22 × 0.11 × 0.07 mm³, monoclinic, P2₁/n (no. 14), a = 13.7607(4), b = 17.3199(5), c = 18.3721(5) Å, α = 108.243(2) °, V = 4158.6(2) Å³, Z = 4, D_x = 1.295 g/cm³, μ = 1.37 mm⁻¹. The crystal appeared to be cracked into two fragments and therefore integrated with two orientation matrices. Only non-overlapping reflections were used for the structure analysis. 44632 Reflections were measured up to a resolution of (sin θ/λ)_{max} = 0.65 Å⁻¹. 9091 Reflections were unique (R_{int} = 0.068), of which 6370 were observed [I > 2 σ (I)]. The crystal structure contains large voids (585 Å³ / unit cell) filled with disordered solvent molecules. Their contribution to the structure factors was secured by back-Fourier transformation using the SQUEEZE routine of the PLATON software, resulting in 180 electrons / unit cell. 451 Parameters were refined with no restraints. R1/wR2 [I > 2 σ (I)]: 0.0554 / 0.1457. R1/wR2 [all refl.]: 0.0888 / 0.1622. S = 1.039. Residual electron density between -2.06 and 1.02 e/Å³.

Compound 6

[C₃₉H₃₉N₆ORu]Br · CH₃OH, Fw = 820.78, yellow plate, 0.32 × 0.21 × 0.04 mm³, monoclinic, P2₁/c (no. 14), a = 18.3580(9), b = 14.6031(8), c = 14.0683(7) Å, α = 93.583(3) °, V = 3764.1(3) Å³, Z = 4, D_x = 1.448 g/cm³, μ = 1.52 mm⁻¹. 51908 Reflections were measured up to a resolution of (sin θ/λ)_{max} = 0.65 Å⁻¹. 8633 Reflections were unique (R_{int} = 0.039), of which 6661 were observed [I > 2σ(I)]. 459 Parameters were refined with no restraints. R1/wR2 [I > 2σ(I)]: 0.0369 / 0.0866. R1/wR2 [all refl.]: 0.0560 / 0.0942. S = 1.036. Residual electron density between -0.61 and 1.93 e/Å³.

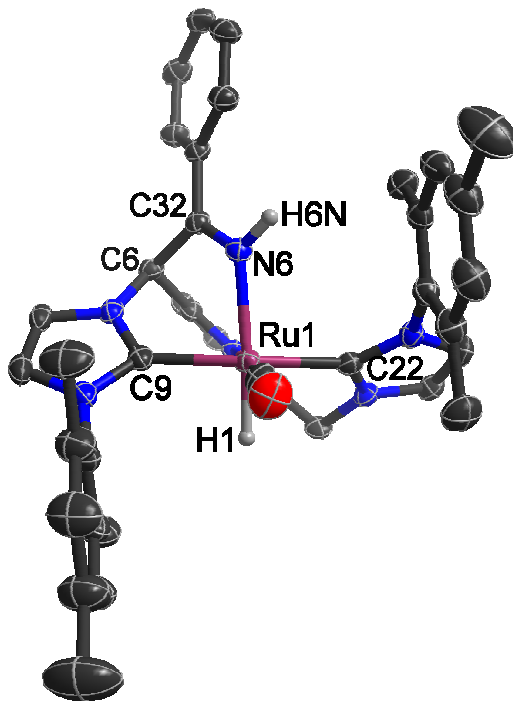


Figure 5.13 X-ray crystal structure of **6** (ellipsoids at the 50% probability level, disordered solvent molecules and all hydrogens, except hydride and imine are omitted for clarity). Selected bond lengths [Å]: Ru1-N6 2.143(2), Ru1-C9 2.047(3), Ru1-C22 2.068(3), Ru1-C39 1.817(3), Ru1-N1 2.184(2)

Compound 3

[C₅₆H₆₁N₅OPRu]Br_{0.65}Cl_{0.35} · 2CH₃CN + disordered solvent, Fw = 1098.59, colorless plate, 0.38 × 0.21 × 0.12 mm³, triclinic, P $\bar{1}$ (no. 2), a = 10.6089(3), b = 15.4581(2), c = 18.9255(4) Å, α = 70.365(1), β = 88.255(1), γ = 84.453(1) °, V = 2909.47(11) Å³, Z = 2, D_x = 1.254 g/cm³, μ = 0.80 mm⁻¹. 54664 Reflections were measured up to a resolution of (sin θ/λ)_{max} = 0.65 Å⁻¹. 13336 Reflections were unique (R_{int} = 0.023), of which 11685 were observed [I > 2σ(I)]. The crystal structure contains large voids (194 Å³ / unit cell) filled with disordered solvent molecules. Their contribution to the structure factors was secured by back-Fourier transformation using the SQUEEZE routine of the

PLATON software resulting in 35 electrons / unit cell. One isopropyl group was refined with a model for orientational disorder, and the halogen position showed substitutional disorder (65% bromine, 35% chlorine). 671 Parameters were refined with 130 restraints (distances, angles and displacement parameters of isopropyl groups). R1/wR2 [I > 2 σ (I)]: 0.0286 / 0.0672. R1/wR2 [all refl.]: 0.0356 / 0.0697. S = 1.045. Residual electron density between -0.61 and 0.57 e/Å³.

5.7 Notes and References

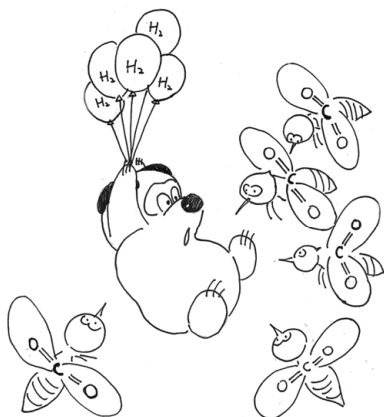
- (1) Balaraman, E.; Milstein, D. In *Top. Organomet. Chem.* **2014**, *77*, 1.
- (2) Gunanathan, C.; Milstein, D. *Science* **2013**, *341*.
- (3) Gunanathan, C.; Milstein, D. *Acc. Chem. Res.* **2011**, *44*, 588.
- (4) Chianese Anthony, R.; Crabtree Robert, H. In *Activation and Functionalization of C-H Bonds*; ACS publishing, **2004**, *885*, 169.
- (5) Benito-Garagorri, D.; Kirchner, K. *Acc. Chem. Res.* **2008**, *41*, 201.
- (6) Friedrich, A.; Drees, M.; Käss, M.; Herdtweck, E.; Schneider, S. *Inorg. Chem.* **2010**, *49*, 5482.
- (7) Huff, C. A.; Sanford, M. S. *ACS Catal.* **2013**, *3*, 2412.
- (8) Filonenko, G. A.; Conley, M. P.; Copéret, C.; Lutz, M.; Hensen, E. J. M.; Pidko, E. A. *ACS Catal.* **2013**, *3*, 2522.
- (9) Filonenko, G. A.; van Putten, R.; Schulpen, E. N.; Hensen, E. J. M.; Pidko, E. A. *ChemCatChem* **2014**, *6*, 1526.
- (10) Hopkinson, M. N.; Richter, C.; Schedler, M.; Glorius, F. *Nature* **2014**, *510*, 485.
- (11) Herrmann, W. A. *Angew. Chem. Int. Ed.* **2002**, *41*, 1290.
- (12) Velazquez, H. D.; Verpoort, F. *Chem. Soc. Rev.* **2012**, *41*, 7032.
- (13) Nolan, S. P.; Clavier, H. *Chem. Soc. Rev.* **2010**, *39*, 3305.
- (14) Ortega, N.; Tang, D.-T. D.; Urban, S.; Zhao, D.; Glorius, F. *Angew. Chem. Int. Ed.* **2013**, *52*, 9500
- (15) Witt, J.; Pöthig, A.; Kühn, F. E.; Baratta, W. *Organometallics* **2013**, *32*, 4042.
- (16) Fernández, F. E.; Puerta, M. C.; Valerga, P. *Organometallics* **2012**, *31*, 6868.
- (17) Ortega, N.; Tang, D.-T. D.; Urban, S.; Zhao, D.; Glorius, F. *Angew. Chem. Int. Ed.* **2013**, *52*, 9500.
- (18) Sun, Y.; Koehler, C.; Tan, R.; Annibale, V. T.; Song, D. *Chem. Commun.* **2011**, *47*, 8349.
- (19) del Pozo, C.; Iglesias, M.; Sánchez, F. I. *Organometallics* **2011**, *30*, 2180.
- (20) Schulze, B.; Escudero, D.; Friebe, C.; Siebert, R.; Görls, H.; Köhn, U.; Altuntas, E.; Baumgaertel, A.; Hager, M. D.; Winter, A.; Dietzek, B.; Popp, J.; González, L.; Schubert, U. S. *Chem. Eur. J.* **2011**, *17*, 5494.
- (21) Hernandez-Juarez, M.; Vaquero, M.; Alvarez, E.; Salazar, V.; Suarez, A. *Dalton Trans.* **2013**, *42*, 351.
- (22) Gunanathan, C.; Milstein, D. *Chem. Rev.* **2014**, *114*, 12024
- (23) Poyatos, M.; Mata, J. A.; Falomir, E.; Crabtree, R. H.; Peris, E. *Organometallics* **2003**, *22*, 1110.
- (24) Wright, J. A.; Danopoulos, A. A.; Motherwell, W. B.; Carroll, R. J.; Ellwood, S. J. *Organomet. Chem.* **2006**, *691*, 5204.
- (25) Naziruddin, A. R.; Huang, Z.-J.; Lai, W.-C.; Lin, W.-J.; Hwang, W.-S. *Dalton Trans.* **2013**, *42*, 13161.
- (26) Chung, L.-H.; Cho, K.-S.; England, J.; Chan, S.-C.; Wieghardt, K.; Wong, C.-Y. *Inorg. Chem.* **2013**, *52*, 9885.
- (27) Naziruddin, A. R.; Kuo, C.-L.; Lin, W.-J.; Lo, W.-H.; Lee, C.-S.; Sun, B.-J.; Chang, A. H. H.; Hwang, W.-S. *Organometallics* **2014**.
- (28) Peris, E. In *N-Heterocyclic Carbenes in Transition Metal Catalysis*; Glorius, F., Ed.; Springer Berlin Heidelberg: **2007**, *21*, 83.
- (29) Gründemann, S.; Kovacevic, A.; Albrecht, M.; Faller, J. W.; Crabtree, R. H. *J. Am. Chem. Soc.* **2002**, *124*, 10473.

- (30) Ellul, C. E.; Mahon, M. F.; Saker, O.; Whittlesey, M. K. *Angew. Chem. Int. Ed.* **2007**, *46*, 6343.
- (31) Day, B. M.; Pugh, T.; Hendriks, D.; Guerra, C. F.; Evans, D. J.; Bickelhaupt, F. M.; Layfield, R. A. *J. Am. Chem. Soc.* **2013**, *135*, 13338.
- (32) Danopoulos, A. A.; Winston, S.; Motherwell, W. B. *Chem. Commun.* **2002**, 1376.
- (33) Schultz, K. M.; Goldberg, K. I.; Gusev, D. G.; Heinekey, D. M. *Organometallics* **2011**, *30*, 1429.
- (34) Burling, S.; Kociok-Köhn, G.; Mahon, M. F.; Whittlesey, M. K.; Williams, J. M. J. *Organometallics* **2005**, *24*, 5868.
- (35) Schuster, O.; Yang, L.; Raubenheimer, H. G.; Albrecht, M. *Chem. Rev.* **2009**, *109*, 3445.
- (36) Kruger, A.; Albrecht, M. In *N-Heterocyclic Carbenes: From Laboratory Curiosities to Efficient Synthetic Tools*; The Royal Society of Chemistry: **2011**, 134.
- (37) Danopoulos, A. A.; Tsoureas, N.; Wright, J. A.; Light, M. E. *Organometallics* **2003**, *23*, 166.
- (38) Zuo, W.; Braunstein, P. *Dalton Trans.* **2012**, *41*, 636.
- (39) Eguillor, B.; Esteruelas, M. A.; Oliván, M.; Puerta, M. *Organometallics* **2008**, *27*, 445.
- (40) Baya, M.; Eguillor, B.; Esteruelas, M. A.; Oliván, M.; Oñate, E. *Organometallics* **2007**, *26*, 6556.
- (41) Kovacevic, A.; Grundemann, S.; Miecznikowski, J. R.; Clot, E.; Eisenstein, O.; Crabtree, R. H. *Chem. Commun.* **2002**, 2580.
- (42) Appelhans, L. N.; Zuccaccia, D.; Kovacevic, A.; Chianese, A. R.; Miecznikowski, J. R.; Macchioni, A.; Clot, E.; Eisenstein, O.; Crabtree, R. H. *J. Am. Chem. Soc.* **2005**, *127*, 16299.
- (43) Vogt, M.; Nerush, A.; Iron, M. A.; Leitius, G.; Diskin-Posner, Y.; Shimon, L. J. W.; Ben-David, Y.; Milstein, D. *J. Am. Chem. Soc.* **2013**, *135*, 17004.
- (44) Giraudon, J. M.; Mandon, D.; Sala-Pala, J.; Guerchais, J. E.; Kerbaol, J. M.; Le Mest, Y.; L'Haridon, P. *Inorg. Chem.* **1990**, *29*, 707.
- (45) Weiss, M. C.; Goedken, V. L. *J. Am. Chem. Soc.* **1976**, *98*, 3389.
- (46) Mertes, K. B.; Corfield, P. W. R.; Busch, D. H. *Inorg. Chem.* **1977**, *16*, 3226.
- (47) Goto, M.; Ishikawa, Y.; Ishihara, T.; Nakatake, C.; Higuchi, T.; Kurosaki, H.; late Virgil L. Goedken, t. *Chem. Commun.* **1997**, 539.
- (48) Zhang, J.; Leitius, G.; Ben-David, Y.; Milstein, D. *Angew. Chem. Int. Ed.* **2006**, *45*, 1113.
- (49) Montag, M.; Zhang, J.; Milstein, D. *J. Am. Chem. Soc.* **2012**, *134*, 10325.

Lutidine-derived Ru-CNC pincer complexes for catalytic hydrogenation of CO₂ and carboxylic acid esters

Do. Or do not. There is no try.

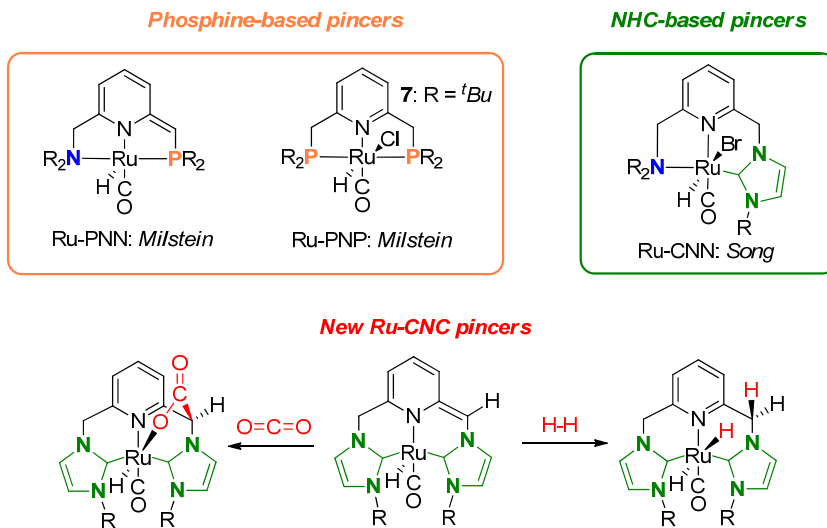
ABSTRACT: The catalytic activity of lutidine-based Ru-CNC pincer complex in hydrogenation of carbon dioxide and carboxylic acid esters was evaluated. Similar to the structurally-related Ru-PNP catalysts, Ru-CNCs can promote hydrogenation of CO₂ to formates in the presence of a non-nucleophilic DBU base. Their catalytic performance is however limited by a rapid catalyst deactivation via a highly favorable formation of a cooperative CO₂ adduct with Ru-CNC. This deactivation path can be suppressed when the reaction is carried out under reduced partial pressure of CO₂. Such conditions allow achieving a high and stable CO₂ hydrogenation activity of Ru-CNC. On the other hand, ester hydrogenation reaction benefits from the more pronounced metal-ligand cooperative function in Ru-CNCs. These catalysts are active in hydrogenation of a wide range of methyl esters and lactones unlike their phosphine-based counterparts.



Parts of this Chapter are published in: *ACS Catal.* **2014**, *4*, 2667 and
ACS Catal., **2015**, *5*, 1145

6.1. Introduction

The development of a new family of bis-N-heterocyclic carbene (NHC) ruthenium pincer complexes showing unusual coordination properties and chemical reactivity has been described in the previous Chapter. Being structurally analogous to Ru-PNP pincers, they exhibit similar reactivity towards ligand dearomatization and subsequent metal-ligand cooperative activation of H₂ and CO₂. Namely, the deprotonation of the ligand backbone upon the reaction of Ru-CNCs with KO^tBu yields the dearomatized Ru-CNC* species that are able to cooperatively activate H₂ or CO₂ (Scheme 6.1). Such a cooperative behavior in the related transition metal complexes based on PNX (X=P,N) pincer systems is often assumed to be crucial for their catalytic activity in hydrogenation reactions.¹⁻³ The replacement of phosphines with substantially stronger NHC donors⁴ can have a strong impact on the catalytic performance of new CNC catalysts when compared with PNPs. Therefore a detailed comparison of the catalytic properties of these two systems will represent the focal point of this study.



Scheme 6.1. Structures of known ruthenium pincer catalysts for hydrogenation of CO₂ or/and esters and new Ru-CNC pincers studied in this Chapter

In previous Chapters we have shown that phosphine based analogue of our Ru-CNC pincers (Scheme 6.1) can catalyze hydrogenation of CO₂ with remarkable initial rates (TOF^o) up to 1 892 000 h⁻¹ at 132°C under 40 bar pressure. After the analysis of a complex reaction network underlying the activity of these catalysts, we concluded that despite Ru-PNP can exhibit a pronounced metal-ligand cooperative behavior, the participation of the

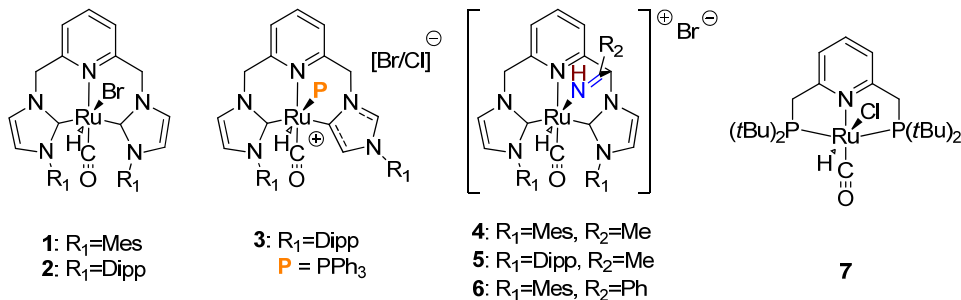
ligand in catalysis is not beneficial. A similar effect is expected for the catalysis with Ru-CNC. Because the outstanding activity of Ru-PNP catalyst in hydrogenation of CO₂ to formates was the major motivation for the development of the Ru-CNC complexes, the detailed investigation of this catalytic reaction will be the primary target of this Chapter.

The application of ruthenium NHC catalysts in hydrogenation of CO₂ has been previously considered. In particular, mono-⁵ and bidentate⁶ Ru-NHCs were shown to be active in hydrogenation of carbon dioxide with either molecular hydrogen or isopropanol as a reducing agent. However these catalysts were only moderately active allowing reaching TON values up to 23 000 at a temperature of 200 °C.⁶

Applications of ruthenium pincer complexes with NHC donor groups for catalytic hydrogenation of CO₂ are not known. However, the beneficial effects of the phosphine replacement with NHCs are known in catalytic hydrogenation of esters. For example, Song and co-workers⁷ reported the NHC analogue of the Milstein Ru-PNN catalyst⁸ (Scheme 6.1). Resulting Ru-CNN catalyst provided a superior ester hydrogenation activity. Inspired by this result, we adopted ester hydrogenation reaction as the second benchmark transformation investigated in this Chapter.

6.2. Catalytic hydrogenation of CO₂: unrealized potential of Ru-CNCs

The starting point of this study was the evaluation of the catalytic activity of Ru-CNC complexes **1-6** (Scheme 6.2) in hydrogenation of CO₂ in the presence of DBU base. With the exception of the mixed normal/abnormal NHC complex **3**, all catalysts were able to promote CO₂ hydrogenation to DBU formate at 70 °C in THF (Table 6.1). Surprisingly, under these conditions Ru-PNP complex **7** outperforms bis-NHC pincers. The structurally related Ru-PNP pincer **7** allows obtaining a nearly 1.5-fold higher formate yield under otherwise identical conditions.



Scheme 6.2. Structures of ruthenium pincers employed in this Chapter.

Table 6.1. Small scale catalytic hydrogenation of CO₂ using Ru pincer catalysts

Catalyst(μmol)	TON	AAR ^a
1 (2.5)	1180	0.88
1 (1)	2595	0.79
2 (2.5)	747	0.55
3 (2.5)	79	0.06
4 (2.5)	1212	0.90
5 (2.5)	1397	1.03
6 (2.5)	959	0.71
7 (2.5)	1963	1.46

Conditions: 40 bar H₂/CO₂=1/1, 70°C, 3/0.5 mL THF/DBU, ^a - acid-to-amine molar ratio. .

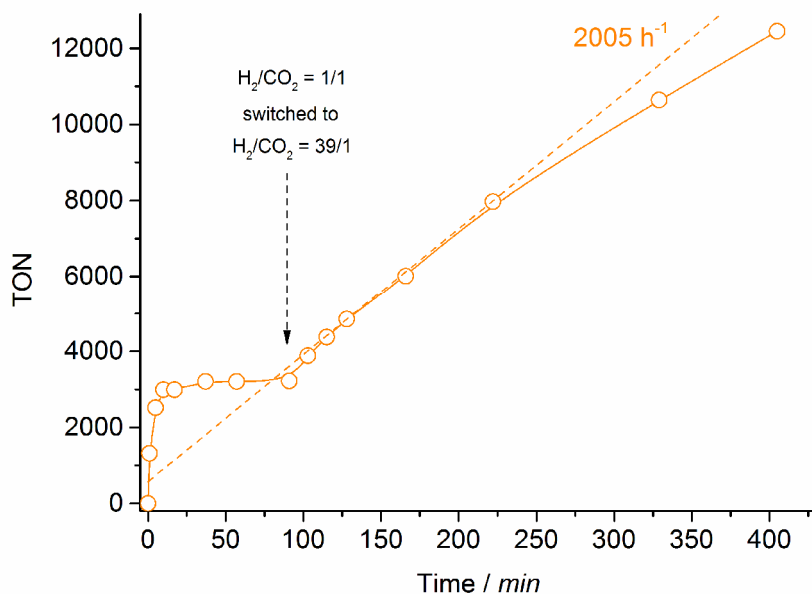


Figure 6.1. Deactivation and gas composition effect on the kinetics of CO₂ hydrogenation with **1** (2.9 μmol). Conditions: 70°C, 20/20 or 39/1 (bar/bar)H₂/CO₂ ratio, 30mL DMF, 5mL DBU. Pressure swing was performed in attempt to reactivate the catalyst.

As we have demonstrated in the previous Chapters, polar solvents, e.g. DMF, are beneficial for the CO₂ hydrogenation activity of pincer catalysts. Since TON values attainable by Ru-CNCs during the initial screening performed in a batch reactor were low, we sought to enhance the catalyst productivity by carrying out the reaction in a polar DMF solvent and using a lower catalyst concentration. Surprisingly, at a nearly 10-fold lower catalyst concentration complex **1** only allowed for a three-fold TON increase. Kinetic data presented in Figure 6.1 indicated the rapid decrease of the high initial TOF (ca. 26 000 h⁻¹) overtime and a complete elimination of the activity after ca. 3000 catalytic turnovers. This result points to the rapid catalyst deactivation under the CO₂ hydrogenation conditions. To analyze potential source of deactivation we employed DFT calculations to identify the relative stability of reactive intermediates of Ru-CNC under catalytic conditions.

Having precatalyst **1** as a starting point of our analysis, we evaluated the reactivity of the respective dearomatized complex **1*** with H₂ and CO₂. In the previous Chapter 6 we have demonstrated the high flexibility of the pincer chelate in Ru-CNC and proposed that this phenomenon may contribute to the reactivity in cooperative addition reactions. In line with the experimental observations, DFT results also point to the high chelate flexibility in complex **1***. The initial deprotonation step can yield two non-equivalent stereoisomers **1*** and **1a*** which are characterized by identical main geometrical parameters and similar relative stabilities (Figure 6.2). They correspond to atropisomers, as their interconversion can be achieved via a frustrated rotation of the methylene bridge with an activation barrier (E_{ZPE}^\ddagger) of only 66 kJ mol⁻¹ and activation Gibbs free energy barrier ($G^\circ, \ddagger_{\text{ZPE}}$) of 70 kJ mol⁻¹. Such a low barrier of internal rotation implies their fast equilibration at relatively low temperatures.⁹

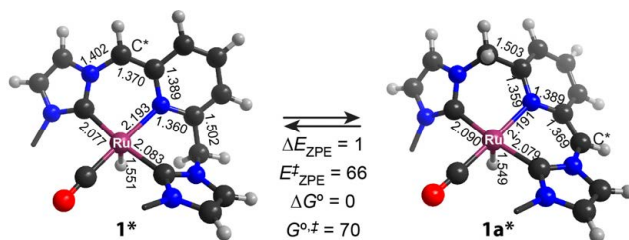


Figure 6.2. Optimized structures of atropisomers **1*** and **1a*** and DFT-computed energetics of their interconversion (in kJ mol⁻¹). Selected interatomic distances are given in Å.

Despite similar geometries, **1*** and **1a*** are expected to exhibit substantially different acid-base cooperative properties because of the different spatial orientation of the reactive Ru and methylene arm (further denoted as C*) sites. Indeed, whereas the empty d₂₂ of the

metal and the p_{C^*} lone pair on C^* are co-aligned in $\mathbf{1}^*$, they point to different directions in $\mathbf{1a}^*$. As a result, the cooperative activation of H_2 towards a rearomatized dihydrido complex $\mathbf{8}$ can be promoted only by $\mathbf{1}^*$ (Figure 6.3),¹⁰ in which the direct cooperation between Ru and C^* centers promotes the heterolytic dissociation of H_2 . The reaction starts with the slightly endergonic ($\Delta G^\circ = 15 \text{ kJ mol}^{-1}$) formation of a σ -complex $\mathbf{1-H}_2$ characterized by symmetric η^2 -coordination of an elongated H_2 molecule ($r(H-H) = 0.809 \text{ \AA}$ as compared to the value of 0.747 \AA computed for the free molecule at the same level of theory). In the next step, the pre-coordinated H_2 dissociates to yield the dihydrido Ru-CNC complex $\mathbf{8}$. This reaction is strongly exothermic ($\Delta E_{ZPE} = -56 \text{ kJ mol}^{-1}$) and proceeds with a barrier of only 15 kJ mol^{-1} that is significantly lower than that for related Ru-PNP system.¹¹

DFT calculations also confirm the possibility of the cooperative addition of CO_2 to $\mathbf{1}^*$ that was shown experimentally in the previous Chapter. The reaction proceeds via the formation of a non-specific molecular complex $\mathbf{1-CO}_2$ followed by a barrierless and highly exothermic ($\Delta E_{ZPE} = -119 \text{ kJ mol}^{-1}$; $E_{ZPE}^\ddagger = 1 \text{ kJ mol}^{-1}$) addition of carbon dioxide across the metal center and the C^*H linker of the ligand (Figure 6.3). Because of the endergonic nature of the initial CO_2 coordination, the overall free energy barrier ($G^{o,\ddagger}$) of the reaction is 39 kJ mol^{-1} , which is 9 kJ mol^{-1} higher than the value predicted for H_2 dissociation on $\mathbf{1}^*$ ($\mathbf{1}^* + H_2 \rightarrow \mathbf{8}$). The reaction proceeds via an early transition state $\mathbf{TS}_{1,3}$ as follows from the small structural perturbations of the reactive species involved compared to the initial state $\mathbf{1-CO}_2$. In line with our earlier proposal,¹¹ this suggests that the [4+2] cycloaddition of CO_2 to $\mathbf{1}^*$ is triggered by the attack of the bent CO_2 molecule by the basic C^* site. The coordination with Ru provides additional stabilization of the CO_2 adduct. This interaction is particularly effective in $\mathbf{10}$ due to the specific geometric properties of the CNC ligand. Its structure features a shorter $Ru \cdots O1$ bond (2.285 \AA) than that in the related Ru-PNP CO_2 adduct ($r(Ru \cdots O1)_{PNP} = 2.319 \text{ \AA}$).¹¹ Furthermore, the larger CNC chelate imposes less constraints onto the rigid tetradentate ligand geometry realized in $\mathbf{10}$ as is evidenced by an almost perfect octahedral environment of Ru (Figure 6.4). This provides a plausible explanation for the approximately twice higher exothermicity of the CO_2 -addition reaction to Ru-CNC* ($\mathbf{1}^* + CO_2 \rightarrow \mathbf{10}$, $\Delta E_{ZPE} = -125 \text{ kJ mol}^{-1}$) compared to that predicted for Ru-PNP* system ($\Delta E_{ZPE} = -61 \text{ kJ mol}^{-1}$).¹¹

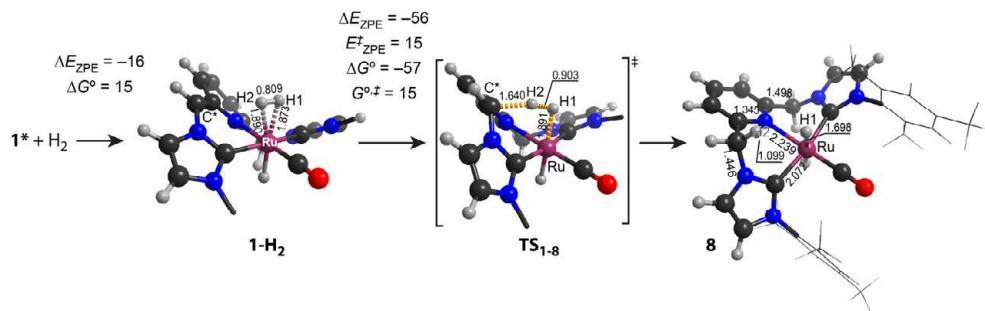


Figure 6.3. Optimized structures of reaction intermediates and transition state of a metal-ligand cooperative H_2 activation by 1^* (in the graphical representation of $1-H_2$ and $TS_{1,2}$, Mes substituents at the NHC moieties are omitted for clarity, in that of **8** a wireframe representation of these groups is used).

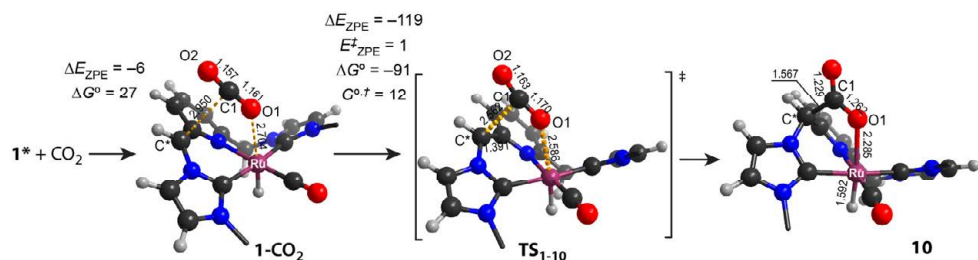


Figure 6.4. Optimized structures of intermediates and transition state of a [4+2] cycloaddition of CO_2 to 1^* (in the graphical representations Mes substituents at the NHC moieties are omitted for clarity).

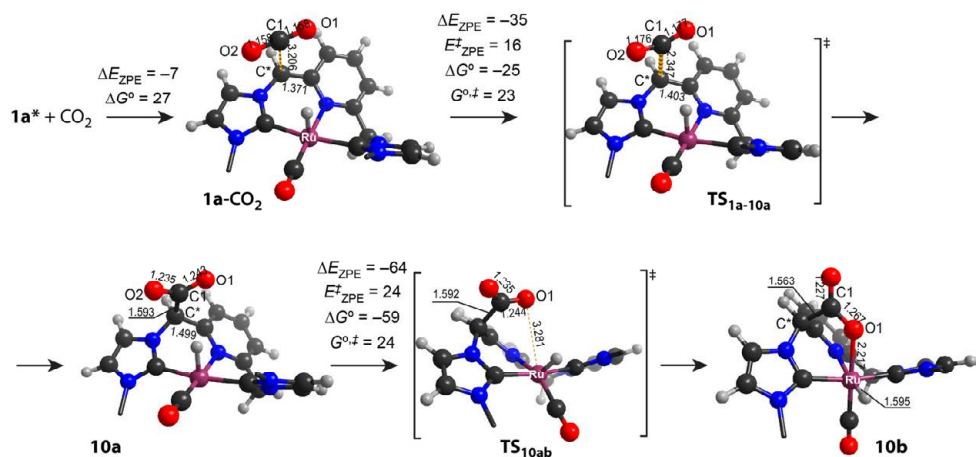


Figure 6.5 Optimized structures of intermediates and transition state of a non-cooperative addition of CO_2 to $1a^*$ (in the graphical representations Mes substituents at the NHC moieties are omitted for clarity).

Considering the key role of the basic ligand site for CO₂ activation, one can assume that CO₂ addition to **1a*** would proceed in different manner compared to **1***. Figure 6.5 summarizes the optimized structures of intermediates and transition states involved in these transformations along with the associated reaction energetics. The reaction of CO₂ with **1a*** starts with non-specific coordination of CO₂ to **1***. Further attack of C* to electrophilic centre in CO₂ leads to a meta-stable intermediate **10a** containing a non-coordinated carboxylate moiety at the pincer arm. The 5-coordinated state of Ru is preserved upon CO₂ addition. This step is thermodynamically favored and proceeds with an activation barrier of only 24 kJ mol⁻¹ (Figure 6.5). The relatively low stability of **10a** is associated with its zwitter-ionic nature. The ligand environment of the Ru center does not allow to coordinate the carboxylate moiety directly and therefore to effectively compensate for its negative charge. The reorganization of the ligand environment in **10a** results in its isomerization to a much more stable species **10b** ($\Delta E_{\text{ZPE}} = -64$ kJ mol⁻¹, Figure 6.5). The rotation of the anionic carboxylate group around the C*-C1 bond displaces the axial hydride ligand into the equatorial position with a concomitant change in the configuration of the CO ligand and the formation of the Ru-O1 coordination bond (**10a** → **TS**_{10ab} → **10b**, Figure 6.5). DFT calculations predict that the overall barrier for the non-cooperative CO₂ addition (**1a*** + CO₂ → **10b**, $G^{\ddagger}_{\text{app}} = 50$ kJ mol⁻¹, $\Delta G^{\circ} = -57$ kJ mol⁻¹) is only 11 kJ mol⁻¹ higher than that for the metal-ligand cooperative path (**1*** + CO₂ → **10**, $G^{\ddagger}_{\text{app}} = 39$ kJ mol⁻¹, $\Delta G^{\circ} = -75$ kJ mol⁻¹). It is also substantially lower than the free energy barrier for the isomerization of **1*** and **1a*** ($G^{\ddagger}_{\text{app}} = 70$ kJ mol⁻¹). It is important to note that **10b** is ca. 5kJ/mol ($\Delta G_{10^{\circ}} - \Delta G_{10b^{\circ}} = -5$) less stable than **10**. That allows for estimating the equilibrium ratio between these complexes in solution at **10/10b** = 85.2/14.8 that is in a perfect agreement with the experimentally detected equilibrium concentrations observed by ¹H NMR for the reaction between the *in situ* generated **1*** and CO₂ (Chapter 5).

The results of DFT calculations discussed above point to the much higher reactivity of the dearomatized Ru-CNC* complex towards the ligand-assisted activation of both H₂ and CO₂ than that of the Ru-PNP* system. Because of the pronounced atropisomerism of Ru-CNC*, two alternative mechanisms of CO₂ addition can be realized, resulting in distinctly different CO₂-adducts **10** and **10b**. Unlike in Ru-PNP* where the reaction with H₂ towards the catalytically active dihydrido complex is the thermodynamically preferred route, the cooperative addition of CO₂ to **1*** is more thermodynamically favorable than the H₂ dissociation and proceeds with comparable free energy barrier.

The pronounced reactivity difference between PNP and CNC ligand systems was further observed experimentally by NMR spectroscopy. In sharp contrast to the behavior of Ru-PNP,¹² the exposure of the starting complex **1** to a H₂/CO₂ (H₂:CO₂ = 2:1 mixture, 3 bar) at 70 °C in the presence of DBU (Figure 6.6) does not result in the formate complex (Chapter 2).¹¹ Instead, under these conditions precatalyst **1** is quantitatively transformed to the CO₂-adducts **10/10b** with a concomitant formation of the DBU-FA product of the catalytic reaction. In agreement with the DFT calculations, the more thermodynamically stable complex **10** dominates the reaction mixture.

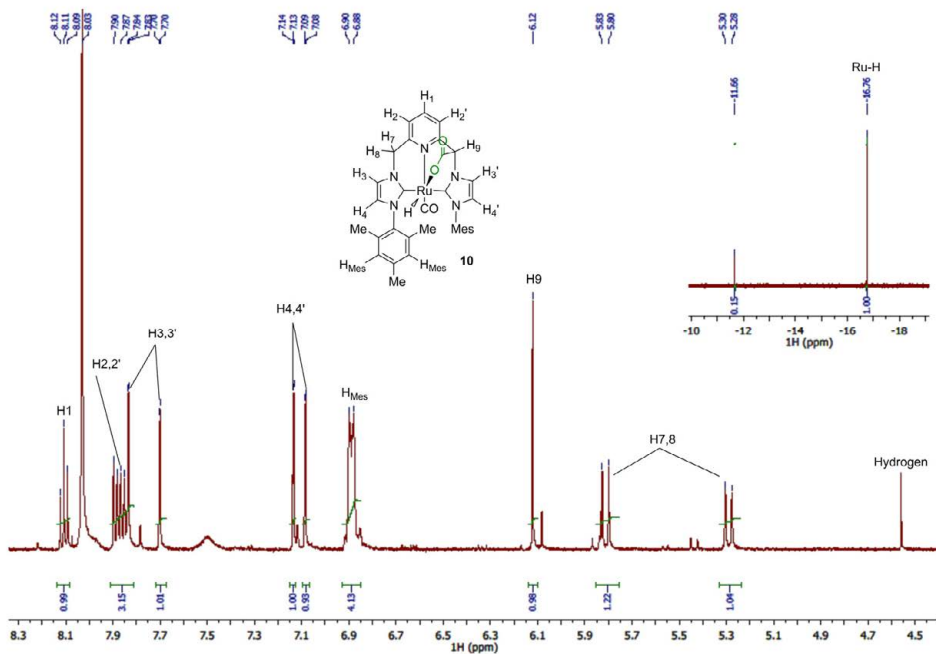


Figure 6.6. ¹H NMR spectrum of the reaction mixture of **1** with H₂/CO₂ = 2/1 bar in DMF-*d*₇. Resonances of **10** integrated where possible. Detected **10/10b** = 87/13.

Unusual reactivity of and catalytic behavior of Ru-CNC should stem from different relative stabilities of the species involved in the catalytic reaction. DFT calculations allowed evaluating the preferred mechanism for CO₂ hydrogenation with Ru-CNC. We used the dihydrido complex **8** as a starting point of our analysis. We propose that reaction over **8** proceeds via the sequence of steps similar to that for the Ru-PNP catalyst described in Chapter 3. The highest barrier along the reaction path is associated with the reaction of CO₂ with dihydrido complex **8** ($E_{\text{app}}^{\ddagger, \text{DFT}} = 13 \text{ kJ mol}^{-1}$, **8**-CO₂ + H₂ → **9***, Figure 6.3). This reaction yields a metastable **9*** that can further rearrange into stable formate complex **9**

($\Delta E_{ZPE} = -39 \text{ kJ mol}^{-1}$, $\mathbf{9}^* \rightarrow \mathbf{9}$, Figure 6.7). Alternatively $\mathbf{9}^*$ can undergo a hydrogen insertion with a concomitant barrierless H_2 cleavage assisted by HCOO^- anion ($E_{\text{app}}^{\ddagger, \text{DFT}} = 1 \text{ kJ mol}^{-1}$, $\mathbf{9}\text{-H}_2 \rightarrow \text{TS}_{\mathbf{9}\text{-8}}$, Figure 6.7). The product of this reaction, $\mathbf{8}\text{-FA}$, is a molecular complex with formic acid that upon the reaction with DBU yields $\text{DBU}\cdot\text{HCOOH}$ adduct and regenerates the initial complex $\mathbf{8}$, thus, closing the cycle.

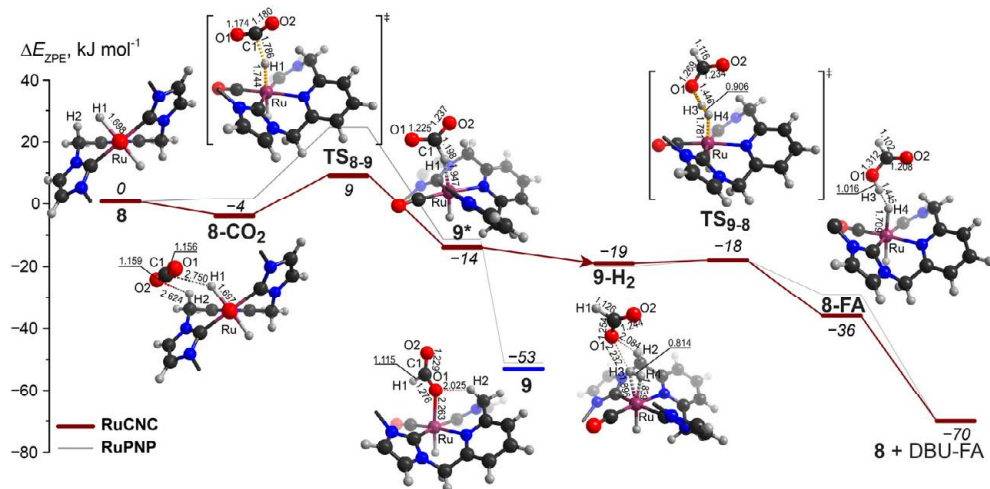


Figure 6.7. DFT computed reaction energy diagram and optimized structures of the intermediate and transition states (*Mes* substituents of the CNC ligand and solvent molecules are omitted for clarity) for the hydrogenation of CO_2 with $\mathbf{8}$.

Under standard conditions formate complex $\mathbf{9}$ is the most thermodynamically stable species in the catalytic cycle over $\mathbf{8}$ (Figure 6.8). Experimentally it is readily produced from dihydride complex $\mathbf{8}$ upon the reaction with CO_2 . However, it was not formed under H_2/CO_2 atmosphere in presence of DBU. The CO_2 adducts $\mathbf{10}/\mathbf{10b}$ were formed instead, that implies that we need to consider ligand participation in catalysis. Most accurately, such analysis can be done by comparing reaction free energies (Figure 6.8).

Similarly to our previous work on Ru-PNP catalysts, we have analyzed transformations of Ru-CNC involving ligand dearomatization (blue path, Figure 6.8) and steps involving the formation of CO_2 adduct $\mathbf{10}$ (green path, Figure 6.8). The cooperative path is initiated by the HCOO^- assisted deprotonation of $\mathbf{9}^*$ to yield $\mathbf{1}\text{-FA}$ – a molecular complex of formic acid with deprotonated complex $\mathbf{1}^*$. This reaction is associated with a high free energy barrier of 61 kJ mol^{-1} . $\mathbf{1}\text{-FA}$ reacts further with DBU to regenerate $\mathbf{1}^*$ that in turn can react with hydrogen or CO_2 . Reaction with hydrogen yields the initial dihydride complex $\mathbf{8}$. An alternative reaction with CO_2 leads to the formation of adduct $\mathbf{10}$, that is in fact 19 kJ mol^{-1} more stable than $\mathbf{8}$. Consecutive transformations of $\mathbf{10}$ are associated with prohibitively

high free energy barriers. This fact, together with the high stability of **10** points to its inevitable accumulation under the catalytic conditions. Our data suggests that accumulation of unreactive **10** may be the major source of deactivation. A much higher stability of cooperative adducts of Ru-CNC, therefore, exemplifies the main difference with Ru-PNP catalyst.

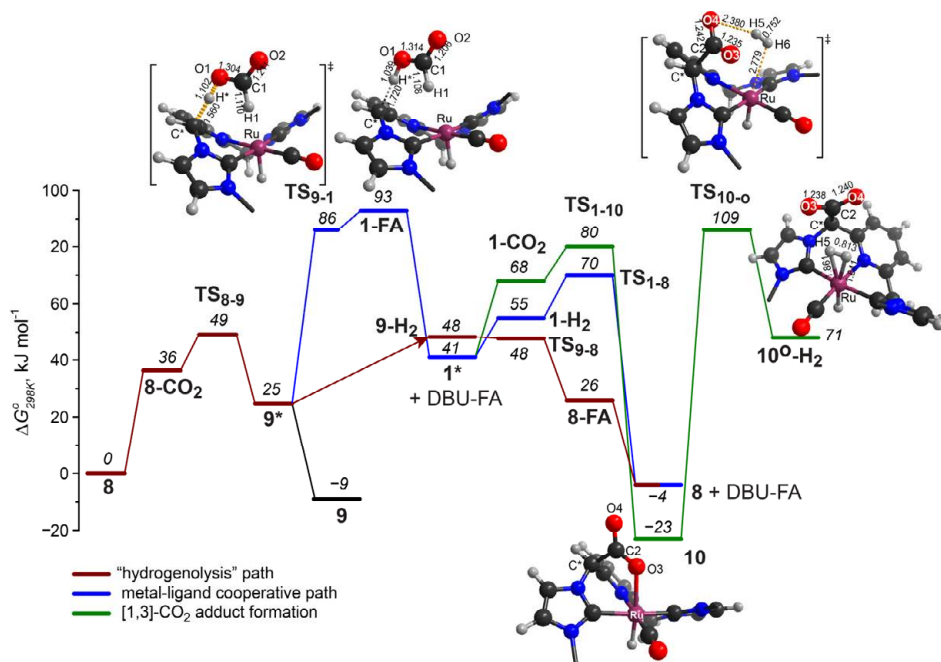


Figure 6.8. Free energy diagram for catalysis with **8** and corresponding ligand-assisted transformations.

Further analysis of the reaction free energy diagrams (Figure 6.8) suggests that the reactions associated with the Ru-CNC deactivation are in competition with the catalytic cycle over **8**. Similar to our work with Ru-PNP catalyst, we attempted to carry out the CO₂ hydrogenation reaction at elevated H₂/CO₂ ratios to favor the catalytic pathway. Our kinetic data supports the proposed hypothesis (Figure 6.9). At H₂/CO₂=39/1 we observed a rapid reaction with initial TOF^o values reaching 99 100h⁻¹ at 84°C. The temperature dependence of the reaction rate allows to estimate the apparent activation energy of ca. 27 kJ mol⁻¹ that is close to the computed value of 34 kJ mol⁻¹ for the hydrogenolysis of complex **9**. Similar transformation was earlier identified as one of the rate determining steps in Ru-PNP-catalyzed CO₂ hydrogenation in Chapter 3.

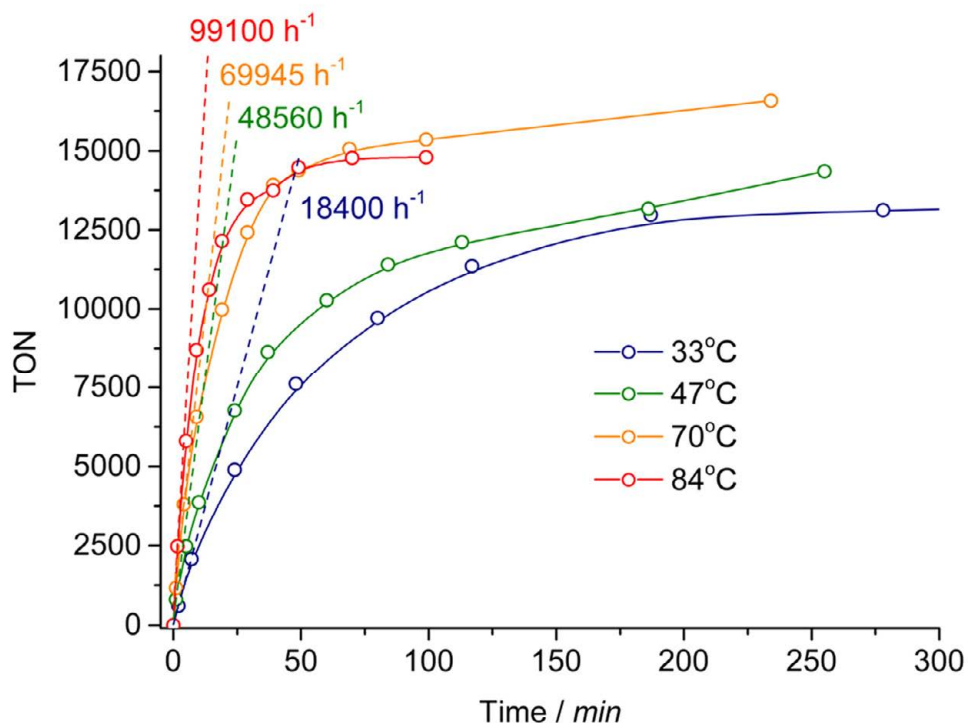


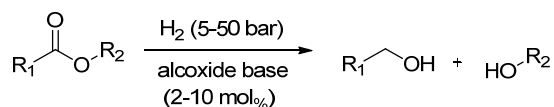
Figure 6.9. Hydrogenation of CO_2 using catalyst **1** ($2.9\mu\text{mol}$) at H_2/CO_2 ratio of 39/1 (bar/bar) at different temperatures. 30mL DMF, 5mL DBU

In summary, when compared to phosphine-based analogue, Ru-CNC complex **1** is more susceptible to form cooperative adducts with H_2 and CO_2 . These adducts are more stable thermodynamically and barriers for their formation are significantly lower. We conclude that the cooperative function in Ru-CNC is more pronounced than in its phosphine based counterparts. This feature of Ru-CNC pincers has a detrimental impact on the CO_2 hydrogenation catalysis.

6.3. Catalytic hydrogenation of carboxylic acid esters

In contrast to CO_2 hydrogenation, majority of Ru pincer-catalyzed transformations benefit from the MLC effects. A typical example of hydrogenation reactions requiring a bifunctional catalyst is the reduction of carboxylic acid esters to corresponding alcohols with molecular hydrogen (Scheme 6.3).^{8,13-16} Only a few catalysts capable of promoting such a transformations have been reported so far and the vast majority of them is based on non-innocent ligands.^{13,16} Therefore, since the MLC behavior of Ru-CNC and Ru-PNP

significantly differs, we expect to observe a different performance of these catalysts in ester hydrogenation.

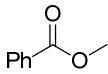
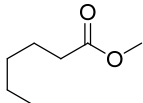
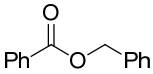
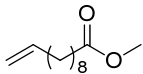
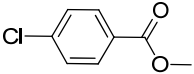
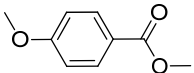


Scheme 6.3. Ester hydrogenation reaction as carried out in this Chapter.

Reduction of esters is usually performed under strongly basic conditions. Although the role of the base in catalysis is still debated, the presence of strong alkoxide base is crucial for achieving high activity.¹⁷ Our tests show that reference Ru-PNP complex **7** does not convert esters at 70°C under 50 bar H₂ pressure in the presence of KOMe base. In sharp contrast, Ru-CNC complexes **1-6** hydrogenate a wide range of esters to the corresponding alcohols (Table 6.2). Ru-CNC catalysts effectively hydrogenate aromatic esters, including chloro- and methoxy-functionalized derivatives (Table 6.2, Entries 23-26). Aliphatic esters and lactones are also hydrogenated in near quantitative yields. The hydrogenation of methyl 10-undecenoate (Table 6.2, Entries 21, 22) resulted in the predominant formation of the fully saturated undecanol product. Good to quantitative yields were obtained in 4-16 h at 70-100 °C and 50 bar H₂ in the presence of KOMe or KO^tBu base promoters. This activity was achieved at 0.5 %_{mol} catalyst loading (Table 6.2).

The stability of the catalyst under the harsh reaction conditions is the primary concern for the correct evaluation of its performance. One should make a distinction between catalysis with molecular species and catalysis over metal nanoparticles or small clusters that can be formed during the experiment. Homogeneous nature of catalysis is usually probed by selective poisoning.¹⁸⁻²¹ Mercury is the most common poison for metal nanoparticles that is also efficient in poisoning sub-nanometer metal clusters.²² We performed mercury poisoning tests using large excess of Hg, added after catalyst activation with alkoxide base (315 eq. Hg per Ru). Poisoning does not affect the hydrogenation of methyl benzoate catalyzed by **1** or **3** (entries 2 and 5, Table 6.2) evidencing therefore the molecular nature of the active catalysts in these cases.

Table 6.2. Catalytic ester hydrogenation with RuCNCs.^a

Entry	Substrate	Catalyst	Yield, %
1		1	97
2		1 +xsHg ^g	100
3		2 ^b	95
4		3	96
5		3 +xsHg ^g	100
6		4	98
7		5	55
8		6	98
9		7	NR ^f
10		1	98
11		2 ^b	99
12		3	99
13		4	100
14		5	92
15		6	100
16		7	NR
17 ^d		1	98
18 ^d		6	96
19 ^d		1	100
20 ^d		6	100
21		1	86 ^e
22		6	79 ^e
23		1	89
24		6	100
25		1	60
26		6	90

Conditions: a) 2 mL THF, 10 %_{mol} KOMe, 6.4 μmol catalyst, S/C =200, 70°C, 50 bar H₂, 4h; b) KO^tBu used; c) Yield of corresponding alcohols; d) 16 h time, 100 °C; e) Undecanol yield; f) NR = not active; g) 315 eq. Hg per Ru were added after catalyst activation.

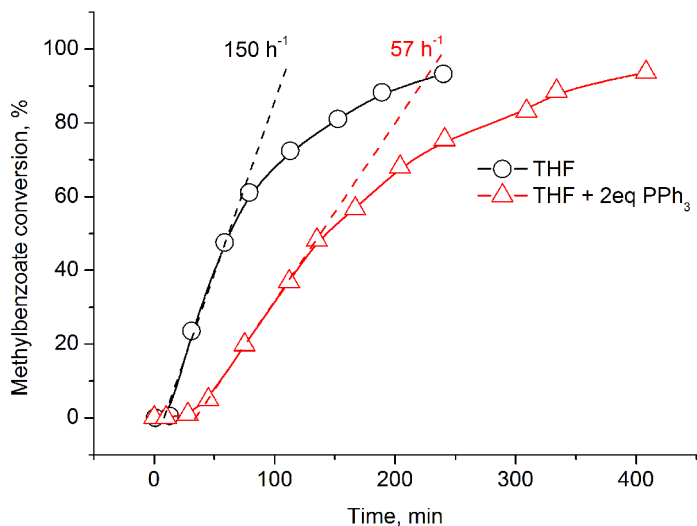


Figure 6.10. *PPh₃ poisoning experiment and a control experiment; conditions: 30 mL THF, 40 μ mol catalyst, 10 %mol KOMe, S/C =200, 70°C, 50 bar H₂.*

Additional evidence for the homogeneous nature of catalysis was obtained in the PPh₃ poisoning experiment. PPh₃ can act as a strong poison for catalysis since it effectively blocks the metal surface. Ligand-to-metal ratio, at which catalysis by nanoparticles is suppressed, is typically 0.2 - 0.5, since only a small fraction of the particle is accessible for reactants. For molecular catalysts, the amount of triphenylphosphine, sufficient of activity inhibition is typically over 1 equivalent.¹⁹ In the case of catalysis by complex **1**, the presence of 2 eq. of triphenylphosphine per Ru was not sufficient to eliminate the catalytic activity. A substantial initial rate (TOF° = 57 h⁻¹) was observed for the reaction in the presence of PPh₃ (Figure 6.10).

The stability of the catalyst **3** under hydrogenating conditions required additional confirmation in view of the recent reports suggesting a decreased stability of abnormal NHCs compared to the normally bound ones.²³ Therefore, we addressed stability of catalyst **3** in more detail using mass spectrometry. Post-catalytic ESI-MS measurements (Figure 6.11) indicate the preservation of the Ru-CNC moiety in complex **3** under the ester hydrogenation conditions. Molecular ions corresponding to mononuclear [RuCl(CNC)]⁺, [Ru(BnO)(CNC)]⁺, [RuH(CO)(PPh₃)(CNC)]⁺ and [RuCl(PPh₃)(CNC)]⁺ species were observed in the mass spectrum of the reaction mixture corresponding to entry 5 in Table 6.2. These data implies that the metal-ligand sphere remains intact during catalysis even under H₂ atmosphere in the presence of a large excess of strong base.

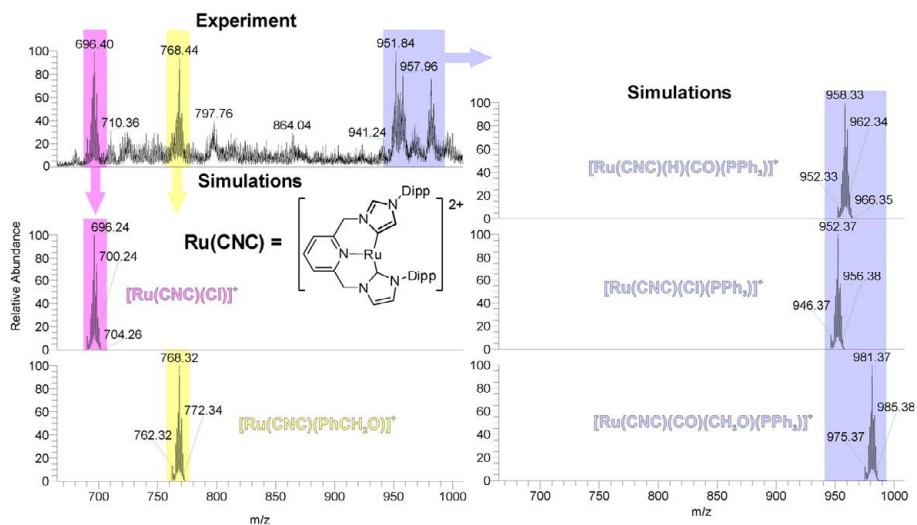


Figure 6.11. Post-catalytic ESI-MS spectra of the reaction mixture with catalyst 3 (Entry 5, Table 6.2).

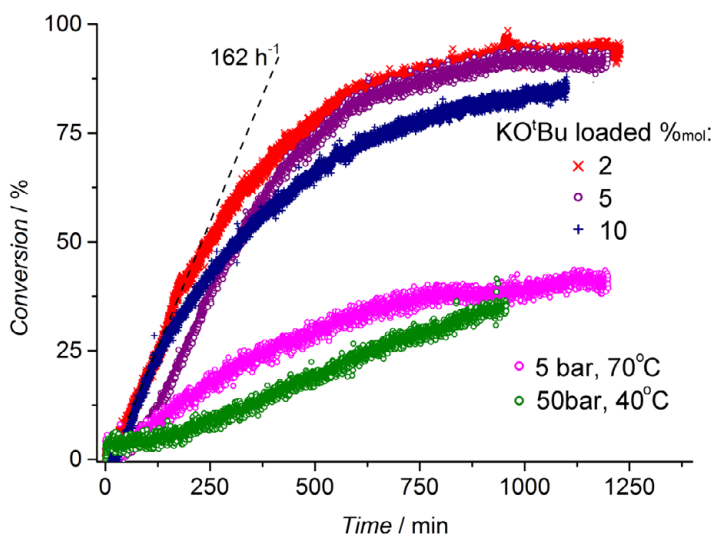


Figure 6.12. Influence of pressure, temperature and base loading on the kinetics of methyl benzoate hydrogenation using **1**. Conditions: 30 mL THF, 8 μmol catalyst, S/C=1000. KO^tBu variation (2, 5 and 10 %_{mol}) done at 50 bar H₂, 70 °C; pressure-temperature variation done at 10 %_{mol} KO^tBu loading.

Our data suggest that Ru-CNCs are stable under reaction conditions and can be used to convert esters on a gram scale (control experiment on Figure 6.10). Therefore, we investigated the possibility of using Ru-CNCs under milder conditions. At only 0.1 %_{mol}

loading that corresponds to a Substrate/Catalyst ratio (S/C) of 1000, catalyst **1** converts methyl benzoate quantitatively to methanol and benzyl alcohol at 70 °C and 50 bar H₂ within 16 h (Figure 6.12). The kinetics of the catalytic reaction is not affected by the concentration of the base promoter. For base loadings in the range of 2-10 %_{mol} the reactions showed very similar time-conversion profiles characterized by the initial turnover frequencies (TOF°) of 150-160 h⁻¹ (Figure 6.12). Decreasing the reaction temperature to 40 °C or H₂ pressure to 5 bar strongly reduced the catalytic performance of **1**. The obtained rates for ester hydrogenation are comparable to those reported for other NHC-based catalysts and superior to the rates attainable with the lutidine-derived Ru-PNN and Ru-CNN systems.^{7,8,24,25} The catalytic reactions can be carried out under conditions significantly milder than in the case of ruthenium catalysts based on TriPhos and TriSulph ligands.²⁶⁻²⁸ However, Ru-CNC catalysts display lower activity than the state-of-the-art aliphatic Ru pincer complexes,²⁹ the Noyori-type catalysts,^{30,31} and, in particular, the most active catalytic system reported to date based on an aliphatic Ru-SNS pincer,¹⁷ which is capable of hydrogenating a wide range of organic esters at 40°C with TOFs above 4000 h⁻¹.

6.4. Conclusions and outlook

Ru bis-NHC pincers show a strikingly different catalytic performance when compared to phosphine based analogues despite the apparent structural similarity and common reactivity of the metal complexes. In catalytic hydrogenation of CO₂, the performance of Ru-CNCs suffers from the undesired ligand participation. The fast accumulation of the product of cooperative CO₂ activation results in the rapid catalyst deactivation. The activity of Ru-CNCs can be remediated when operating at the reduced CO₂ partial pressure. Such conditions allow to shift the equilibrium towards the more catalytically potent dihydrido complex and effectively inhibit the ligand-assisted reaction paths.

Catalytic hydrogenation of carboxylic acid esters, inaccessible for Ru-PNPs, can be efficiently promoted by Ru-CNC, with which initial TOF° values up to 160 h⁻¹ are attainable at 70°C under 50 bar pressure of H₂. The substrate scope of Ru-CNC catalysts includes aliphatic and aromatic esters and lactones.

Such a peculiar catalytic behavior of Ru-CNC is a result of a more pronounced metal-ligand cooperative properties in these compounds when compared with the phosphine-based pincers. While not being beneficial for the hydrogenation of CO₂ to formates, the enhancement of MLC properties in Ru-CNC enables its activity in ester hydrogenation. We

propose that the enhancement of the metal-ligand cooperative behavior can be a promising way to improve the catalytic performance of Ru pincer ester hydrogenation catalysts.

6.5. Experimental

All manipulations unless stated otherwise were performed using Schlenk or high vacuum line ($\sim 5 \times 10^{-6}$ mbar) techniques. Argon was dried with a Sicapent column. Air sensitive compounds were stored in a MBraun glovebox under an atmosphere of dry argon. Anhydrous solvents were dispensed from the MBraun purification system and degassed prior to use. Deuterated DMF was purchased from Eurisotop, dried over molecular sieves, degassed and stored over freshly activated molecular sieves. NMR spectra were recorded on Varian Mercury 400 MHz and Varian Inova 500 MHz spectrometers. Chemical shifts were referenced to residual solvent peaks.

NMR experiments

Hydrogenation of CO₂ in NMR tube

Complex **1** (1.2 mg, 1.75 μmol) was introduced to a solution of ca. 200 equivalents of DBU in DMF- d_7 (0.2 mL) in a heavy wall Wilmad NMR tube. The tube was then pressurized with CO₂/H₂ = 1/2 up to total pressure of 3 bar and heated in an oil bath at 70°C overnight. Together with formation of DBU·HCOOH adduct we observed the formation of complex **10** as a major isomer (87%) and minor amount of complex **10b**. Similar experiment was conducted using ¹³CO₂ to observe a two-bond C-H coupling between added CO₂ and remaining methylene bridge proton. Observed $J^2_{CH} = 5.3$ MHz is consistent with proposed structure of **10**. Respective data presented in the Chapter on Figure 6.6

Hydrogenation procedures

Small scale CO₂ hydrogenation experiments were performed in 10 mL stainless steel autoclave at the initial 40 bar H₂/CO₂=1/1 pressure at 70°C (3mL THF, 0.5 mL DBU, 1-2.5 μmol of catalyst). The yields of formate were determined with HPLC.

Large scale CO₂ hydrogenation tests were performed in Top Industrie 100 mL stainless steel autoclave. The vessel was evacuated overnight at 150 °C, purged several times with argon, and the reaction medium was introduced by cannula transfer. The autoclave was flushed with hydrogen, preheated to reaction temperature and filled with hydrogen and eqimolar H₂/CO₂ up to operating pressure. The catalyst was then introduced via a dosage device and the reaction started. Constant pressure was maintained by a compensation device fitted with Bronkhorst EL-FLOW MFC unit and digital pressure meter. The compensation was done with equimolar H₂/CO₂ mixture to maintain constant partial pressure of gases in the reactor. Samples were withdrawn via dip-tube installation (dead volume 4 μl , sampling volume 110 μl), diluted to 1mL with EtOH and immediately analyzed by HPLC and GC-FID. Loadings used in all experiments were 30 mL DMF, 5 mL DBU (33.4 mmol), 1mL THF (internal standard) and 2 mg of **1**(2.9 μmol). TOF values were determined at the initial

stage of the reaction as the derivative of the $\text{TON}=f(t)$ curve. Arrhenius equation was used to estimate the apparent activation energy of reaction.

Identical setup was used for *PPh₃ poisoning test* in methyl benzoate hydrogenation catalysis.

Small scale ester hydrogenation procedure

In the glove box, a stock solution of catalyst, KOMe, THF solvent, dodecane and ester were combined in a crimp cap vial. The vial was sealed with a septum and transferred to the Premex A96 hydrogenation reactor. The reactor was purged 5 times with N₂ (10 bar) then H₂ (10 bar), pressurized with H₂ (50 bar), warmed up to the desired temperature and stirred at 300 rpm. Reaction conditions and results are reported in the chapter. At the end of the reaction, the reactor was purged with N₂ and the samples analyzed by GC/FID and GC/MS. The retention times of products and starting material were determined by using the commercially available reference materials. All mass balance were closed within +/- 10% error margin.

Hydrogenation of ester on 50mL scale autoclave

The hydrogenation of methyl benzoate with catalyst **1** was chosen as test reaction. A Premex Andorra autoclave (<http://premix-reactorag.ch/index.php?page=86>) was charged and closed in a N₂ glove box. The reaction was performed at 70 °C for 16h, at different pressures or amounts of base. *Typical experimental procedure:* In the glove box, to a stock solution of **1** in THF (5,3 mg, 0.008 mmol in 3 mL THF), t-BuOK was added (10%: 89.8 mg, 0.8 mmol), then methyl benzoate as stock solution in THF (1,089 g, 8 mmol, in 15 mL THF and 1 mL dodecane as internal standard), THF up to $V_f = 30$ mL.

Density functional theory calculations

Calculations were performed by Dr. E.A. Pidko. The computational methodology employed in our previous studies^{11,12} to describe the catalytic properties of the related Ru-PNP pincer system was used in this work. All calculations were carried out in the framework of density functional theory (DFT) using the hybrid PBE0³² exchange-correlation functional as implemented in Gaussian 09 D.01 program.³³ The all electron 6-311G(d,p) basis set was used for all atoms except ruthenium, for which the LanL2DZ basis set was employed. Bulk solvent effects were accounted for by using the polarized continuum model (PCM) during geometry optimization and frequency analysis. All complexes were treated as neutral species. The nature of the stationary points was evaluated from the analytically computed harmonic modes. No imaginary frequencies were found for the optimized structures, confirming that these correspond to local minima on the potential energy surface. All transition states exhibited a single imaginary frequency, corresponding to the eigenvector along the reaction path. The assignment of the transition state structure to a particular reaction path was tested by perturbing the structure along the reaction path eigenvector in the directions of the product and the reagent followed by geometry optimization. The reaction (ΔE_{ZPE}) and activation energies (E_{ZPE}^\ddagger) reported in the manuscript were corrected for zero point energy contribution computed using the results of the

normal-mode analysis. Reaction Gibbs free energies (ΔG°) and activation Gibbs free energies (G^\ddagger) were computed using the results of the normal-mode analysis within the ideal gas approximation at a pressure of 1 atm and temperatures of 298 K. Further computational details can be found in Ref. 11.

6.6. Notes and References

- (1) Balaraman, E., Milstein, D. *Top. Organomet. Chem.* **2014**, *77*, 1.
- (2) Gunanathan, C., Milstein, D. *Science* **2013**, *341*.
- (3) Gunanathan, C., Milstein, D. *Acc. Chem. Res.* **2011**, *44*, 588.
- (4) Hopkinson, M. N., Richter, C., Schedler, M., Glorius, F. *Nature* **2014**, *510*, 485.
- (5) Baffert, M., Maishal, T. K., Mathey, L., Copéret, C., Thieuleux, C. *ChemSusChem* **2011**, *4*, 1762.
- (6) Sanz, S., Azua, A., Peris, E. *Dalton Trans.* **2010**, *39*, 6339.
- (7) Sun, Y., Koehler, C., Tan, R., Annibale, V. T., Song, D. *Chem. Commun.* **2011**, *47*, 8349.
- (8) Zhang, J., Leitius, G., Ben-David, Y., Milstein, D. *Angew. Chem. Int. Ed.* **2006**, *45*, 1113.
- (9) Mueller, C.; Pidko, E. A.; Staring, A. J. P. M.; Lutz, M.; Spek, A. L.; van Santen, R. A.; Vogt, D. *Chem. Eur. J.* **2008**, *14*, 4899.
- (10) Filonenko, G. A.; Cosimi, E.; Lefort, L.; Conley, M. P.; Coperet, C.; Lutz, M.; Hensen, E. J. M.; Pidko, E. A. *ACS Catal.* **2014**, *4*, 2667.
- (11) Filonenko, G. A.; Hensen, E. J. M.; Pidko, E. A. *Catal. Sci. Technol.* **2014**, *4*, 3474.
- (12) Filonenko, G. A.; Conley, M. P.; Copéret, C.; Lutz, M.; Hensen, E. J. M.; Pidko, E. A. *ACS Catal.* **2013**, *3*, 2522.
- (13) Dub, P. A.; Ikariya, T. *ACS Catal.* **2012**, *2*, 1718.
- (14) Spasyuk, D.; Smith, S.; Gusev, D. G. *Angew. Chem. Int. Ed.* **2012**, *51*, 2772.
- (15) Werkmeister, S.; Junge, K.; Beller, M. *Org. Proc. Res. Devel.* **2014**, *18*, 289.
- (16) C. Gunanathan; D. Milstein, *Chem. Rev.* 2014, DOI: 10.1021/cr5002782.
- (17) Spasyuk, D.; Smith, S.; Gusev, D. G. *Angew. Chem. Int. Ed.* **2013**, *52*, 2538.
- (18) Lin, Y.; Finke, R. G. *Inorg. Chem.* **1994**, *33*, 4891.
- (19) Crabtree, R. H. *Chem. Rev.* **2011**, *112*, 1536.
- (20) Widegren, J. A.; Finke, R. G. *J. Mol. Catal. A: Chem.* **2003**, *198*, 317.
- (21) Widegren, J. A.; Bennett, M. A.; Finke, R. G. *J. Am. Chem. Soc.* **2003**, *125*, 10301.
- (22) Bayram, E.; Linehan, J. C.; Fulton, J. L.; Roberts, J. A. S.; Szymczak, N. K.; Smurthwaite, T. D.; Özkaz, S.; Balasubramanian, M.; Finke, R. G. *J. Am. Chem. Soc.* **2011**, *133*, 18889.
- (23) Canseco-Gonzalez, D.; Petronilho, A.; Mueller-Bunz, H.; Ohmatsu, K.; Ooi, T.; Albrecht, M. *J. Am. Chem. Soc.* **2013**, *135*, 13193.
- (24) Zhang, J.; Balaraman, E.; Leitius, G.; Milstein, D. *Organometallics* **2011**, *30*, 5716.
- (25) O, W. W. N.; Morris, R. H. *ACS Catal.* **2012**, *3*, 32.
- (26) Teunissen, H., T. ; Elsevier, C., J. *Chem. Commun.* **1998**, 1367.
- (27) Boardman, B.; Hanton, M. J.; van Rensburg, H.; Tooze, R. P. *Chem. Commun.* 2006, 2289.
- (28) Rosi, L.; Frediani, M.; Frediani, P. *J. Organomet. Chem.* **2010**, *695*, 1314.
- (29) Kuriyama, W.; Matsumoto, T.; Ogata, O.; Ino, Y.; Aoki, K.; Tanaka, S.; Ishida, K.; Kobayashi, T.; Sayo, N.; Saito, T. *Org. Proc. Res. Devel.* **2011**, *16*, 166.
- (30) Saudan, L. A.; Saudan, C. M.; Debieux, C.; Wyss, P. *Angew. Chem. Int. Ed.* **2007**, *46*, 7473.
- (31) Carpenter, I.; Eckelmann, S. C.; Kuntz, M. T.; Fuentes, J. A.; France, M. B.; Clarke, M. L. *Dalton Trans.* **2012**, *41*, 10136.
- (32) Adamo, C.; Barone, V. *J. Chem. Phys.* **1999**, *110*, 6158.
- (33) *Gaussian 09 Revision D.01*, Frisch, M. J. et al. Gaussian, Inc.: Wallingford CT, 2009.

Amino bis-N-heterocyclic carbene pincer ligands for the efficient hydrogenation of esters

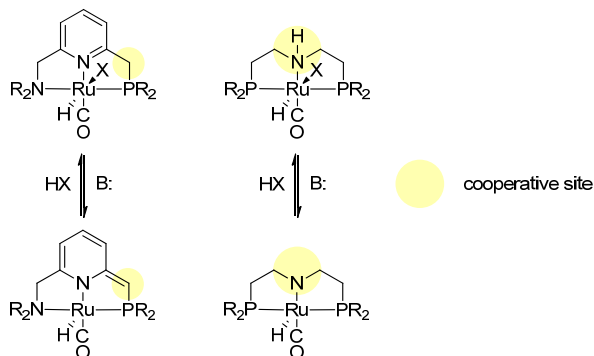
C'est pas le tout d'y dire y faut encore y faire

ABSTRACT: Amino bis-N-heterocyclic carbene (NHC) ligands enable unprecedented activities in Ru- and Ir-catalyzed ester hydrogenation. The deprotonation of the imidazolium salt ligand precursors upon the reaction with LiHMDS base in the presence of a $\text{Ru}(\text{PPh}_3)_4\text{Cl}_2$ *in situ* yields a highly active Ru catalysts for hydrogenation of a wide range of carboxylic acid esters. Similarly, a very active Ir ester hydrogenation catalysts can be generated using $[\text{Ir}(\text{COE})\text{Cl}]_2$ precursor. Optimization of the precatalyst synthesis leads to unprecedentedly high TOF^o values of over 120 000 h⁻¹ in hydrogenation of ethyl hexanoate at 70 °C. The nature of the precatalyst species in the Ru-catalyzed reaction was investigated in detail. NMR spectroscopy, mass spectrometry and X-ray analysis reveal the dimeric structure of the Ru precatalyst, featuring facial ligand coordination. Ligands developed in this work show a high versatility in modification of both the steric and electronic properties of the ligand that can be achieved by altering the structure of the NHC donors using a simple and straightforward strategy. The representative members of this ligand family can be readily prepared in multigram quantities. These ligands allow achieving the highest activity for ruthenium and iridium-catalyzed ester hydrogenation reported to date.

The content of this chapter is protected by US and international patent law.

7.1. Introduction

Bifunctional nature of the catalyst appears to be the cornerstone in ester hydrogenation by transition metal complexes.¹ With the exception of early examples by Grey^{2,3} and Elsevier^{4,5} all active ester hydrogenation catalysts rely on the non-innocence of their ligands. The first example of such catalyst was developed by Milstein and co-workers.⁶ The deprotonation of the methylene pincer arm of the lutidine-based ligand in this ruthenium PNN pincer results in the formation of a basic site in a close proximity to the 5-coordinated metal center (Scheme 7.1). These highly reactive sites can act cooperatively towards activation of reaction substrates, e.g. dihydrogen.⁷ The spatial arrangement of the cooperating metal and ligand moieties in the lutidine-based pincers may not be optimal for catalysis. The relatively large separation of the reactive sites with at least two bonds may hamper their cooperative action towards the activation of hydrogen or other substrates. As we have demonstrated in Chapters 3 and 6 with the examples of lutidine-derived Ru-PNP and Ru-CNC catalysts, the metal-ligand cooperative activation of H₂ represents the most difficult step in the CO₂ hydrogenation path with the dearomatized Ru-PNP* and Ru-CNC* complexes, respectively. The heterolytic dissociation of H₂ via the metal-ligand cooperative mechanism is also often considered a key step in ester hydrogenation catalysis.⁸ Therefore, improvements in catalytic performance of the bifunctional catalyst formulations can be achieved through the modifications of the cooperative function of the ligand.



Scheme 7.1. Cooperative sites in Milstein catalyst and Ru-MACHO catalyst.

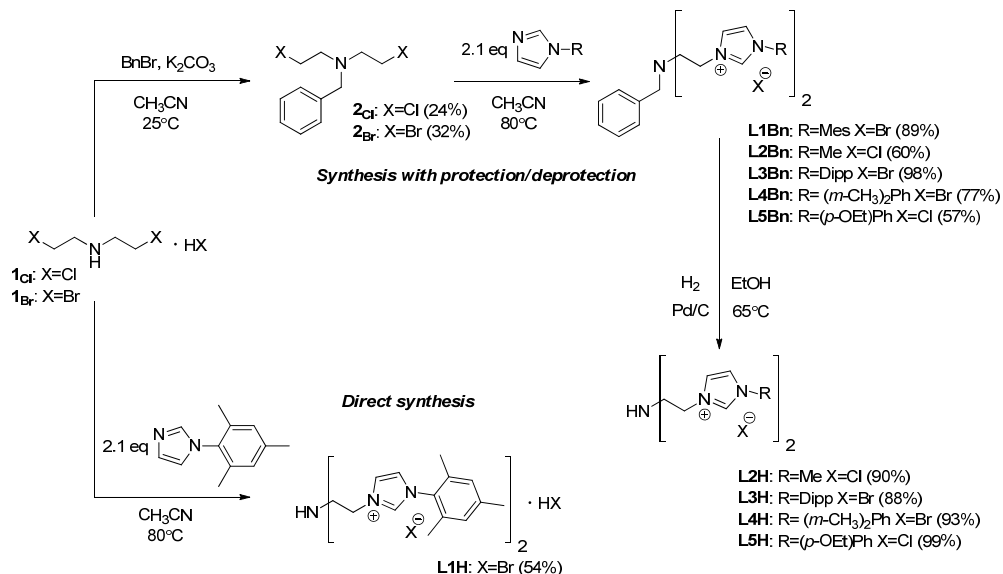
A representative example of this approach is the Ru-MACHO catalyst (Scheme 7.1). Although never directly compared in literature, the amine-based Ru-MACHO and lutidine-derived Ru-PNP both bearing phosphine donor groups, employ a different mechanism of ligand transformations to achieve the acid-base cooperativity. Ru-PNP employs a long-range pyridylmethylenic function, while Ru-MACHO relies on the reversible amine-amide

transformation typical for the Noyori-type catalysts.^{9,10} In the latter case, a more intimate contact between the metal and the cooperative site is established. This can potentially be one of the reasons for the superior catalytic performance of the Ru-MACHO catalyst in ester hydrogenation compared to the lutidine-derived Ru-PNP. This hypothesis is in line with the high ester hydrogenation activity of the related lutidine-derived bis-NHC Ru-CNC catalysts, which exhibit a more pronounced metal-ligand cooperative behavior compared to their phosphine-based counterparts (Chapter 6). Recently, Gusev and co-workers employed such an amino-pincer platform to develop highly efficient ester hydrogenation catalysts containing pyridine¹¹ and sulfur¹² donor groups.

In the previous Chapter we have demonstrated that a substantial improvement in catalytic ester hydrogenation activity of lutidine-based Ru pincers can be achieved by the replacement of the phosphine donor groups of the ligand with the N-heterocyclic carbenes. An increased reactivity towards metal-ligand cooperative transformations was one of the results of such substitution. Building upon the knowledge generated so far, this last Chapter of the Thesis is devoted to the synthesis and catalytic application of amino *bis*-NHC pincer ligands. Their application in Ir- and Ru-catalyzed hydrogenation of a wide range of esters was investigated. Special attention in this Chapter is devoted to the optimization of the catalyst synthesis procedure and identification of the active component in the Ru-catalyzed reactions.

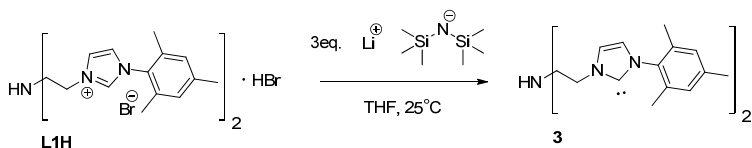
7.2. Synthesis of bis-NHC ligands and generation of free carbenes

Similar to the analogous SNS¹² and PNP¹³ ligands, the backbone of the target amino bis-NHC ligands can be built from bis-(2-haloethyl) amine reagents also known as the nitrogen mustards. Ligand **L1H** (Scheme 7.2) is a known compound¹⁴ that can be easily prepared via the reaction of 1-mesityl imidazole and bis-(2-bromoethyl)amine hydrobromide upon heating in CH₃CN at 80 °C for 2 days. Precipitation of the target compound from CH₃CN is probably the major driving force for this reaction, because the use of other imidazole reagents led to an extensive formation of mustard oligomerization byproducts (see examples in Scheme 7.2). Despite being very convenient, this procedure suffers from the undesired protonation of the starting imidazole by the mustard-bound HBr. This slows down the reaction considerably and leads to the formation of by-products. More importantly, the protonated mustard does not react with strongly basic 1-methyl- or 1-(*p*-ethoxyphenyl) imidazoles decreasing thus the applicability of the respective synthetic procedure as the generic route towards versatile amino bis-NHC ligand platform.



Scheme 7.2. Preparation of bis-imidazolium salt precursors of CNC amino pincer ligands

The oligomerization of the nitrogen mustard can be prevented by the introduction of benzyl protective group at the amine moiety. The respective precursors **2_{Cl}** and **2_{Br}** can be prepared via a straightforward reaction with benzyl bromide in the presence of potassium carbonate (top path, Scheme 7.2). No tedious purification was necessary for these compounds. Non-volatile impurities were removed by filtration through a silica plug, while subsequent vacuum treatment at 50 °C removed traces of the unreacted benzyl bromide. Mustards **2_{Cl}** and **2_{Br}** were further reacted with the corresponding imidazoles to yield the Bn-protected bis-NHC ligand precursors in good to near quantitative yields. The purification of the corresponding imidazolium salts **L1Bn** – **L5Bn** is straightforward because of their very low solubility in non-polar solvents. Deprotection of the benzylated imidazolium salts via the catalytic hydrogenation with Pd/C in ethanol leads to a near quantitative formation of the target ligands **L2H-L5H** (Scheme 7.2).



Scheme 7.3. Generation of the free NHC from ligand **L1H**

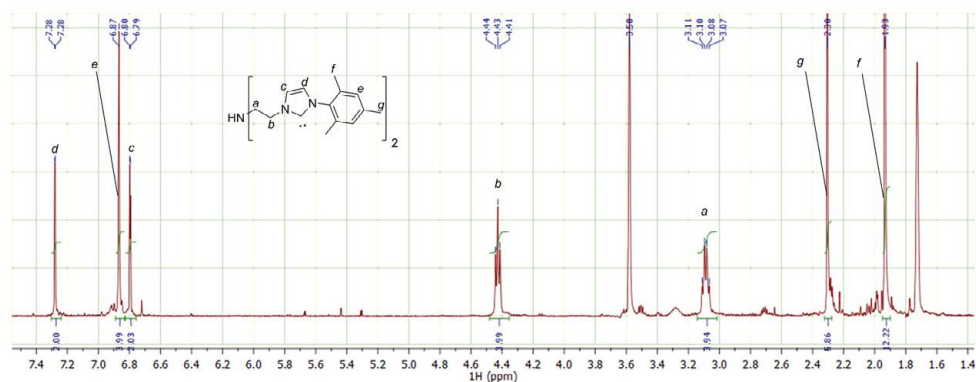


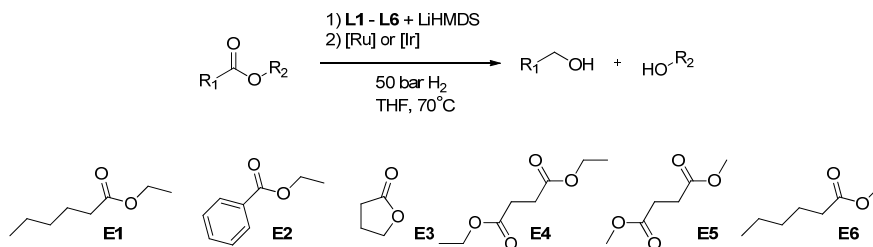
Figure 7.1. ^1H NMR spectrum of the free carbene **3** generated from **LIH**

The metallation of bis-NHC ligand precursors can be achieved via several different routes. One of the cleanest and practically feasible paths involves the generation of the free NHC carbene prior to the coordination with the metal precursor (Scheme 7.3). The reaction of ligand **LIH** with 3 eq. of lithium hexamethyldisilazide (LiHMDS) at room temperature in THF leads to an instant formation of the corresponding free NHC **3**. ^1H NMR spectrum (Figure 7.1) of **3** contains two doublets at $\delta = 7.3$ and 6.8 ppm ($^3J_{\text{HH}} = 1.5$ Hz) corresponding to the protons of the imidazolium backbone. Ethylene linker protons appear at $\delta = 4.4$ and 3.1 ppm as triplet and quartet, respectively, showing a similar $^3J_{\text{HH}} = 6$ Hz. The free NHC **3** derived from **LIH** was stable at room temperature for two hours under Ar atmosphere. Overtime the solutions of **3** darkened and the ^1H NMR showed signs of decomposition. No detectible signals associated with the free NHC species could be observed in the ^1H NMR spectrum after approx. 8 hours in solution. Nevertheless, the relatively high stability of **3** allowed us to use the corresponding free-NHC metallation route for the complexation of bis-NHC ligands in situ to generate Ru and Ir bis-NHC precatalysts for ester hydrogenation.

7.3. Catalytic hydrogenation of esters

With a set of 10 ligand precursors prepared, we studied their application in transition metal catalyzed ester hydrogenation (Scheme 7.4). The catalysts were generated *in situ* using the approach previously described by Beller and co-workers.¹⁵ In a typical run, the suspension of the imidazolium salt was treated with LiHMDS solution followed by stirring for 5 minutes, after which it was transferred to the solution or suspension of the appropriate metal precursor. The resulting clear THF solutions were used as the catalyst stocks. Unless

specified otherwise, the catalytic reactions were carried out under 50 bar hydrogen pressure at 70°C with 16 hours reaction time. The results of the respective catalyst activity screening and substrate scope studies are summarized in Table 7.1.



Scheme 7.4. Catalytic hydrogenation of esters as performed in this Chapter.

Ligand structure had a strong influence on the activity of *in situ* generated Ru catalysts (Entries 1-8, Table 7.1). In line with the observations made by Gusev and co-workers,¹² the substitution at the cooperative NH site (Entries 1-3, Table 7.1) yields essentially inactive catalysts. This effect does not depend on the structure of the NHC moieties.

The substituents at the NHC groups were also found to have an impact on the catalytic performance. No activity was observed with *methyl* and *p-ethoxyphenyl* substituted ligands, whereas *mesityl*, *diisopropylphenyl* and *m-dimethylphenyl* substituted ligands provided substantial conversions (Entries 4-8 and 12-16, Table 7.1).

The nature of the ruthenium precursor employed for the *in situ* catalysis had also a great impact on the catalytic performance. Relatively low conversions of ethyl hexanoate (E1) and ethyl benzoate (E2) substrates could be achieved with RuHCl(CO)(PPh₃)₃ precursor (entries 9-11 and 17-19, Table 7.1). For this precursor, the highest activity was achieved in combination with the **L1H** ligand bearing *mesityl* substituents on imidazolium groups, that allowed for 70% and 62% alcohol yield in the hydrogenation of E1 and E2, respectively.

For all metal precursors considered in this study, the use of ligands **L1H** and **L3H** bearing *mesityl* and *diisopropylphenyl* substituents on imidazolium groups resulted in the highest activity of the *in situ* generated catalysts. In combination with Ru(PPh₃)₄Cl₂, **L1H** and **L3H** allowed for a near quantitative conversion of ethyl hexanoate within 16 hours at the substrate-to-catalyst ratio (S/C ratio) as high as 15 000 that corresponded to approx. 77 ppm catalyst loading with respect to substrate. For comparison, the best example of bis-NHC catalyzed hydrogenation of esters reported in literature requires a metal loading of 10 000 ppm to reach comparable conversions.¹⁵

Table 7.1. Results of the CNC ligand screening in Ru-catalyzed ester hydrogenation

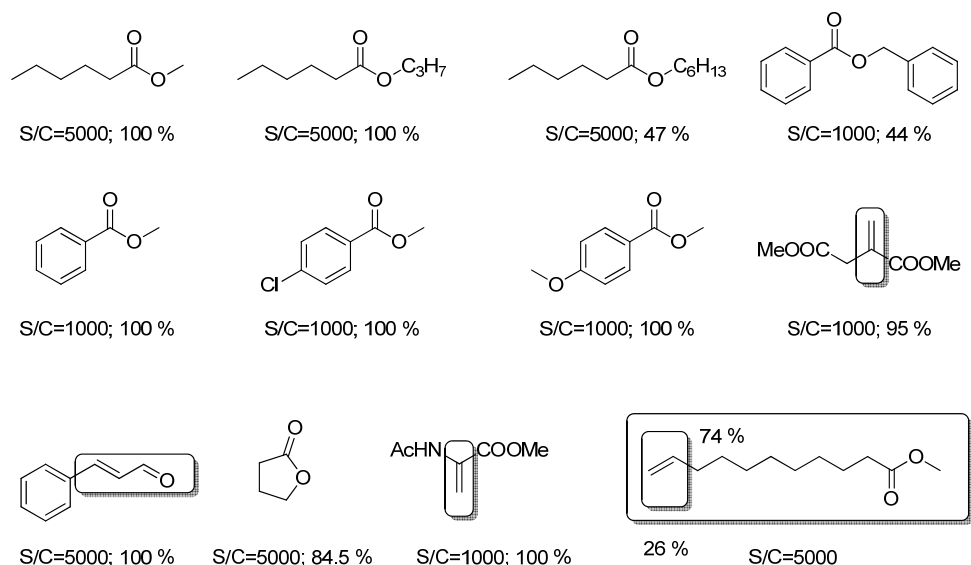
Entry	Substrate	Ligand	Ru source	Base	S/C ^b	Yield(%) ^c
1	E1	L2Bn	Ru(PPh ₃) ₄ Cl ₂	KO ^t Bu	15000	0
2	E1	L4Bn	Ru(PPh ₃) ₄ Cl ₂	KO ^t Bu	15000	0
3	E1	L1Bn	Ru(PPh ₃) ₄ Cl ₂	KO ^t Bu	15000	0
4	E1	L2H	Ru(PPh ₃) ₄ Cl ₂	KO ^t Bu	15000	1
5	E1	L4H	Ru(PPh ₃) ₄ Cl ₂	KO ^t Bu	15000	40
6	E1	L1H	Ru(PPh ₃) ₄ Cl ₂	KO ^t Bu	15000	95
7	E1	L3H	Ru(PPh ₃) ₄ Cl ₂	KO ^t Bu	15000	100
8	E1	L5H	Ru(PPh ₃) ₄ Cl ₂	KO ^t Bu	15000	2
9	E1	L4H	RuHCl(CO)(PPh ₃) ₃	KO ^t Bu	15000	26
10	E1	L1H	RuHCl(CO)(PPh ₃) ₃	KO ^t Bu	15000	70
11	E1	L5H	RuHCl(CO)(PPh ₃) ₃	KO ^t Bu	15000	9
12	E2	L2H	Ru(PPh ₃) ₄ Cl ₂	KO ^t Bu	5000	0
13	E2	L4H	Ru(PPh ₃) ₄ Cl ₂	KO ^t Bu	5000	50
14	E2	L1H	Ru(PPh ₃) ₄ Cl ₂	KO ^t Bu	5000	83
15	E2	L3H	Ru(PPh ₃) ₄ Cl ₂	KO ^t Bu	5000	65
16	E2	L5H	Ru(PPh ₃) ₄ Cl ₂	KO ^t Bu	5000	37
17	E2	L4H	RuHCl(CO)(PPh ₃) ₃	KO ^t Bu	5000	25
18	E2	L1H	RuHCl(CO)(PPh ₃) ₃	KO ^t Bu	5000	62
19	E2	L5H	RuHCl(CO)(PPh ₃) ₃	KO ^t Bu	5000	36
20	E2	L1H	Ru(PPh ₃) ₄ Cl ₂	KO ^t Bu	1000	96
21	E2	L1H	Ru(PPh ₃) ₄ Cl ₂	KO ^t Bu	2500	89
22	E1	L1H	Ru(PPh ₃) ₄ Cl ₂	KO ^t Bu	10000	99
23	E1	L1H	Ru(PPh ₃) ₄ Cl ₂	KO ^t Bu	30000	89
24	E1	L1H	Ru(PPh ₃) ₄ Cl ₂	KOEt	30000	12
25	E1	L1H	Ru(PPh ₃) ₄ Cl ₂	KOMe	30000	71
26 ^a	E3	L1H	Ru(PPh ₃) ₄ Cl ₂	KO ^t Bu	8000	97
27 ^a	E4	L1H	Ru(PPh ₃) ₄ Cl ₂	KO ^t Bu	4000	40
28 ^a	E5	L1H	Ru(PPh ₃) ₄ Cl ₂	KOMe	1500	100

Conditions: 2 mL THF, 5 mmol substrate, 2 %_{mol} KO^tBu, 70°C, 50 bar H₂, 16h; ^a 1 mmol substrate used, ^b Substrate-to-Catalyst ratio based on total metal loading, ^c alcohol yield

Notably, only *ortho* substituted aryl imidazoles comprised catalytically competent ligands. The absence of *ortho*-substituents at the imidazole aryl group led to significantly lower yields in catalysis. Precatalysts generated in situ from the *p*-ethoxyphenyl substituted **L5H** showed a near zero conversion in hydrogenation of ethyl hexanoate. A slightly better performance was observed with the **L4H** ligand bearing *meta* substituted aryl group at the imidazolium moieties. This may be explained by the lower stability of free-NHCs derived from ligands with no *ortho* substitution.¹⁶ Alternatively, one can expect reactivity of **L4H** and **L5H** towards orthometallation of Ru center, that could also have a negative impact on activity as it was shown for metathesis catalysts.¹⁷

Ligand **L1H** that showed superior performance in hydrogenation of ethyl hexanoate was also the best in hydrogenation of ethyl benzoate. At S/C = 5000 the best performing catalyst derived from **L1H** provides 83 % yield of benzyl alcohol (Entry 14, Table 7.1). With increase of the catalyst loading to S/C = 1000 – 2500 (400-100 ppm) allowed to increase the yield of benzyl alcohol up to 96 and 89% respectively (Entries 20-21, Table 7.1). With the same catalyst ethyl hexanoate can be hydrogenated with 99 and 89 % yield at 100 and 33 ppm loading (Entries 22-23, Table 7.1). The type of alkoxide base, used in these reactions, had an influence on the final product yield (Entries 23-25, Table 7.1). Potassium *tetr*-butoxide was found to be superior to methoxide and ethoxide bases. Finally, we were able to hydrogenate lactones (Entry 26, Table 7.1) and diesters (Entries 27-28, Table 7.1) using **L1H** ligand precursor in combination with Ru(PPh₃)₄Cl₂. Excellent yields are achieved for γ -butyrolactone (**E3**, 97%) and dimethylsuccinate (**E5**, 100%). Conversion of diethylsuccinate (**E4**) was incomplete due to the high S/C ratio used. The substrate scope of Ru-catalyzed hydrogenation can be expanded further to various aromatic and aliphatic esters, lactones and aldehydes (Scheme 7.5).

The activity of the **L1H**/Ru(PPh₃)₄Cl₂ combination is comparable to the current state of the art. Catalysts based on bis-NHC ligands are particularly efficient in hydrogenation of aliphatic esters. They outperform the isolated Ru-PNN¹¹ catalyst developed by Gusev and co-workers in hydrogenation of hexanoates, but show a slightly lower activity than the best catalyst in the field – the well-defined Ru-SNS pincer complex.¹² The productivity of our *in situ* catalyst in hydrogenation of aromatic esters is somewhat lower than that of the two best catalysts in the field. For example Ru-SNS and Ru-PNN allow for identical yields in hydrogenation of ethyl benzoate within the same reaction time, but require a four-fold lower loading of the isolated catalyst. With the exception of Gusev's catalysts,^{11,12} the current *in situ*-formed system is superior to any other catalyst in the field.



Scheme 7.5. Product yields and selectivities for the catalytic hydrogenation of esters, ketones and olefins by a $\text{Ru}(\text{PPh}_3)_4\text{Cl}_2/\text{LIH}$ catalyst. Conditions: 2 mL THF, 5 mmol substrate, 2 %_{mol} KO^tBu , 70°C, 50 bar H_2 , 16 h, S/C = 1000 or 5000. Product yields shown on the Scheme, for functionalized substrate selectivity for specific functionality is indicated separately.

Much to our surprise, the amino bis-NHC ligands enabled iridium catalyzed hydrogenation of esters (Table 7.2). This is only the second known example of iridium-based catalytic system, because the activity of Ir in ester hydrogenation was not known until 2014.¹⁸ At 0.5 – 1 %_{mol} metal loading quantitative to near quantitative yields were obtained in hydrogenation of ethyl hexanoate and ethyl benzoate at 70 °C and 50 bar H_2 . The use of amino bis-NHC pincer ligands allows to carry out ester hydrogenation at a much lower reaction temperature, compared to the only alternative Ir-based system reported recently.¹⁸ Furthermore, aliphatic ethyl hexanoate ester can be hydrogenated with quantitative yield at a ten-fold lower catalyst loading.

The catalytic activity of the iridium-CNC catalysts was further assessed in the hydrogenation of various aromatic and aliphatic esters and lactones using the ligand **LIH** (Scheme 7.5). At 0.5 %_{mol} metal loading, quantitative conversions of eight aromatic and aliphatic esters were obtained. Namely, substituted methyl benzoates and benzyl benzoates were fully converted to corresponding alcohols. Methyl, propyl and hexyl hexanoates were also fully hydrogenated. The olefin functionality in methyl cinnamate was not tolerated and corresponding double bond was fully hydrogenated. However, hydrogenation of

cinnamaldehyde showed significant chemoselectivity towards cinnamyl alcohol (ca. 72%). The remaining reaction product was 3-phenylpropanol. The latter allows to conclude that the hydrogenation of the olefin function is more facile than that of the ester group, but proceeds slower than the hydrogenation of aldehyde moieties. Furthermore, at several instances Ir catalyst was 100% selective for olefin functionality and retained ester function completely unreduced in methyl undecenoate and dimethyl itaconate (Scheme 7.6).

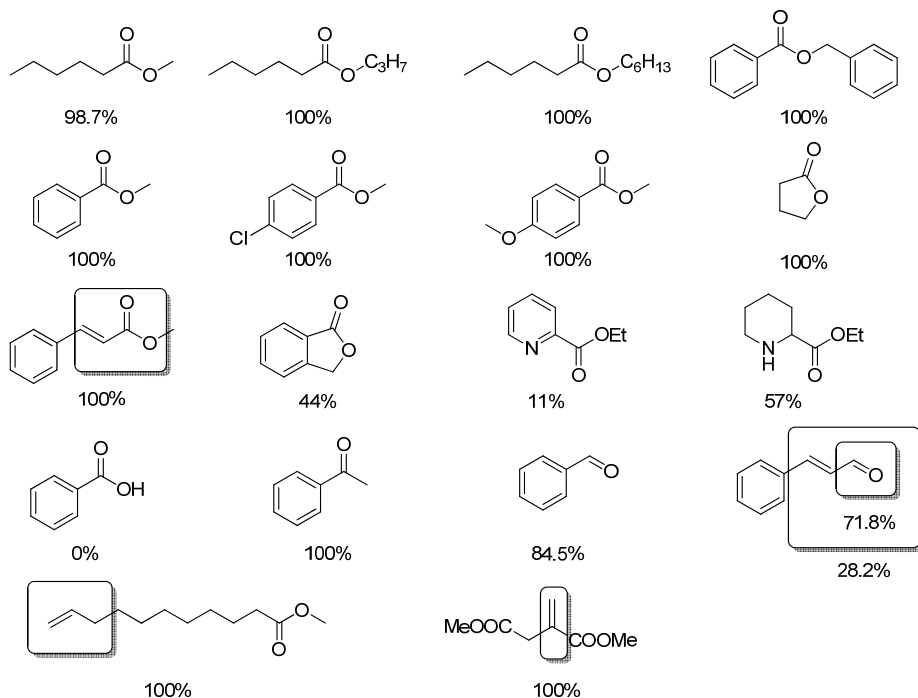
Table 7.2. Results of CNC ligand screening in Ir-catalyzed hydrogenation of ethylhexanoate (E1) and ethylbenzoate (E2).

Entry	Substrate	Ligand	Precursor	Base	S/C	Yield (%)
1	E1	L4H	[Ir(COE)Cl] ₂	KO ^t Bu	200	100
2	E1	L1H	[Ir(COE)Cl] ₂	KO ^t Bu	200	100
3	E1	L3H	[Ir(COE)Cl] ₂	KO ^t Bu	200	100
4	E1	L5H	[Ir(COE)Cl] ₂	KO ^t Bu	200	25
5	E2	L4H	[Ir(COE)Cl] ₂	KO ^t Bu	100	97
6	E2	L1H	[Ir(COE)Cl] ₂	KO ^t Bu	100	97
7	E2	L3H	[Ir(COE)Cl] ₂	KO ^t Bu	100	99
8	E2	L5H	[Ir(COE)Cl] ₂	KO ^t Bu	100	68
9	E1	L1H	[Ir(COE)Cl] ₂	KO ^t Bu	500	100
10	E1	L1H	[Ir(COE)Cl] ₂	KO ^t Bu	1000	100

Conditions: [Ir(COE)₂Cl]₂, 2 %_{mol} KO^tBu base, 2 mL THF, 5 mmol substrate, 70°C, 50 bar H₂, 16 h; ^a 1 mmol substrate used, ^b S/C ratio based on total metal loading, ^c alcohol yield

The kinetic analysis is important for the optimization of the catalytic performance, reaction times and catalyst loadings. In addition, initial rate, determined from kinetic data, provides the most reliable basis for the comparison of different catalysts. Therefore, we evaluated the performance of the earlier disclosed *in situ* generated catalysts in the hydrogenation of methyl and ethyl hexanoates. The kinetics of methyl hexanoate hydrogenation using a catalyst derived from RuHCl(CO)(PPh₃)₃ confirms the conclusion of the initial screening study on the low catalytic activity of this precursor in combination with **L1H** (Table 7.1). The kinetic analysis of this system (Figure 7.2) points to the rapid catalyst deactivation upon the hydrogenation at 70°C under 50 bar H₂ pressure. Although the initial TOF^o is rather high (ca. 5000 h⁻¹), the reaction develops very slowly after ca. 15% conversion. This data is consistent with the literature reports¹² pointing to the negative

effect of the carbonyl ligands on the catalyst performance. Furthermore, carbonylation of the metal complex was previously proposed as a potential route for the deactivation of ester hydrogenation catalysts.¹³



Scheme 7.6. Product yields and selectivities for the catalytic hydrogenation of esters, ketones and olefins by an Ir/LIH catalyst. Conditions: 2 mL THF, 1 mmol substrate, 70°C, 50 bar H₂, 16 h, 0.5 %_{mob} metal, 2 %_{mol} KO^tBu. Product yields shown on the Scheme, for functionalized substrate selectivity for specific functionality is indicated separately.

Catalytic performance is greatly improved when Ru(PPh₃)₄Cl₂ precursor is used (Figure 7.3). At 70°C initial TOF reach values of ca. 22 000 h⁻¹ that is the highest reported rate of ester hydrogenation up to date. Importantly, similar initial TOF were observed for hydrogenation of ethyl and methyl hexanoates (Figure 7.3). This is consistent with the report of Morris and co-workers,¹⁹ who proposed that the bulk at the acid side of the ester has the major influence on the activity, rather than the bulk of the alkoxy moiety. We also observed the decrease of the catalytic activity at higher conversions, namely, at conversions above 60 % the reaction rate decayed rapidly, that introduced the main deviation from the first order kinetics. This behavior was different for ethyl and methyl esters of hexanoic acid. Reduction of ethyl ester (E1) was less prone to the activity inhibition and the rate

decrease in this case was observed at ca. 10% higher conversion. This data is consistent with a known phenomenon of the catalysis inhibition by methanol.¹³

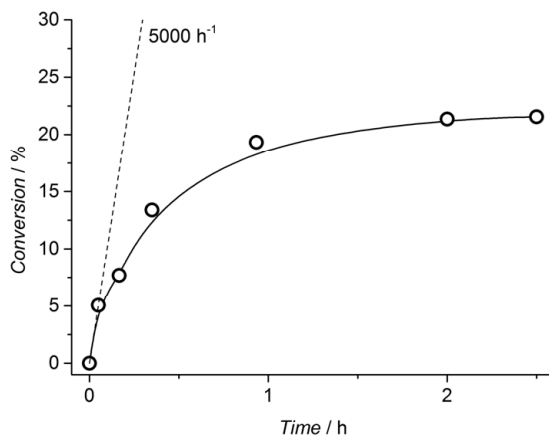


Figure 7.2. Kinetic trace for methyl hexanoate (E6) hydrogenation with an in situ generated Ru-CNC catalyst employing $RuHCl(CO)(PPh_3)_3$ and **LIH** precursors. Conditions: 70°C, 50 bar H_2 , 50 mmol ester, $S/C = 5000$, 1%_{mol} KO^tBu .

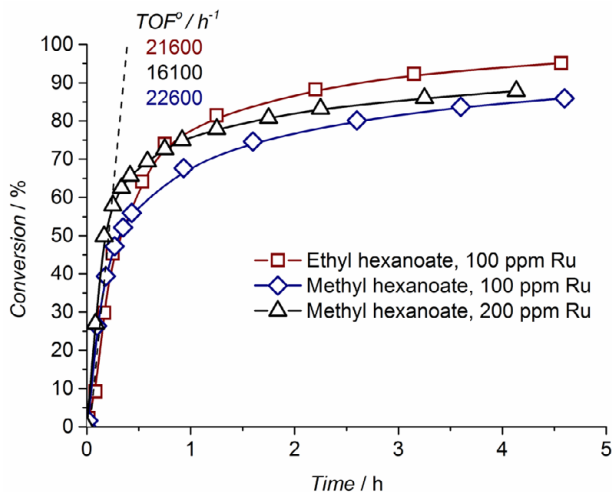


Figure 7.3. The effect of catalyst loading and substrate variation on the kinetics of hydrogenation of methyl- and ethyl hexanoate. Conditions: 30 mL THF, 70°C, 50 bar H_2 , 50 mmol ester, 1%_{mol} KO^tBu . Catalyst formed in situ by combining **LIH** / $Ru(PPh_3)_4Cl_2/LiHMDS$ (See Experimental Section)

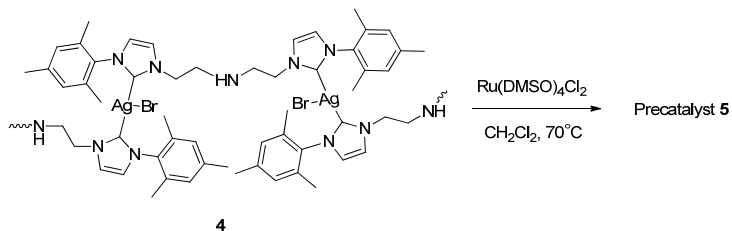
Another important observation is the similarity of the absolute rates of ester hydrogenation for all experiments presented in Figure 7.3. Initial stages of conversion vs. time profiles were independent of the catalyst loading and even the type of hexanoate used

for the reduction. This results in a higher TOF values attainable for lower catalyst loading, as demonstrated by methyl hexanoate hydrogenation data on Figure 7.3.

7.4. On the nature of the ruthenium bis-NHC precatalyst

With the goal to improve the hydrogenation activity we focused the last part of this Chapter on the investigation of Ru precatalyst species, responsible for catalysis. While the reaction of the free NHC **3** with $\text{RuHCl}(\text{CO})(\text{PPh}_3)_3$ precursor leads to a near quantitative formation of the corresponding bis-NHC complex, a similar reaction with $\text{Ru}(\text{PPh}_3)_4\text{Cl}_2$ did not yield reliably detectible bis-NHC complexes of Ru. This implies that only a small fraction of Ru is involved in catalysis and, therefore, the activity of ruthenium is underestimated when the catalyst is generated in situ. Consequently, the hydrogenation efficiency can be improved if the precatalyst is synthesized in a cleaner way. One of the alternatives to the catalyst formation via the free carbene route is a carbene transfer from silver NHC complexes. The Ag-NHC complex **4** derived from **L1H** is a known compound.²⁰ Unlike many other halide containing silver NHC complexes, **4** adopts a polymeric structure and contains only one AgX unit per two NHC groups. This feature has a strong negative impact on the transmetalation to ruthenium. Namely, the reactions of **4** with $\text{Ru}(\text{PPh}_3)_4\text{Cl}_2$ or $\text{Ru}(\text{DMSO})_4\text{Cl}_2$ in dichloromethane at 60 °C (Scheme 7.7) only result in ca. 50% conversion of **4** while the remaining Ag-NHC is converted back to the starting imidazolium salt as is evidenced by the appearance of singlet resonances in ¹H NMR in the C2-imidazolium region. This points to the regeneration of the imidazolium groups during the breakdown of polymeric **4**. However the loss of the ligand can be remediated in the presence of organic base. Namely, when the reaction was performed in the presence of free or resin-supported BEMP base, no formation of imidazolium protons was observed due to the *in situ* regeneration of Ag-NHC and subsequent metallation of Ru precursor. The resulting precatalyst **5** can be characterized by NMR and mass spectrometry. As evidenced by electrospray ionization mass spectrometry, complex **5** is a dimer with a mass of 1093.3 a.m.u., corresponding to a brutto formula $[\text{Ru}_2(\text{L1H})_2\text{Cl}_3]^+$. This dimeric structure introduces an uncertainty regarding the connectivity between **L1H** and Ru centers in **5**. Two possibilities can be realized. One hand, each **L1H** can bridge both metal centers similar to Ag-NHC complex **4**. Such connectivity would make the dimeric **5** impervious towards the cleavage with strong ligands such as CO. On the other hand, the two isolated Ru-NHC moieties can be connected via bridging Cl ligands, which is very common for coordination chemistry of ruthenium. To confirm the latter configuration, solutions of **5** were heated under 3 bar of CO at 70 °C in THF. The ESI-MS of the resulting reaction

mixture contained only masses corresponding to mononuclear mono- and di-carbonyl complexes of Ru(L1H)Cl(CO)_x stoichiometry.



Scheme 7.7. Generation of a precatalyst **5** via the transmetallation route with the Ag-NHC **4**

Crude **5** was contaminated with the products of decomposition of the starting material. However, we managed to obtain pure **5** in amounts sufficient for spectral and X-ray characterization. Molecular structure analysis confirms the dimeric structure of **5** (Figure 7.4). Dimer **5** adopts a bis-trigonal antiprism geometry with three chlorine ligands bridging ruthenium octahedral complexes. **5** is a cationic complex, bearing a dibromoargenate counterion that originated from Ag-NHC used for the preparation of **5**. The CNC ligands in **5** are *facially* coordinated. Unfortunately the quality of the crystal of **5** was insufficient for reliable refinement of the hydrogen atom positions (R_f ca. 0.1). When crystallization was performed in the presence of *tert*-butyl isocyanide, that is a strong ligand is electronic to CO, we managed to obtain a crystalline sample of the monomer complex **5**_{ICN} where the CNC ligand was also *facially* coordinated. Due to the higher quality of monocrystal sample in the latter case, we were able to refine the structure with $R_f = 0.05$ that allowed to unambiguously confirm the presence of NH proton in the aminopincer ligand backbone (Figure 7.4). The dimer **5** has a highly symmetric arrangement that is characterized by a nearly identical set of Ru-Cl distances for Ru1 and Ru2 atoms. The Ru-N distance in **5** is at least 0.03 Å shorter than one reported for Ru-SNS pincers in *fac*- and *mer*- configurations¹² or in Ru-PNN aminophosphine pincers.¹¹ Ru-NHC bonds in **5** are also shorter than Ru-NHC bonds in lutidine-derived bis-NHC pincers ($\Delta > 0.06$ Å). Upon the dimer cleavage the respective distances in **5**_{ICN} are within typical ranges for both Ru-N and Ru-C bonds.

The highly symmetrical arrangement of the CNC ligands in **5** can also be observed in solution. ¹H NMR of **5** (Figure 7.5) features a set of resonances corresponding to a single CNC ligand unit that was confirmed by the correlation spectroscopy measurements (gCOSY).

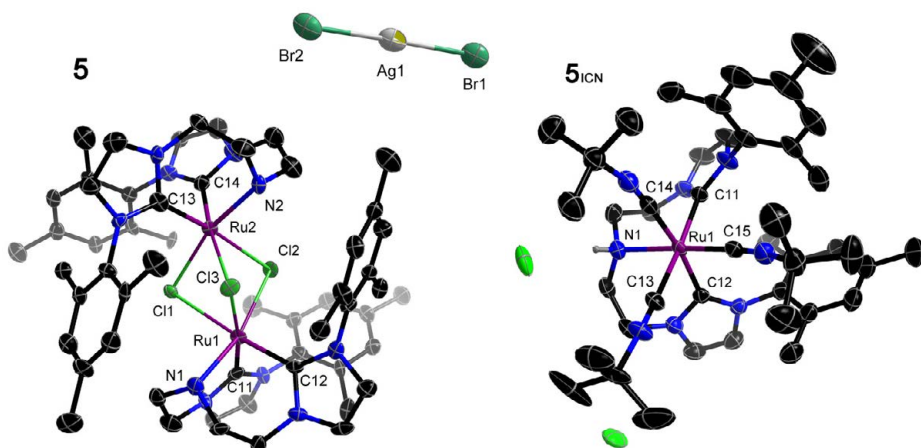


Figure 7.4. Crystal structure of **5** (left) and the dimer cleavage product **5_{ICN}**, crystallized in the presence of ^tBu isocyanide (ellipsoids at the 50% probability level, all hydrogens except NH are omitted for clarity) Selected bond lengths [Å]:**5**: Ru1-C11 2.5589, Ru1-Cl2 2.5459, Ru1-Cl3 2.4725, Ru2-Cl1 2.4565, Ru2-Cl2 2.5588, Ru2-Cl3 2.4716, Ru1-N1 2.1198, Ru1-C11 1.9781, Ru1-C12 1.9864, Ru2-N2 2.1015, Ru2-C13 1.9842, Ru1-C14 1.9771 **5_{ICN}**: Ru1-N1 2.2215, Ru1-C11 2.1190, Ru1-C12 2.1139, Ru1-C13 2.0137, Ru1-C14 1.9884, Ru1-C15 1.9406

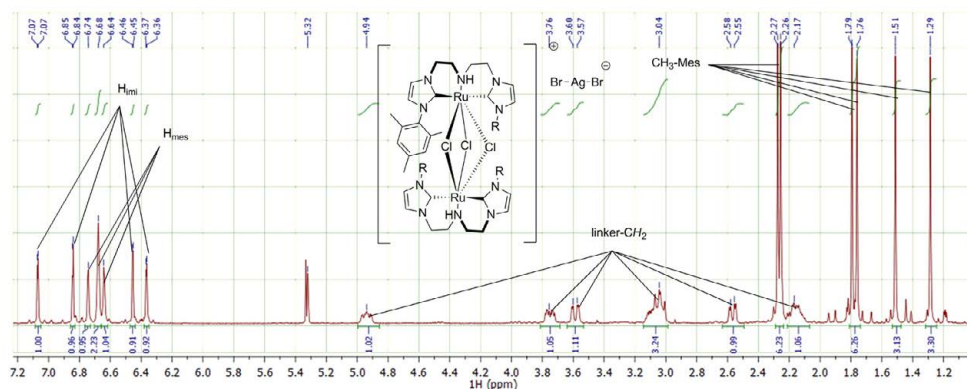


Figure 7.5. ¹H NMR spectrum of **5** in CD₂Cl₂

Attempted purification of **5** by recrystallization, precipitation or column chromatography was either inefficient or led to the decomposition of the complex. Due to the loss of target compound upon purification, crude material obtained after the transmetallation was used in the catalytic tests. Ruthenium content was verified by elemental analysis to reference the metal loadings accurately. Hydrogenation of ethyl hexanoate was selected as a model reaction to evaluate the performance of **5**. A very high

initial TOF = 124 600 h⁻¹ (Figure 7.6) was developed at 70 °C at only 17 ppm catalyst loading. Precatalyst **5** was also efficient at 40 °C at a slightly higher Ru loading of 84 ppm with respect to the substrate. The initial rate in this case was 23 300 h⁻¹ that is approximately 5-fold higher than that of the best catalyst reported to date at the same reaction temperature.¹²

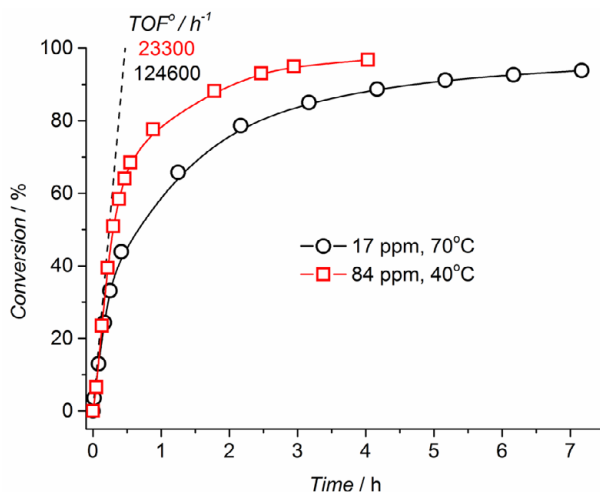
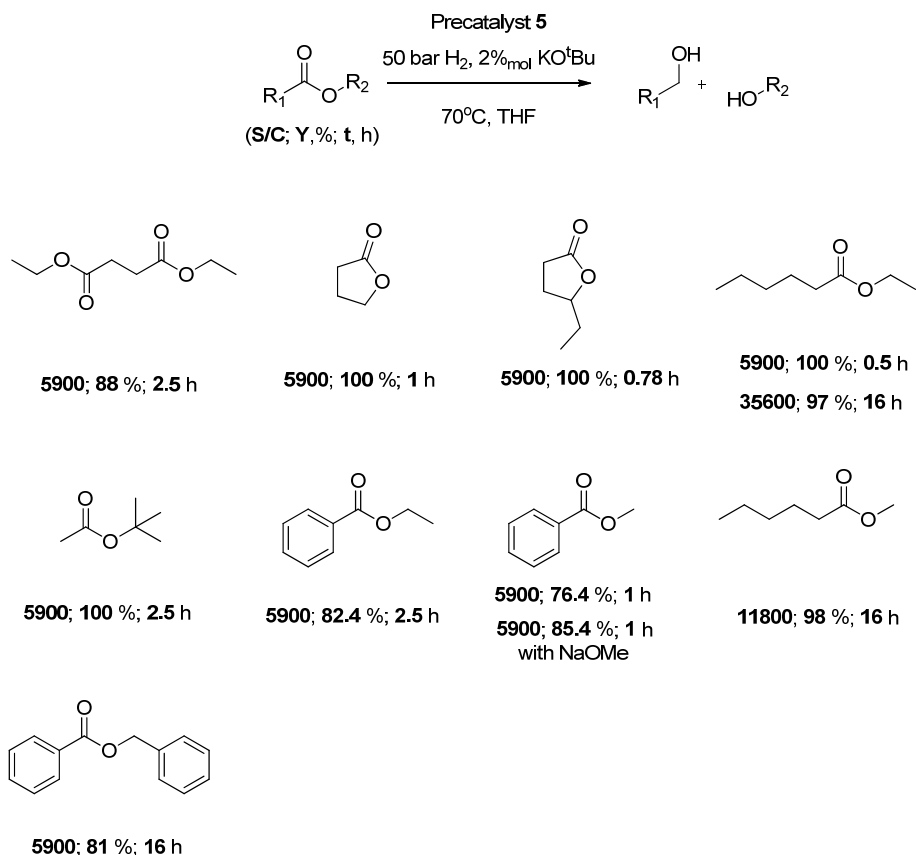


Figure 7.6. Kinetic traces for ethyl-hexanoate (E1) hydrogenation with precatalyst **5**. Conditions: 50 bar H₂, 50 mmol ester, 1%_{mol} KO^tBu, temperature and catalyst loading indicated on the graph.

Since precatalyst **5** was not sufficiently purified prior to the testing, additional experiments were carried out to prove the molecular nature of catalysis and rule out the possible involvement of catalysis by nanoparticles. When activated in the presence of 400 eq. of metallic Hg, catalyst **5** provides the activity identical to the control experiment. Similar 92 % and 100 % conversions of ethyl hexanoate were obtained at S/C = 5900 within 30 minute reaction at 70°C. At this temperature the most active Ru-SNS catalyst allowed for a lower conversion of 86 % at S/C = 5000 in 30 minutes that evidenced the superior performance of **5**. We further evaluated the substrate scope of the precatalyst **5** in ester hydrogenation (Scheme 7.8). A range of aromatic and aliphatic esters can be readily hydrogenated using **5** with no purification needed. At S/C = 5900 lactones are quantitatively converted within less than 1 hour. Benzoic acid esters generally required longer reaction times but good yields >80% at S/C=5900 could also be attained. Finally, aliphatic esters and diesters can be converted easily within 0.5-2.5 hours at S/C=5900 in good yields of 88-100%.



Scheme 7.8. Product yields for the catalytic hydrogenation of esters by precatalyst 5. Conditions: 3 mL THF, 5 mmol substrate, 70°C, 50 bar H₂, 0.5-16h, S/C ratios, reaction times and product yields are given in the Scheme

7.5. Conclusions and outlook

The replacement of the lutidine based C-H cooperative site with an amine functionality in bis-NHC pincer ligands results in a dramatic increase of the catalytic activity of the respective transition metal complexes in ester hydrogenation. Active precatalysts can easily be formed *in situ* by combining bis-NHC ligands with Ru or Ir metal precursors in the presence of a strong base. A wide range of aliphatic and aromatic esters and lactones can be converted to corresponding alcohols in good to quantitative yields by using only 100-500 ppm Ru with respect to the substrate. The performance of such *in situ* formed catalysts is comparable to that of well-defined state-of-the-art systems.

The activity of Ru bis-NHCs can be further improved by optimizing the procedure of the catalyst preparation. With no imperative purification, precatalyst **5**, obtained by reacting Ag-NHC complex **4** with a Ru(PPh₃)₃Cl₂ precursor, allowed hydrogenation of ethyl hexanoate with an outstanding initial TOF values up to 124 000 h⁻¹ at 70 °C. These rates represent the highest reported ester hydrogenation activities to date. Combined NMR, ESI-MS and X-ray studies allowed for identification of the active catalyst as a dimeric complex with metal centers linked via μ-Cl bridges. Taken together, our findings outline the potential of bis-NHC ligand platform and pave the way towards the development of new highly active hydrogenation catalysts based on easily accessible NHC ligands.

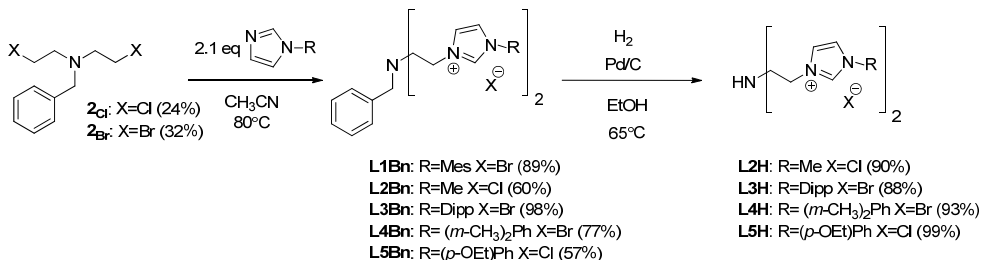
7.6. Experimental

General considerations

All manipulations unless stated otherwise were performed using Schlenk or high vacuum line (~5 · 10⁻⁶ mbar) techniques. Argon was dried with a Sicapent column. Air sensitive compounds were stored in an MBraun glovebox under an atmosphere of dry argon. Anhydrous solvents were dispensed from MBraun purification system and degassed prior to use. Acetonitrile (DNA synthesis grade, Biosolve) was distilled over CaH₂ and stored over molecular sieves. BEMP solution was purchased from Sigma and degassed by three freeze-pump-thaw cycles. Deuterated solvents were purchased from Eurisotop and dried over Na/benzophenone (C₆D₆, THF-d₈), calcium hydride (CD₃CN) or phosphorus pentoxide (CD₂Cl₂), degassed using three freeze-pump-thaw cycles, high-vacuum transferred in storage vessels and used in the glovebox. All imidazoles except methyl imidazole (Sigma) were prepared according to literature procedures and sublimed or distilled under vacuum (8 · 10⁻² mbar) before use.²¹ Known compounds **L1H** and **4** were prepared according to literature procedures.^{14,20} Bis-(2-bromoethyl)amine hydrobromide was prepared according to published procedure.²² Benzyl-protected mustards **2_{Cl}** and **2_{Br}** were prepared according to report of Douthwaite et al. with SiO₂ plug filtration and evaporation of unreacted benzyl bromide as the only work-up steps. Spectral data identical to published one.^{23,24}

NMR spectra were recorded on Varian Mercury 400 MHz spectrometer. Chemical shifts were referenced to residual solvent peaks. ESI-MS measurements were performed on Thermo Scientific LCQ Fleet apparatus, isotope distribution patterns were used as a composition proof in addition M/Z signal. Elemental analyses were performed in Kolbe laboratory (Mulheim an der Ruhr, Germany).

Ligand synthesis



Scheme 7.9. Synthesis of CNC ligands via “Protective group route”

A general procedure was adopted from Douthwaite et al.²⁴ Yields of new compounds are indicated on Scheme 7.9. All bis-imidazolium salts were obtained as white powders. Spectral data:

L1Bn: ¹H NMR (400 MHz, D₂O) C₂-H not observed, δ 7.52 (d, *J* = 1.9 Hz, 2H), 7.36 (d, *J* = 1.9 Hz, 2H), 7.16 – 7.01 (m, 5H), 6.99 (s, 4H), 4.32 (t, *J* = 5.8 Hz, 4H), 3.61 (s, 2H), 3.07 (t, *J* = 5.8 Hz, 4H), 2.20 (s, 6H), 1.81 (s, 12H). ¹³C NMR (100 MHz, D₂O) δ 141.44 (s), 137.78 (s), 134.20 (s), 130.43 (s), 129.26 (s), 129.24 (s), 128.63 (s), 127.73 (s), 124.00 (s), 123.04 (s), 57.78 (s), 52.78 (s), 47.51 (s), 20.06 (s), 16.37 (s).

L2Bn: ¹H NMR (400 MHz, D₂O) δ 8.31 (s, 2H), 7.28 (d, *J* = 1.6 Hz, 2H), 7.23 (m, 3H), 7.16 (d, *J* = 1.6 Hz, 2H), 6.99 (m, 2H), 4.12 (t, *J* = 5.9 Hz, 4H), 3.72 (s, 6H), 3.52 (s, 2H), 2.91 (t, *J* = 5.9 Hz, 4H). ¹³C NMR (100 MHz, D₂O) δ 138.18 (s), 135.76 (s), 129.11 (s), 128.43 (s), 127.51 (s), 123.19 (s), 123.14 (s), 122.43 (s), 122.38 (s), 57.34 (s), 52.96 (s), 47.31 (s), 35.64 (s). ESI/MS: *M/Z* - Found (Calcd.): 162.60(162.61, CNC²⁺), 360.04(360.19, CNC²⁺+Cl⁻)

L3Bn: ¹H NMR (400 MHz, CD₂Cl₂) δ 10.77 (s, 2H), 8.25 (t, *J* = 1.5 Hz, 2H), 7.57 (t, *J* = 7.8 Hz, 2H), 7.35 (d, *J* = 7.9 Hz, 4H), 7.31 – 7.23 (m, 5H), 7.08 (t, *J* = 1.7 Hz, 2H), 4.91 (t, *J* = 7.0 Hz, 4H), 4.03 (s, 2H), 3.28 (t, *J* = 7.0 Hz, 4H), 2.31 (m, 4H), 1.23 (d, *J* = 6.8 Hz, 12H), 1.18 (d, *J* = 6.8 Hz, 12H). ¹³C NMR (100 MHz, CD₂Cl₂) δ 145.39 (s), 138.62 (s), 138.49 (s), 131.69 (s), 130.23 (s), 129.68 (s), 128.32 (s), 127.36 (s), 124.58 (s), 123.69 (s), 123.51 (s), 59.46 (s), 53.21 (s), 47.38 (s), 28.64 (s), 24.31 (s), 23.74 (s).

L4Bn: ¹H NMR (400 MHz, CD₂Cl₂) δ 9.98 (s, 2H), 7.73 (m, 2H), 7.60 (m, 2H), 7.26 (s, 4H), 7.18 (m, 5H), 7.11 (m, 2H), 4.61 (t, *J* = 6.6 Hz, 4H), 3.78 (s, 2H), 3.19 (t, *J* = 6.7 Hz, 4H), 2.41 (s, 12H). ¹³C NMR (100 MHz, CD₂Cl₂) δ 140.82 (s), 138.02 (s), 134.97 (s), 134.35 (s), 131.72 (s), 128.92 (s), 128.38 (s), 127.39 (s), 123.55 (s), 120.54 (s), 119.20 (s), 58.65 (s), 53.35 (s), 47.90 (s), 20.75 (s). ESI/MS: *M/Z* - Found (Calcd.): 252.72 (252.66, CNC²⁺), 584.20/586.12 (584.23/586.23 CNC²⁺+Br⁻)

L5Bn: ¹H NMR (400 MHz, CD₂Cl₂) δ 11.12 (s, 2H), 8.09 (t, *J* = 1.8 Hz, 2H), 7.64 (d, *J* = 9.0 Hz, 4H), 7.55 (t, *J* = 1.8 Hz, 2H), 7.14 – 7.09 (m, 3H), 7.02 (d, *J* = 9.0 Hz, 4H + m, 2H), 4.78 (t, *J* = 6.6 Hz, 4H), 4.07 (q, *J* = 7.0 Hz, 4H), 3.84 (s, 2H), 3.15 (t, *J* = 6.6 Hz, 4H), 1.42 (t, *J* = 7.0 Hz, 6H). ¹³C NMR (100 MHz, CD₂Cl₂) δ 159.92 (s), 138.52 (s), 136.14 (s), 129.02 (s), 128.21 (s), 127.59 (s),

127.09 (s), 123.69 (s), 122.90 (s), 119.78 (s), 115.75 (s), 64.13 (s), 58.55 (s), 53.41 (s), 47.60 (s), 14.43 (s). ESI/MS: M/Z - Found (Calcd.): 268.76 (268.65, CNC²⁺), 572.16 (584.28 CNC²⁺+Cl⁻)

L2H: ¹H NMR (400 MHz, D₂O) δ 8.56 (s, 1H instead of 2H due to exchange with D₂O), 7.36 (d, *J* = 14.6 Hz, 4H), 4.20 (t, *J* = 6.0 Hz, 4H), 3.79 (s, 5H), 3.00 (t, *J* = 6.0 Hz, 4H). ¹³C NMR (100 MHz, D₂O) δ 136.24 (s), 123.62 (d, *J* = 4.4 Hz), 122.25 (d, *J* = 4.7 Hz), 48.43 (s), 47.33 (s), 35.70 (d, *J* = 2.9 Hz).

L3H: ¹H NMR (200 MHz, D₂O) δ 8.97 (s, 2H), 7.66 (br s, 2H), 7.47 (br s, 2H), 7.30 (m, 6H), 4.24 (t, *J* = 5.9 Hz, 4H), 3.00 (t, *J* = 5.9 Hz, 4H), 2.10 (m, 4H), 0.92 (d, *J* = 6.8 Hz, 24H). ¹³C NMR (100 MHz, D₂O) δ 145.35 (s), 137.07 (s), 131.74 (s), 129.95 (s), 125.18 (s), 124.49II (s), 123.12 (s), 49.46 (s), 47.76 (s), 28.23 (s), 23.22 (s), 23.08 (s). ESI/MS: M/Z - Found (Calcd.): 263.80 (263.70, CNC²⁺), 606.20/608.16 (606.31/608.31 CNC²⁺+Br⁻)

L4H: ¹H NMR (400 MHz, CD₂Cl₂) δ 9.74 (t, *J* = 1.6 Hz, 2H), 7.84 (t, *J* = 1.8 Hz, 2H), 7.55 (t, *J* = 1.9 Hz, 2H), 7.22 (br s, 4H), 7.12 (br, 2H), 4.48 (t, *J* = 5.6 Hz, 4H), 3.21 (t, *J* = 5.6 Hz, 4H), 2.35 (br, 12H). ¹³C NMR (100 MHz, CD₂Cl₂) δ 140.70 (s), 135.08 (s), 134.41 (s), 131.57 (s), 123.77 (s), 120.53 (s), 119.22 (s), 49.56 (s), 47.58 (s), 20.68 (s). ESI/MS: M/Z - Found (Calcd.): 207.68 (207.64, CNC²⁺), 494.08/496.10 (494.19/496.19 CNC²⁺+Br⁻)

L5H: ¹H NMR (400 MHz, CD₂Cl₂) δ 10.67 (s, 2H), 8.16 (t, *J* = 1.5 Hz, 2H), 7.62 (d, *J* = 9.0 Hz, 4H), 7.56 (t, *J* = 1.7 Hz, 2H), 6.91 (d, *J* = 9.0 Hz, 4H), 4.63 (t, *J* = 5.5 Hz, 4H), 4.01 (q, *J* = 7.0 Hz, 4H), 3.25 (t, *J* = 5.5 Hz, 4H), 1.41 (t, *J* = 7.0 Hz, 6H). ¹³C NMR (100 MHz, cd₂cl₂) δ 159.75 (s), 136.11 (s), 127.63 (s), 124.08 (s), 123.07 (s), 119.88 (s), 115.54 (s), 64.05 (s), 49.15 (s), 47.87 (s), 14.44 (s). ESI/MS: M/Z - Found (Calcd.): 223.68 (223.63, CNC²⁺), 482.04 (482.23 CNC²⁺+Cl⁻)

Generation and characterization of precatalyst 5:

Solution of Ag-NHC **4** (315 mg, 0.5 mmol) and Ru(DMSO)₄Cl₂ (242.15, 0.5 mmol) in 20 mL dichloromethane was added to 250 mg of resin supported BEMP base (2-2.5 mmol/g loading on 2% DVB cross-linked polystyrene). The suspension was heated overnight at 60 °C. During this time solution color changed to deep blue and grey precipitate formed. Upon cooling, the solution was filtered and CH₂Cl₂ was evaporated until *ca.* 2-3 mL remained. Diethyl ether was added (30 mL) while stirring to precipitate the blue solid. After removal of the solvent by filtration, redissolution/precipitation was repeated twice and the blue solid was dried in vacuum. Resulting samples containing **5** were used directly for catalysis without any purification. Elemental analysis: C:49.54; H:5.95; N:9.50; Ru:13.88 was used to calculate the metal loading.

Small amounts of precatalyst **5** can be purified by passing through short basic alumina plug. 240 mg of crude material eluted with dichloromethane yield 20 mg of green solid, which can be crystallized by vapor diffusion (DCM/Et₂O). Crystallization from THF-DCM/pentane in the presence of *ca.* 5 eq of ^tBu-isocyanide leads to formation of **5**_{ICN} that was only used for molecular structure analysis.

Complex **5**: full spectrum presented on Figure 7.5. ^1H NMR (400 MHz, CD_2Cl_2) δ 7.07 (d, $J = 2.0$ Hz, 1H), 6.84 (d, $J = 2.0$ Hz, 1H), 6.74 (s, 1H), 6.68 (s, 2H), 6.64 (s, 1H), 6.45 (d, $J = 2.0$ Hz, 1H), 6.37 (d, $J = 1.9$ Hz, 1H), 4.94 (m, 1H), 3.76 (m, 1H), 3.59 (d, $J = 11.2$ Hz, 1H), 3.04 (m, 3H), 2.57 (d, $J = 9.6$ Hz, 1H), 2.27 (s, 3H), 2.13 (m, 1H), 1.79 (s, 3H), 1.76 (s, 3H), 1.51 (s, 3H), 1.29 (s, 3H). ESI-MS: Found: 1193.32. Calcd: $[\text{Ru}_2(\text{CNC})_2\text{Cl}_3]^+$ 1193.2947. HRMS (ESI-TOF): Found: 1193.2943 ($\Delta=0.3$ ppm)

Catalytic ester hydrogenation

For *in situ* protocol catalyst stocks were prepared according to the following procedure: 25 μmol of ligand were suspended in 1 mL THF and treated with 50 μmol of LiHMDS in 0.5 mL THF (75 μmol for **L1H**). The suspension was agitated at room temperature for 1-2 minutes until no solid was visible and added to solution/suspension of metal precursor in 0.5 mL THF. The mixture was agitated for 1-2 minutes until a clear solution was formed. For Ir-catalyzed hydrogenations, the loadings were increased to 30 μmol metal and ligand in 1 mL THF.

Small scale ester hydrogenation procedure

In the glove box, a stock solution of catalyst, alkoxide base, THF solvent, dodecane and ester were combined in a crimp cap vial. The vial was sealed with a septum and transferred to the Premex A96 hydrogenation reactor. The reactor was purged 5 times with N_2 (10 bar) then H_2 (10 bar), pressurized with H_2 (50 bar), warmed up to the desired temperature and stirred at 300 rpm. Reaction conditions and results are reported in the chapter. At the end of the reaction, the reactor was purged with N_2 and the samples analyzed by GC/FID and GC/MS. The retention times of products and starting material were determined by using the commercially available reference materials. All mass balance were closed within +/- 10% error margin. Analogous procedure for S/C = 5900 experiments on Scheme 7.8 was used for hydrogenation in 10 mL stainless steel autoclaves.

Hydrogenation of ester on 50mmol scale

Tests were performed in Top Industrie 100 mL stainless steel autoclave. The vessel was evacuated at 150 $^\circ\text{C}$, purged several times with argon, and the reaction medium was introduced by cannula transfer. The autoclave was flushed with hydrogen, preheated to reaction temperature and filled with hydrogen up to operating pressure of 50 bar. The catalyst was then introduced via a dosage device and the reaction started. Constant pressure was maintained by a compensation device fitted with Bronkhorst EL-FLOW MFC unit and digital pressure meter. The compensation was done with H_2 to maintain constant partial pressure in the reactor. Samples were withdrawn via dip-tube installation (dead volume 4 μl , sampling volume 110 μl), diluted to 1mL with EtOH and immediately analyzed by GC-FID. Loadings are indicated in the Chapter on Figures 7.3 and 7.6. TOF values were determined at the initial stage of the reaction as the derivative of the $\text{TON}=f(t)$ curve.

7.7. Notes and References

- (1) Dub, P. A.; Ikariya, T. *ACS Catal.* **2012**, *2*, 1718.
- (2) Grey, R. A.; Pez, G. P.; Wallo, A.; Corsi, J. *Chem. Commun.* **1980**, 783.
- (3) Grey, R. A.; Pez, G. P.; Wallo, A. *J. Am. Chem. Soc.* **1981**, *103*, 7536.
- (4) T. Teunissen, H.; J. Elsevier, C. *Chem. Commun.* **1997**, 667.
- (5) Teunissen, H., T. ; Elsevier, C., J. *Chem. Commun.* **1998**, 1367.
- (6) Zhang, J.; Leitus, G.; Ben-David, Y.; Milstein, D. *Angew. Chem. Int. Ed.* **2006**, *45*, 1113.
- (7) C. Gunanathan; D. Milstein, *Chem. Rev.* 2014, DOI: 10.1021/cr5002782.
- (8) Abdur-Rashid, K.; Clapham, S. E.; Hadzovic, A.; Harvey, J. N.; Lough, A. J.; Morris, R. H. *J. Am. Chem. Soc.* **2002**, *124*, 15104.
- (9) Ikariya, T.; Murata, K.; Noyori, R. *Org. Biomol. Chem.* **2006**, *4*, 393.
- (10) Gunanathan, C.; Milstein, D. *Acc. Chem. Res.* **2011**, *44*, 588.
- (11) Spasyuk, D.; Smith, S.; Gusev, D. G. *Angew. Chem. Int. Ed.* **2012**, *51*, 2772.
- (12) Spasyuk, D.; Smith, S.; Gusev, D. G. *Angew. Chem. Int. Ed.* **2013**, *52*, 2538.
- (13) Kuriyama, W.; Matsumoto, T.; Ogata, O.; Ino, Y.; Aoki, K.; Tanaka, S.; Ishida, K.; Kobayashi, T.; Sayo, N.; Saito, T. *Org. Proc. Res. Devel.* **2011**, *16*, 166.
- (14) Edworthy, I. S.; Blake, A. J.; Wilson, C.; Arnold, P. L. *Organometallics* **2007**, *26*, 3684.
- (15) Westerhaus, F. A.; Wendt, B.; Dumrath, A.; Wienhöfer, G.; Junge, K.; Beller, M. *ChemSusChem* **2013**, *6*, 1001.
- (16) Hopkinson, M. N.; Richter, C.; Schedler, M.; Glorius, F. *Nature* **2014**, *510*, 485.
- (17) Delaude, L.; Szypa, M.; Demonceau, A.; Noels, A. F. *Adv. Synt. Catal.* **2002**, *344*, 749.
- (18) Junge, K.; Wendt, B.; Jiao, H.; Beller, M. *ChemCatChem* **2014**, *6*, 2810.
- (19) O, W. W. N.; Morris, R. H. *ACS Catal.* **2012**, *3*, 32.
- (20) Edworthy, I. S.; Rodden, M.; Mungur, S. A.; Davis, K. M.; Blake, A. J.; Wilson, C.; Schröder, M.; Arnold, P. L. *J. Organomet. Chem.* **2005**, *690*, 5710.
- (21) Occhipinti, G.; Bjørsvik, H.-R.; Törnroos, K. W.; Fürstner, A.; Jensen, V. R. *Organometallics* **2007**, *26*, 4383.
- (22) Flader, C.; Liu, J.; Borch, R. F. *J. Med. Chem.* **2000**, *43*, 3157.
- (23) Dong, Q.; Rose, M. J.; Wong, W.-Y.; Gray, H. B. *Inorg. Chem.* **2011**, *50*, 10213.
- (24) Douthwaite, R. E.; Houghton, J.; Kariuki, B. M. *Chem. Commun.* **2004**, 698.

On the catalytic hydrogenation of CO₂ and carboxylic acid esters

The growing abundance of carbon dioxide, associated mainly with the fossil fuel combustion, sparked the search for efficient CO₂ utilization techniques. Catalytic transformation of CO₂ is recognized as one of the solutions to this challenging problem. In fact, catalysis allows recycling the CO₂ by transforming it back into the liquid fuel. This possibility is realized in the reversible CO₂ hydrogenation to formic acid, where the latter serves as a liquid storage agent for H₂. The reverse reaction – dehydrogenation of formates - liberates the H₂ that can be utilized in fuel-cell applications. To make this concept viable, one requires a catalyst capable of fast hydrogen loading and liberation via formic acid generation or decomposition. Therefore, the search for such system was the main initial focus of the current work. Inspired by pioneering works of Nozaki and Fujita who disclosed exceptionally active Ir catalysts for CO₂ hydrogenation, we turned our attention to bifunctional catalysis, as the latter was proposed to be the cornerstone of their activity in CO₂ hydrogenation. With this remarkable prior art, we targeted our research at the analysis of how the CO₂ hydrogenation catalysts function and how the bifunctional behavior impacts their catalytic performance.

Bifunctional catalysts are widely used in modern chemical industry. Coined in its modern form in late 1990's, the term “bifunctional” or sometimes “metal-ligand bifunctional” implies the participation of two catalyst functionalities in the catalytic reaction. Such cooperation enables the new reaction pathways that would be impossible in conventional catalysis that relies on the reactivity of the metal alone. For example, both H₂ and CO₂ can be activated via bifunctional mechanism using the cooperative Ru-PNP pincer complex described by Milstein and co-workers. However, the activity of bifunctional Ru catalysts in CO₂ hydrogenation has never been addressed before and the relevance of the metal-ligand cooperation in catalysis remained unknown.

The first use of cooperative Ru-PNP pincer catalyst in hydrogenation of CO₂ is reported in Chapter 2. Particular focus was laid on the detailed investigation of the mechanism of catalyst transformations under CO₂ hydrogenation conditions, namely in the presence of a base and gaseous reactants. We discovered a complex and interconnected reaction network underlying the chemistry of Ru-PNP under the catalytic conditions which led to an Ru-PNP formate intermediate as the most thermodynamically stable species that

was also identified as the resting state of the catalytic reaction. We made a clear distinction between the catalytic role of the two products of cooperative substrate activation by the dearomatized Ru-PNP* species. Namely, hydrogen activation leads to a *trans*-dihydrido Ru-PNP complex that showed the best catalytic performance, whereas the cooperative activation of CO₂ by Ru-PNP* inhibited the CO₂ hydrogenation activity of Ru pincer catalyst. The addition of water during catalysis was demonstrated to counter the inhibition via the selective hydrolysis of inactive species leading to catalytically competent ones.

Having demonstrated the promising activity of Ru-PNP catalyst in hydrogenation of CO₂ the research in Chapter 3 was focused on the optimization of catalytic activity of this system in hydrogenation of CO₂ as well as in the reverse transformation – dehydrogenation of formates. We established the activity of Ru-PNP in the latter reaction and demonstrated the outstanding catalyst stability by reaching TON values of over a million with no catalyst deactivation. We report on the critical role of the base promoter in the decomposition reaction. The strength of the base controls the rate-determining step of the formate dehydrogenation. In the presence of a weak base, the reaction is controlled by the cleavage of the C-H bond in the H-COO⁻ anion. On the contrary, the H₂ recombination from Ru hydride and [BH]⁺ pair determines the rate of the reaction in the presence of strong bases. The respective catalytic reactions were characterized by strikingly different kinetic behavior and exhibited opposite kinetic isotope effects in the decomposition of OH/OD and CH/CD labeled formic acid.

The efficiency of the CO₂ hydrogenation reaction with Ru-PNP catalyst was further optimized in the second part of Chapter 3. In this case we carried out a detailed mechanistic analysis of the underlying reaction paths which pointed towards the conditions of the catalytic reaction that allowed reaching outstanding reaction rates (TOF) up to 1 800 000 h⁻¹ that is an order of magnitude higher than the previous record, set at significantly higher temperature and pressure. The mechanistic analysis of the catalytic CO₂ hydrogenation further pointed out the negative effect of the non-innocent ligand participation in catalysis. In addition, we experimentally confirmed the possibility of the RDS control in CO₂ hydrogenation, that was proposed in our theoretical investigation.

We further sought to apply our mechanistic insight in heterogeneously-catalyzed hydrogenation of CO₂. A search for the heterogeneous CO₂ hydrogenation catalyst was conducted in Chapter 4. Supported Au/Al₂O₃ catalysts showed the best performance in an extensive screening study employing a wide range of supported and free gold nanoparticulate catalysts. This study established the crucial role of metal-support

interactions for Au-catalyzed CO₂ hydrogenation. Namely, basic supports were found beneficial for the catalyst performance and the exclusion of the support resulted in no activity at all. Au/Al₂O₃ was stable under basic reaction conditions and capable of providing equilibrium conversions at relatively low temperature without observed deactivation. The interface between metallic gold and alumina support is proposed as the active site in CO₂ hydrogenation.

With a goal to develop a stable and sustainable alternative to Ru-PNP pincers we prepared a new family of Ru pincers based on N-heterocyclic carbene donor groups. Their synthesis and reactivity was the subject of Chapter 5. Ru-CNCs are shown to be very versatile compounds. The CNC ligand in these compounds can either bind to Ru in a conventional manner forming normal NHCs or it can coordinate in a mixed normal/abnormal manner. This selection is controlled by the steric properties of the ligand and by the anionic composition of the reaction medium. Furthermore, in the presence of nitriles, Ru-CNCs form cooperative adducts akin of Ru-PNP adducts with CO₂, where the added moiety is bridging the ligand and metal via newly formed C-C and Ru-heteroatom bonds. Interestingly, Ru-PNP is not capable of nitrile activation under studied conditions. Dearomatization of the pyridine ligand backbone in Ru-CNCs can be triggered by the reaction with alkoxide base. Further reactivity of deprotonated Ru-CNC with H₂ and CO₂ resembles closely that of its phosphine counterparts with the exception of a much higher stability of the cooperative Ru-CNC adducts.

A high stability of the cooperative Ru-CNC adduct with CO₂ raised a concern for the catalyst performance in CO₂ hydrogenation. Indeed, in Chapter 6 we observed a rapid deactivation of Ru-CNC in this reaction, that was directly associated with cooperative adduct formation. Experimental and theoretical observations point out that cooperative CO₂ adduct of Ru-CNC is the most stable intermediate that can be formed with Ru-CNC under the catalytic conditions. This situation was strikingly different from that in the case of Ru-PNP, where the most stable intermediate was the catalytically competent Ru-formate complex. Therefore, Ru-CNC catalyst was destined to deactivate unless the cooperative adduct formation was surpassed. This can be done by reducing the partial pressure of CO₂ during operation that favors the catalytically potent intermediates over the inhibiting ones. Under optimized conditions, Ru-CNC performs steadily with no deactivation observed.

Having performed the reactivity analysis for Ru-CNC, we found that metal-ligand cooperative transformations are more favorable for this catalyst compared to the phosphine

analogue. Therefore, we expected a better performance for Ru-CNC in reactions, where metal-ligand cooperation was shown to have beneficial effects such as hydrogenation of esters. While Ru-PNP is essentially inactive in this reaction, Ru-CNC provides good activity in reduction of aromatic, aliphatic and cyclic esters.

Last section of our work presents further development of the bis-NHC-catalyzed ester hydrogenation. In Chapter 6 we observed how the use of NHC donors instead of phosphines enables new catalytic properties in Ru pincers based on lutidine backbone. Chapter 7 deals with tuning of the remaining part of the pincer ligand – its cooperative site. When the long-range pyridilmethylene cooperative function is replaced with an amine one, a more intimate contact between the metal and the reactive ligand site is realized. The benefit of this modification was demonstrated by at least a hundred-fold increase of ester hydrogenation activity in the case of an amino pincer. In fact, the simplest “*in situ*” catalyst formation approach already gives a catalytic system competitive with the state-of-the-art. Further improvement of the catalyst formation protocol leads to unprecedented initial TOF values of 120 000 h⁻¹ in hydrogenation of ethyl hexanoate at 70 °C. The active precatalyst in the latter case was identified. Easy synthesis and isolation of this compound is a promising undertaking that can potentially yield a very active catalyst based on cheap and easily accessible bis-NHC ligands.

Throughout this Thesis we have investigated the activity of a number of cooperative catalysts in hydrogenation of polar substrates. We firstly concluded that metal-ligand cooperation (MLC) is not necessarily involved in the actual catalytic reaction. Moreover, in the case of CO₂ hydrogenation, MLC can lead to the activity inhibition. The strength of this negative impact correlates with the ability of the catalyst to participate in cooperative substrate activation. However MLC effects can be very beneficial for hydrogenation of esters.

Secondly, we demonstrated how a careful analysis of reaction mechanisms in reversible hydrogenation of CO₂ can prompt the ways to improve the catalyst efficiency, reactivate the inhibited catalyst or protect the catalyst from deactivation. Taken together, our findings place Ru pincer systems in the focus for further application in reduction of CO₂ and formate-based H₂ storage.

Throughout this work we show that the critical look on the catalytic reaction is necessary to make progress, especially when cooperative catalysts are employed. These multi-tool systems have a broad set of tunable functionalities – donor groups, cooperative function type, flexibility of the ligand backbone, etc. Each catalytic reaction may require a

specific set of functions. One, two or all of them may be important for catalysis. Without a clear view of the reaction mechanism, the experimental search for the optimal catalyst formulation may take years of work.

Therefore, we believe the key factor to the success lies in the communication between different expertise areas including experimental homogeneous and heterogeneous catalysis and computational chemistry. An example in Chapter 4 shows how one can find similarities between very different homogeneous and heterogeneous catalysts for CO₂ hydrogenation. Only with combined effort in experiment and theory we can expect to make the basis for such discoveries predictive and not coincidental.

Acknowledgement

Four years in the IMC made me a better person. For that I should firstly thank my promoters. Evgeny, you embody a set of qualities that can shape any person into a decent member of society. In my case the “доработка напильником” may have taken a bit more effort due to the impurity of the starting material, but I’m happy with what you did. My mental stability, critical approach and overwhelming sense of urgency are results of your work. Thank you! Emiel, thank you for your patience and guidance. You were always there to set a beacon when I was finding my way.

Each of my Doctorate Committee members taught me a lesson that I kept in mind over these years. Dear Christophe, the July of 2012 was the toughest time I can recall. But you have to sand the log to make it smooth, they say. Dear Laurent, thank you for brightly exemplifying the term “efficient”. Dear prof. Müller, thank you for putting me in a proper framework at the beginning of my work. It was, is and hopefully will be the pleasure to work with you. Dear Bas and Rint, thank you for the valuable input during the N3C’s and at the TU/e. Your sincere interest and openness were a genuine inspiration.

Matthew Patrick Conley, thank you for attaching my hands where they are supposed to grow from. It’s you who showed me that cutting the corners is never worth it.

I would like to thank ICMS for sponsoring my work, for making my trip to ETH possible and for providing a unique and highly responsive environment, that is a true pleasure to be in. Thank you, prof. Meijer! Thank you, Sagitta!

A special thanks to my youngest co-authors Erik (aka Hamster) Schulpen and Robbert (aka Bob Putin) van Putten. Boys, you were wonderful students. I wish you good luck with whatever you choose to come your way. Another bright member of our group, whom I had a pleasure to work with, had already made a career choice. So, good luck, Wilbert. If your work does no longer involve HPLC you know which song to listen to ☺

Nikolay, I forgive you. Masha, the credit is actually yours. Andrey, I forgive you too, but the credit is Nikolay’s this time. Evgeny the Jr. – good luck on the new spot - не посрами!

Christiaan, every time I board a ship I will think of what happened in Lyon and stayed in Lyon. Our long walk was unforgettable. William, please preserve your charm - it illuminates everything and everyone around you. Arno, p2 116:p40 12: p61 12: p80 15: p99 18: you got the rest ☺. Lennart, keep on shining!

My groupmates also deserve a special notice: Padre – you have proven the concept once, but don’t forget about reproducibility studies; Jan – thanks for a picky eye; Johan – your phrase “look at me – I’m 50 years old and I still get this mess” was an eye opener.

And thank you for a valuable lesson that most important things are better done “after lunch”. Adelheid, Brahim, Ad thank you for your remarkable skills and handyness. Ivo, thanks for providing the critical look and your outstanding social and physical agility. And of course your help in improving my aesthetic perception. Emma, shame we haven’t seen the war horse on kinderdijk, but as they say – the night is young. James, we will meet one day to come back to the one of those block rockin’ beats.

My dear hom-ous Evert and Alberto, our time together was short, but it was the one to remember. I learned from you guys that purity of the workbench does not correlate with the purity of compounds made on it. And of course to stay away the windows after midnight – you never know what is on the other side.

Henkk, Serge, Bram, Janus, Matt, Lech, Joost, Jose – thank you gents for throwing the ideas in when I needed them. Frans, Ad and Ad - veel danken voor uw coöperatie and uitstekende hulp!

Special thanks for Todd Helmenstine of sciencenotes.org who generously provided the periodic table design on the back cover.

Norman and Wancy, thank you guys for keeping me fed! Same stands for José and Janine who always took care of me in Helix. Bedankt, dames! Vorrei esprimere la mia gratitudine ai Napoletani per aver inventato la mozzarella, che ha contribuito in modo decisivo alla mia dieta durante il mio percorso di ricerca!

Jan! I promise to strum as good as I can!

И, наконец, спасибо моей семье за поддержку и терпение! Мама, папа, Миша, бабушка - спасибо вам! Вера, солнце, ну ты знаешь :)=

List of publications

- 1) Filonenko, G. A.; Cosimi, E.; Lefort, L.; Conley, M. P.; Coperet, C.; Lutz, M.; Hensen, E. J. M.; Pidko, E. A. *ACS Catal.* **2014**, *4*, 2667
- 2) Filonenko, G. A.; Hensen, E. J. M.; Pidko, E. A. *Catal. Sci. Technol.* **2014**, *4*, 3474
- 3) Filonenko, G. A.; van Putten, R.; Schulpen, E. N.; Hensen, E. J. M.; Pidko, E. A. *ChemCatChem* **2014**, *6*, 1526
Front cover. Highlighted in *ChemistryViews* and Dutch national newspaper *NRC handelsblad*
- 4) Filonenko, G. A.; Conley, M. P.; Copéret, C.; Lutz, M.; Hensen, E. J. M.; Pidko, E. A. *ACS Catal.* **2013**, *3*, 2522
- 5) Filonenko, G. A.; Smykowski, D.; Szyja, B. M.; Li, G.; Szczygieł, J.; Hensen E. J. M.; Pidko, E. A. *ACS Catal.*, **2015**, *5*, 1145
- 6) Pritchard, J.; Filonenko, G. A.; van Putten, R.; Hensen E. J. M.; Pidko, E. A. manuscript is currently submitted to *Chem. Soc. Rev.*

Publications outside of the scope of current thesis:

- 7) Almutairi, S. M. T.; Mezari, B.; Filonenko, G. A.; Magusin, P. C. M. M.; Rigutto, M. S.; Pidko, E. A.; Hensen, E. J. M. *ChemCatChem* **2013**, *5*, 452
- 8) Zhu, X.; Rohling, R.; Filonenko, G.; Mezari, B.; Hofmann, J. P.; Asahina, S.; Hensen, E. J. M. *Chem. Commun.* **2014**, *50*, 14658
- 9) Khassin, A. A.; Kustova G.N.; Jobic, H.; Yurieva, T. M.; Chesalov, Y. A; Filonenko, G. A.; Plyasova L. M.; Parmon, V. N. *Phys. Chem. Chem. Phys.* **2009**, *11*, 6090
- 10) Khassin, A. A.; Jobic, H.; Filonenko, G. A.; Dokuchits, E. V.; Khasin, A. V.; Minyukova, T. P.; Shtertser, N. V.; Plyasova L. M.; Yurieva, T. M. *J. Mol. Catal. A:Chem* **2013**, *373*, 151
- 11) Khassin, A. A.; Filonenko, G. A.; Minyukova, T. P.; Molina, I. Yu.; Plyasova L. M.; Larina, T. V.; Anufrienko, V. F. *React. Kinet. Mech. Catal.* **2010**, *101*, 73
- 12) Simentsova, I. I.; Khassin, A. A.; Filonenko, G. A.; Chermashentseva, G. K.; Bulavchenko, O. A.; Cherepanova, S. V.; Yurieva, T. M. *Rus. Chem. Bul.* **2011**, *60*, 1827
- 13) Minyukova, T. P.; Khassin, A. A.; Baronskaya, N. A.; Plyasova L. M.; Kriventsov, V. V.; Rozhko, E. S.; Filonenko, G. A.; Yurieva, T. M. *Kinet. Catal.* **2011**, *53*, 504

Curriculum Vitae

Georgy A. Filonenko was born on June 13, 1988 in Elizovo (Kamchatka, USSR). After graduating from the high school in his hometown in 2005 he entered a Natural Sciences department in the Novosibirsk State University (NSU). He specialized in the Catalysis and Adsorption Chair and performed his graduate research under the supervision of dr. Alexander Khassin at Boreskov Institute of Catalysis. Specializing mainly in non-isothermal kinetics he graduated in 2010 with *summa cum laude* with thesis entitled “The study of the activation features of copper-containing mixed oxide catalysts”.



In 2011 he joined the IMC group at TU Eindhoven under supervision of prof. Emiel Hensen and dr. Evgeny Pidko. His research, featured in this book, was focused on the development of active catalysts for the reduction of CO₂ and esters.

